

ATOM GUIDING IN FREE-SPACE
LIGHT BEAMS AND PHOTONIC
CRYSTAL FIBRES

by

John Gregor Livesey



University
of
St Andrews

Thesis submitted for the degree of

Doctor of Philosophy

30th January 2007

Declarations

In submitting this thesis to the University of St Andrews I understand that I am giving permission for it to be made available for use in accordance with the regulations of the University Library for the time being in force, subject to any copyright vested in the work not being affected thereby. I also understand that the title and abstract will be published, and that a copy of the work may be made and supplied to any bone fide library or research worker.

Signature of candidate..... date.....

I,, hereby certify that this thesis, which is approximately 60,000 words in length, has been written by me, that it is the record of work carried out by me and that it has not been submitted in any previous application for a higher degree.

Signature of candidate..... date.....

I was admitted as a research student in September, 2000 and as a candidate for the degree of Doctor of Philosophy in September, 2000; the higher study for which this is a record was carried out in the University of St Andrews between 2000 and 2005.

signature of candidate..... date.....

I hereby certify that the candidate has fulfilled the conditions of the Resolution and Regulations appropriate for the degree of Doctor of Philosophy in the University of St Andrews and that the candidate is qualified to submit this thesis in application for that degree.

signature of supervisor..... date.....

Dedications

In “the lab” there were a few people without whom the place felt more cold, these friends were Hannah Melville, Klaus Metzger, Graham Milne, David Gherardi, Tanya Lake, and especially Daniel Rhodes. Daniel deserves particular credit for preventing numerous experimental mishaps where angels-fear-to-tread, for an endless source of wry wit and for being one of the few who understood my film-related humour; “Now there’s something you don’t see every day”. I must also give him credit for a number of diagrams seen herein and a large quantity of information drawn from his thesis used in chapter 3, thank you Daniel.

I owe sincere gratitude to Proff. Kishan Dholakia for inspiration, guidance and support throughout my entire Ph.D. I could not have wished for a better supervisor. Jointly, Kishan and Dr. Donatella Casateri provided those all-important solutions to experiments that felt as if they would never work – those magical tweaks that only supervisors seem capable of.

To my parents for providing unending love and support throughout an extended university stay where low income, seemingly uninterrupted distractions and cavalier indifference must have generated inordinate concern. This thesis represents the culmination of 29 years of parental enthusiasm and support given with no provisos. Where I go now is a choice they have left me free to make; I will forever be *extremely* grateful for that. I can’t thank you enough guys.

Finally, there are a few who have made university and in fact, every activity, feel more worthwhile. Their opinion has always been important and their friendship more so. These are people whom I hold as family, they are (in no set order), Matt Bell, Tim Karle, Melanie Ayre, Elaine Cross, James Whyte, Andrew Lyle, David Hunt, Leon Jackson, Mark Wharry, David Tosh, Mark Paxton, Grant Williams and Catriona Wilson. I would not be the same person if these people were not around. I hope life provides me with an opportunity to manifest my gratitude to them.

Abstract

In this thesis I describe experimental work and present data on the guiding of Rubidium atoms along free-space propagating light beams as well as within hollow core glass fibres, namely photonic crystal fibres. I describe experiments, laser systems and vacuum trap assemblies designed to facilitate this guiding.

These experiments are intended to aid progression within the field of cold atom guidance wherein narrow diameter, long distance hollow-fibre guides are a current goal. Realisation of these guides could lead to promising applications such as atom interferometers and spatially accurate, multi-source, atom depositors.

Herein, guided fluxes are observed in free-space guiding experiments for distances up to 50mm and up to 10GHz red-detuning from resonance. Additionally hollow-core, Kagome structured, quasi- and true-photonic crystal fibres are characterised. Finally a number of detailed fibre-guiding magneto-optic traps are developed.

Both cold atomic-beams and cold atomic clouds are reliably positioned above fibre entrance facets in conjunction with a guiding laser beam coupled into the fibre core.

Issues regarding optical flux detection outwith fibre confinement appear to have hindered observation of guided atoms. A far more sensitive detection system has been developed for use in current, ongoing fibre-guide experiments.

“This is your life, and it’s ending one minute at a time”

- Sinister, but motivational comment from Mr. Tyler Durden.

Contents

Dedications	i
Abstract.....	ii
Contents	iv
Publications.....	vii
Glossary of Acronyms	viii
Chapter 1	1
Laser Cooling & Guiding of Rubidium Atoms	1
1.1 Brief history of Laser Cooling	2
1.1.1 Basic Mechanics of Laser Cooling.....	4
1.1.2 Sub-Doppler Cooling – Polarisation Gradient Cooling	11
1.1.3 Progressing from Atom Cooling to Atom Trapping	18
1.1.4 Beyond MOT Cooling.....	21
1.2 Guiding atoms	21
1.2.1 The Dipole Force.....	21
1.2.2 Red Guide, Blue Guide and Scatter	25
1.2.3 Blue Detuned LG and Bessel beams	27
1.2.4 Atom Extraction from a MOT.....	31
1.3 Hollow-Capillary Fibre Guiding of Atoms	34
1.3.1 Capillary fibre	36
1.3.2 Van der Waals Interaction.....	38
1.3.3 Red Detuned Capillary Guiding.....	39
1.3.4 A Hybrid Theory?	42
1.4 Guiding in Photonic Crystal Fibres.....	43
1.4.1 The Photonic Band Gap	44
1.4.2 Multi-Dimensional PBG	45
1.4.3 Photonic Crystal Fibre.....	47
1.5 Bibliography	57
Chapter 2.....	61
Review of Published Red-Detuned Hollow-Fibre Atom Guiding Experiments	61
2.1 Optical Fibre Guides	61
2.1.1 Red-Detuned Capillary Fibre Guiding	63
2.1.2 Further Considerations for Red-Detuned Fibre Guides	68
2.1.3 Optical Fibre-Guides, Conclusion.....	76
2.2 Dark Hollow Beam Guidance in a Hollow Core.....	77
2.3 Chapter Conclusion	78
2.4 Bibliography	79
Chapter 3.....	80
Laser Systems for Cooling, Guiding and detection of Atoms.....	80
3.1 Trapping Lasers.....	81

3.2	Frequency Stabilisation	88
3.2.1	Doppler-Free Saturated Absorption	90
3.2.2	Current and PZT Locking - ECDLs	92
3.2.3	Current and PZT Locking – TUI Laser	95
3.3	Titanium Sapphire Guide laser.....	96
3.4	Nd:YVO ₄ Guide Laser	99
3.5	Laser Shuttering	100
3.6	Optical Atom Detection Systems	102
3.6.1	Fluorescence Probe	103
3.6.2	Absorption Probes	106
3.6.3	CCD Detection	107
3.7	Conclusion.....	108
3.8	Bibliography.....	109
Chapter 4.....		110
Realisation of Magneto-Optic Traps for Atom Guiding		110
4.1	Atom Traps for Free-Space Guiding	111
4.1.1	Fundamental Trap Requirements	111
4.2	Realising a Magneto-Optic Trap for fibre-Guiding Experiments	117
4.2.1	Differences Between Free-Space and Fibre-Guiding Traps	118
4.2.2	Superstructure Assembly.....	122
4.3	Fibres in an Atom Trap	124
4.3.1	Assembly	124
4.3.2	In Operation.....	125
4.4	Conclusion.....	127
Chapter 5.....		129
Free-Space Red-Detuned Atom Guiding Experiments		129
5.1	Collinear Far-Off Resonance Gaussian Guiding in the 10-Port Trap	130
5.1.1	Particulars of the 10-Port trap	131
5.1.2	LVIS Generation	133
5.1.3	Atom Detection	135
5.1.4	Guiding Procedure.....	136
5.1.5	Guiding Results.....	137
5.1.6	Concluding Comments on the 10-Port Trap	139
5.2	Dropped Cloud Near-Resonance Guiding in the Drum Trap.....	140
5.2.1	The Drum Trap Particulars.....	141
5.2.2	Atom Detection	143
5.2.3	Guiding Procedure.....	145
5.2.4	Guiding Results	148
5.3	Conclusion.....	160
5.4	Bibliography	162
Chapter 6.....		163
Experimental Fibre Characterisation.....		163
6.1	Important Fibre Parameters.....	164
6.2	Transmission Measurement	167
6.3	Fibre Transmission Results	170
6.3.1	Transmission Efficiency.....	170
6.4	Fibres Selected for Atom Guiding	174

6.5	Conclusion.....	174
6.6	Bibliography.....	176
Chapter 7.....		177
Experimental Fibre Guiding of Atoms.....		177
7.1	Guide Details.....	178
7.2	Atom Flux Detection System.....	181
7.3	Atom Fibre-Guiding Experiments.....	185
7.3.1	Thermal-Vapour Guiding.....	187
7.3.2	Guiding From a LVIS	190
7.3.3	Guiding from a MOT	197
7.4	Fluorescence Probe Detection Efficiency	201
7.5	Conclusion.....	206
7.6	Bibliography.....	208
Chapter 8.....		209
Thesis Conclusion		209
8.1	Summary of Activities	209
8.2	Critique.....	210
8.3	Hotwire Fibre-Guiding Trap	211
8.4	Relevance and Outlook	214
8.5	Bibliography.....	216
Appendix i.....		i
Bessel Beam Guiding in the Glass Trap.....		i
Appendix ii		v
Method of MOT Characterisation		v
Appendix iii		vii
Measurement of Trap Filling Time		vii
Appendix iv.....		viii
Oblique LG Guidance from a LVIS.....		viii

Publications

I successfully presented my 1st year Ph.D. work in a lecture at St. Andrews University and gained the Arthur Maitland prize for best-lecture.

I presented a lecture at the U.K. 2001 “Young Physicist Conference” and won the best postgraduate-lecture prize.

I have presented my research at Physics Congress 2002.

I have presented at the 2003 International Conference of Physics Students (ICPS) and was awarded a ‘best presentation’ prize.

Papers

- **Atom guiding along holographically generated high order Laguerre-Gaussian light beams**
D.P. Rhodes, D.M. Gherardi, J. Livesey, D. McGloin, H. Melville, T. Freearge and K. Dholakia, J. Mod. Opt. **53**, 4, 547-556 (2006)
- **Transient response of a cold atomic beam in the presence of a far-off resonance light guide**
J.G. Livesey, D.P. Rhodes, D. McGloin and K. Dholakia, J. Mod. Opt. **50**, 11, 1751-1755 (2003)
- **Guiding a cold atomic beam along a co-propagating and oblique hollow light guide**
D.P. Rhodes, G.P.T. Lancaster, J.G. Livesey, D. McGloin, J. Arlt and K. Dholakia, Opt. Commun. **214**, 219 (2002)

Conference Paper :

- **All optical guiding and splitting of a cold atomic beam**
Rhodes, D.P. Livesey, J.G. Lancaster, G.P.T. Arlt, J. Dholakia, K.
This paper appears in: Quantum Electronics and Laser Science Conference: QELS '02. Technical Digest, 90-91 (2002)

Glossary of Acronyms

\varnothing	Diameter
AC	Annular core
AOM	Acousto-Optic Modulator
BEC	Bose-Einstein Condensate
BiFi	Birefringent Filter
CCD	Charged Coupled Device (camera)
DHB	Dark Hollow Beam
ECDL	Extended Cavity Diode Laser
EH / HE	Dominant Electric/Magnetic Field
FoV	Field of View
FSR	Free Spectral Range
FWHM	Full Width at Half Maximum
HC	Hollow Core
HeNe	Helium Neon
HWP	Half-Wave Plate
LG	Laguerre-Gaussian
LP	Linearly Polarised (mode)
LVIS	Low Velocity Intense Source
MOT	Magneto Optic Trap
ND	Neutral Density
NIR	Near Infra Red
PBG	Photonic Band Gap
PBS	Polarising Beam Splitter
PCF	Photonic Crystal Fibre
PSD	Phase Sensitive Detector
PZT	Piezo Electric Transducer
Q-PCF	Quasi-Photonic Crystal Fibre
QWP	Quarter-wave plate
Rb	Rubidium
SHIM	Term for secondary magnetic coils
SLM	Spatial light modulator
TEM ₀₀	Transverse Electro-Magnetic (mode)
TIR	Total Internal Reflection
UHV	Ultra High Vacuum
GUI	Graphical User Interface
k_B	Boltzmann's constant

Chapter 1

Laser Cooling & Guiding of Rubidium Atoms

Introduction

At room temperature atoms are moving too fast to be studied. They move in completely random directions at up to 1000m/s, hence they do not remain in view for long enough. Crudely, we can think of the motion of a particle as a measure of its temperature, as we slow it down, we cool it. However, when we cool atoms or molecules in atmosphere, they first condense into liquid then freeze to a solid hence making study more difficult. By cooling in a vacuum, particles find no nucleation sites to condense around and so remain in a low density ensemble, ready for study.

However, atoms need to be cooled to within a few 10s of micro-Kelvin (μK) before they become slow enough for study. Rubidium for example, requires cooling to $\sim 100\mu\text{K}$ before slowing to $\sim 17\text{cm s}^{-1}$. So how do we cool to this level?

In 1997 and again in 2001, the Nobel prize in Physics was awarded for work in the field of atom cooling by light beams and subsequent realisation of a Bose-Einstein Condensate¹ (BEC). For the latter, atoms were condensed into a BEC, wherein all particles occupy the same supremely low, fundamental, energy level. This type of experiment can yield good examples of the phenomena seen at these temperatures; two super-cold clouds of Rubidium atoms have been seen to behave as coherent light does; they were seen to interfere. This was one of the most revealing studies of matter ever.

Let us return to the question of *how* we cool atoms. In their 1997 work the Nobel laureates demonstrate how streams of photons, in a laser beam can be directed against the motion of an atom to slow it down. Given that photons can be thought of as small packets of energy moving very rapidly, incident atoms will absorb their momenta (if they are tuned in wavelength to the correct position relative to a resonance). After

scattering, the atom's velocity against the flow of photons is reduced. Hence laser light works to influence matter by imparting momenta and so providing a powerful method of cooling atoms.

Once optically cooled atoms can be influenced by relatively weak laser fields and so manipulated for accurate study. However, a significant and current task, is to extract atoms from this cold reservoir and subsequently transport them without allowing their temperature to rise beyond unmanageable levels. Thus atom extraction and in particular, efficient atom guidance are the subjects of this thesis.

1.1 Brief history of Laser Cooling

Simply put, laser cooling is the process of removing kinetic energy from atoms through use of optical fields. This energy can be reduced by the transfer of photon momenta from incident laser beams. Atoms can be routinely cooled with light to temperatures as low as $\sim 100\mu\text{K}$ in basic atom traps. Further cooling mechanisms are known to reach temperatures of the order of a few nano Kelvin, at which, quantum degeneracy is observed.

Although the concept of a force from light, 'light pressure', was familiar by the year 1900², its slowing ability was discounted until the invention of narrow linewidth tunable lasers. In 1975 T. Hänsch and A. Schawlow realised that such light sources could exert a substantial force on atoms and potentially be used for cooling³. In 1978, the use of lasers for atom trapping was proposed by Ashkin⁴. Important experimental milestones were reported almost a decade later; the first stopping of a thermal beam⁵ in 1982, the first 3-D cooling⁶ in 1985 and the first 'atom trapping'⁷ in 1986.

Nowadays the majority of research in the field of atom guidance involves creation of BEC atom sources in order to have the coldest atom source for loading into free-space optical guides. The key is to then successfully couple atoms from these free-space beams into modes supported by one of a range of possible waveguide media. This thesis has chosen hollow optical fibres as the waveguides of interest as they offer a number of significant future applications for guided cold atoms, primarily through their mechanical flexibility and the promise of extremely low loss optical throughput.

Setting the Scene

At present there are around 170 cold atom laboratories globally. Of these the majority specialise in BEC generation and resonant effects within the cold cloud. Approximately 20 are involved in the improvement of cold atom transport and only a handful of these are believed to work with hollow-fibres; capillary or crystal structured. To our knowledge there are 3 other research teams^{8,9,10} using photonic crystal fibres (PCF) as their optical-guiding medium and none of them, as yet, have detected atoms emitted from the exit facet of a fibre. Wolfgang Ketterle's research team appear to have come closest by guiding BEC temperature atoms guided into a fibre and detecting 5% of these returning back out the entrance facet after 30ms within the fibre core. In the spirit of research I hope all these groups garner useful results for the atom-guiding community. In the spirit of continued funding I hope St Andrews achieves the same, and publishes soon.

Our work at St Andrews could feasibly provide a landmark result with the realisation and refinement of an extremely efficient cold-atom "hosepipe" wherein atoms could be transported along flexible paths with minimal loss in numbers and negligible temperature increase. The key features, such as optimal laser tuning and power, coupling method, pulsed or continuous-wave guiding, etc. could provide a rough blue-print for similar systems guiding other atomic elements. Which in turn could lead to such devices as multi-element atom depositors, capable of building complex structures (on an atomic scale) layer by layer. Presently this remains a motivational goal to aim for.

There are very few manufacturers of PCF. The majority specialise in solid core designs for the telecoms industry. The available hollow-core (HC) PCF caters mainly for high power beam transport, wherein non-linear effects in a gaseous core can be investigated with less chance of fibre damage. There are few commercially available HC PCFs and fewer still capable of supporting wavelengths necessary for alkalis-atom guidance. At time of writing a metre of such fibre will cost ~£700. Thus we are very fortunate to have Professor P. Russell's research team at Bath university as our partners in research. They agreed at the beginning of this research to provide us with suitably structured PCF segments capable of supporting 780nm light (for guiding Rubidium atoms), and thus significantly boosted our prospects. This collaboration continues today with the ongoing atom guiding experiments outlined in chapter 8.

1.1.1 Basic Mechanics of Laser Cooling

Optical slowing, or cooling is not enough to provide particles for study, they must have a positional dependence so they can be trapped in one place. The idea for the first magneto-optic trap¹¹ (MOT), was conceived by J. Dalibard, who proposed the use of circularly polarised light to slow atoms and the addition of a spherical quadrupole magnetic field such that an atom moving *away* from an origin is Zeeman shifted into resonance with a *counter*-propagating beam which pushes it back towards the origin. Most of the early trapping was performed on Sodium (Na) because it has an almost ideal level structure, with cooling transitions which could be driven by the more efficient cw dye lasers of the time.

At St Andrews we cool and trap Rubidium vapour as it has resonances within the output range of cheap commercially available near infra-red (NIR) diode lasers. The ultimate goal of work reported herein is the efficient transport of atoms through hollow-core photonic crystal fibres. On route to this goal, atom coupling from a MOT into a free-space light beam is investigated. Three atomic sources of distinct velocity groups are used as atomic sources, these are: thermal vapour, ‘low velocity intense sources’ and magneto-optic traps.

The incident photons from on-resonance laser beams transfer small packets of momentum to oncoming atoms. These are absorbed counter to atomic motion, and thus slow the atoms down. The momentum of a single photon is miniscule compared to that of the massive atom, however a laser beam can provide vast numbers of photons. The analogy of a free-wheeling cyclist being stopped by countless numbers of wind-blown rain drops is appropriate. Thus resonant laser light depletes kinetic energy along the axis of the laser beam. This is termed atom cooling. Strictly speaking this is not a change in temperature, as the atom is not exchanging any thermal energy nor does it reach thermal equilibrium with its surroundings despite maintaining a steady state. However it is convenient to express the motion of an atomic ensemble with a well defined average kinetic energy, E_k , in one dimension as a temperature, T , where:

$$E_k = \frac{1}{2} k_B T \tag{1.1}$$

An atom absorbs an oncoming photon by virtue of its constituent electron energy level transitions; provided the photon has a wavelength in resonance with an atomic transition and the majority of atoms repeatedly de-excite to the same initial level, cooling can be achieved. A transition within the tuning range of available lasers and with a strong optical field interaction is chosen to simplify the experimental setup, (the relative interaction strengths of the multiple transitions depend on the orientation of their atomic dipole moment with respect to the polarisation of the input light). On absorbing a photon and receiving a momentum kick of $\mathbf{p} = \hbar \mathbf{k}$ where $\hbar = h/2\pi$, the wavevector $k = 2\pi/\lambda$ and λ is the wavelength of the photon, an electron within the atom is raised to an excited level. Subsequent de-excitation occurs after a time τ , the excited state lifetime of the transition. For Rb^{85} , used here, this is $\tau = 26.63\text{ns}$. De-excitation emits a photon of similar energy. This emission would cancel the slowing effect if the emitted photon were directed parallel to the input photon, however de-excitation emission is isotropic therefore, time averaged absorption and re-emission pushes the atom in the direction of the photon flux, against its original direction. This process is cyclic and is the basis for atom cooling, whereby a photon is absorbed and spontaneously emitted, it is depicted in Figure 1.1.

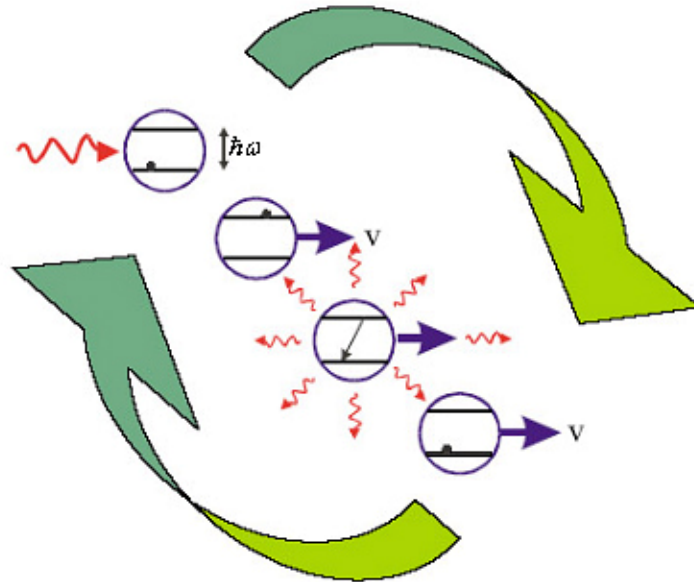


Figure 1.1 : The cyclic nature of photon absorption and re-emission acting to move the atom in the direction of the photon. The atom undergoes an average velocity change of $\hbar k/m$ per cycle.

Radiation Pressure Force

The cooling cycle gives rise to a damping force known as the “Radiation Pressure” force. It is one of two forces induced by laser light passing through an atomic vapour and is experienced only when incident laser light is *close* to resonance with a strong optical transition within an atom. The second induced force is called the “Dipole” force and is discussed in later sections. In his 1978 work, Ashkin mathematically formulated the radiation pressure force induced on an atom as:

$$F = \frac{\Delta p}{\Delta t} = \frac{\hbar k}{\tau / f} \quad 1.2$$

where $\hbar k$ is the aforementioned photon momentum directed along the propagation direction of the light, τ is the natural lifetime of the excited state, and f is a dimensionless intensity saturation parameter.

Doppler Cooling and Optical Molasses

In order to reduce the longitudinal velocity of the atoms from their initial velocities of approximately 10^3ms^{-1} to near zero, approximately 30,000 photon collisions per atom are required. In one dimension it is easy to imagine an atom slowing due to radiation pressure then accelerating beyond control in the opposite direction. A laser tuned to a strong electronic transition can scatter $\sim 10^7$ photons per second, giving rise to an acceleration of $10^4 g$. However, in a rare case of nature aiding experimentation a Doppler shift of atomic transition frequency works to tailor photon absorption dependent on an atom’s velocity. This shift $\omega_D = -k \cdot v$, is induced by atomic velocity v in either direction collinear to the incident laser; note a velocity *parallel* to incoming laser light produces a negative Doppler shift, *anti-parallel* produces a positive shift. A laser frequency below the atomic resonance (red detuned), will cause atoms to preferentially absorb counter propagating photons. Thus, if an input beam is retro-reflected back upon itself exposed atoms will receive a damping force from each of the opposing cooling beams of F_+ and F_- which sum to provide a total damping force of F_{om} described below¹²:

$$F_{\pm} = \pm \frac{\hbar k \gamma}{2} \frac{s_0}{1 + s_0 + [2(\delta \mp |\omega_D|)/\gamma]^2} \quad 1.3$$

and the sum:

$$F_{om} \cong \frac{8\hbar k^2 \delta s_0 v}{\gamma(1 + s_0 + (2\delta/\gamma)^2)^2} \equiv -\beta v \quad 1.4$$

where $s_0 = I/I_{sat}$, $\delta = \omega_l - \omega_{atom}$ is the laser frequency (ω_l) detuning from atomic resonance (ω_{atom}), and $I_{sat} = \pi\hbar c/3\lambda^3\tau$ is the saturation intensity¹³ beyond which atoms do not increase their rate of interaction with the light field; this interaction limit arises due to the lifetime of the excited state and the atomic cross-section for absorption. Benefits in cooling efficiency are not seen beyond $I_{sat} = 1.6 \text{ mW/cm}^2$ for Rb⁸⁵. In order to eliminate consideration of stimulated emission events the cooling laser should have an intensity $I < I_{sat}$. γ is the characteristic spontaneous decay rate $1/\tau$ of the excited atom ($\sim 37.5 \text{ MHz}$ for Rb⁸⁵). The damping coefficient β , in equation 1.4 is linear in the limit of small detunings ($\delta < \gamma$) and low intensities ($I < I_{sat}$), outside of these limits there is a saturation and subsequent decreasing of β .

Importantly, for $\delta < 0$, F_{om} acts against atomic velocity and so viscously damps its motion, conversely for $\delta > 0$, it acts in the direction of atomic velocity thus preventing cooling. Figure 1.2 helps explain this. Atoms travelling against one laser beam will experience photons Doppler blue-shifted closer to resonance thus increasing scatter and momentum transfer. Conversely atoms travelling away from a laser source will experience photons Doppler red-shifted further from resonance, which scatter less and thus impinge on atom velocity far less. Thus momenta transferred from oppositely directed photons act against atomic motion in the axis of the laser light. The slowing is proportional to atom velocity for small enough initial velocities giving rise to viscous damping which in turn leads to the term “Optical Molasses”. This term is aptly descriptive given the slow molasses syrup-like damped motion of atoms in a cooling field.

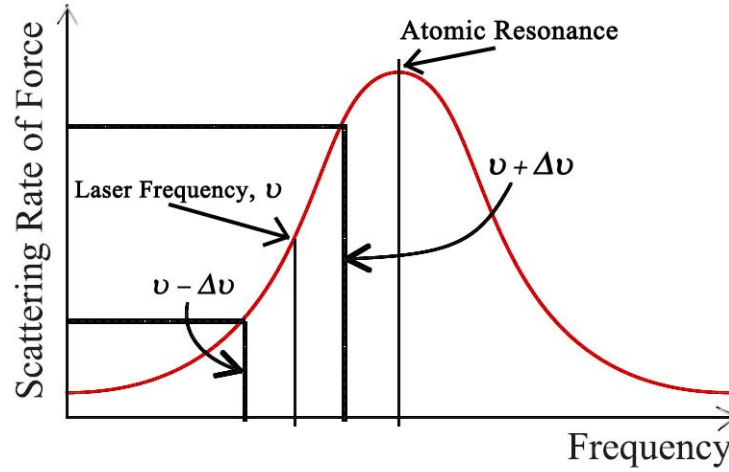


Figure 1.2 An illustration of the level of absorption (or scatter) of incoming light dependent on its detuning from resonance. Provided input cooling light is detuned a small amount, induced Doppler shifts allow tailored absorption of light dependent on atom velocity. Optimum cooling of Rb^{85} is achieved at $\delta \approx \gamma/2$, where $\gamma = 2\pi \times 6.1\text{MHz}$, the natural linewidth of the cooling transition.

Intuitively the optical molasses effect would reduce atom temperature down to $T = 0$, however this is not the case. Each absorption is followed by a spontaneous decay which predominantly emits in a different direction to that of the input photon, therefore a residual energy remains to heat atoms. This heating can ultimately be attributed to the random direction of spontaneously emitted photons and the quantised nature of momentum transfer between photons and atoms in the molasses field; each absorption-emission combination changes atomic momentum by $\Delta p = \hbar k$, and so, on average its kinetic energy changes by a minimum of:

$$E_r = \hbar^2 k^2 / 2M = \hbar \omega_r \quad 1.5$$

where E_r and M are the recoil energy and atomic mass, respectively. Hence the *average* energy gained in each absorption is $\hbar \omega_{abs} = \hbar \omega_a + \hbar \omega_r$ where $\hbar \omega_a$ is the rest frame transition energy (ω_a the atomic resonance). Similarly the average energy of each emission is $\hbar \omega_{emiss} = \hbar \omega_a - \hbar \omega_r$, thus the average energy lost from the optical field over each scattering is $\hbar(\omega_{abs} - \omega_{emit}) = 2\hbar \omega_r$. This occurs at a rate of twice the characteristic absorption and scattering rate γ_s , where the doubling accounts for the presence of two beams. Equation 1.7 defines the characteristic scattering rate (per atom per second):

$$\gamma_s = \frac{s_0\gamma/2}{1 + s_0 + [2(\delta + \omega_D)/\gamma]^2} \quad 1.6$$

where ω_D is the Doppler frequency shift as previously described. This lost energy manifests as kinetic energy of the atom as it recoils from the scattering. Thus the time averaged temperature of an atom after cooling is a minimum defined by the number of recoils it performs. This steady state results in a kinetic energy of:

$$E_k = (\hbar\gamma/8)(2|\delta|/\gamma + \gamma/2|\delta|) \quad 1.7$$

which can achieve a minimum at $2|\delta|/\gamma=1$, which in turn yields the aforementioned ideal detuning for cooling light of $\delta = -\gamma/2$. Thus a minimum temperature $T_D = \hbar\gamma/2k_B$ is reached which is $\sim 240\mu\text{K}$ for Rb⁸⁵. This is termed the Doppler limit whereby the process of cooling to this level is termed Doppler Cooling.

Hyperfine Re-Pumping

Atoms are more complex than the simple two level system depicted so far. Extra energy levels revealed in a more detailed model illuminate a detrimental mechanism for cooling efficiency.

An enhanced definition of the atomic energy levels allows us to describe the 2nd highlighted transition shown in Figure 1.3. This is an extra pumping applied to address the problem of electrons falling out of the cooling cycle via decay to the lower hyperfine ground level, $5S_{1/2}F = 2$. This occurs when an electron illuminated by cooling light, (tuned just below the $F = 3 \rightarrow F' = 4$ transition), is instead excited into the $F' = 3$ level. From there it can decay into the $F = 2$ ground state where it is rendered inaccessible to the cooling field and thus lost from the cooling process.

Approximately one de-excitation in every 1000 results in an atom dropping to this state. This is significant enough to prevent coalescence of a cold cloud within a functional atom trap. In order to prevent this, a second laser source, dubbed the “hyperfine” or “re-pump” laser, is tuned to the $5S_{1/2}F = 2 \rightarrow 5P_{3/2}F' = 3$ transition (for Rb⁸⁵), thus elevating valence electrons back to an excited state from which they de-

excite back down to the ground level of the cooling transition. Hereafter I will refer to the re-pump source as the “hyperfine” source.

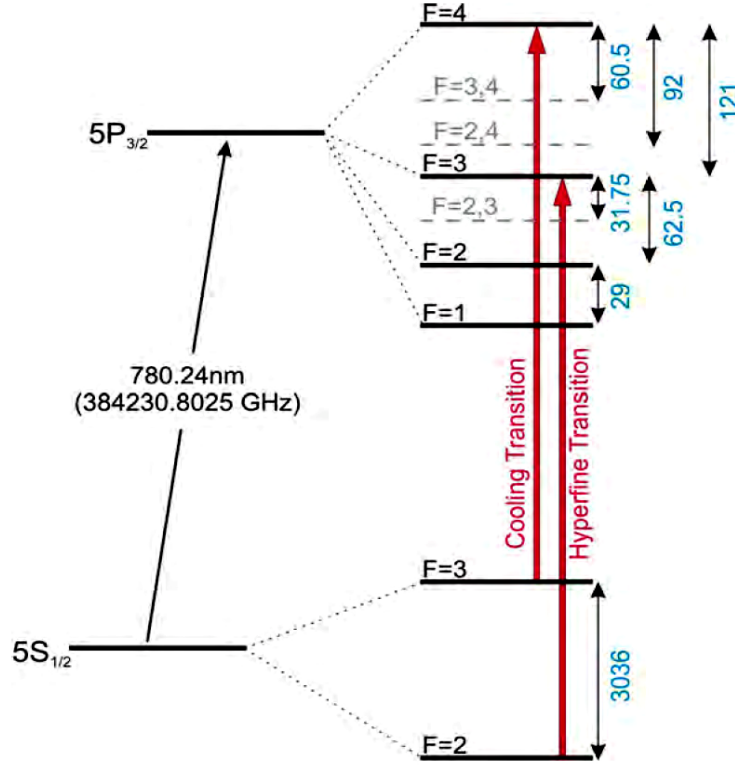


Figure 1.3 : The fine (LHS) and Hyperfine (RHS) structure of Rb^{85} D2 lines. The values in blue are in MHz. Transitions excited by the respective lasers are indicated in red.

Extension to 3D

Optical molasses theory was originally formulated for the 1D case but it accounts for many of the features seen in 3D optical molasses, thus the 3D model is taken as a direct extension. As described for optical molasses, arranging two counter-propagating “atom slowing” beams allows removal of energy in one axis, thus atoms caught in either beam will experience forces centred around $v = 0$. Arranging similar beams on each axis allows atoms caught in the locus to experience a frictional force component in all directions and thus cool in all axes. However, it is important to note that this setup alone is not sufficient for optical trapping because the atoms are able to escape the cooling locus with a drift velocity V_D . This velocity is dictated by the aforementioned residual recoil momentum described by equation 1.9, at this speed an atom can travel 1cm after approximately 10^7 photon interactions, taking $\sim 30\text{s}$ to do so.

$$\frac{V_D}{\omega_R} = \frac{\lambda}{2\pi\sqrt{2\varepsilon}} \quad 1.8$$

where $\varepsilon = \omega_r/\gamma$ is the ratio of the recoil frequency to the natural linewidth of the transition. Such diffusion can be appreciated upon realising the lack of centralising force; atoms caught in any one beam outwith the crossover region will only be slowed in the axis pertinent to that beam. If they enter with velocity components transverse to that beam they will only suffer reduction of velocities in the cooling beam axis and thus exit the optical field with the same transverse velocity components. This happens because there is no centralising force.

Nevertheless, in 3 dimensions nature is again kind to atom trappers, as it was discovered that in practice temperatures of atomic ensembles dropped below the Doppler limit; as much as ~ 10 times lower than the $240\mu\text{K}$ predicted¹⁴. This was ultimately explained through a combination of three factors; light induced a.c.-Stark shifting of the atomic energy levels, *polarisation gradients* in the optical field locus and the probability of optical pumping between hyperfine structure levels. Through these factors a mechanism operates which allows the Doppler cooling limit to be breached. Techniques achieving temperatures below the Doppler limit are identified as Sub-Doppler cooling methods. A description of sub-Doppler cooling is presented in the following sections.

1.1.2 Sub-Doppler Cooling – Polarisation Gradient Cooling

Light Shifts and Optical Pumping

In the presence of a nearly resonant optical field atoms experience slight changes in their energy levels. Termed *light shifts*, these changes are directly related to the intensity of the incident light and result from analysis of the Hamiltonian operator in the presence of off-diagonal elements of the Hamiltonian matrix, as described by Metcalf¹⁵. The magnitude of these shifts, for magnetic ground states in a 1D arrangement of two counter-propagating travelling waves of low intensity I , is given by:

$$\Delta E_g = \frac{\hbar \delta C_{ge}^2}{I_{sat} (1 + (2\delta/\gamma)^2)} \quad 1.9$$

where C_{ge} is the Cabsch-Gordan coefficient describing the coupling between the light field and the atom¹⁶. The value of C_{ge} depends on the magnetic quantum numbers and on the polarisation of the light field. It includes the hyperfine multiplicity of the ground state, thus the magnitude of the light shifts are different for different magnetic sublevels. Essentially the shift results from the Stark effect of the electric field of the applied light and so is called the a.c.-Stark shift. Figure 1.4 provides a simple depiction of the energy shift dictated by optical field intensity. Dependence on field intensity implies that a tailored intensity profile would cause shifting of the energy-levels described by the spatial characteristics of the light.

Further spatial dependence is introduced by the polarisation relationship contained within C_{ge} . Transitions between fine structure $J = 1/2 \rightarrow 3/2$ have ground substates, denoted by their magnetic quantum number $M_g = +1/2$ and $M_g = -1/2$, where this is the projection of their angular momentum along the field. The magnitude of light shifts for each substate is defined by the incident polarisation. Specifically, the light shift for $M_g = +1/2$ is three times larger in light of right-circular polarisation (σ^+), than in left-circular polarisation (σ^-).

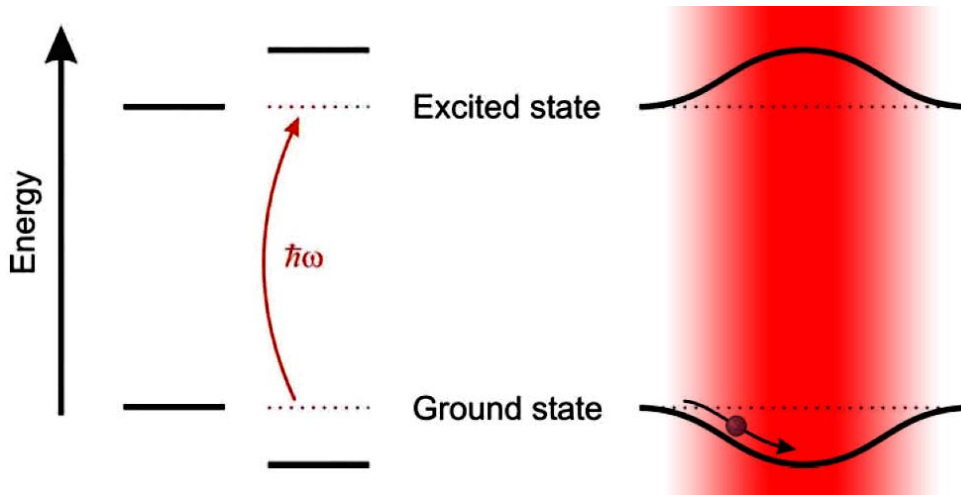


Figure 1.4 : The light shift for a two level atom. Red-detuned light (shown as vertical red stripe) shifts the ground state down, and the excited state up, by the same amount. The amount of shift is dependent on the intensity experienced. Thus the energy level bowing is spatially dependent on the incident intensity profile. A Gaussian profile would create shifts similar to those shown, (right).

Optical pumping into a given magnetic sublevel is caused by different averaged selection rules which occur for each polarisation. That is, σ^+ has an absorption characteristic of $\Delta M = +1$, and subsequent spontaneous emission of $\Delta M = \pm 1, 0$, thus an averaged selection rule of $\Delta M \geq 0$ for each scattering event is generated for σ^+ . This drives the ground-state population into the $M_g = +1/2$ sublevel. Conversely, oppositely polarised light σ^- , will drive the ground-state population into the $M_g = -1/2$ sublevel via an average scattering event selection rule of $\Delta M \leq 0$. Thus it can be arranged that atoms are driven into magnetic ground substates with the greatest lightshifts.

Ultimately a combination of light shifts and circularly polarised light serves to alter the ground state energy of already partially cooled atoms. This is particularly pertinent in a molasses environment where atoms are slow enough to benefit from inherent *polarisation gradients* which serve to perpetually alternate the drive towards each ground magnetic substate.

Polarisation Gradients

Let us consider two linearly polarised beams of similar magnitude, which are oppositely directed and linearly polarised orthogonal to each other (denoted; $\text{lin} \perp \text{lin}$). Interference will cause a cycling of the combined polarisation such that over half a wavelength the polarisation will change from linear vertical (say), to left circular (σ^-), to linear horizontal, to right circular (σ^+) and back to linear vertical again. Thus, atoms within will experience *polarisation gradients*, the rapidity of which singles out a subset of atoms for pumping and subsequent displacement into one of the magnetic ground states, $M_g = +1/2$ and $M_g = -1/2$. This process is illustrated in Figure 1.5 where a cycling polarisation and associated drive into each magnetic ground-state is shown. It can be seen that for the above polarisation arrangement, and in general for any transition \mathbf{J}_g to $\mathbf{J}_e = \mathbf{J}_g + 1$, ground state atoms are predominantly driven into the state with the larger light shift. Provided the detuning is red of resonance ($\delta < 0$), larger light shifts will imply lower energies and thus cool the atoms by dissipating energy.

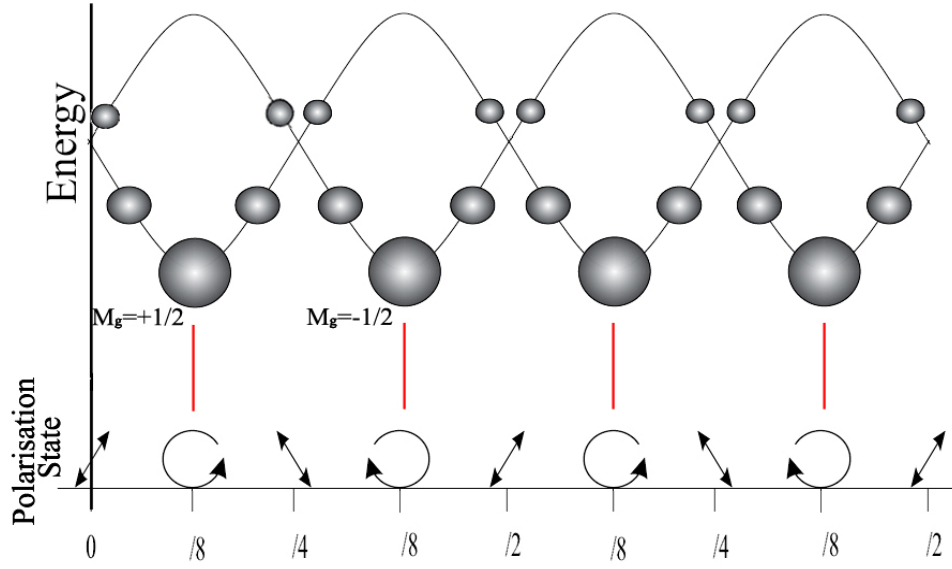


Figure 1.5 : Atoms are preferentially pumped into the lower of two ground state sublevels as they experience spatially varying polarisations in the interference of two counter-propagating, oppositely polarised cooling beams. The driving polarisations are shown on the lower graph. The ground state sublevels are shown on the upper graph, the relative population of each sublevel is indicated by the size of atom depicted.

This cooling mechanism is effective over a limited range of atomic velocities. Damping is maximum for atoms that undergo 1 optical pumping process over a distance of $\lambda/4$ of the cooling light, or time-wise, when the time taken for an atom to work its way from the bottom of a ‘valley’ to the top of an adjacent potential ‘hill’ matches the time to optically pump from one magnetic ground state to the other. In the simple 1D molasses described above an optimal velocity of $v_c \cong \gamma_p/k$ is defined where the pumping rate γ_p increases by a factor of 2 to account for the presence of two beams thus $\gamma_p = s_0 \gamma^3 / 4\delta^2$. (refer to equation 1.7 for the case where $\delta \gg \Gamma$, there γ_s equates to γ_p). The resultant damping force is given by:

$$F = \Delta W / \Delta z \cong \Delta E k \equiv -\beta v_c \quad 1.10$$

where ΔW is the change in potential over distance Δz , ΔE is the light shift and v_c the capture velocity. Assuming a detuning $|\delta| \gg \gamma$ and $C_{ge}^2 = 1$ is chosen for the light shift evaluation in equation 1.10 (as well as substituting $s_0 I_{sat}$ for I), then the damping rate $\beta/M = \hbar k^2 \delta / 2M\gamma = \omega_r \delta / \gamma$. This illustrates a velocity dependent force of equivalent magnitude to the Doppler cooling force described in equation 1.4, but with an influence

over a lesser velocity range γ_p/k . Comparison of the damping coefficient to the maximum of Doppler cooling shows a factor of $(2|\delta|/\gamma)$ increase. Furthermore it can be shown¹⁷ that the momentum diffusion to the optical field is of the same order to that of Doppler cooling, thus lower temperatures can be reached.

Mathematically the damping coefficient for polarisation gradient cooling in Rb⁸⁵ can be written as¹⁸:

$$\beta_p = -\frac{24}{17} \hbar k^2 \frac{(\delta/\gamma)}{1 + 4(\delta/\gamma)^2} \quad 1.11$$

Which differs from equation 1.5 notably by its lack of intensity dependence, thus, in contrast to Doppler cooling, the damping rate for polarisation gradient cooling is constant for increasing input intensity. However this is counterbalanced by the now intensity dependent velocity capture range, which is proportional to I and is ~ 10 to 100 times smaller than that of Doppler cooling. Polarisation gradient cooling therefore comes into play when Doppler cooling begins to break down.

Sub-Doppler cooling was an unexpected experimental result reported and well described by Phillips *et al.*. The temperature achieved by polarisation gradient cooling can be expressed specifically for Rb⁸⁵ as:

$$k_B T = \frac{\hbar \gamma^2}{2|\delta|} \frac{I}{I_{sat}} \left[\frac{29}{300} + \frac{254}{75} \frac{1}{4(\delta/\gamma)^2 + 1} \right] \quad 1.12$$

This sub-Doppler cooling is called ‘‘Sisyphus laser cooling’’ from the Greek myth concerning Sisyphus, the former King who was condemned to push a heavy weight up a never ending series of hills. The atoms lose energy by virtue of having to climb perpetual *potential* hills. This continues until they can no longer surmount the energy barrier, whereby they reach a steady state up to 10 times lower than the Doppler limit (typical values for Rb⁸⁵, $T_D=143\mu\text{K}$, $T_{MOT}\approx 100\mu\text{K}$).

Optical Cooling Limit

Ultimately all optical cooling methods discussed are limited to a minimal temperature called the *recoil-limit*, T_r given by:

$$k_B T_r = \frac{(\hbar k)^2}{2M} \quad 1.13$$

where M is the mass of the atom. Similar to the Doppler-limit, the recoil-limit arises due to the residual energy distributed between cooled atoms due to the quantised nature of optical scattering. While the damping coefficient is independent of input intensity I , the heating rate due to this perpetually scattered residual energy does depend on I . The minimum temperature obtainable thus depends on the ratio of viscous cooling to the heating rate and is therefore proportional to laser intensity.

Polarisation Cooling with Circularly Polarised Input Light

Predominantly, the optical traps used herein employed circularly polarised cooling beams, hence it may be helpful to discuss the mechanism through which circularly polarised light achieves sub-Doppler cooling. Atoms are similarly driven into separate magnetic substates according to the polarisation absorbed, however there are differences in the method by which these substates are addressed and populated. Returning to the previously discussed 1D situation, the magnitude of light shifts for each ground magnetic substate was dependent on position within the cycling polarisation. However two counter-propagating, orthogonal, circularly polarised beams generate an optical electric field with constant magnitude and linear polarisation throughout¹⁹. This means light shifts are spatially uniform and thus cause no energy variations in the ground state levels thus eliminating any Sysiphus cooling. Nevertheless access to a similar cooling mechanism is provided by the combined linear polarisation which precesses at a rate of 2π over one wavelength. This rotating polarisation serves as the quantization axis for the optical electric field, so now the *orientation* instead of positional alignment, of the atomic ground-states relative to the quantization axis becomes the pertinent factor. In accordance, the simplest model must therefore have $J_g = 1$. Atoms have their ground state populations optically pumped to available magnetic substates dependent on the local polarisation experienced.

Additionally, atomic velocities within the light field allow non-adiabatic dissipation of energy into the light field and define selection rules. That is, atoms at rest experience a stationary polarisation direction and thus have their substate populations driven to $M_g = 0$ sublevel. Atoms with $v > 0$ experience a rotating polarisation and undergo pumping in order to follow its orientation. Thus moving atoms attempt to mimic the quantization direction and are driven into $M_g = \pm 1$ substates while doing so. Hence the population of ground magnetic substates tends to lag behind the steady-state distribution of stationary atoms pumped to match the local polarisation/quantisation axis. Specifically, it has been shown²⁰ that atoms travelling towards a beam of σ^+ polarisation are preferentially pumped into the substate of $M_g = +1$ and vice-versa.

Because of different Clebsch-Gordan coefficients, atoms in each substate scatter light six times more efficiently from their preferred polarisation (ie. σ^+ for $M_g = +1$) than from the orthogonal. Moreover, atoms remain in their sublevel following absorption and spontaneous emission hence scattering more light and receiving a large momentum transfer against their motion. Thus atomic motion is damped, to an extent comparable to the $\text{lin} \perp \text{lin}$ configuration, whereby similar temperatures are expected to those of Sympyus Cooling. Figure 1.6 and Figure 1.7 allow comparison of the force rendered on an atom in both $\text{lin} \perp \text{lin}$ and $\sigma^+ - \sigma^-$ situations respectively.

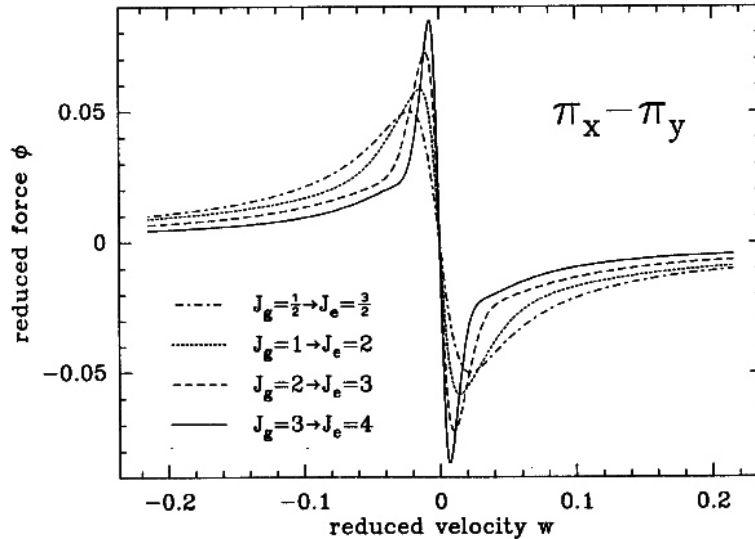


Figure 1.6 : Calculated force on an atom vs. velocity in a 1D molasses where the input polarisations are linear and orthogonal. π_x and π_y denote the orthogonal linear polarisations. Adapted from reference²¹.

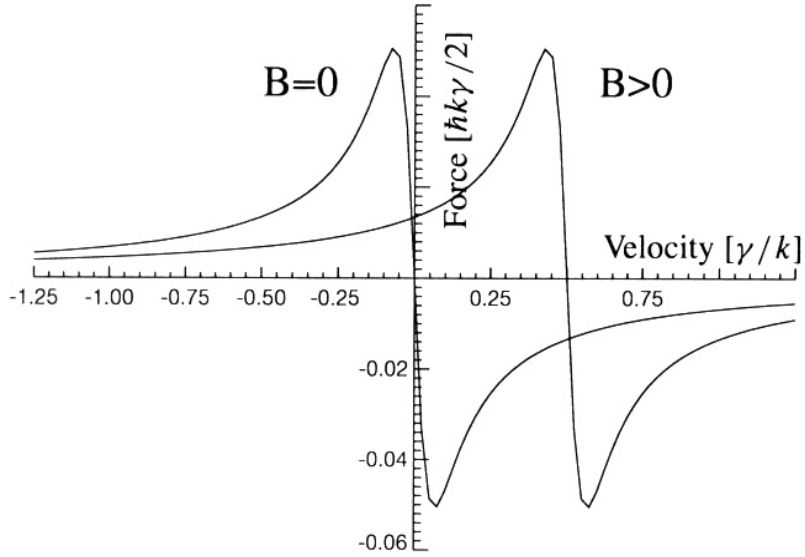


Figure 1.7 : A graph showing force on an atom vs. velocity in a 1D molasses where the input polarisations are orthogonal circularly polarised. Plots are shown for magnetic fields $B=0$ and $B \neq 0$. For $B \neq 0$ atoms are cooled to velocity $v = \omega_z/k$, where $F=0$. $B=0$ at quadrupole centre. The role of magnetic cooling is introduced in 1.1.3. Figure reproduced from reference²²

In the circularly polarised case damping is achieved by virtue of the magnetic substate population imbalance created by the time lag between the atomic orientation and the precessing local polarisation (in the frame of motion of the atom). Comparing this with Doppler cooling, the population imbalance serves to replace the Doppler shift as the mechanism which allows differentiation between the atomic velocity sets and which laser beam they scatter from.

1.1.3 Progressing from Atom Cooling to Atom Trapping

Returning to a 3D situation, three pairs of nearly-resonant counter-propagating, $\sigma^+ \sigma^-$ laser beams with an additional hyperfine beam, combine to produce a molasses region. In our experiments this situation is obtained with three orthogonal retro-reflected cooling beams and a hyperfine squeezed under a cooling beam optic, as shown schematically in Figure 1.. Considering the crossover region of the cooling beams, it can be deduced²³ that the flow of optical energy cannot be directed inwards at all points on the surface of the trapping region, thus the damping force on the atom similarly cannot be directed inwards at all points. Consequently, an entirely optical trap cannot be stable for so long as the trapping force is proportional only to the light intensity²⁴. This is analogous to Earnshaw's theorem for electrostatics, and hence is

called the “optical Earnshaw theorem”. In actuality an all-optical trap is possible²⁵ however a hybrid “Magneto-Optical Trap” (MOT) is more simple and practical.

The magnetic field of a MOT is introduced in order to impose positional dependence upon molasses atoms. This is easily achieved by winding two circular coils with approximately $\sim 50-70$ windings and $\sim 2-3\text{A}$ drive current dependent on coil separation. Provided they are driven in an anti-Helmholtz configuration (as shown in Figure 1.) a magnetic quadrupole is created where a MOT region can exist at $\mathbf{B} = 0$. The linearly inhomogeneous field produces Zeeman splitting of the atomic energy levels proportional to distance from $\mathbf{B}=0$.

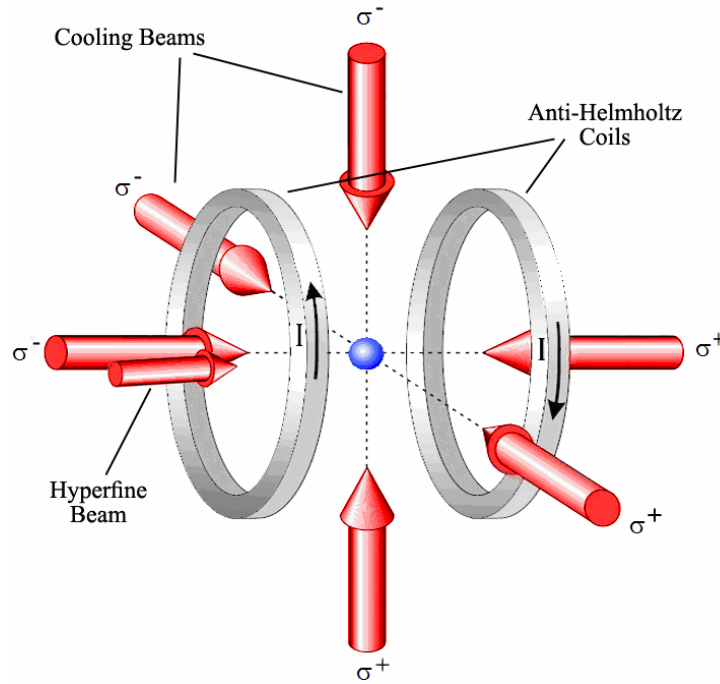


Figure 1.8 : Schematic arrangement of a MOT. Six orthogonal, circularly polarised beams create a 3D optical molasses. Magnetic coils in anti-Helmholtz configuration create positional dependence. The hyperfine beam prevents atoms falling out of the two level cooling cycle.

If counter-propagating cooling beams travelling within an inhomogeneous magnetic field B , are frequency detuned by a small amount δ from the *zero-field* atomic resonance their proximity to resonance varies dependent on their position within the magnetic field. This is due to the three Zeeman components generated in the presence of the magnetic field, these are denoted: $M_e = +1$, $M_e = -1$ and $M_e = 0$. Each level is a Zeeman component of the excited-state of a cooling transition (for which $\mathbf{J}_e = \mathbf{J}_g + 1$), and each is brought closer to resonance with a particular polarisation of light as they undergo Zeeman splitting. As can be seen in the 1 dimensional representation in Figure

1.9, an atom which moves from $z = 0$ has the frequency of each $M_e = \pm 1$ state tuned closer to resonance with a particular polarisation. Thus an atom scatters a specific light polarisation more strongly as it moves further from MOT centre. At $z < 0$, the atom scatters mainly σ^+ light because this light is closer to resonance with the $M_g=0 \rightarrow M_e=1$ transition. Similarly, at $z > 0$ the atom scatters mainly σ^- light. Hence, correct arrangement of σ^+ and σ^- renders a positional dependence centred on $\mathbf{B} = z = 0$ by encouraging scattering of counter-propagating photons.

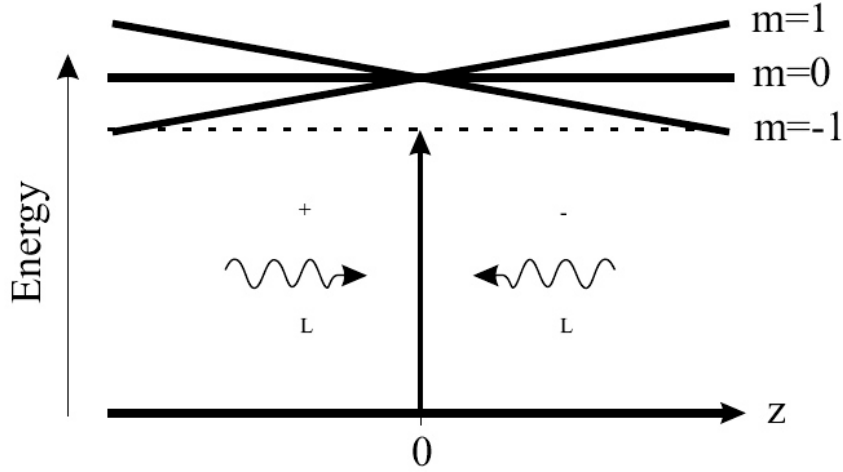


Figure 1.9 : The Zeeman shift instigates a splitting of magnetic sublevels in a 1D MOT. Incident cooling light detuned δ beneath the $\mathbf{B} = 0$ atomic resonance will be closer to resonance with an atom's magnetic sub-levels dependent on position around $z=0$. For an atom positioned at $z > 0$ its $m = +1$ level is raised and its $m = -1$ level is lowered, (reversed for $z < 0$). Thus, polarisations σ^+ and σ^- directed in the $+z$ and $-z$ directions respectively will provide positional trapping and compression of atoms within beam locus.

This viscous damping is similar to that of Doppler cooling but now the effect operates on position via Zeeman splitting as well as velocity via Doppler shift. A $\sim 10 \text{ G cm}^{-1}$ field gradient is sufficient for trapping, though cold clouds have been observed²⁶ with field gradients as low as 4 G cm^{-1} . The relative simplicity, robustness, low-cost and considerable tolerance for beam misdirection, polarisation anisotropy and intensity mismatch of such MOT's have made them the backbone of atom cooling research in the last decade.

1.1.4 Beyond MOT Cooling

Other confinement mechanisms exist beyond those discussed so far, these can be used on route to achieving the sought-after temperatures of Bose-Einstein condensate^{27,28} (BEC) temperatures.

In particular atoms can be trapped in shallow magnetic fields²⁹ through interaction with intrinsic ground- or meta-stable magnetic dipole moments. Where an inhomogeneous magnetic field \mathbf{B} interacts with a magnetic moment $\boldsymbol{\mu}$, to produce a variation in an atoms potential energy, $-\boldsymbol{\mu}\cdot\mathbf{B}$ through a force \mathbf{F} acting upon it;

$$\mathbf{F} = \nabla(\boldsymbol{\mu}\cdot\mathbf{B}) \quad 1.14$$

Further cooling to BEC temperatures can be achieved through techniques such as evaporative cooling. These are not discussed here; for brevity only MOT cooling mechanisms are included. However good reviews can be found in the publications of Cornell & Wieman³⁰ and Adams & Riis³¹.

1.2 Guiding atoms

1.2.1 The Dipole Force

It is now necessary to expand our understanding of the forces experienced by an atom in an optical field. There is an extra force³², over and above those associated with radiation pressure cooling, which derives from the spatial gradient of light shifts induced by the optical field. Known as the *dipole force*, it can be tailored to attract or repel atoms from high intensity regions as the frequency of the light is tuned below or above resonance respectively. The dipole force is commonly used for guiding and manipulating atom flux, however since light shifts scale with intensity high spatial gradients can be created which in turn imply strong potential barriers capable of creating all-optical traps³³. However atom traps based on the dipole force often require efficient cooling mechanisms since their trap depths are ordinarily more shallow (due to residual viscous elements discussed later) than those achievable through use of the radiation pressure force. In this situation initial MOT cooling prior to trap loading is often employed.

Predominantly the dipole force is used to *guide* atoms whereby red and blue detuned beams can be tailored to confine atomic paths and help convey them through free space. It is important to stress that sufficient detuning from resonance removes any longitudinal push, that is atoms mainly experience dipole force in the axis of rapidly changing potential gradient, *transverse* to the beam direction. This is because the radiation pressure scales as I/δ^2 for large detunings whereas the dipole force scales as I/δ , as we shall see below (where δ is the laser detuning from atomic resonance). Hence atom flux in far-off resonance beams must have separate propulsion, e.g. a separate near-resonance beam, gravity or unidirectional ballistic expansion within the guide, another.

In contrast to the radiation pressure force, the dipole force occurs as a result of absorption and subsequent *stimulated* emission, hence it is not limited to the same maximum value of the radiation pressure force ($F_{\max} = \hbar k \gamma / 2$). It derives from a dipole moment p induced in an atom when exposed to an intense optical field. If the strength of the electric field is defined as E , then the dipole moment is given by:

$$p = \alpha E \quad 1.15$$

where α is the polarisability of the atom. For an atom in its groundstate, α has a dispersive nature and is indicated by the blue line in Figure 1.10. Here the relationship between absorption and polarisability is dictated mathematically by the Kramers-Kronig relations³⁴. Thus the dipole force given in equation 1.17 will be positive for frequency detunings below resonance and negative above resonance³⁵:

$$F_d = \frac{1}{2\epsilon_0 c} \alpha \nabla I \quad 1.16$$

where I is the light intensity and ϵ_0 is the permittivity of free space. Hence atoms can be selectively attracted to or repelled from high intensity regions depending on whether the light is detuned below or above atomic resonance respectively.

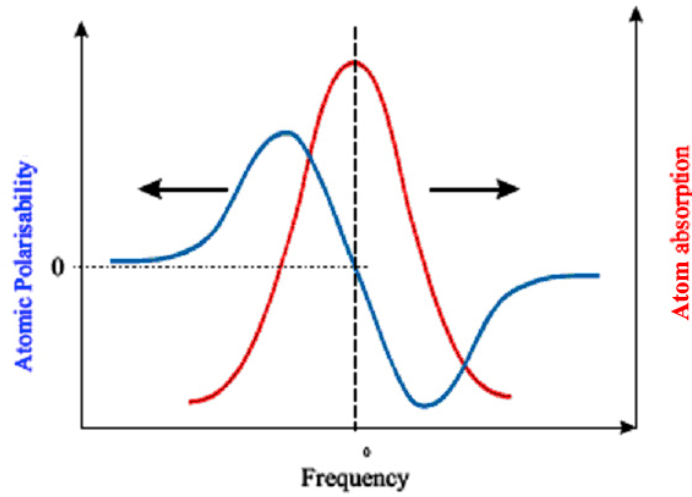


Figure 1.10 : An atomic transition with a characteristic absorption profile as indicated by the red line, will experience a polarisability (blue line) positive for detunings below resonance, and negative for detunings above resonance, as defined by the Kramers-Kronig relations. The change in sign of the polarisability causes the atom to be either repelled or attracted to regions of light depending on the laser frequency.

Thus atoms can be described as experiencing potential wells, or potential walls, dependent on which detuning they are exposed to. If the potential an atom experiences is expressed as a plane surface, the atom itself can be thought of as a marble rolling on this surface continually seeking the lowest potential. This useful and simple description is illustrated in Figure 1.11 which shows the potential well of a red-detuned Gaussian guide and Figure 1.12 which shows the potential barrier of a blue detuned guide (in this case a Laguerre Gaussian ($l=1$) beam). Both have beam waists of $100\mu\text{m}$ and are detuned -10GHz and $+10\text{GHz}$ from resonance for the red- and blue-detuned guide respectively.

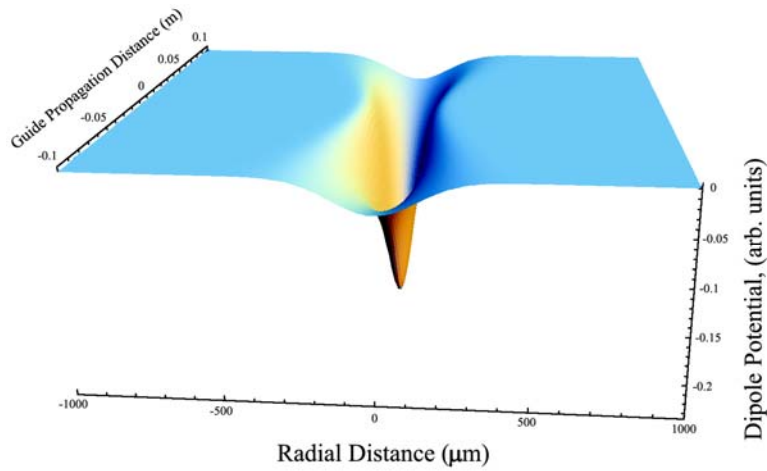


Figure 1.11 : Calculation of the dipole potential of a -10GHz detuned (red-detuned) Gaussian beam of $100\mu\text{m}$ waist. Atoms are drawn into the high intensity region in the centre of this beam, just as marbles would roll into the potential trough.

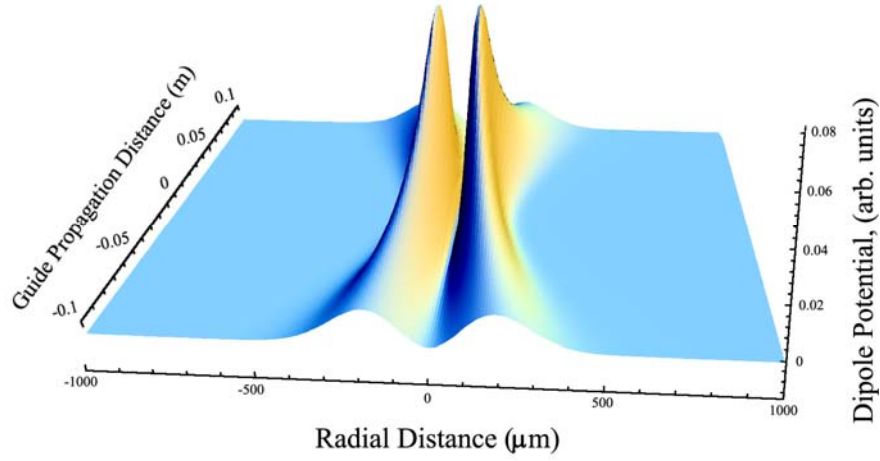


Figure 1.12 : Calculation of the dipole potential of a +10GHz detuned (blue-detuned) Laguerre-Gaussian beam of 100μm waist and azimuthal index $l=1$. Marbles caught within the potential walls would roll along the guide till the surrounding walls were small enough to roll over. Similarly, atoms are pushed from the high intensity regions and can be channelled between them.

Provided a single input beam has a detuning greater than both the transition linewidth ($\delta \gg \gamma$), and the Rabi frequency ($\delta \gg \Omega$), an atom with arbitrary spin state can be strongly affected. The force directing groundstate atoms towards a high intensity region is³⁶:

$$F \cong -\frac{\hbar}{4\delta} \nabla(\Omega(r)^2) = -\frac{\hbar\gamma^2}{8\delta} \frac{\nabla I(r)}{I_{sat}} \quad 1.17$$

where the Rabi frequency, given by $\hbar\Omega = -\mu_{eg}E_0$, defines the coupling between the atom and the light field, of amplitude E_0 , and polarisation $\hat{\epsilon}$ through the atomic dipole moment $\mu_{eg} = e\langle e|\hat{\epsilon} \cdot r|g\rangle$. The Rabi frequency can be written as $\Omega = \gamma\sqrt{I/2I_{sat}}$ where I_{sat} is the saturation intensity. Assuming the beam has a transverse Gaussian profile varying with r described as,

$$I(r) = I_0 e^{-r^2/\omega_0^2} \quad 1.18$$

the above force experienced in the transverse axis can be expressed as,

$$F \cong \frac{\hbar\gamma^2}{4\delta} \frac{I_0}{I_{sat}} \frac{r}{\omega_0^2} e^{-r^2/\omega_0^2} \quad 1.19$$

A longitudinal force, arising from tight focusing, is more complicated and has a greater dependence on the focusing method, however three dimensional trapping can be achieved with this force alone. The seeming contradiction of the *optical Earnshaw's theorem* can be explained by the dependence on *both* the incident intensity and the gradient thereof. Although greater forces can be achieved through the dipole force, the trap depth remains shallow due to a viscous heating component. This is discussed below in the context of its effect on dipole-potential guides.

1.2.2 Red Guide, Blue Guide and Scatter

Returning to a collimated guide removes any *longitudinal* component of the dipole force but retains it's *transverse* confinement properties dependent on its transverse intensity profile. Thus provided atoms are less energetic than the potential depth of the guide, they can be conveyed efficiently. However there are a few factors which can impinge on this efficiency, such as the detuning and intensity of the guide and the subsequent amount of induced scattering.

As previously mentioned, there is no longitudinal pushing force associated with a dipole guide sufficiently detuned from resonance. Since the radiation pressure force (due to scattering) scales with $1/|\delta|^2$ while the dipole force scales with a gentler $1/|\delta|$, only a few GHz detuning is necessary to remove most longitudinal pushing force, particularly in the less stringent collimated-guide configuration (c.f. far off resonance dipole traps^{37,38}). However an intensity increase is needed to compensate for the linear drop off in confining force (as can be seen from equation 1.19). Such an intensity increase could be continued without limit, up to the maximum source capability, if it were not for an associated increase in scatter. Spontaneous scatter induces heating within an atomic ensemble which can ultimately provide enough energy for an atom to escape the potential wells. Assuming the detuning δ is greater than a few linewidths, equation 1.7 can be adjusted to provide the spontaneous scattering γ_s from a single beam:

$$\gamma_s = \frac{\Omega^2 \gamma}{4\delta^2} \tag{1.20}$$

where the Rabi frequency Ω can be re-expressed to illuminate an intensity dependence, as³⁹:

$$\Omega^2 = \frac{2\mu_{eg}^2 I}{\hbar^2 \epsilon_0 c} \quad 1.21$$

where c the speed of light and μ_{eg} the dipole moment described earlier. Thus the scatter rate can be seen to be linearly dependent on intensity, hence implying a value whereby scattering will exceed acceptable limits. Thus conveyance of atoms over arbitrary distance is simultaneously limited by a $1/|\delta|$ dipole force dependence and a linear spontaneous scattering dependence on intensity. A balance between dipole potential and scatter rate must be struck to maximise flux volume and conveyance distance. In this situation the initial loading temperature of the atoms will play the greatest role in deciding the ultimate guidable distance; a lower launching temperature would relax the dipole potential requirements for the guide thus permitting lower intensities and lower scatter. In fact, lowering the initial ensemble temperature is believed to be the single most effective method of increasing guide efficiency.

This problematic scatter agrees with an intuitive perception of red detuned guidance whereby atoms transported within regions of high intensity suffer heating. Physically, this is induced by viscous forces which are inherent in red detuned guides. This heating can be circumvented by use of blue detuned light and a slightly more complex intensity profile. Consideration of equation 1.17 with identical parameters save for a shift from negative to positive (blue) frequency detuning indicates a repulsive force. This force has been put to use in the creation of numerous devices often referred to as *atom optics*. Over and above *dark-traps*^{40,41,42} which are blue-detuned hollow equivalents of the tightly focused dipole-traps, atomic mirrors^{43,44}, lenses⁴⁵ and gratings^{46,47,48} have been created. By using an intensity profile whereby a central dark region is surrounded by blue detuned light, a guide can be created where atoms are transported in the low intensity region by reflections from the surrounding light *walls*. The removal of atoms from *high* intensity regions opens great possibilities for extending the distance over which cold ensembles can be transported efficiently. A *dark hollow beam* (DHB) guide offers confinement and a greatly reduced scatter rate since a grazing incidence path will inflict a minimal time in higher intensity regions, sufficient only to eject atoms back into the low field centre.

1.2.3 Blue Detuned LG and Bessel beams

A method employed at St Andrews to create DHB guides is well described by J. Arlt *et al.*⁴⁹ and is summarised here. Laguerre Gaussian (LG) modes provide annular-shaped intensity profiles where the principle features are, core diameter, radial wall thickness and potential barrier gradient. An LG mode is stable and propagates over large distances and can be chosen to have the majority of its power in the principle annulus. This latter characteristic elevates LG modes above another format called Bessel Beams; also studied at St Andrews, (comparisons were made between fundamental Bessel beams of varying size and LG of varying l index; not reported here, see Dr Rhodes' thesis⁵⁰).

Construction of a LG beam is a relatively simple process of aligning a Gaussian TEM₀₀ mode with an appropriate hologram on an etched glass slide or on a re-writable spatial light modulator⁵¹, both employed at St Andrews. These holograms are designed to provide a phase anisotropy in the input Gaussian which results in a beam with helical wavefronts continually spiralling azimuthally round the propagation axis. In the centre of the mode (on axis) is a phase discontinuity which results in a zero field region in the centre. The modes are labelled as LG_p^l . The indices denote the azimuthal index l , which tells the number of 2π phase cycles around the circumference of the mode, and $p+l$ which tells the number of rings. The p index is of particular importance to DHB guiding as it dictates the portion of light contained in the inner ring. Thus $p=0$ will yield a more efficient guide since all available intensity exists in a single fundamental ring. The effect of the azimuthal, l , index is to alter the separation, gradient, maxima and divergence of the ring structure, Figure 1.13 illustrates these factors.

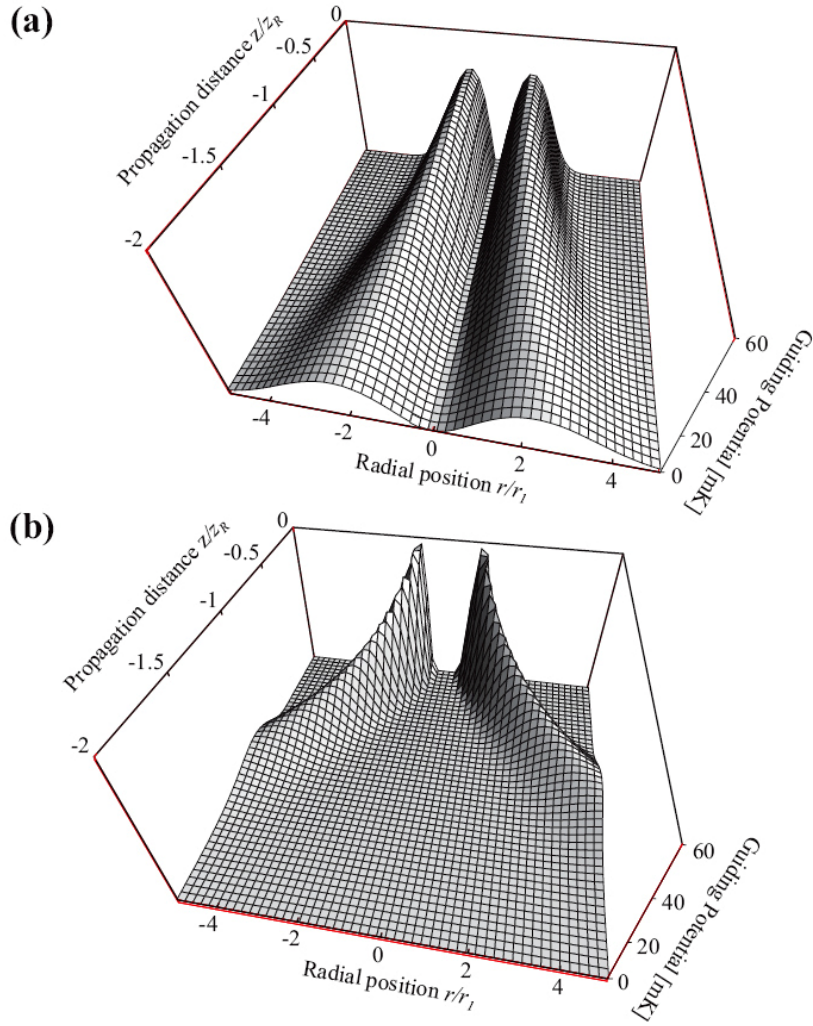


Figure 1.13 : The variation of maximum guiding potential as a function of propagation distance away from the focal region ($z=0$, at top of image). The ring size is fixed. The graphs show the potential for LG orders **a)** $l=1$ and **b)** $l=4$. Note the increase in potential barrier for the $l=4$ beam and also the larger cross-sectional ring diameter, a possible advantage when capturing atoms. The p index here, is fixed at zero, ($p+1$ gives the number of rings).

In Figure 1.13 the dipole potential profiles of $l=1$ and $l=4$ LG modes are shown, they are arranged to have matching ring diameters. An increasing azimuthal index can be seen to provide thinner ringed annuli with correspondingly higher potential maxima and steeper barrier gradients. These are factors which improve atom flux guidance efficiency. Notably, when guiding Neon atoms, an improvement of 8 times the flux was recorded with an $l=5$ mode over an $l=1$ mode⁵². The annular beams ring diameter can also be seen to diverge more rapidly with higher l thus, the broader cross section of high l beams may help funnel atoms into their profile, specifically atoms released from a MOT, as discussed later. A high-order l mode with $p=0$ is believed to provide the most efficient DHB guide.

LG beams confine atoms within potential barriers deriving from atomic dipole moments induced as described earlier. Their resultant dipole force is again defined by equation 1.17, but the intensity profiles which define the shape of the potential barriers are different. An LG_p^l mode has an intensity profile:

$$I(r, z) = \frac{2p!}{\pi(p+|l|)!} \frac{P_0}{w^2(z)} \exp\left(\frac{-2r^2}{w^2(z)}\right) \left(\frac{2r^2}{w^2(z)}\right)^{|l|} \left\{ L_p^{|l|}\left(\frac{2r^2}{w^2(z)}\right) \right\}^2 \quad 1.22$$

where the beam radius $w(z)$, (not to be confused with frequency term ω), is the radius at which a normal Gaussian with a matching outer surface profile falls to 1/e of its on-axis value. This is given at any position z from beam waist w_0 , as:

$$w(z) = w_0 \sqrt{1 + \left(\frac{\lambda z}{\pi w_0^2}\right)^2} \quad 1.23$$

P_0 in equation 1.22 is the power of the beam and $L_p^{|l|}$ is the generalised Laguerre polynomial. This intensity profile is particularly important as it implies a rapid drop in intensity, and hence dipole potential with propagation distance z from beam waist. Hence the experienced dipole-potential is now a function of distance along the guide. Thus a choice must be made to optimise detuning for a particular z position along the guide length. Optimising (by way of changing intensity or detuning) for any z not at beam waist may result in lower guide quality at the waist, where, for example, an increased intensity may generate excess spontaneous emission. However varying the detuning of a fixed intensity beam, in order to optimise dipole potential at a $z \neq 0$ position will serve to spread the guide potential-peak out, making it plateau for a longer distance.

Spontaneous Emission

The chief motivation for use of DHB guides is the reduction in spontaneous emission rate relative to red-detuned guides. In Arlt's paper the spontaneous emission rate of cold atoms falling into a high-order ($l > 0$) LG guide from a MOT is approximated by:

$$\gamma_{sp} \approx \frac{v_r}{2r_{apd}} \left[1 - v_r \exp\left(-\frac{Mw_a\gamma}{\hbar\delta}\right) \right] \quad 1.24$$

where v_r , r_{apd} , w_a and γ , are, the average transverse velocity of the atomic sample, the average penetration depth into the potential barrier from the centre of the dark hollow region, the average width of the optical potential barrier, and the transition linewidth, respectively. The research showed successive l modes with matched ring positions (c.f. beam waists) coupled with an experimental value of $v_r=7\text{cm/s}$ ($T\approx 100\mu\text{K}$), an r_{apd} calculated from energy conservation laws and a detuning of $\delta=7.39\text{GHz}$, provided a spontaneous emission γ_{sp} , which scaled with azimuthal index as shown in Figure 1.14,

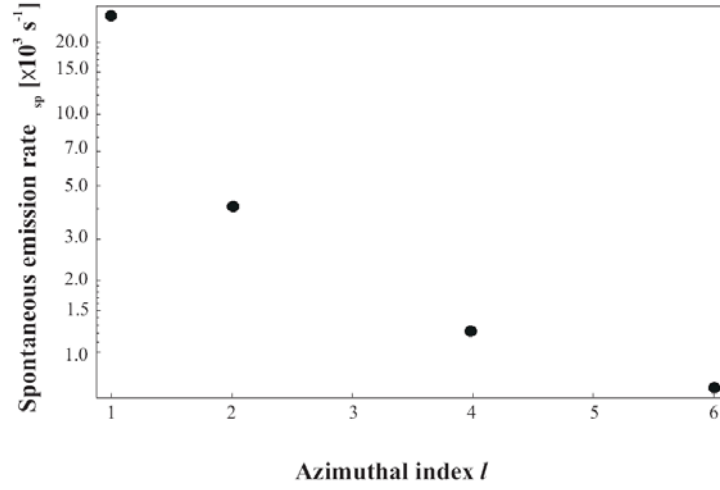


Figure 1.14 : Spontaneous emission rates, γ_{sp} , for Laguerre-Gaussian light beams of different azimuthal indices l averaged over the propagation distance of $2z_R$. A beam power $P_0 = 100\text{mW}$ and $M = 85m_a$, where m_a is the atomic mass unit. Reproduced from J. Arlt.

J. Arlt and K. Dholakia's research team have provided a useful comparison between the scattering rates of differing azimuthal index LG modes, in particular the order of magnitude decrease between a fundamental LG mode and one of high azimuthal index. The decrease in scattering rates can be attributed to atoms spending less time in high intensity guide walls. They are repelled more sharply into the dark centre by steeper gradient walls with increased dipole potential, factors inherent with elevated l modes, thus scatter is further reduced from levels associated with red-detuned guides. In the following paragraph, data regarding the LG_1^4 mode are used to provide a qualitative comparison of spontaneous emission rates of red and blue guides. This is a

very rough comparison given the differing method of confinement and associated variables (e.g. barrier width and gradient, ring separation, dipole potential, atom mean free path before damping, detuning, etc.).

The $l=4$ mode marked on Figure 1.13, is estimated to confine atoms up to a maximum transverse velocity of $\sim 1.18\text{ms}^{-1}$ ($\sim 58\text{mK}$ guide depth) while inducing a scattering rate of $\sim 1.2 \times 10^3$ per second (averaged over twice the Rayleigh range). If a red-detuned, Gaussian guide of diameter matching the FWHM of the LG_1^4 *hollow core* ($\sim 46\mu\text{m}$), was arranged with similar potential depth at opposite detuning (that is $\delta = -7.39\text{GHz}$), it would be able to confine atoms of the same velocity with less power ($\sim 20\%$). However atoms dropped directly from a MOT into this guide would suffer a spontaneous scatter rate of $\sim 3.7 \times 10^6$ per second, a clear 3 orders of magnitude increase. In their work a blue-detuned guide can be seen to provide a reduction in scatter over that of an approximately matching red-detuned Gaussian guide. Thus, in the low temperature regime, where scattering is the chief inhibitor, blue detuned, high l index, dark hollow beams may prove to be the best answer for long distance guiding.

1.2.4 Atom Extraction from a MOT

Having successfully cooled and trapped an atomic ensemble, it is often necessary to extract atoms from the confining MOT potentials for use elsewhere. If a dipole-force guide is simply overlapped across the trapping region, atoms will have to surmount the surrounding potential barriers of the MOT before escaping. This would reduce the efficiency of the guide as atoms would require a minimum energy to enter it. Ultimately, where it is necessary to maintain cold temperatures, a method of lowering or removing the MOT barriers is desirable.

Thermal atomic beams are well established in atomic physics^{53,54}, however here we require transport of high density ensembles with low velocity in the guiding direction, a low velocity distribution and in particular, low kinetic energy transverse to the guide. Such cold atomic beams are of importance in atom lithography and atom interferometry. In particular atom interferometry^{55,56} is seen as a primary motivation for research in this field.

Cloud Release and Guide Coupling

Atoms can simply be released from a MOT region by removal of trapping parameters (by cutting cooling beams or deactivating magnetic coils), indeed this provides the slowest, most versatile atoms for experimenting on. However any separation between MOT region and waiting optical potentials, spatially or temporally, allows ballistic expansion of the cold cloud. Hence it is preferable to locate a guide beam close to a MOT region and to exert a degree of control over the transverse and longitudinal velocities of atoms escaping it.

Studies of atom-loading into a guide have indicated efficient coupling occurs when cloud and guide are arranged to have comparable diameters⁵⁷, hence a guide perfectly overlaid on a MOT cloud (with matching diameters) at the moment it is released (or very slightly before) will receive the greatest number of lowest temperature atoms. However guide width is often dictated by available optics or by a necessity to match the guide mode to that of a hollow-fibre core diameter.

It must be noted that the release of a cloud in this manner does not provide a continuous source of cold atoms for channelling. For cases where a continual source of atoms is required complete removal of MOT parameters is inappropriate, instead atoms can be channelled through a defect in a MOT potential barrier. This is the subject of the following section.

A Low Velocity Intense Source of Atoms

A number of experiments performed herein involved a low velocity intense source of atoms (LVIS). This term is used to describe atoms emitted from a MOT via an imbalance in the radiation pressure forces. This was an effective method of extracting a continuous stream of atoms along a single arm of a standard six-beam MOT arrangement. The imbalance can be created by aperturing one of the MOT beam mirrors⁵⁸, by directly shadowing a MOT beam or by replacing one of the MOT beams with a hollow-beam mode (eg. Laguerre Gaussian). The latter two methods were employed in St Andrews with preference given to the former. This involved inserting a glass slide with a narrow diameter opaque spot into one of the cooling beams. The spot shadow-masked the MOT beam and was typically around 900 μm in diameter (despite attempts to reduce it). Thus molasses cooling was removed from the volume shadowed.

In cases where the cloud size was comparable to, or smaller than, the dark spot, the slide was positioned to overlap only a portion of the MOT with the shadow region. As Figure 1.15 shows, atoms entering the MOT and encountering the shadow region were able to flow out along the diffractively filling shadow. These atoms are referred to as LVIS atoms.

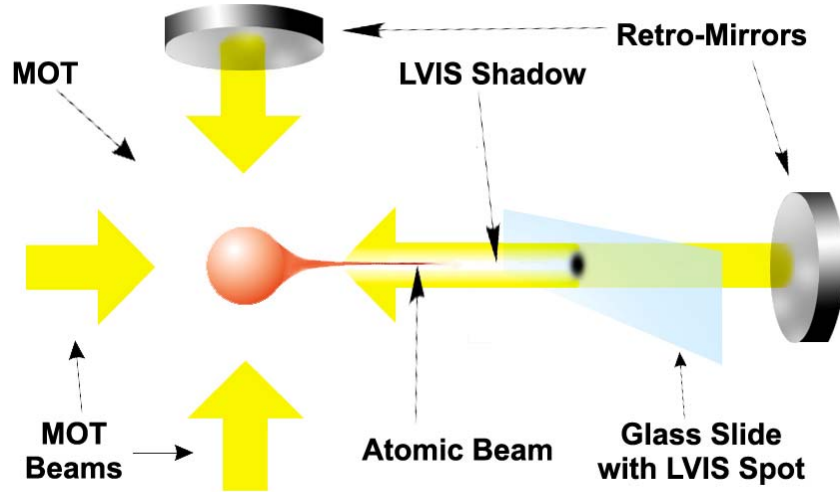


Figure 1.15 : Schematic depicting LVIS generation using an ink spot on a glass slide. The slide can be translated to alter the LVIS intercept point on the MOT cloud. Not drawn to scale.

Ordinarily in St Andrews, atoms in an LVIS remained illuminated by the hyperfine re-pump beam and so were kept in the cooling cycle. Hence atoms falling from the LVIS path were immediately exposed to the full cooling cycle and so recycled back into the MOT. This recycling coupled with a relatively unhindered cooling process continually replenished the MOT maintaining atom population sufficient for continuous operation.

Since the drive to exit the MOT region comes from an imbalance in the radiation pressure force, LVIS atom velocity is determined by the number of photons scattered from the unbalanced portion running collinear to LVIS direction (defining it). Typical LVIS velocities are $\sim 14\text{ms}^{-1}$ for the longitudinal component and a more MOT related $\sim 3\text{cms}^{-1}$ transverse to the LVIS flux. Since a significant portion of the LVIS path remains within the cooling beam locus, accurate balancing of transverse cooling beams is necessary to prevent deflection of the LVIS flux while in transit. Furthermore, atoms enter the LVIS shadow region at random positions within the $\sim 1\text{mm}$ diameter

MOT. Thus atoms receive accelerating scatter for differing amounts of time. This implies a velocity spread in their longitudinal component, typically $\sim 2.7\text{ms}^{-1}$.

Diffraction filling of the LVIS shadow coupled with the atom's fall under gravity gave the LVIS beam a maximum length of $\sim 1\text{cm}$. This length could be extended with a collinear overlapping guide beam, as is demonstrated in our work⁵⁹, though care should be taken to avoid exclusion of atoms from MOT centre when overlapping a near-resonance red-detuned guide or a blue-detuned guide (see Appendix iv).

LVIS is very easy to implement, requiring no components installed within the vacuum system. Atoms siphoned into a LVIS have transverse velocity components small enough to allow subsequent optical manipulation. For these reasons the LVIS was frequently employed in experiments at St Andrews. However, when achievable, a dropped MOT cloud was the most desirable atom loading method; it yielded the coldest atoms. Figure 1.16 illustrates an LVIS cloud generated at St Andrews.



Figure 1.16 : A video still-image of an LVIS cloud observed at St Andrews.

1.3 Hollow-Capillary Fibre Guiding of Atoms

The introduction of optical fibres in the following section leads us towards the ultimate goal of the author's experiments, that is to achieve cold atom channelling through hollow-core optical fibres. The method by which the beam is confined is a key parameter and is discussed in section 1.3.

Flexibility is the prime advantage of fibre guides over free space beams, potentially allowing them to guide atoms around bends in 3 dimensions. This flexibility is limited by loss due to forces at these bends; atoms having a significant mass relative to photons will suffer forces directed toward the fibre wall when any deviation from a straight path is presented. Intuitively a stronger dipole potential will be needed to hold atoms within the guiding beam. However flux loss is not entirely dependent on this simple momentum argument (see Jhe).

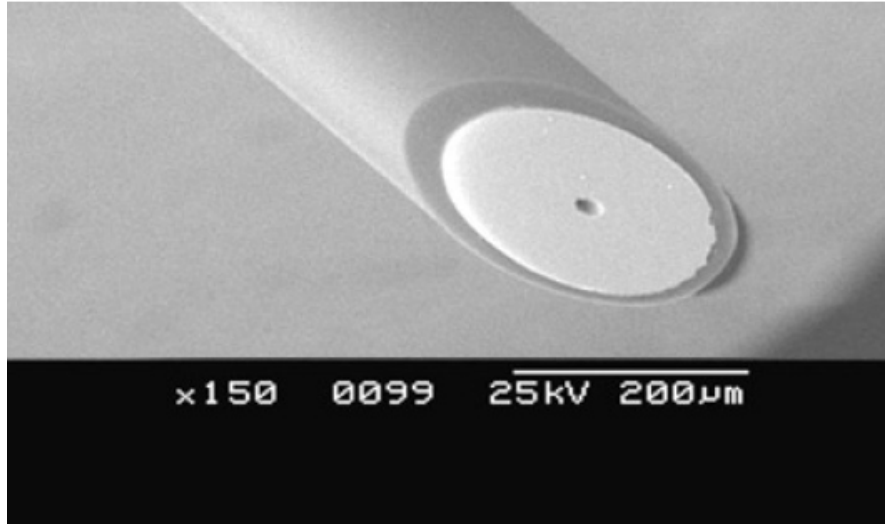


Figure 1.17 : An example of a hollow core capillary fibre, as used by Dall *et al.*

Hollow core fibres consist of a dielectric cylinder with a central missing core, (see Figure 1.17). Light is guided in the waveguide providing a dipole force which is used to confine atoms within the hollow core and keep them away from all internal surfaces. Fibre guidance offers advantages over magnetic guidance as atoms can be transmitted in any magnetic substates⁶⁰. The guiding can be rapidly switched on or off by changing the optical wavelength or laser power. The greatest advantage is that the fibre forms a flexible vacuum chamber, independent of the surrounding atmosphere. and can support an internal vacuum while passing through atmospheric pressure. Disadvantages include possible heating induced by spontaneous emission in the light field, difficulties in outgassing the fibre when pumping down to vacuum pressure, and fabrication imperfections making it difficult to maintain uniformity in the guiding light field. Nevertheless beneficial applications of fibre guidance include ensemble filtering into ‘clean’ vacuums, intra-fibre atom spectroscopy, very accurate positioning⁶¹ for atom deposition⁶², atom transport in-air with flexible directionality and the possibility of mode compression in narrow core fibres. In particular the last of these may prove to

be advantageous for extended cold transport of coherent atoms. Conveyance of atoms in a single atomic mode state is again crucial for all applications involving atom interferometry. For these reasons fibre guidance of atoms is currently an exciting field.

As with free space guidance, the two approaches for fibre atom guiding are based on red solid core guiding (proposed theoretically by Ol' Shanii *et al.*⁶³) and blue detuned light pipe guiding (proposed theoretically by Savage *et al.*^{64,65}). This work initiated fibre-atom research, however the more recent development of photonic crystal fibres (PCF) offers physical solutions to many problems inherent to capillary guidance.

In the following sections capillary fibre guides are discussed along with their relative merits. An introduction to PCF is then given in advance of research presented in later chapters.

1.3.1 Capillary fibre

Capillary fibre typically takes the form of a basic glass (or silicate) annulus with an inner diameter of $\sim 10\text{-}50\mu\text{m}$ forming the hollow core. The annulus is often surrounded by a thick cladding layer of lower refractive index. Conventional optical fibres confine light in a high index core, by total internal reflection (TIR) at the lower-index cladding interface. With a hollow core fibre this is not possible and two separate approaches are necessary for the red and blue optical fields. For the red beam the light is confined by grazing incidence reflections inside the hollow core creating an optical potential along the fibre axis in which atoms can be guided. For the blue detuned guide, light is confined in an annular distribution in the cladding, using TIR at both the inner air boundary and the outer cladding boundary. Evanescent leakage from the annulus enters a short radial distance into the core. This evanescent mode tail shields passing atoms from Van der Waals attraction and so provides the guiding mechanism.

These two methods of light guidance define red- and blue-detuned fibre atom-guiding respectively, both simultaneously prevent energetic atoms from exiting the guide and restrict loss of atoms to attractive Van der Waals forces. Van der Waals (VDW) attraction acts radially from the fibre walls, over a very short range, scaling with the inverse cube of distance from the wall. In the case of hollow fibres it acts within a few

nanometers of the fibre surface to trap atoms on the walls, where they eventually thermalize and later emit into the background vapour.

If VDW attraction and diffusive scattering of laser light from the fibre surfaces can be overcome, the next step involves a narrowing of the fibre core diameter to approach the size of de Broglie wavelengths of an atom ensemble. Atoms travelling within this guide are coerced into modes hence their motion becomes quantised; a significant step to coherent atom propagation. This is a significant future goal of cold atom work and a motivating factor for this thesis.

Bending Capillary Fibre

In 1995 Renn *et al.* completed an experimental investigation on red detuned capillary guidance of Rubidium atoms⁶⁶. They detailed the effects of fibre curvature and followed this in 1996⁶⁷ with theoretical and experimental work describing pertinent aspects of red detuned capillary fibre guiding. These papers were summarized in a comprehensive review of the field published in 2002, in which Jhe⁶⁸ concluded that the tightest bend around which atom guidance can be achieved is limited by the critical radius of curvature of *effective optical guidance* not by a radius dictated by atomic momentum properties. That is, as the bend radius decreases flux loss from optical mode displacement overtakes loss from centrifugal spin-out. Therefore, provided that the laser detuning and intensity generate sufficient dipole potential to saturate guided flux over the entire fibre length, flux reduction will scale primarily with degradation of the optical field (as opposed to any atom-dependent characteristic).

Optical Scatter

Scatter diminishes guide efficiency in two ways; back-scatter from the entry-facet annulus can serve to obscure guiding potentials and it can induce atom-repulsive modes. In particular blue detuned evanescent guiding is most susceptible to repulsive grazing-incidence modes within the HC (generated at indiscriminate distances along the fibre). Such modes can spontaneously heat the atoms and generate transverse momenta large enough to overcome confining potentials. This problem is inherent to evanescent guiding and imperfectly manufactured fibres. In the case of initial facet-scatter in evanescent guides this problem can be circumvented by a secondary Gaussian courier laser (as in Renn *et al.* 1996) or by novel coupling methods demonstrated by Ito *et al.*⁶⁹

where guide light was coupled by total internal reflection off a 45°-cut entrance facet, the experimental setup for this is displayed in Figure 1.18.

In red detuned fibre guides a lesser form of the same problem exists whereby the guiding efficiency of the grazing incidence mode can be diminished by weaker, scatter-generated modes again spontaneously heating the atoms. These modes can be prevented by reduction of the hollow-core diameter, however entry facet scatter can only be removed by better matching of the supported mode.

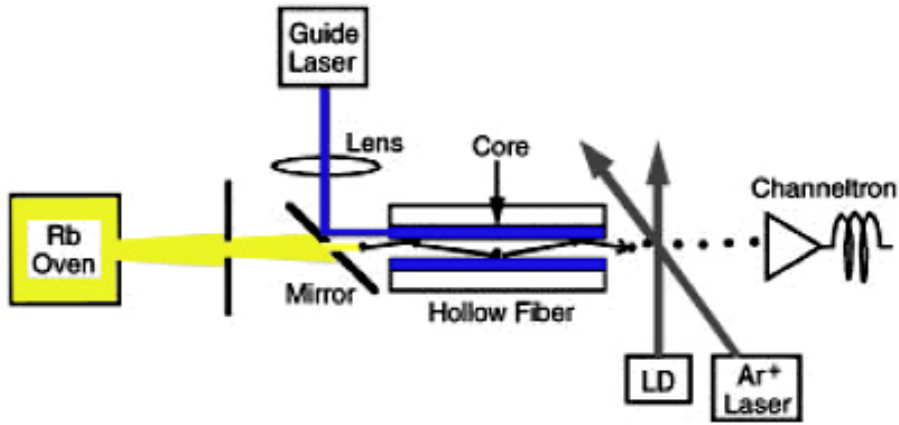


Figure 1.18 : Experimental setup showing 90° coupling geometry for an evanescent capillary guide. Implemented by Ito. *et al.*⁶⁹

1.3.2 Van der Waals Interaction

The absence of Van der Waals attraction would make guiding atoms down a hollow core fibre relatively easy; following coupling into the core, atoms would migrate down the fibre and exit ready for capture in the next vacuum system. However, given the sources of transverse momentum which atoms are susceptible to; collision and radiation from neighbouring atoms, scattering from guide beams and their inherent kinetic energy, it is inevitable that the majority of atoms will approach the fibre walls at some time during transit. When this occurs they will encounter a Van der Waals attraction pulling and trapping them onto the fibre wall. This force was expressed by Chevrollier *et al.* in their 1992 paper⁷⁰ as;

$$U_{vdw} = -\frac{1}{4\pi\epsilon_0} \left(\frac{\epsilon - 1}{\epsilon + 1} \right) \frac{\langle g|d^2|g \rangle}{8k_B x^3} \quad 1.25$$

where ε is the dielectric constant of the fibre material, $\langle g | d^2 | g \rangle$ is the matrix element of the square of the dipole operator d , atomic distance from the fibre wall is denoted by x and k_B is Boltzmann's constant. This force originates from an altering of the density of modes within the electromagnetic field in close proximity to the fibre wall. This results in a spatial variation in the Lamb shift and thus a force. It has been recognised⁷¹ that when the distance between the atomic dipole and the fibre wall is greater than the wavelengths of the atomic transitions, the $1/x^3$ relationship in equation 1.25 above no longer holds. Thus, following the radial exponential decrease of VDW attraction, no significant force is experienced beyond a distance approximating the resonant wavelength (several hundred nanometers), which allows evanescent leakage to surpass VDW attraction. Of course, this implies more stringent requirements on the evanescent field quality when fibre HCs approach single figure micrometer diameters.

Experimental work quantifying VDW forces^{72,73} is fairly sparse. In Alain Aspect's research group in Paris, however, an evanescent wave mirror was used to bounce cold atoms away from a surface⁷⁴. This evanescent mirror allowed measurement of the amount of force required to counteract VDW attraction. Further evanescent guiding work in Renn's aforementioned 1996 paper, demonstrated a threshold intensity of $I_{th}=10^5 W/m^2$ for a 1GHz detuned laser counteracting VDW force at a distance of $\sim 1/4\lambda$ from the wall of a 20 μm diameter hollow core.

Atoms ejected from the guided flux path which are caught in VDW forces stick to the inner fibre walls until they rethermalise and re-emitted. Their high kinetic energy eventually allows them to work their way out of the fibre.

1.3.3 Red Detuned Capillary Guiding

Red detuned capillary guiding involves coupling a Gaussian beam into the fibre core which excites Hermitian (HE) modes suitable for atom guidance. The coupling angle and mode matching quality play a strong role in determining the quality of mode generated within the fibre. Typically ~ 30 -50% of the guide laser power is lost due to mode mismatch, this scattering obstructs atom entry and diminishes effective guiding length. This must be anticipated and compensated for prior to flux guidance calculations. The scatter, can only be minimised by better mode matching.

Atoms travelling in the fibre guide do so in a manner similar to *light* propagating in a multimode fibre, that is, motion along the fibre axis is unconstrained whereas grazing incidence modes provide a series of coherent reflections in the transverse axis defined by the dipole-potential well generated. As expected, a stronger guide dipole potential can confine greater transverse atomic momenta.

The primary drawback of red-detuned capillary guides, is a rapid attenuation of the guide intensity in the core, particularly in narrow core fibres. The following approximation describes this attenuation, it is a critical, and stifling, transmission characteristic of hollow-core fibres:

$$l_{1/e} \approx \frac{2.4a^3}{\lambda^2} \quad 1.26$$

where the hollow-core radius is a , the guide wavelength is λ , and $l_{1/e}$ is the length at which guide light falls to $1/e$ of its input intensity.

Elaboration on this and a review of experimental work on red-detuned fibre guides is discussed in chapter 3. Further experimental concerns regarding atom heating during transit are also discussed in context there. Since evanescent fibre guiding was not performed in St Andrews and in the interest of brevity, blue detuned capillary guiding is not discussed here, however thorough descriptions can be found in the works of Ito^{61,69} and Muller & Cornell⁷⁵.

However, scatter further along the fibre is less easy to minimise; imperfections can siphon off annulus coupled light anywhere along the fibre length. Thus the best method of reduction employs the hitherto *negative* attribute of fibre attenuation. The severe attenuation of grazing incidence modes associated with narrow diameter HC's rapidly eliminates extraneous modes. Both modes induced via facet or imperfection scatter can be strongly suppressed by the HC's inherent attenuation rate.

Another difference between red and blue capillary guides is highlighted by Muller & Cornell *et al.* They state that, with dipole potential optimised, guiding efficiency is not actually a maximum when coupling efficiency is greatest. Instead guiding is enhanced when the speckle pattern in the evanescent field is engineered to

minimise the number of “unprotected” regions on the annulus surface. That is, the speckle pattern which occurs due to interference between multiple laser modes within the annular core (AC) which sporadically stifles the evanescent field along the fibre walls, should be minimised such that no gaps appear in the evanescent field. This represents a fundamental impediment to blue-detuned fibre guides.

Coherent Guidance

The applicability of blue-detuned capillary guidance to *coherent* atom transport comes from the practical possibility of very narrow diameter guide paths. The chief impediment to red detuned coherent transport was field attenuation, blue detuned guidance does not suffer from this problem. However the requisite narrowing of the HC and the dependence on evanescent leakage for an atomic grazing incidence path brings attractive VDW forces much closer to the atom flux. This risks a higher loss rate, particularly in fibres with multiple modes in the annular core. Nevertheless, intuitively, if a guide laser can be tuned far enough from resonance to reduce spontaneous emission, if sufficient intensity can be coupled into a fibre annulus to maintain a high level of evanescent repulsive dipole potential, and if speckle can be removed, then blue detuned guidance will, in principle, be the most efficient form of capillary guidance.

However it must be stated that, to the authors knowledge, blue detuned capillary guidance of atoms, has not yet been demonstrated within *single-optical mode* HC fibres; despite the reductions in both speckle and requisite laser power, the narrow annulus core, typically only a few guide wavelengths in diameter, inflicts optical mode coupling difficulties and subsequent optical blockage of the flux path into the HC. That is, light coupled from the front or rear of the fibre presents excessive scatter⁷⁶ or rapidly converging annuli modes which seal within a few tens of microns^{77,78}, both of which serve to obstruct atom entry to the HC.

Figure 1.19 shows the intensity profile of an LP₀₁ mode on exit from a capillary annulus capable of supporting only the lowest order mode; the mode on exit from the fibre (important for establishing correct guide launch profile) can be seen to have completely filled, by diffraction, within 100µm’s from the fibre facet. Following the recent work of M.Hautakorpi, *et al.*⁷⁹ future work in this field is likely to involve

launching $LP_{m,p}$ modes of order $m \neq 0$, where the mode output yields a hollow beam more suitable for flux loading.

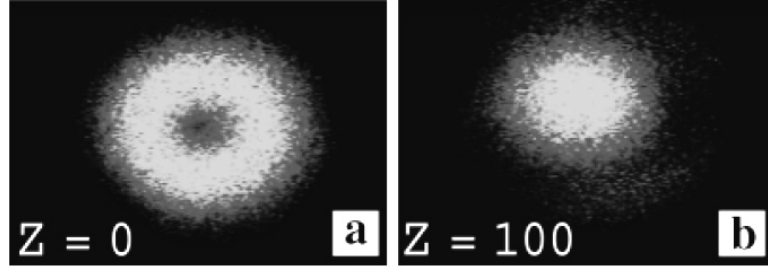


Figure 1.19 : The spatial profile of light output from a capillary fibre capable of supporting only a single optical mode in its annular core. Data given at **a)** the fibre exit facet and **b)** 100 μ m from the fibre facet. Fibre dimensions are 6 μ m hollow-core diameter, 3 μ m annular thickness and 50mm length. Diagram reproduced from Dall *et al.*

1.3.4 A Hybrid Theory?

Narrow core flux conveyance has the potential to be useful for studies of cavity quantum electro-dynamic effects in a cylindrical dielectric, eg. the gravitational cavity⁸⁰ and the atomic quantum wire⁸¹, furthermore it could enhance spatial resolution of atom manipulation for applications involving atom lithography^{82,83}. However narrow hollow-core fibre research discussed herein concerns coherent atom guidance, in particular single mode de Broglie wave transport

A possibility for such coherent atom transfer involves the launch of a hybrid of red and blue detuned guiding practices, that is, a blue-detuned dark hollow beam, (DHB) is launched into the hollow-core of a capillary fibre. This raises questions concerning which modes can be supported by grazing incidence reflections; can capillary fibre support hollow-mode profiles such as high-order Laguerre Gaussian beams? If so, it may be possible to focus suitably matched DHBs into a narrow core where-in the atomic flux path is further confined to within the diameter of the newly generated hollow mode. This would provide a narrower flux path than an evanescently shielded HC alone and so would compress the phase space population, as well as guiding atoms in a region further removed from the core walls. Of course, the primary concerns are optical attenuation with length and grazing incidence mode support, these will be significant if not prohibitive, nevertheless research furthering initial work by Dall *et al.* may be justified.

1.4 Guiding in Photonic Crystal Fibres

The basic principles of periodic structures influencing electromagnetic radiation stem from early work by Yeh *et al.*⁸⁴ in 1977 and by Zengerle⁸⁵ in 1987. However the application of this to generate photonic band gap (PBG) structures was mostly propelled in the late 80's by Sajeev John of the University of Toronto, Canada, and Eli Yablonovitch of Bellcore, US. Their work combined, describes the generation of PBGs in multiple configurations, in 1, 2 and 3 dimensional structures, and with many possible applications.

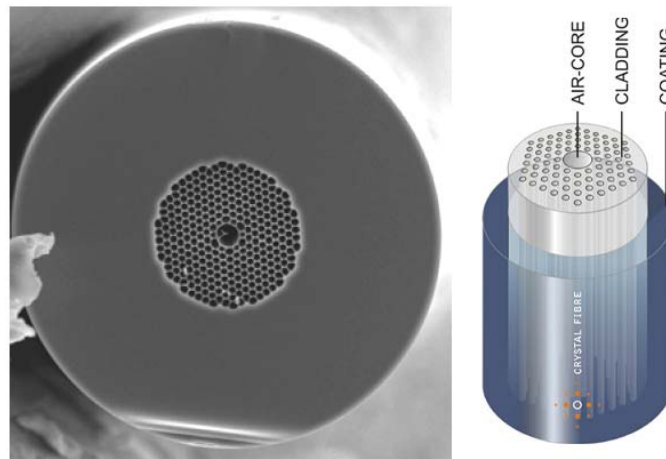


Figure 1.20 : An SEM micrograph of the end facet of a hollow core crystal fibre. On the right a schematic of a crystal fibre showing its key layers. Figures reproduced from Thorlabs (www.thorlabs.com) and Crystal Fibre (www.crystal-fibre.com) websites.

The use of this relatively new technology to confine light within fibres by interference, instead of total internal reflection, was first proposed and developed by P. Russell and co-workers at Bath University^{86,87}. Structures on the scale of an optical wavelength were realised by a stacking technique which produced silica fibres with a periodic array of several hundred air holes all running the length of the fibre. These fibres were the first to approach photonic band gap confinement of light, they had solid cores and thus were not intended for atom conveyance, more for efficient transfer of telecommunication signals. Nevertheless this work initiated research into hollow core fibres and subsequently optical mode support within the hollow cores. The ultimate goal of this thesis is to convey atoms within such modes inside the hollow cores of these photonic crystal fibres (PCF). The following sections introduce photonic band gap theory and discuss a few incarnations of photonic structures before finishing on photonic band gap fibre; PCF.

1.4.1 The Photonic Band Gap

The photonic band gap (PBG) can be described as a range of frequencies which are forbidden from propagating through a material structure. Thus for materials engineered with a PBG the frequencies encompassed will experience strong reflection from the material surface and exponential decay within the material. PBGs are also angle specific, thus in the 1D case, much like a Bragg reflector, complete blocking will occur for a single-frequency wave over a finite angular spread and for a perfectly collimated beam over a finite frequency bandwidth. Strictly speaking a complete PBG is described as a stop-band which blocks propagation in all directions over a finite bandwidth for all polarisation states, however here the term PBG is used to describe any frequency blocking in any single arbitrary direction.

As with periodic electronic crystals (such as semiconductors) which exhibit an electronic bandgap, periodic dielectric structures can exhibit a photonic bandgap. The properties of this bandgap are dependent on the period (lattice constant in fibres), filling factor and index contrast. The PBG arises due to the material periodicity which causes destructive interference between waves travelling forwards and backwards in the structure, (transverse to fibre axis in the case of PCF). The band gap width is determined by the modulation depth of the refractive indices. In contrast to the weak guiding seen in blue-detuned capillaries where refractive index varies by $\Delta n \sim 0.01$ between core and outer annuli, PBG materials are often engineered to maintain a high modulation depth ($\Delta n = 0.45$), this creates a more pronounced PBG with a broader stop-band.

Bloch Description

One of the best ways of describing PBGs and their composition is through the Bloch theorem. This extends the previous description and comes from a principle proposed by Achille Floquet in 1884 which describes modes travelling normal to a periodic structure as a superposition of a set of plane waves whose wavevectors are linked by momentum conservation by:

$$\mathbf{k}_n = \mathbf{k}_0 + n\mathbf{K} \quad 1.27$$

where \mathbf{k}_n is a wavevector of the n th wave, \mathbf{k}_0 is an arbitrary initial wavevector, \mathbf{K} is a reciprocal lattice vector and the periodicity, or lattice constant A , is described as $A=2\pi/|\mathbf{K}|$. This approach closely resembles Fourier synthesis of waveforms; any wavevector can be represented by adding or subtracting an integer number of \mathbf{K} wavevectors. It was Bloch who later expanded this theorem to describe multidimensional materials as part of his treatment of electrons in crystals.

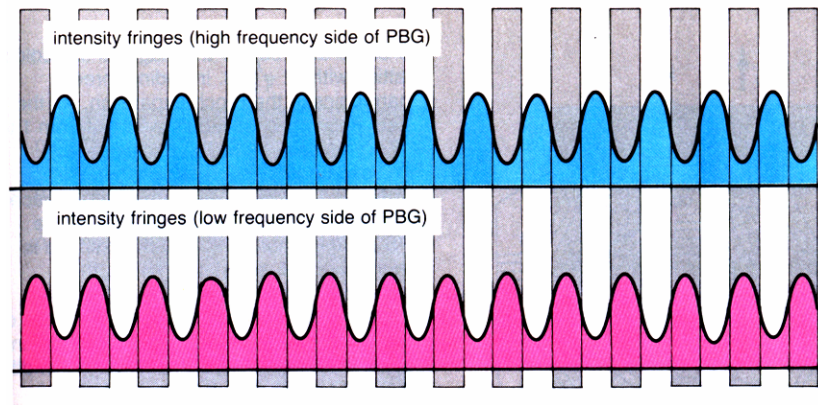


Figure 1.21 : A depiction of a horizontal periodic stack of slabs. The slabs have different refractive indices and thus propagating waves within suffer an ‘arranging’ into phase with one species of material. Diagram reproduced from P. St. Russell’s review publication.

Waves entering PBG material are only permitted to propagate if their wavevectors can match an integral superposition of grating vectors. In fact, as depicted in Figure 1.21, waves inside the periodic lattice will be arranged such that for frequencies above the PBG they are in phase with the *higher* index regions and below the PBG they are in phase with the *lower* index regions. This “arranging” can be explained by the average refractive index experienced; waves with fringes in the higher index region will have a shorter effective wavelength while waves in-sync with the lower index regions will have a longer effective wavelength. Incident wavelengths matching those of the band gap itself cannot be arranged in-phase or out-of-phase with the periodic structure and so will be reflected as if the material were an ideal metal. For comparison reflection from an air-glass interface provides 4% reflection, whereas >99% can be achieved from a photonic bandgap structure.

1.4.2 Multi-Dimensional PBG

Waves incident at arbitrary angles must have wavevectors which can be deconstructed to a superposition of the lattice vector. This returns us to the earlier

description of the trade off between frequency and incident angle, clearly waves passing parallel to the periodic interface will experience no index modulation and thus no PBG, so there will be a range of angles, spread around normal incidence, over which the PBG is experienced.

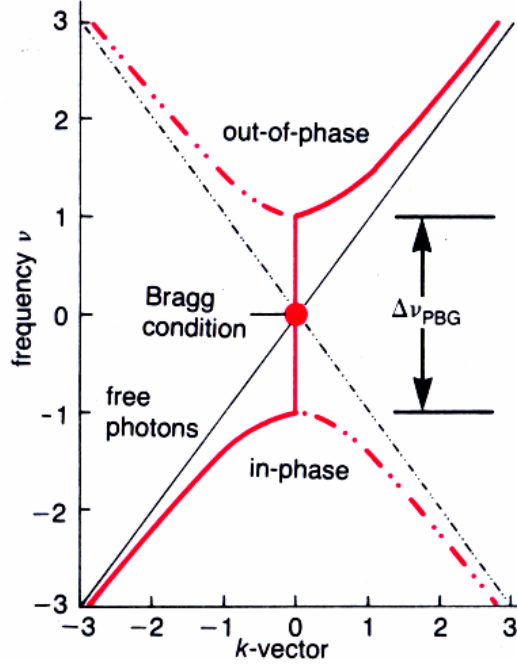


Figure 1.22 : A plot of the k-vector against the frequency, as the k-vector approaches the edge of being in or out of phase with single species in the material it leaps to propagating in the opposite material; crossing the bandgap. Thus demonstrating an inability to propagate within the bandgap region. Diagram reproduced from P. St. Russel.

This trade-off is well illustrated in Figure 1.22, where perfect reflection will occur on the satisfaction of the Bragg condition $m\lambda_{eff}=2\Lambda\sin\theta$, where m is the order of Bragg condition, λ_{eff} is the mean wavelength within the grating and θ is the angle of incidence. As expected, the group velocity, $v_g=2\pi\partial\nu/\partial k$, tends to zero at the band gap edges⁸⁸. This is shown as the thick red vertical line which crosses the band gap through the Bragg condition point.

It is quite apparent that the simplest PBG in 1D is a simple multilayer stack, often referred to as a Bragg Reflector. Such films have been studied since the 19th century. In order to control photons in three dimensions we can extend this principle to two and then three dimensions. This involves structuring the periodicity in 2 or 3 dimensions and, to maximise the bandgap, increasing the modulation depth of the refractive indices to increase the spread of solid angles and frequencies covered. A

simplistic progression from 1 to 3 dimensions is shown in Figure 1.23. Provided the modulation depth is deep enough travelling modes within a material can be suppressed by stop-bands until all of k -space is empty – where k -space is used to describe the spectrum of possible \mathbf{k} -vectors ($\mathbf{k}=2\pi/\lambda_{eff}$ =wavevector) which can exist in a material, as demonstrated along the x-axis of Figure 1.22. As we show in section 1.4.3, it is possible to demonstrate a full bandgap in a 2D structure where we make use of the near-infinite length of the fibre. Achieving a PBG for optical frequencies requires very small lattice spacing of the order of $\sim 400\text{nm}$ for $1.5\mu\text{m}$ light in GaAs.

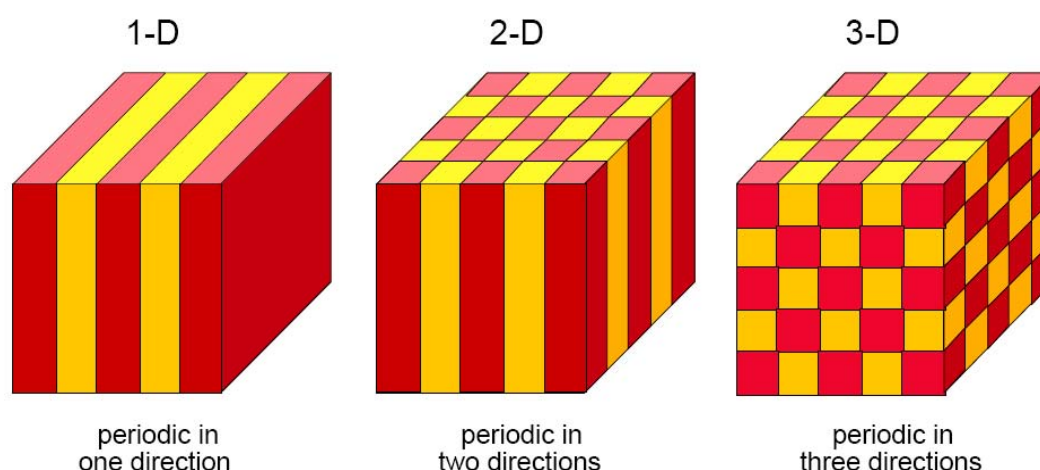


Figure 1.23 : Schematic depiction of the increasing periodicity of photonic crystals from 1 to 3 directions. The periodicity here is introduced through the material structure. However an even more complex structure than the 3D example shown here is required for a fully omni-directional photonic bandgap. Diagram reproduced from J.D. Joannopoulos⁸⁹

1.4.3 Photonic Crystal Fibre

Research in recent years has focused on planar PBG waveguides^{90,91} for the manipulation of telecommunications frequency light^{92,93}. Numerous applications are being updated continually, predominantly microstructured optics devices^{94,95}, including lasers^{96,97}, splitters^{98,99}, optical circuits^{100,101} and ultrafast optical switches¹⁰². Study of the field of PBG devices and recent publications^{103,104} help the author re-discover a feeling of childhood wonder.

For the purposes of this thesis we will limit our discussion to the application of PBGs to photonic crystal fibres (PCF). In conventional optical fibre the core and cladding layers are deposited to form one single rod which is then drawn to form the fibre. Photonic crystal fibre however, is manufactured by stacking identical cylindrical

silica rods into a preform. This is heated to $\sim 2000^{\circ}\text{C}$ and drawn into fibres which reduces the preform pattern to a micron scale. The air holes are not fully collapsed, thus a series of periodic holes remain. These run the length of the fibres. In fact, in some fibres the volume within the cladding is filled almost entirely with air rather than silica to create a honeycomb like structure. Figure 1.24 below illustrates such designs.

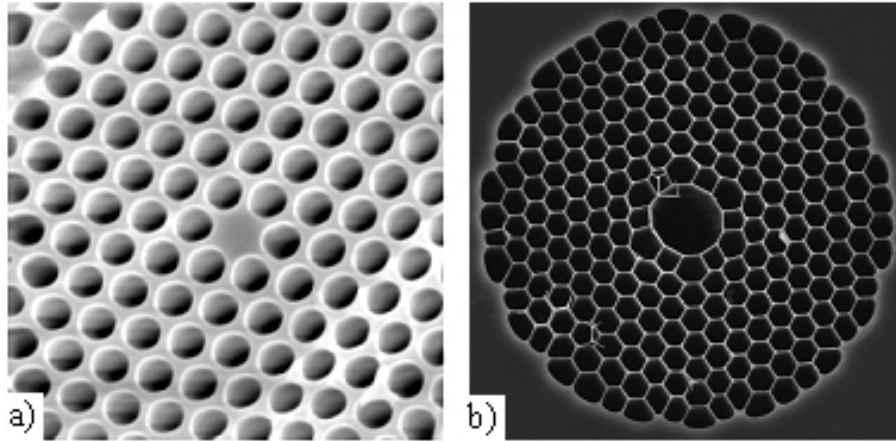


Figure 1.24 : a) solid core PCF design with a pitch of less than $2\mu\text{m}$, b) hollow core PCF design wherein a rod has been removed from the centre of the preform to produce the HC.

Solid¹⁰⁵ or hollow core¹⁰⁶ PCF can be manufactured, however those with hollow cores are of particular interest here as they present an access route for guided atomic flux. They can provide the necessary 2D band gap structure for supporting a high intensity potential within their air core. In fact PBG material is predicted to support a steeper transverse field gradient within the core¹⁰⁷ relative to potentials confined through total internal reflection (TIR). The triangular lattice of PCF has a very high symmetry which provides 2 dimensional reflectivity in the plane of the lattice (ie. in the plane of the paper when looking at Figure 1.24b). By introducing a defect to the centre of the fibre, either additional dielectric or air, a channel can be formed for optical waveguiding. In the air-core fibre, this presents a possible atom guide channel without the slab style substrate and without any out-of plane loss endemic to planar waveguides. Predictably, manufacturing imperfections and coupling losses are still the biggest source of scattering problems, these are an ever present thorn when coupling through far field optics.

Most PCF guides aim to take advantage of their PBG nature to confine, or trap, a guide beam within the core. Theoretically a fibre designed to have a stop-band centred on a wavelength incident upon its hollow core will allow no power loss along

its length. Of course the existence of higher order modes may serve to deteriorate this claim. PCF has been developed with two separate guiding mechanisms labelled here as “quasi-PBG” fibre (or index-guiding fibre), and “full-PBG” fibre (or PBG guiding fibre). These both have periodic lattice structures but employ them to confine light in different ways.

Quasi-PBG Fibre

Early crystal fibre work^{86,87,108} produced solid core fibres with enhanced guiding capabilities relative to standard TIR fibres. However it was soon realised that these were not utilising proper PBG confinement of light, rather TIR permitted by an altering of the average index seen by the propagating mode in the lattice structure. That is, the air filled regions in the lattice structure surrounding the solid core were presenting an effective index, n_{eff} less than the index of the core n_{co} and the substantial index difference Δn , between the two was sufficient enough to provide good core confinement of light. The size of Δn was determined by the air-filling factor of the lattice structure, or similarly, by the pitch of the air holes relative to the guided wavelength. Figure 1.25 illustrates this well.

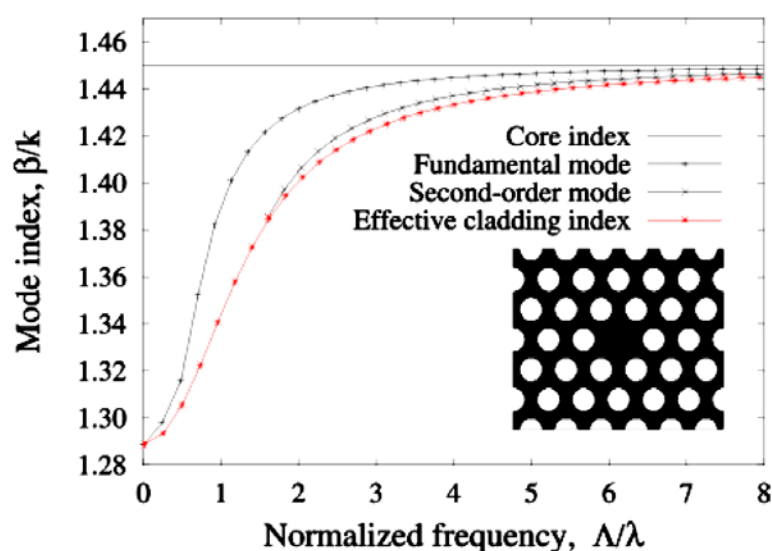


Figure 1.25 : Here the effective cladding index, n_{eff} can be seen to drop significantly below the core index for lattice spacings approaching wavelength sizes. The index experienced by the fundamental and 2nd order modes are also indicated, note the single mode cut-off point. Figures shown are for the triangular lattice in the inset. Figure reproduced from J.Breong.

In Phillip Russel's 1997 paper the entire lattice structure of the reported PCF was only 40µm across and provided single mode operation over a broad spectrum; 337nm to 1550nm in a core of ~2.3µm radius. Absolute power loss figures are not supplied however an investigation was performed on the severe loss occurring when the fibre was bent beyond a critical radius of curvature $R_c \propto \Lambda^3/\lambda^2$. Bending the fibre served to compress the pitch spacing Λ , and thus the effective index seen by the propagating mode. Beyond R_c the guiding efficiency dropped radically, narrowing the single-mode bandwidth and allowing prohibitive power loss. The wavelength at which power loss occurred is shown as the "loss edge" in Figure 1.26.

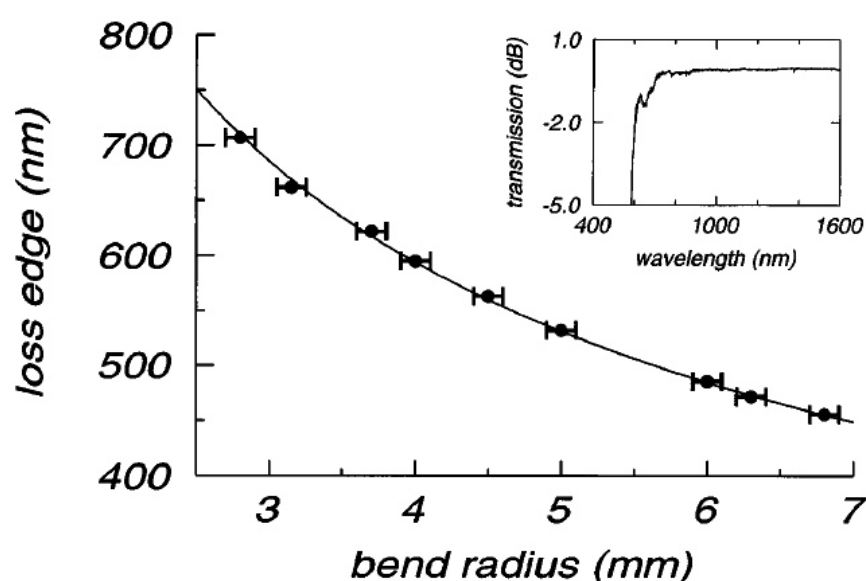


Figure 1.26 : Measured short-wavelength loss edge (for 3dB loss) versus bend radius for a photonic crystal fibre with a single-turn bend, together with a fit to $\lambda = \text{const.}/\sqrt{R}$. Diagram reproduced from P.St.Russell.

Photonic Crystal fibre

In PCF where a rod is omitted from the centre of the preform, (or several are omitted), an air-core is formed. This is similar to the HC in capillary fibres however it has a shape defined by the lattice structure; polygonal instead of circular. This air core is often referred to as a defect state, as it is a break in the periodicity of the fibre lattice. If this defect state supports modes with frequencies which fall within the stop bands of the PBG, these modes will be strongly confined to the defect.

The index contrast presented by the air-silica fibre is not strong enough to create a photonic band gap for light propagating in the two-dimensional plane of the triangular lattice ($k_x, k_y, k_z=0$). However if we consider light propagating at an oblique angle of incidence, in the z direction, $k_z \neq 0$, then we observe that a complete PBG can indeed open up. Plotting the dependence of the 2D band structure upon the k_z vector in Figure 1.27, we see a band gap. This gap coincides with the air light line, indicating that the field is mainly guided in the air. To centre the lower gap at 785nm, we require a lattice constant of approximately $1\mu\text{m}$.

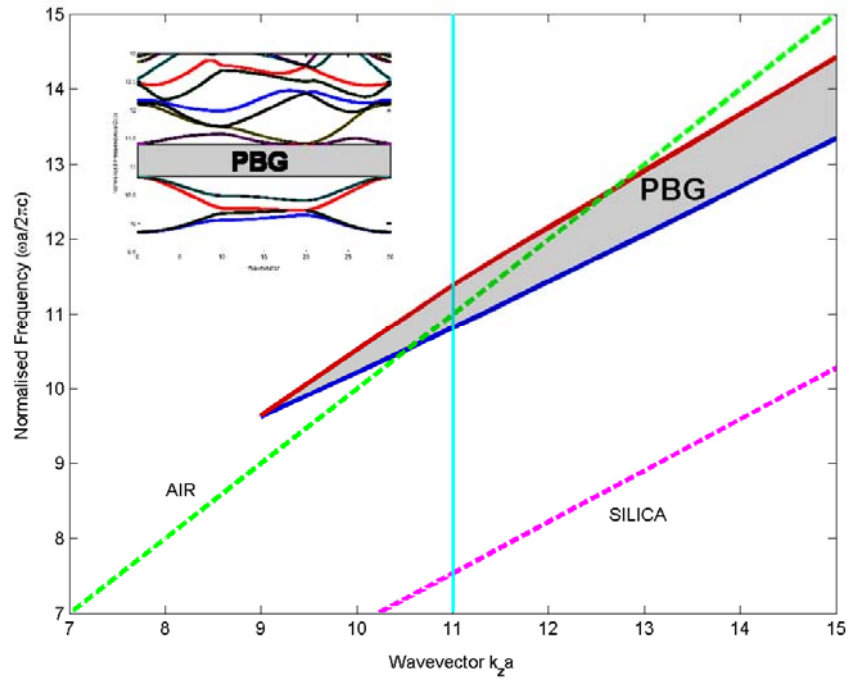


Figure 1.27 : This is the photonic band structure¹⁰⁹ for an infinite 2D triangular lattice of air holes in silica for wavevectors propagating with finite k_x , k_y and k_z . Note the ratio $R/a=0.48$, where R is the radius of the air holes and a is the lattice constant. Inset is the 2D triangular lattice bandstructure for $k_z a=11$, (ie. it is a sample along the vertical cyan line). Solving for the waveguiding modes using a similar model has successfully matched theory to experiment, takes into account the Density Of Photonic States^{110,111}

Ordinarily the index, β/k experienced by a mode propagating within the core, is bounded by the core and cladding indices as,

$$n_{co} \geq \beta/k \geq n_{cl} \quad 1.28$$

where each index is dictated by the material properties of the core and cladding. However in a crystal fibre the same material is used throughout thus the core and

cladding are thermally and mechanically matched, and Δn is not limited by material incompatibilities. Light guidance can be demonstrated in solid or hollow core fibre's even when their air filling fractions and index contrast are both too small to observe band gaps in the periodic plane, however increasing the air filling fraction of the lattice structure significantly improves the likelihood of supporting PBGs at low values of β/k (low $\beta/k \Rightarrow$ increasing θ). In situations where the periodic structure satisfies equation 1.27, and especially when there is an air filled core to confirm the lack of TIR, guiding ability can only be attributed to PBG effects. This type of guiding has also been termed Bragg PBG guidance due to its similar dependence on the Bragg condition for confinement of optical modes.

In 1999 Phillip Russell's research group observed a guided mode within the HC¹¹². Of a triangular-lattice structured fibre shown in Figure 1.28, several rods had been removed from the preform to create a HC in which several bands of near-zero loss, HC transmission, across the visible spectrum and into the infrared occurred. Out with these bands the transmission was stifled by large power loss, these regions were attributed to PBG suppression. As expected, the chief source of power loss for guided modes was the coupling loss. A supplemental loss came from fabrication anisotropies typically incurring a variation in fibre parameters causing the PBG-supported wavelength to vary along the fibre length.

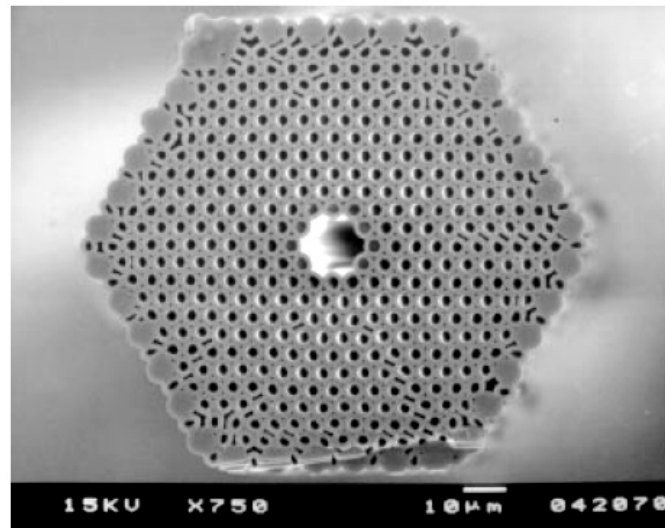


Figure 1.28 : Scanning electron micrograph of the 1999 PCF fibre from Phillip Russell's group. Outside diameter 105 μm (across the flat faces), a HC of 14.8 μm diameter, the surrounding lattice had a pitch of 4.9 μm (centre to centre) and an air filling fraction of 39%

The intensity profiles of supported fundamental modes are typically dependent on the structure of the fibre lattice and the resulting core shape. In the broad HC of the triangular lattice the phase is constant across the air core so a simple Gaussian-like intensity profile is supported. In general the fundamental mode supported within PBG fibres forms a Bessel beam with a circular profile at its centre, however the edges of the mode will bend to mimic the surrounding structure. Figure 1.29, a) and b) illustrate the degree of morphing and include a leaky 2nd order mode which shows even more morphing for comparison, these higher order modes clearly exist closer to PBG edges as they are not perfectly contained within the core.

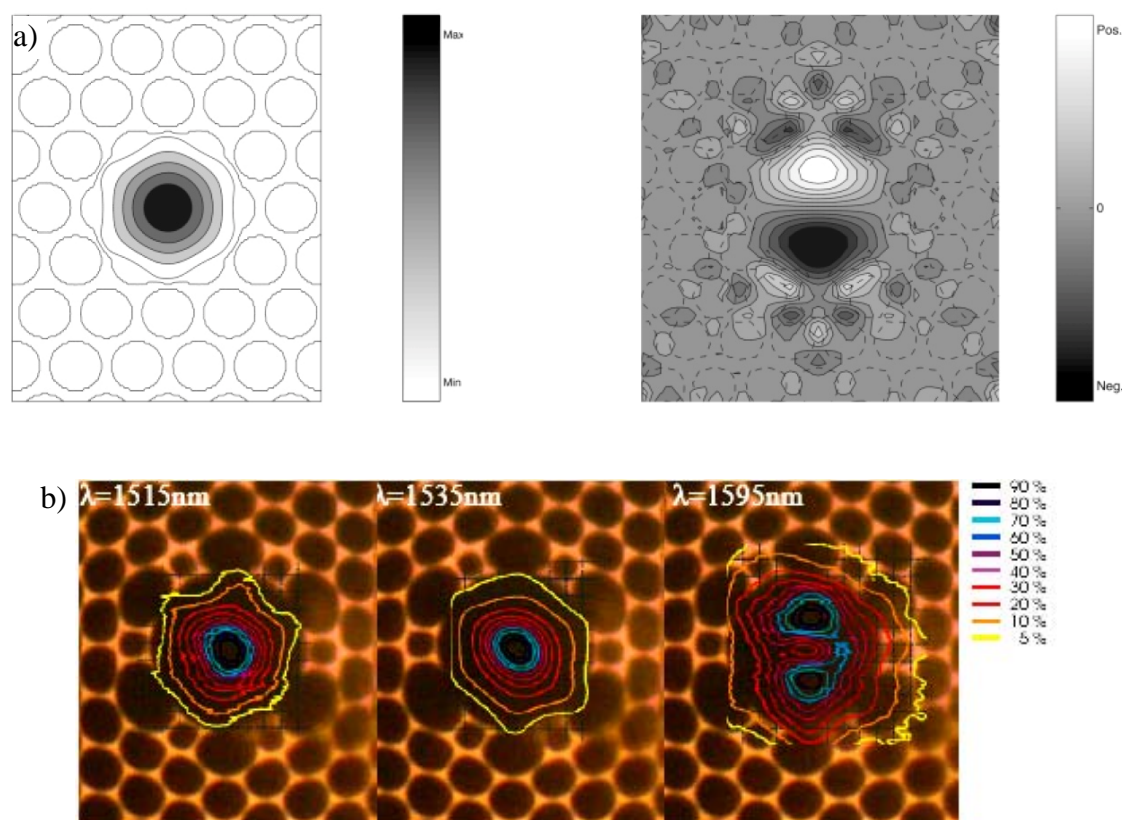


Figure 1.29 : **a)** Field distribution of the fundamental, air guided mode(left)and 2nd order mode (right). The 2nd order mode has a 180° phase shift between the two maxima. Note in the right hand side image, the zero intensity level is indicated by a medium grey colour here. **b)** Measured mode-fields(contour lines) for selected wavelengths at the exit of a 50m long HC PCF section, superimposed on the fibre structure. Diagrams reproduced from M. Wegmuller and J.Broeng *et al.*¹¹³.

The degree of localisation of a propagating mode within the HC is important for nonlinear and, in particular, particle guiding applications. An important fibre parameter in this respect is the effective area A_{eff} of the guided mode¹¹⁴. Unlike long-haul and

high-capacity fibre links, particle transport benefits from a narrow effective. Hollow-core PCFs predominantly have broader effective area's than solid-core PCFs, ($\sim 5.25\mu\text{m}^2$ compared to $2.45\mu\text{m}^2$ respectively, at $\lambda=1.3\mu\text{m}$), however both are an order of magnitude smaller than those of conventional optical fibres, ($50\text{-}100\mu\text{m}^2$). In conventional fibres this parameter is strongly dependent on the fibre core diameter and is related to the mode field diameter by the expression $A_{\text{eff}}=\pi\omega^2$ where 2ω is the mode field diameter. This still functions as a general rule of thumb for PCF however recent studies¹¹⁵ have shown a departure from the relationship at longer wavelengths and notably an independence on the number of rings of unit cells in the lattice structure.

The number of modes supported within HC PBG-guiding fibre is provided by,

$$V = \frac{2\pi\Lambda F^{1/2}}{\lambda} (n_0^2 - n_a^2)^{1/2} \quad 1.29$$

this indicates the *V-number*, and so the number of modes which can propagate in a PCF core $N \sim V^2/2$, where n_o is the silica index, n_a is the effective index of the lattice structure, Λ is the lattice pitch, and $F^{1/2}$ is the air filling factor of the cladding structure. Although the condition for single mode operation will not be defined specifically by $V < 2.405$ for PCF (it may be possible for shorter wavelengths to set up multimode propagation), the $V < 2.405$ relation is still a useful rule of thumb as larger cores increase the likelihood of multiple modes. The number of modes predicted for Russell's fibre (shown in Figure 1.28) was $N=1.61$, which suggests at least one transverse mode and perhaps a second, dependent on the laser wavelength.

Algebraic descriptions of profiles supported within HC PCF are a composite of Bessel and modified Bessel functions in the radial direction with a field dependence in the azimuthal direction, ϕ , described in terms of sinusoidal functions $\cos(m\phi)$ and $\sin(m\phi)$, and propagation in the positive z direction described by a $e^{(j\beta z)}$ term, where β is the axial propagation term as before. A good vector analysis of modes within fibres of low and high index cores is provided in a 2003 thesis by J.I. Kim¹¹⁶. Expressions are provided for longitudinal, axial and azimuthal, electric and magnetic components, these are again, a composite of Bessel functions. The familiar solutions for the electric and magnetic polarisations propagating along the fibre in the positive z direction within the hollow core can be described as;

$$\begin{aligned} E_z &= [AI_m(k_1 r) + BK_m(k_1 r)] \cos(m\phi + \phi_0) \\ H_z &= [CI_m(k_1 r) + DK_m(k_1 r)] \sin(m\phi + \phi_0) \end{aligned} \quad r < r_c \quad 1.30$$

where the amplitude coefficients A, B, C, and D are calculated at the boundary conditions between the HC and lattice structure. I_m and K_m are the modified Bessel functions of the first and second kind respectively and the wavevector $k_1 = k_0 \sqrt{n_1^2 - \beta^2}$ where n_1 is the index of the silica cladding material and the free-space wavenumber $k_0 = 2\pi/\lambda$. The azimuthal phase constant ϕ_0 can be either 0 or $\pi/2$ to yield $\cos(n\phi)$ or $\sin(n\phi)$.

The use of proper PBG confinement will theoretically provide a near lossless form of mode transport, with the proviso that fabrication inconsistencies in the fibre parameters can be smoothed out. An extra benefit of coupling into a hollow core is the removal of Fresnel reflections hence a reduction in coupling loss is made, since the index discontinuity between core and outside environment is nearly negligible. However the primary coupling loss mechanism of spatial mismatch between external and guided mode still remain. Exciting a particular mode through the fibre facet is challenging. The propagating modes in the fibre may be well designed, but scattering at the interface can cause disruptive fields in the coupling region. One possible solution is to couple power through the side of the fibre¹¹⁷.

Research groups around the world are continuing to address loss issues of PCF, recent work by N.Venkataraman *et al.* reported HC PCF losses of only 13dB/km¹¹⁸, though even this was surpassed by a record low loss of 1.2dB/km¹¹⁹ reported earlier this year (2005) by the Bath university team. Although this is still greater than that of single mode conventional fibre it is low enough to encourage work on all other pertinent parameters; mode structures, chromatic dispersion, bend loss, fibre splicing, etc. Furthermore, for research groups beginning fibre particle guidance work today the loss is no longer excessively prohibitive for precision experiments, though the newly identified loss mechanism of surface modes¹²⁰ is of concern for those working in fibres with fabrication inconsistencies.

Given the high degree of optical localisation within the core of a PBG guiding fibre, the high power conveyance capability and the natural ability to suppress unwanted wavelengths (falling outside the PBG), a hollow core PCF presents a tantalising opportunity to guide particles with all the benefits associated with fibre light guidance; through atmosphere, round corners ($R > R_c$) and in narrow single optical modes. However, to the authors knowledge, atom guidance in PBG fibres has not yet been achieved. The ultimate goal of HC fibre guides is to provide a single fundamental optical mode, tightly confined to the centre of the HC which gives no opportunity for guided particles to spontaneously emit or break free and escape the guide. The low loss nature should not permit significant intensity drop-off with propagation distance and in particular the removal of the cubed core-radius dependence of the attenuation length puts PCF in a far superior league to conventional capillary fibre. Ultimately these factors lend themselves well to the target of atom transport in a single matter wave, where only the fundamental de Broglie wave propagates. However, prolonged single atomic mode transport will depend heavily on the preclusion of scatter within the HC, hence surface modes and other extraneous optical energy must be entirely suppressed for this to occur. Initial proof of concept experiments have been conducted in St Andrews, with the intention of demonstrating narrow-core ($\sim 12\mu\text{m}$ diameter) guidance of cold atoms. The following chapters detail the steps taken to fulfil this goal.

1.5 Bibliography

- ¹ Nobel prize in Physics in 1997 awarded to Professors Steven Chu, Claude Cohen-Tannoudji, and William Phillips, “for development of methods to cool and trap atoms with laser light”. The Nobel prize in physics in 2001, was awarded to Professors Eric Cornell, Wolfgang Ketterle and Carl Wieman, “for the achievement of Bose-Einstein condensation in dilute gases of alkali atoms, and for early fundamental studies of the properties of the condensates”.
- ² P.N. Lebedev, “Experimental Examination of Light Pressure”, *Ann. der Physik*, Vol. 6, #433, (1901).
- ³ T. W. Hänsch and A. L. Schawlow, *Opt. Comm.* #13, p68 (1975).
- ⁴ A. Ashkin, “Trapping of Atoms by Resonance Radiation Pressure”, *Phys. Rev. Lett.* #40, p729, (1978).
- ⁵ W. D. Phillips and H. Metcalf, *Phys. Rev. Lett.* #48, p596 (1982).
- ⁶ S.Chu, L.Hollberg, J.E.Bjorkholm, A.Cable and A.Ashkin, *Phys. Rev. Lett.* #55, p48,(1985).
- ⁷ S.Chu, J. E.Bjorkholm, A.Ashkin and A.Cable, *Phys. Rev. Lett.* #57, p314 (1986).
- ⁸ Wolfgang Ketterle and Carl Wieman, MIT, http://cua.mit.edu/ketterle_group/home.htm
- ⁹ Klaus Sengstock, Universität Hamburg, <http://www.physnet.uni-hamburg.de/ilp/sengstock/en/AtomGuiding.php>
- ¹⁰ Tetsu Takekoshi, Brian Patterson, Brooke George, Randy Knize, “Atom guiding in hollow core photonic bandgap fibers”, (U.S. Air Force Academy), (2006).
- ¹¹ E.L.Raab, M.Prentiss, A.Cable, S.Chu and D.E.Pritchard, *Phys. Rev. Lett.* #56, p2631, (1987).
- ¹² P. D. Lett, W. D. Phillips, S. L. Rolston, C. E. Tanner, R. N.Watts, and C. I. Westbrook, “Optical Molasses,” *Journal of the Optical Society of America B* 6, 2084 (1989).
- ¹³ H. J. Metcalf and P. van der Straten, “Laser Cooling and Trapping”, Springer- Verlag Inc., USA, pages 219-229, (1999).
- ¹⁴ P.D. Lett, R.N.Watts, C.I.Westbrook, W.D.Phillips, “Observation of Atoms Laser Cooled Below the Doppler Limit”, *Phys. Rev. Lett.*, vol. 61, #2, p169, (1988).
- ¹⁵ See “Laser cooling and Trapping”, H.J.Metcalf, P.v.d.Straten, Springer, (2002), section 1.2.1, p8/9.
- ¹⁶ M. Rotenberg, N. Metropolis, R.Birins and J. Wooten Jr, “The 3 j and 6 j Symbols“, Technology Press, Cambridge (1959).
- ¹⁷ See “Laser cooling and Trapping”, H.J.Metcalf, P.v.d.Straten, Springer, (2002), section 8.2.2, p103.
- ¹⁸ See “Experimental Studies of Diode Lasers And Cold Atom Guiding”, doctoral thesis of Dr. G.P.T Lancaster, (2001), chapter 6, equations 6.8 & 6.9.
- ¹⁹ A.Kastler, Champ Lumineux a Structure Helicoidale dans un Cavite Laser, Possibilite d’Imprimer cette Structure Helicoidale a un Milieu Materiel Transparente Isotrope, *Compt. Rend. Acad. Scien., Paris* #271, 999 (1971)
- ²⁰ J. Dalibard, C.Cohen-Tannoudji, “Laser Cooling below the Doppler Limit by polaristaion Gradients – Simple Theoretical Models”, *J. Opt. Soc. Am. B*, #6, p2023-45, (1989).
- ²¹ G.Nienhuis, P. van der Straten, S-Q. Shang, “Operator Description of Laser Cooling Below the Doppler Limit”, *Phys. Rev. A*, vol 44, #1, p462, (1991).
- ²² S-Q. Shang, B. Sheehy, H. Metcalf, P. van der Straten, G. Nienhuis, “Velocity-Selective Resonances and Sub-Doppler Laser Cooling” *Phys. Rev. Lett.*, vol. 67, #9, p1094, (1991).
- ²³ A. Ashkin, J.Gordon, “Stability of Radiation Pressure Traps: an Optical Earnshaw Theorem”, *Opt. Lett.*, #8, p511, (1983).
- ²⁴ D.E. Pritchard, E.L. Raab, V. Bagnato, C.E. Wieman, R.N. Watts, “Light traps using spontaneous forces”, *Phys. Rev. Lett.* #57, p310, (1986).
- ²⁵ D. Pritchard, E. Raab, V. Bagnato, C.Wieman and R. Watts, Light Traps Using Spontaneous Forces, *Phys. Rev. Lett.* #57, 310 (1986),
P. Bouyer, P. Lemonde, M. Bendahan, A. Michaud, C. Salomon and J. Dalibard, An Atom Trap Relying on Optical-Punmping, *Europhys. Lett.* #27, 569-574 (1994)
- ²⁶ G.P.T. Lancaster, “Experimental Studies of Diode Lasers and Cold Atom Guiding”, doctoral thesis, submitted to University of St Andrews, UK, (2001).
- ²⁷ M.H. Anderson, J.R. Ensher, M.R. Matthews, C.E. Wieman, and E.A. Cornell, "Observation of Bose-Einstein Condensation in a Dilute Atomic Vapor", *Science*, #269, 198 (1995).
- ²⁸ M.-O. Mewes, M.R. Andrews, N.J. van Druten, D.M. Kurn, D.S. Durfee, and W. Ketterle, "Bose-Einstein condensation in a tightly confining dc magnetic trap",
- ²⁹ E A Hinds and I G Hughes, “Magnetic atom optics: mirrors, guides, traps, and chips for atoms”, *J. Phys. D: Appl. Phys.* 32 (1999) R119–R146.
- ³⁰ E. A. Cornell and C. E. Wieman “Nobel Lecture: Bose-Einstein condensation in a dilute gas, the first 70 years and some recent experiments”, *Reviews of Modern Physics*, Vol. 74, p876,(2002).
- ³¹ C.S.Adams, E.Riis, “Laser Cooling and Trapping of Neutral Atoms”, *Prog. Quonr. Electr.* Vol. 21, No. 1, pp. 1-79, (1997)
- ³² J.P. Gordon, A. Ashkin, “Motion of atoms in a radiation trap”, *Phys. Rev. A*, #21, p1606-17, (1980).

- ³³ S. Chu, J. E. Bjorkholm, A. Ashkin, A. Cable, "Experimental Observation of Optically Trapped Atoms", *Phys. Rev. Lett.*, #57, p314-17, (1986).
- ³⁴ H.A.Kramers, *Nature*, #117, p775, (1926) & R. de L. Kronig, *J. Opt. Soc. Am.* #12, p547. (1926).
- ³⁵ R. Grimm, M. Weidemuller, and Y. B. Ovchinnikov, "Optical dipole traps for neutral atoms," *Adv. At. Mol. Opt. Phys.* 42, 95-170 (2000).
- ³⁶ See "Laser cooling and Trapping", H.J.Metcalf, P.v.d.Straten, Springer, (2002).
- ³⁷ C. S. Adams, H. J. Lee, N. Davidson, M. Kasevich and S. Chu, "Evaporative Cooling in a Crossed Dipole Trap", *Phys. Rev. Lett* #74, 3577-3580 (1995)
- ³⁸ T.Takekoshi and R. J. Knize, "CO₂-Laser Trap for Cesium Atoms", *Opt. Lett.* #21, 77-79 (1996)
- ³⁹ M.J. Renn, A.A. Zozulya, E.A. Donley, E.A. Cornell, D.Z. Anderson, "Optical-Dipole-Force Fiber Guiding and Heating of Atoms", *Phys. Rev. A*, vol.55, #5, (1997).
- ⁴⁰ N. Davidson, H. J. Lee, C. S. Adams, M. Kasevich, and S. Chu, "Long atomic coherence times in an optical dipole trap," *Physical Review Letters* 74, 1311{1314 (1995).
- ⁴¹ H. J. Lee, C. S. Adams, M. Kasevich, and S. Chu, "Raman Cooling of Atoms in an Optical Dipole Trap," *Physical Review Letters* 76, 2658{2661 (1996).
- ⁴² T. Kuga, Y. Torii, N. Shiokawa, T. Hirano, Y. Shimizu, and H. Sasada, "Novel optical trap of atoms with a Doughnut beam," *Physical Review Letters* 78, 4713{4716 (1997).
- ⁴³ V. I. Balykin, V. S. Letokhov, Y. B. Ovchinnikov, and A. I. Sidorov, "Quantum-state-selective mirror refection of atoms by laser light," *Physical Review Letters* 60, 2137-2140, (1988).
- ⁴⁴ M. A. Kasevich, D. S. Weiss, and S. Chu, "Normal incidence reaction of slow atoms from an optical evanescent wave," *Optics Letters* 15, 607-609 (1990).
- ⁴⁵ J. Birkholm, R. Freeman, A. Ashkin and D. Pearson, "Observation of Focussing of Neutral Atoms by the Dipole Forces of Resonance-Radiation Pressure", *Phys. Rev. Lett.* #41, 1361 (1978).
- ⁴⁶ G. Timp, R. E. Behringer, D. M. Tennant, J. E. Cunningham, M. Prentiss and K. K. Berggren, "Using Light as a Lens for Submicron Neutral Atom Lithography", *Phys. Rev. Lett.* #69, 1636-1639 (1992)
- ⁴⁷ K. K. Berggren, M. Prentiss, G. Timp and R. E. Behringer, "Neutral Atom Nanolithography", *Inst. Phys. Conf. Ser.* #127, 79-84 (1992)
- ⁴⁸ J. J. McClelland, R. E. Scholten, E. C. Palm and R. J. Celotta, "Laser-Focused Atomic Deposition", *Science* #262, 877-880 (1993)
- ⁴⁹ J. Arlt, T. Hitomi, K. Dholakia "Atom guiding along Laguerre-Gaussian and Bessel light beams" *Applied Physics B*, 71, 549, *Lasers and Optics*, Aug (2000).
- ⁵⁰ D. P. Rhodes, Doctoral thesis, "Experimental Studies of Cold Atom Guiding Using Hollow Light Beams", Feb, 2005.
- ⁵¹ D.P.Rhodes, D.M.Gherardi, J.Livesey, D.McGloin, H.Melville, T.Freearde, K.Dholakia, "Atom Guiding along Holographically generated high-order Laguerre-Gaussian light beams", unpublished.
- ⁵² M.Schiffer, M.Rauner, S.Kuppens, M.Zinner, K.Sengstock, W.Ertmer, "Guiding, focusing, and cooling of atoms in a strong dipole potential", *Appl. Phys. B.* #67, p705, (1998).
- ⁵³ H.Ito, T.Nakata, K.Sakaki, M.Ohtsu, "Laser Spectroscopy of Atoms Guided by Evanescent Waves in Micron-Sized Hollow Optical Fibers", *Phys. Rev. Lett.*, Vol. 76, #24, (1996).
- ⁵⁴ R G Dall, M D Hoogerland, K G H Baldwin and S J Buckman, "Guiding of metastable helium atoms through hollow optical fibres", *J. Opt. B: Quantum Semiclass. Opt.* #1, p396-401, (1999).
- ⁵⁵ H. J. Metcalf and P. van der Straten, *Laser Cooling and Trapping* (Springer-Verlag Inc., 175 Fifth Avenue, New York, NY 10010, USA, pages 219-229, (1999).
- ⁵⁶ H. Hinderthur, W. Ertmer *et al.* "Atom Interferometry with Polarizing Beam Splitters", *Physical Review A*, Vol. 57, #6, p4730, (1997).
- ⁵⁷ B.T. Wolschrijn, R.A. Cornelussen, R.J.C. Spreeuw and H.B. van Linden van den Heuvell, "Guiding of cold atoms by a red-detuned laser beam of moderate power", *New Journal of Physics* vol. 4, #69 p1-10, (2002).
- ⁵⁸ Z. T. Lu, K. L. Corwin, M. J. Renn, M. H. Anderson, E. A. Cornell, and C. E. Wieman, "Low-Velocity Intense Source of Atoms from a Magneto-optical Trap," *Physical Review Letters* 77, 3331-3334 (1996).
- ⁵⁹ D.P. Rhodes, G.P.T.Lancaster, J.Livesey, D.McGloin, J. Arlt, K.Dholakia, "Guiding a cold atomic beam along a co-propagating and oblique hollow light guide" *Optics Communications*, 214, p247-254, (2002)
- ⁶⁰ R.G.Dall, M.D.Hoogerland, *et al.* "Single-Mode Hollow Optical Fibres for Atom Guiding", *Applied Physics B*, #74, p11-18, (2002)
- ⁶¹ H. Ito, K. Sakaki, M. Ohtsu, W. Jhe, "Evanescent-light guiding of atoms through hollow optical fiber for optically controlled atomic deposition", *Applied Physics Letters*, Vol. 70, # 19, pp. 2496-2498, (1997).
- ⁶² A Bard, K.K Berggren, J.L Wilbur, J.J.McClelland, M.Prentiss, G.M Whitesides, "Self-assembled monolayers exposed by metastable argon and metastable helium for neutral atom lithography and

-
- atomic beam imaging”, *Journal of Vacuum Science & Technology B: Microelectronics and Nanometer Structures*, Vol. 15, # 5, pp. 1805-1810, (1997).
- ⁶³ M.A. Ol’ Shanii, Yu.B.Ovchinnikov, V.S.Letokhov, *Opto. Communications*, vol98, #77, (1993).
- ⁶⁴ C.M.Savage, S.Marksteiner, P.Zoller, in “Fundamentals of Quantum Optics III: Proceedings of the fifth meeting on laser phenomena” University of Innsbruck (F.Ehlotzky, Ed.), p60, (Berlin: Springer-Verlag)(1993)
- ⁶⁵ S.Marksteiner, C.M.Savage, P.Zoller, S.L.Rolston, *Physical Review A*, 50, p2680, (1994)
- ⁶⁶ M.J.Renn *et al.* JILA & University of Colorado Dept. of Physics, “Guided Atoms in Hollow-Core Optical Fibres”, *Physical Review A*, Vol. 75, #18, p3253-56, (1995)
- ⁶⁷ M.J.Renn *et al.* JILA & University of Colorado Dept. of Physics, “Optical-Dipole-Force Fibre Guiding and Heating of Atoms”, *Physical Review A*, Vol. 55, #5, p3684-96, (1997)
- ⁶⁸ H.R Noh, W.Jhe, “Atom Optics with Hollow Optical Systems”, Elsevier Science, 02/03/2002.
- ⁶⁹ H.Ito, K.Sakaki, W.Jhe, M.Ohtsu, *Optical Communications*, #141, p43, (1996)
- ⁷⁰ Martine Chevrollier, Michèle Fichet, Marcos Oria, Gabriel Rahmat, Daniel Bloch and Martial Ducloy “High resolution selective reflection spectroscopy as a probe of long-range surface interaction : measurement of the surface van der Waals attraction exerted on excited Cs atoms”, *J. Phys. II, France* 2, p631-657, (1992).
- ⁷¹ Timothy H. Boyer, “Retarded van der Waals Forces at All Distances Derived from Classical electrodynamics with Classical Electromagnetic Zero-Point Radiation,” *Phys. Rev. A*, #7, p1832–1840 (1973).
- ⁷² V Sandoghdar, CI Sukenik, EA Hinds, S Haroche, “Direct measurement of the van der Waals interaction between an atom and its images in a micron-sized cavity”, *Phys. Rev. Lett.* #68, p3432–3435, (1992).
- ⁷³ C.I. Sukenik, “Measurement of the casimir-Polder Forces”, *Physical review Letters*, #70, p560. (1993).
- ⁷⁴ A.Landragin, “Measurement of the van der Waals force in an atomic mirror”, *Phys. Rev. Lett.*, #77 : p1464, (1996),
- ⁷⁵ D. Muller, E. Cornell, D.Z. Anderson, E.R.I. Abraham, “Guiding Laser Cooled Atoms in Hollow-Core Fibres”, *Phys. Rev. A*. #61, 033411-1, (2000).
- ⁷⁶ A. Takamizawa, H. Ito, M. Ohtsu, *Japanese Journal of Applied Physics* #39 p6737, (2000).
- ⁷⁷ C. Won, S.H. Yoo, K. Oh, U.C. Paek, W. Jhe, *Optics Communications*. #161, p25, (1999).
- ⁷⁸ Y.I. Shin, M. Heo, J.W. Kim, W. Shim, H.R. Noh, W. Jhe, *Journal of the Optical Society of America B: Opt. Phys.* #20, p937, (2003).
- ⁷⁹ Markus Hautakorpi *, A. Shevchenko, M. Kaivola, “Spatially smooth evanescent-wave profiles in a multimode hollow optical fiber for atom guiding”, *Optics Comm’s*, Optics 9642, Elsevier, (2004).
- ⁸⁰ D.J.Harris, C.M.Savage, *Physical Review A*. #51, p3967, (1995).
- ⁸¹ J.P.Dowling, J.Gea-Banacloche, *Physical Review A* #52, p3997, (1995)
- ⁸² G.Timp, R.E.Behringer, D.M. Tennant, J.E. Cunningham, M.Prentiss, K.K.Berggren, *Physical Review Letters* #69, p1636, (1992).
- ⁸³ J.J.McClelland, R.E.Scholten, E.C.Palm, R.J. Celotta, *Science*, #262, p887, (1993)
- ⁸⁴ P. Yeh, A.Yariv and C-S Hong, “Electromagnetic Propagation in a Periodic Stratified Media”, *Journal of the Optics Society of America*, #67, p423, (1977).
- ⁸⁵ R. Zengerle, “Light Propagation in Single and Doubly Periodic Planar Waveguides”, *Journal of Modern Optics*, #34, p1589, (1987)
- ⁸⁶ J. Knight, P. Russell *et al.* “Pure silica single-mode fibre with hexagonal photonic crystal cladding”, *Optical Fibre Communication Conference*, paper PD3-1, 1996.
- ⁸⁷ Birks, Atkin, P Russel *et al.* “2D Photonic Band Gap Structures in Fibre Form”, *Photonic Band Gap Materials*, Kluwer, 1996.
- ⁸⁸ Phillip St. Russel, “Photonic Band Gaps” *Physics World* article, August, p37, (1992).
- ⁸⁹ Joannopoulos JD, Meade RD, and Winn JN, “Photonic Crystals: Molding the Flow of Light”, Princeton: Princeton University Press, (1995).
- ⁹⁰ A. Mekis, J. C. Chen, I. Kurland, S. Fan, P. R. Villeneuve, and J. D. Joannopoulos, “High transmission through sharp bends in photonic crystal waveguides,” *Physics Review.Letters*, #77, 3787–3790 (1996).
- ⁹¹ M. Bayindir, B. Temelkuran, and E. Ozbay, “Propagation of photons by hopping: A waveguiding mechanism through localized coupled-cavities in three-dimensional photonic crystals,” *Physics Review B*, #61, R11855–R11858 (2000).
- ⁹² M. Loncar, T.P.Pearsall, *et al.* “Waveguiding in Planar Photonic Crystals”, *Applied Physics Letters*, Vol.77, #13, p1937, (2000)
- ⁹³ N.Fukaya, D. Ohsaki, T. Baba, “Two-Dimensional Photonic Crsytal Waveguides with 60° Bends in a Thin Slab Structure”, *Japanese Journal of Applied Physics*, Vol.39, #5A, p2619, (2000)
- ⁹⁴ T.F.Krauss, "Photonic crystals for integrated optics", *Proc. Summer School on Nanoscale Linear and Non-linear Optics*, Erice, Italy (2000)

- ⁹⁵ H. Kosaka, S. Kawakami, *et al.* "Superprism Phenomena in Photonic Crystals: Toward Microscale Lightwave Circuits", *Journal of Lightwave technology*, Vol. 17, #11, p2032, (1999)
- ⁹⁶ O. Painter, R. K. Lee, A. Scherer, A. Yariv, J. D. O'Brien, P. D. Dapkus, and I. Kim, "Two dimensional photonic band-gap defect mode laser," *Science* #284, p1819–1821, (1999).
- ⁹⁷ S. Noda, M. Yokoyama, M. Imada, A. Chutinan, and M. Mochizuki, "Polarization mode control of two-dimensional photonic crystal laser by unit cell structure design," *Science* 293, 1123–1125 (2001).
- ⁹⁸ J. Yonekura, M. Ikeda, and T. Baba, "Analysis of finite 2-D photonic crystals of columns and lightwave devices using the scattering matrix method," *J. Lightwave Technology*, #17, p1500–1508 (1999).
- ⁹⁹ M. Bayindir, B. Temelkuran, and E. Ozbay, "Photonic crystal based beam splitters," *Appl. Phys. Lett.* #77, p3902–3904 (2000).
- ¹⁰⁰ H. Kosaka, T. Kawashima, A. Tomita, M. Notomi, T. Tamamura, T. Sato, and S. Kawakami, "Photonic crystals for micro lightwave circuits using wavelength-dependent angular beam steering," *Applied Physics Letters*, #74, p1370–1372 (1999).
- ¹⁰¹ A. de Lustrac, F. Gadot, S. Cabaret, J.-M. Lourtioz, T. Brillat, A. Priou, and A. E. Akmansoy, "Experimental demonstration of electrically controllable photonic crystals at centimeter wavelengths," *Applied Physics Letters* #75, p1625–1627, (1999).
- ¹⁰² P. R. Villeneuve, D. S. Abrams, S. Fan, and J. D. Joannopoulos, "Single-mode waveguide microcavity for fast optical switching," *Optics Letters*, #21, p2017–2019, (1996).
- ¹⁰³ Belle Dumé, "Photonic crystals move into new areas", article published online for *PhysicsWeb* magazine, (2005).
- ¹⁰⁴ J.K Rowling, Mary Grandpre, "Harry Potter and the Order of the Pheonix", Bantam Press, (2003).
- ¹⁰⁵ J. Broeng, S. E. Barkou, E. Knudsen *et al.* "Review: Crystal fibre Technology", internal publication within "Crystal Fibre A/S" company, DOPS-NYT, (2000).
- ¹⁰⁶ G. Humbert, J.C. Knight, G. Bouwmans, P.St.J. Russell, "Hollow core photonic crystal fibers for beam delivery", *Optics Express*, Vol.12, #8, (2004).
- ¹⁰⁷ A.V. Tarasishin, S.A. Magnitskii, V.A. Shuvaev, A.M.Zheltikov, "Constructing a light-field distribution for the laser guiding of atoms in photonic crystals", *Optics Comm's*, #184, p391, (2000).
- ¹⁰⁸ T.A. Birks, J.C. Knight, P.St.Russell, "Endlessly single-mode photonic crystal fibre", *Optics Letters*, Vol.22, #13, p961, (1997).
- ¹⁰⁹ S. Guo and S. Albin, "Simple plane wave implementation for photonic crystal calculations," *Opt. Express*, 11, 167-175, (2003).
- ¹¹⁰ F. Couny, H. Sabert, P. J. Roberts, D. P. Williams, A. Tomlinson, B. J. Mangan, L. Farr, J. C. Knight, T. A. Birks, and P. S. J. Russell, "Visualizing the photonic band gap in hollow core photonic crystal fibers," *Opt. Express*, #13, p558-563 (2005),
- ¹¹¹ J. M. Pottage, D. Bird, T. D. Hedley, J. C. Knight, T. A. Birks, P. S. J. Russell, and P. J. Roberts, "Robust photonic band gaps for hollow core guidance in PCF made from high index glass," *Opt. Express*, #11, p2854-2861, (2003).
- ¹¹² R.F. Cregan, B.J. Mangan, J.C. Knight, T.A. Birks, P.St.J. Russell, P.J. Roberts, D.C.Allan, "Single-Mode Photonic Bandgap Guidance of Light in Air", *Science*, 285, (1537-1539), 1999.
- ¹¹³ Mark Wegmuller, Matthieu Legré, Nicolas Gisin Theis P. Hansen, Christian Jakobsen, Jes Broeng "Experimental investigation of the polarization properties of a hollow core photonic bandgap fiber for 1550 nm", *Optics Express*, Vol.13, #5, (2005).
- ¹¹⁴ H. T. Hattori and A. Safaai-Jazi, "Fiber designs with significantly reduced nonlinearity for very long distance transmission," *Applied Optics*, Vol. 37, pp. 3190-3197, (1998)
- ¹¹⁵ M. Koshiba, K. Saitoh, "Structural dependence of effective area and mode field diameter for holey fibers", *Optics Express*, vol.11, #15, p1747, (2003).
- ¹¹⁶ Joeng I. Kim, "Analysis and Applications of Microstructure and Holey Optical Fibres", PhD thesis, Virginia Polytechnic Institute and State University, (2003).
- ¹¹⁷ A.D. Galea, F. Couny, S. Coupland, P. J. Roberts, H. Sabert, J.C.Knight, T.A.Birk, P.St.J.Russell, "Selective mode excitation in hollow-core photonic crystal fibre", *Optics Letters*, vol. 30, #7, (2005).
- ¹¹⁸ N.Venkataraman, M.T.Gallagher, C.M.Smith, *et al.*, "Low Loss, (13dB/Km) Air Core Photonic Band-Gap Fibre", presented at the Ecoc 2002, Copenhagen, unpublished,(2002).
- ¹¹⁹ P. J. Roberts, F. Couny, H. Sabert, B. J. Mangan, D. P. Williams, L. Farr, M. W. Mason, A.Tomlinson, T. A. Birks, J. C. Knight, and P. St. J. Russell, "Ultimate low loss of hollow-core photonic crystal fibres," *Optics Express*, vol.13, p236-244, (2005).
- ¹²⁰ James A. West, Charlene M. Smith, Nicholas F. Borrelli, Douglas C. Allan, and Karl W. Koch, "Surface modes in air-core photonic band-gap fibers", *Optics Express*, Vol. 12, #8, p1485, (2004).

Chapter 2

Review of Published Red-Detuned Hollow-Fibre Atom Guiding Experiments

Introduction

In this chapter published works will be discussed in order to set the scene of hollow-fibre atom guiding research. Here we restrict ourselves to red-detuned optical fibre-guiding experiments, hence this report is not comprehensive. Readers seeking full reviews of atom-cooling or free-space atom guiding should see, the publications of Adams¹ and Pritchard² for atom-cooling methods, Ketterle³, Kim⁴ and Sengstock⁵, for ultra-cold atom work, and Spreeuw⁶, Dholakia⁷ and Jhe for free-space guidance. Broad based reviews on cold atom guidance, can be found in the works of Jhe⁸, Song⁹ and Hinds¹⁰.

2.1 Optical Fibre Guides

There are currently three kinds of atom fibre-guides, these are; optical red-detuned, optical blue-detuned and magnetic-field fibre-guides. A basic description of optical red- and blue-detuned atom fibre-guides has been given briefly in chapter 1. This chapter will enlarge on this by discussing experimental realisations in capillary fibres and some associated theory of optical fibre modes. A brief introduction to optical blue-detuned fibre guides will also be given for comparison.

To the authors knowledge no atom guidance has been performed in photonic crystal fibre (PCF) to date. Hence discussions on supported optical modes are based on capillary fibres; the majority of theory discussed is also fully applicable to PCF.

A rudimentary schematic of red- and blue-detuned capillary guiding regimes is shown in Figure 2.1. As a snapshot summary, red-detuned capillary guides have a strong attenuation of guide intensity in narrow core fibres due to a reliance on grazing incidence mode support. This requires a compensatory higher input guide power, which conflicts with an atom-heating term, in turn acting to limit input intensity (and so guiding distance) through increased scatter. This can only be reduced through lower guide intensities or higher detunings (which reduce guide effectiveness). Optical coupling into hollow cores suffers an inherent coupling loss which can also generate disruptive scatter. However the intensity profile of light inside the hollow core generally maintains a good spatial separation between the guided flux and fibre walls.

Similarly, the pertinent features of blue-detuned guides are as follows; a greatly reduced spontaneous emission heating effect and thus the capacity for longer distance guiding, a non-trivial annulus coupling process which has prompted numerous novel coupling techniques^{11,12,13}, and a loss of guided flux through laser speckle in the guiding evanescent field. The last of these is perhaps the primary hurdle to be overcome; a few methods have been established to overcome it^{16,17,14}.

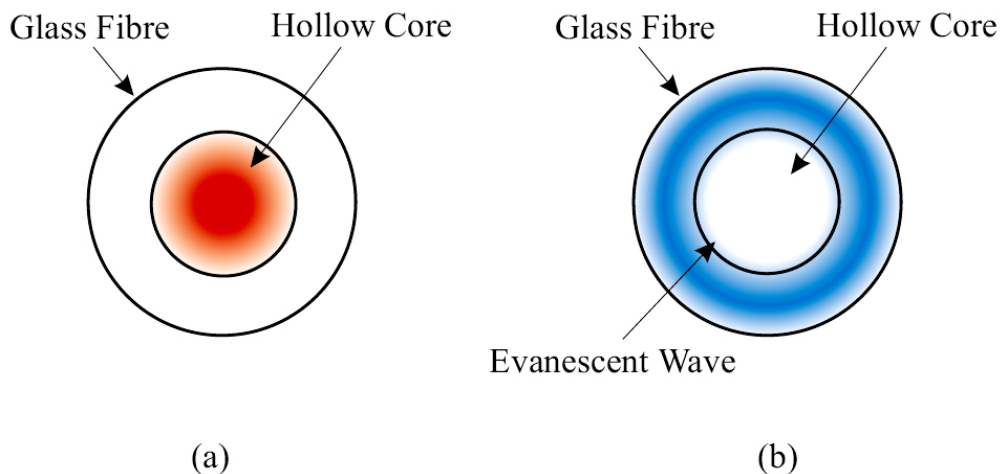


Figure 2.1 : Illustration of the light fields in hollow-core capillary fibres, when guiding (a) using red-detuned light and (b) blue-detuned light.

As an aside, guiding of micron sized particles (using a variant on optical guiding forces described in Chapter 1) has been performed at Bath university¹⁵. This

is the closest approximation to my PCF research performed to date, however the guiding of micron scale particles involves dissimilar physics and so is not considered pertinent to our atom guiding discussion.

2.1.1 Red-Detuned Capillary Fibre Guiding

In his 2002 review¹⁶ Jhe provided an algebraic summary of red guiding within a core whose width was much greater than the atomic de Broglie wavelength, ie. $ka \gg 1$, where $k=2\pi/\lambda$, and $2a$ is the hollow-core (HC) diameter. He states, in cylindrical coordinates the lowest order EH₁₁ mode is approximately given by,

$$I(\rho) = I_0 J_0^2(\chi\rho) \quad 2.1$$

where I_0 is the peak on-axis laser intensity, ρ is the radial distance from HC axis and J_0 is the fundamental Bessel function. Here χ can be determined by,

$$\gamma J_0(\chi a) K_1(\gamma a) + \chi J_1(\chi a) K_0(\gamma a) = 0 \quad 2.2$$

where J_m and K_m are the respective Bessel and modified Bessel functions of order m . β is the axial propagation wavevector (modified form of k to account for propagation direction within the fibre, often expressed for fibre-supported modes as $\beta = k n \cos\theta$, where modes propagate at an angle θ to the fibre axis), χ and γ are generally complex numbers related by,

$$\begin{aligned} \chi^2 &= k^2 - \beta^2 \\ \gamma^2 &= \beta^2 - n^2 k^2 \end{aligned} \quad 2.3$$

where n is the index of refraction of the glass. Applying $ka \gg 1$ to equation 2.2 we can restate $I(\rho)$, as,

$$J_0(\chi a) = \frac{i\chi}{2k} \frac{n^2 + 1}{\sqrt{n^2 - 1}} J_1(\chi a) \quad 2.4$$

Reinsertion into $I(\rho) = I_0 J_0^2(\chi \rho)$ provides both a mode diameter and an attenuation length for the chosen wavelength. The mode diameter is the width at which the guiding mode falls to $1/e$ of its on-axis value, and the attenuation length; the distance where the guide falls to $1/e$ of its initial fibre-entry value, is characteristic to the fibre and can be obtained from the imaginary part of β , explicitly given in the $ka \gg 1$ limit by equation 2.5, where $[\text{Im}(\beta)]^{-1}$ is the attenuation length, $l_{1/e}$.

$$\text{Im}(\beta) = \left(\frac{\chi a}{2\pi} \right)^2 \frac{\lambda^2}{2a^3} \frac{n^2 + 1}{\sqrt{n^2 - 1}} \quad 2.5$$

First Demonstration of Red-Detuned capillary Atom Guiding

Following theoretical proposals set out by Ol'Shanii¹⁷ and Savage¹⁸ in 1993 and 1994, respectively, the first demonstration of red-detuned atom fibre-guiding was reported by Renn *et al.*¹⁹ (of JILA, Colorado). Figure 2.2 shows their experimental arrangement. Two separate vacuum chambers were connected by a 6.2cm length of 40 μm hollow-core diameter capillary. The source cell contained Rubidium (Rb) vapour at room temperature. An ionising hotwire and channeltron detector were used for atom counting in the detection chamber.

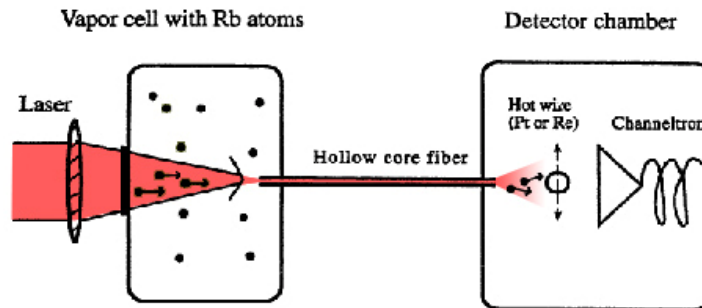


Figure 2.2 : Schematic of the experimental arrangement for the first successful fibre guiding. A 3.1cm capillary fibre is mounted between two vacuum chambers. Red-detuned guide light is launched into the core, this separates the propagating atoms from attractive Van der Waals forces inside the fibre. Reproduced from Renn *et al.*²¹

Simplifying equation 2.2 by substituting 2.4 in, and subsequently entering into 1.22 (in cylindrical coordinates), provides the following expression for the dipole potential experienced by atoms within the EH₁₁ mode,

$$U(\rho) = \frac{\hbar\Delta}{2} \ln \left(1 + \frac{\omega^2}{\Delta^2 + \gamma^2} \right) \quad 2.6$$

where Δ is the detuning from atomic resonance including Doppler shift. Evaluating this on-axis, $U(0)$, will allow calculation of the maximum guidable transverse velocity by the simple equation, $v_m = \sqrt{2U(0)/m}$. In Renn's work a guide of 45mW provided a dipole potential of 71mK. Thus atoms up to 3.7ms⁻¹ transverse velocity were capturable from the thermal background atom source. Integrating up to this velocity over the Maxwell velocity distribution transverse to the fibre axis and over all longitudinal velocities provides an expression for the expected flux output;

$$F_0 \approx \frac{1}{2} \sqrt{\frac{m}{2\pi k_B T}} n_0 A_h v_m^2 \quad 2.7$$

where the EH₁₁ mode diameter calculated earlier is used as the effective area A_h , T is the temperature of the atoms and n_0 is the atom density of the capture region. With a room temperature density of $n_0 = 10^{16} \text{ m}^{-3}$ a flux of 10⁵s⁻¹ was the predicted fibre input and an experimental output flux of 3×10³s⁻¹ after ~6.2cm of fibre was observed. Hence ~3% flux transmission efficiency was demonstrated. (It is worth noting this figure, as the fibre length, and guide beam parameters used for our guiding attempts at St Andrews are similar).

Guide Detuning

Detunings over a few GHz demonstrate the δ^{-1} dependence predicted by equation 1.19. With increasing intensity the signal increases and the position of greatest flux moves to larger red detunings, this is shown in Figure 2.3.

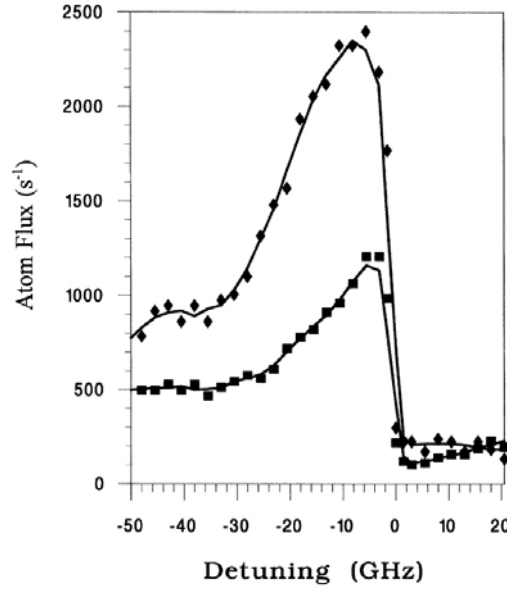


Figure 2.3 : Guided flux level from the 6.2cm, 40 μ m diameter Renn fibre, versus guide detuning at two intensities; $I_o=3.6\times 10^3$ W/cm 2 (45mW input power) and $I_o=1.3\times 10^3$ W/cm 2 (16.3mW input power). A sharp turn-on of guiding is seen as the guide crosses from blue (+ve) to red (-ve) detuning. The solid line is included to show the data trend. Reproduced from Renn et al.²¹

Fibre Curvature

The propagating mode in the hollow core was assumed to be spatially symmetric for the straight fibre case. In a curved fibre, atom velocity generates a centrifugal force around curves. This threatens to pull atoms from a guide and lose them to attractive Van der Waals forces. The tightest bend manageable is dictated by the centripetal force offered by the guide. This, in turn, is decided by the depth of dipole potential such that the tightest bend is given by a radius of curvature:

$$R_{\min} = mr_o v_z^2 / U(0) \quad 2.8$$

where $U(0)$ is the dipole potential experienced in the centre of the guide and r_o is the guide mode-radius. Atoms with velocities faster than v_z will be lost to the fibre walls at bends of radii $R \leq R_{\min}$. Renn *et al.* observed a typical R_{\min} value, for median v_z , of 18cm, and took further data characterising the dependence on input intensity for various bend radii. These are depicted in Figure 2.4.

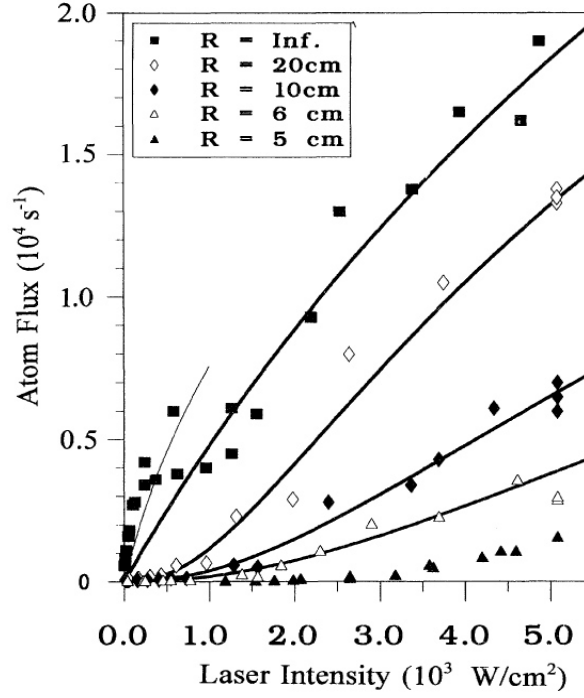


Figure 2.4 : Intensity dependence of the guided atom flux in the 40 μ m diameter hollow core. Multiple radii of curvature bends are indicated. The darker line for $R=\infty$ is a theoretical plot of the predicted flux, normalised to experimental parameters. This plot came from an integration of the Maxwell velocity distribution up to the maximum velocity confinable by the guide (on input), it assumes a detuning of -6GHz and that atoms are optically pumped into the lowest ground-state hyperfine level. The lighter line (for $R=\infty$) is the same but with the assumption that at low intensity the atoms are distributed equally among the ground-state levels. The remaining lines for $R<\infty$ are included to highlight trends in the data. Reproduced from Renn *et al.*

It is concluded that as the fibre becomes more curved, particularly at bend radii smaller than twice the attenuation length, ($R \approx 6\text{cm}$), the guided intensity profile becomes more asymmetric²⁰ and the intensity on the surface of the core walls increases. At these tight radii the simple model above breaks down as higher than expected losses are experienced. Thus optical guiding ability of the fibre is the governing mechanism for efficient atom guidance around tight bends. That is, the critical guiding radius is determined by optical properties rather than properties of the guided atoms.

Attenuation Length

The 1995 Renn *et al.* paper touches on the primary disadvantage of red-detuned capillary fibre-guiding; fibre attenuation length. As depicted in equation 2.5 this scales with the square of the laser wavelength and inversely with the cube of the core radius. This can be approximated by;

$$L_{1/e} = [\text{Im}(\beta)]^{-1} = 6.8(a^3 / \lambda^2) \frac{\sqrt{n^2 - 1}}{n^2 + 1} \quad 2.9$$

where n is the refractive index of the fibre annulus, a is the radius of the fibre hollow-core, and λ is the guide light wavelength. This is often simplified to $L_{1/e} = 2.3(a^3 / \lambda^2)$ for quick comparisons. Explicitly, for the 40 μm hollow core this is $L_{1/e} = 3.1\text{cm}$, (χa from equation 2.5 was given as $2.405 + 0.022i$). The rapid intensity attenuation with hollow core narrowing is compounded by an increase in coupling difficulty and initial scatter, both resulting from the difficulty of far-field-optics mode matching. Furthermore VDW forces impinge on guided flux more when fibre walls are close to the flux path. However if these hurdles can be overcome a secondary benefit of narrowing the core is an elimination of unwanted higher order modes; prolonged scatter along the fibre length would be greatly reduced if the V -number of the fibre fell below the single-mode threshold of $V \sim 2.4$

Thus, in summary of Renn's 1995 paper, red detuned capillary guidance is achievable over short distances with hollow cores broad compared to the guiding wavelength. However the goal of coherent atom transfer, achievable through core narrowing, is severely limited due to laser attenuation concerns.

2.1.2 Further Considerations for Red-Detuned Fibre Guides

The JILA team, (now including Drs. A.A. Zozulya and E.A. Donley), in their second fibre guide paper²¹, in 1997 discuss, in greater depth, the flux dependence on laser detuning, laser intensity and fibre curvature. In particular they detail the evolution of atom-flux versus laser detuning with increasing intensity. At low

intensities observations are similar to those in the previous paper, however at high intensities ($I=50\text{MW/m}^2$), radiation pressure scattering, or “viscous dipole force” is seen to “burn a hole” in the flux-detuning curve. This is relevant to my work as it is believed a similar result has been witnessed in free-space guiding experiments (described in chapter 4).

Viscous Dipole Force Heating

A loss mechanism for an atomic flux within a red-detuned fibre guide (or any optical guide where the atoms are high-field seeking), stems from a combination of three factors; the use of dipole force, increased scatter from high intensities, and the A.C. Stark effect. This loss mechanism produces a range of detunings and intensities where guided flux rates are far less than optimum.

As described earlier, the dipole-potential of a guide scales inversely with its detuning, whereas radiation-pressure scales with the inverse *square* of the detuning. Also, the atomic scatter rate from a guide is linearly dependent on its intensity. Hence spontaneous emission from radiation pressure is more likely to occur at lower detunings and higher intensities.

In Figure 2.5a) the flux rate of atoms emitted from a red-detuned guide is monitored over a range of detunings with four guide intensities. It is important to note the fibre in this case was quite short; 3.1cm, which was half of the attenuation length of the 40 μm diameter hollow-core fibre. Here the interplay between radiation pressure force and dipole potential can be seen. The plot of a low intensity guiding regime seen in Figure 2.5 a) demonstrates how a high radiation pressure kicks atoms through a short fibre before they can be heated thus providing the rapid flux boost in the low detuning (where scatter, or spontaneous emission, heating in longer fibres would be expected to significantly reduce atom flux). As the flux kick slopes off after -1GHz detuning, the dipole force is not sufficient (due to the low intensity) to cause a resurgence of flux. However in the higher intensity regime, the drop off in radiation pressure after -1GHz is eventually compensated for by the higher dipole-potential

which acts to confine a greater number of atoms and push the flux up to a secondary peak.

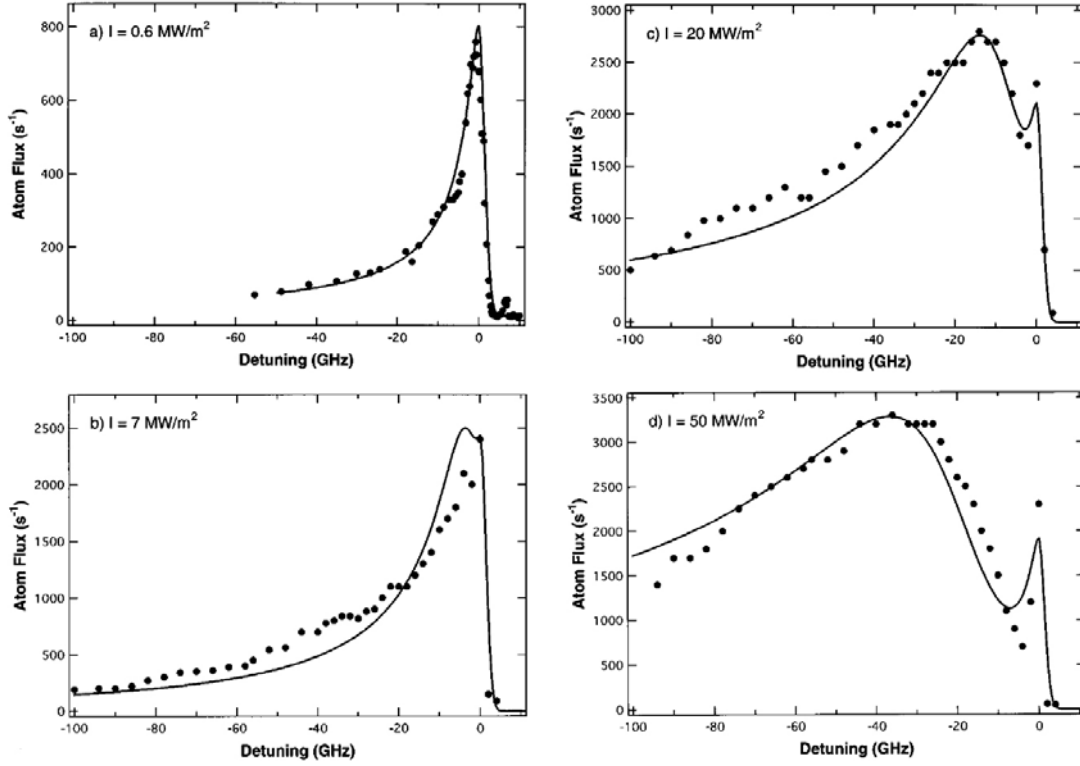


Figure 2.5 : Atom flux guided through a 40 μ m diameter core capillary fibre vs. laser detuning from resonance, at four laser intensities. The fibre lengths are 3.1cm and 6.2cm for figures a) and b)-d) respectively. Data in figure a) were collected using the lower power diode laser, whereas figures b)-d) use the Titanium Sapphire laser source. The dots are experimental data, the line is intended highlight trends in the data. A rapid turn-on of guided flux is seen immediately following detuning from resonance. In the higher intensity regime this spike is followed by a dip in the curve and a subsequent higher flux peak. Figure reproduced from Renn *et al.*²³

In summary, the initial levels of guided flux are dictated by the radiation pressure pushing/heating of atoms and the length of the fibre. This dictates the time over which atoms can be heated, (short fibres will have a high flux turn-on and long fibres will have a reduced level of initial turn-on). Also, the flux at greater detunings is dictated primarily by the dipole potential available; which in turn depends on intensity and attenuation length. Thus, it could be said that, as the detuning increases from resonance, the flux rates at near-zero detunings and those >20GHz (approx.) are sufficiently well matched to theory.

Dressed State Model

Only the crossover point between radiation pressure scattering and dipole confinement remains to be explained. Specifically, why is there a lowering of flux and not a peak in the detuning range $-1\text{GHz} < \delta < 10\text{GHz}$, where radiation-pressure could still be accelerating atoms through the guide and the dipole potential should be contributing more atom confinement.

Explanation of this requires understanding of the A.C.Stark effect and the dressed-atom picture²². The former is shown in Figure 2.6, it can easily be understood as a dynamic bowing of an atoms energy levels when exposed to an optical intensity. In the low intensity limit where the Rabi frequency Ω , and the detuning δ can be said to satisfy equation 2.10, atoms travelling in an optical guide spend the majority of their time in their ground state.

$$\Omega^2 / \delta^2 \ll 1 \quad 2.10$$

Where definitions of δ and Ω can be found in section 1.2. From Figure 2.6 we can see the A.C. Stark bowing of the ground state is towards a lower energy level. Hence an atom will experience a pull into the high intensity region, if the atom is propagating down the guide with any transverse velocity component it will oscillate about guide centre and continually experience attractive forces returning it to beam centre. This is the origin of the conservative dipole force (described in section 1.21). In the low intensity limit (and with linewidth $\gamma \ll \delta$) the dipole force scales linearly with intensity and inversely with detuning.

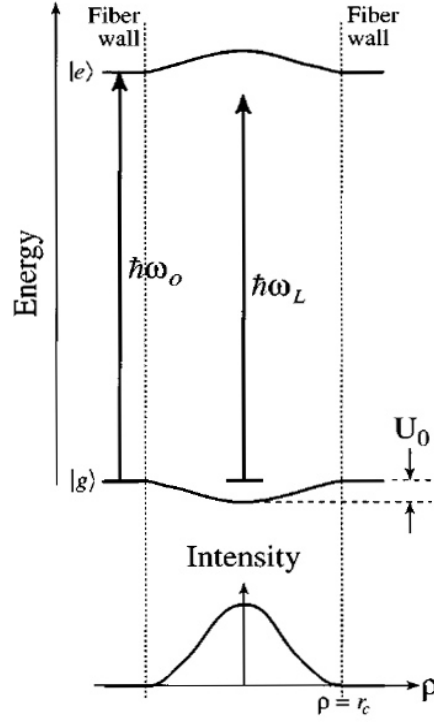


Figure 2.6 : The A.C Stark effect displays a bowing of an 2 level atom's energy levels dependent on incident intensity $I(\rho)$. In the low intensity limit an atom spends the majority of its time in the ground state, $|g\rangle$, and experiences a simple harmonic restoring force towards $\rho=0$. Here $\omega_l + \delta = \omega_o$, where ω_l corresponds to the laser frequency and ω_o the transition frequency. Figure reproduced from Renn *et al.*²³

This situation changes when switching to a high intensity optical field. In this case increased radiation-pressure scattering encourages an atom to make the previously unobtainable jump from ground to an excited state. It stays in this state for a time $\tau_a = 2(\pi\gamma)^{-1}$ and continues any transverse motion. Figure 2.6 shows that, in the excited state, the A.C. Stark bowing is in the positive energy direction; atoms are repelled from guide centre. Thus atoms in this state are accelerated towards the low intensity regions at the sides of the guide. This unwanted acceleration is worsened by the fact that the scattering necessary for jumping up to an excited state is strongest in the high intensity region at guide centre. Whereas the propensity for dropping back down to ground-state is highest in the low intensity region. So an atom is excited to the high energy portion of an energy level and de-excites down onto a similarly high energy portion of the ground level (see Figure 2.7). Thus regardless of level, the atom continually experiences a transverse acceleration back into the region which encourages further energetic interaction with the surrounding light field. Figure 2.7

helps show how ultimately this creates a cyclic repetition of excitation and de-excitation which continually adds transverse momentum to the atom.

Hence spontaneously jumping up to one excited level, falling down to the corresponding ground level, and jumping up to another excited state and on continually, could rapidly give an atom sufficient transverse energy to escape the guide potential. In fact, Renn *et al.*^{ref} describe a worst case scenario where an atom could gain an energy equal to twice the dipole-potential energy and escape the optical field before even making a complete circuit of the two levels.

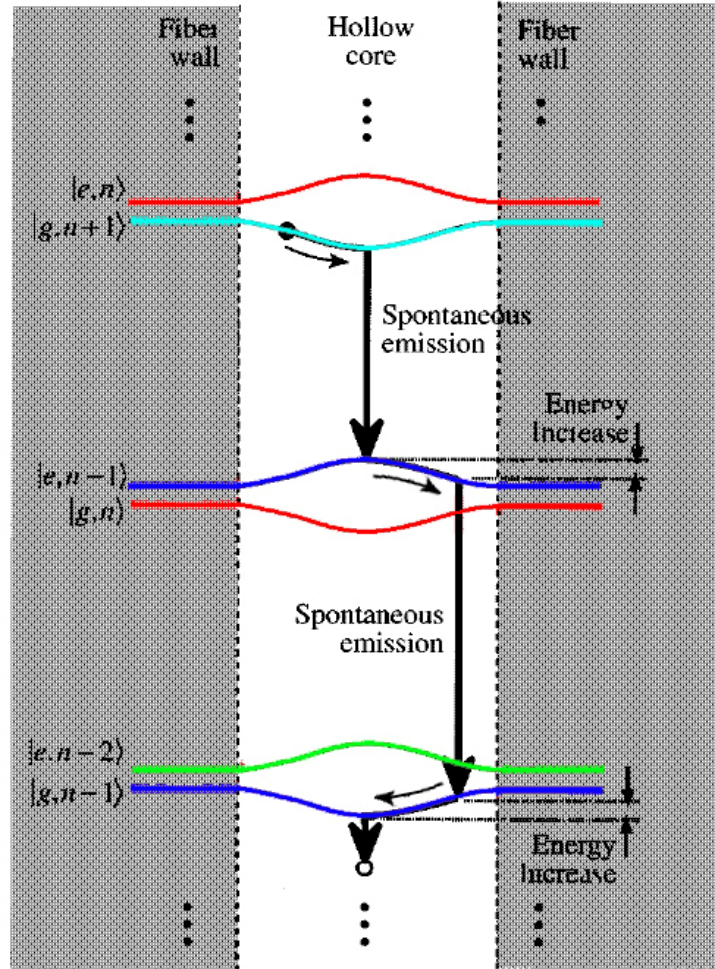


Figure 2.7 : Dressed state picture of a two level atom interacting with a laser field propagating within a hollow fibre core. Pairs of excited and ground state energy levels are shown in matching colours to help identify the atoms path. Note, an excitation *up* in energy is made on each thick dark downward arrow centred in the middle of the guide, however transitions on the edge of the guide are de-excitations; down in energy. Regardless of transition, an atom interacting in this way will experience an increase in transverse momentum, reducing the likelihood of successful guiding. Diagram reproduced from Renn *et al.*²³, (colour added to aid understanding).

Of course further detuning reduces viscous-heating loss by reducing spontaneous emission and simultaneously increasing the confining dipole potential. Nevertheless in between the radiation-pressure dominant regime and conservative-dipole regime, there is a loss of guided flux due to a viscous heating term. This viscous heating has now been explained; it relies on a combination of the dipole potential and on radiation pressure scattering (or spontaneous emission). In the absence of the scattering an atom would behave as if in a perfect dipole potential guide; simply oscillating back and forth within the bowl of its Stark-shifted ground state as it propagated along the guide.

Guiding Distance

Importantly the JILA team define the currently accepted limiting factor on red-detuned guiding distance; that being a *combination* of attenuation length and scatter from the guide. This is of particular interest to our work at St. Andrews as it highlights an inherent drawback of capillary fibre guides which PCF can theoretically circumvent. That being the need to increase input guide intensity in a bid to compensate for attenuation in the fibre core; length independence in PCF prevents lower intensities occurring further down the fibre. Thus a lower input intensity will reduce viscous dipole heating for atoms travelling in the PCF hollow core.

Atom Temperature, Guide Potential and Guide-Cloud Size Matching

An important advancement over early fibre guide experiments was the use of a MOT to provide cold atoms for guiding. Significantly lower atom temperatures (typically $\sim 100\mu\text{K}$) greatly enhanced guide beam efficiency. Capture of atoms from MOT regions now involved far superior flux rates since cold atoms have transverse velocities of a few cm s^{-1} , not the $\sim 10^3 \text{ms}^{-1}$ of thermal atoms, (for comparison Renn's 1995 paper used a guide capable of capturing atoms up to 3.7ms^{-1} to sample atoms from a thermal source).

Though not strictly fibre-guiding, the free-space capture of atoms from a MOT into a guide beam will dictate how many atoms can be guided into a hollow fibre

core. Thus a 2002 paper⁶ by Wolschrijn *et al.* is briefly mentioned here in order to describe the effects of deepening the guide potential relative to atom temperature and increasing the guide width relative to MOT cloud size. This summarises with an informative graph showing the fraction of atoms guided from a cold cloud, which is critical for subsequent fibre loading.

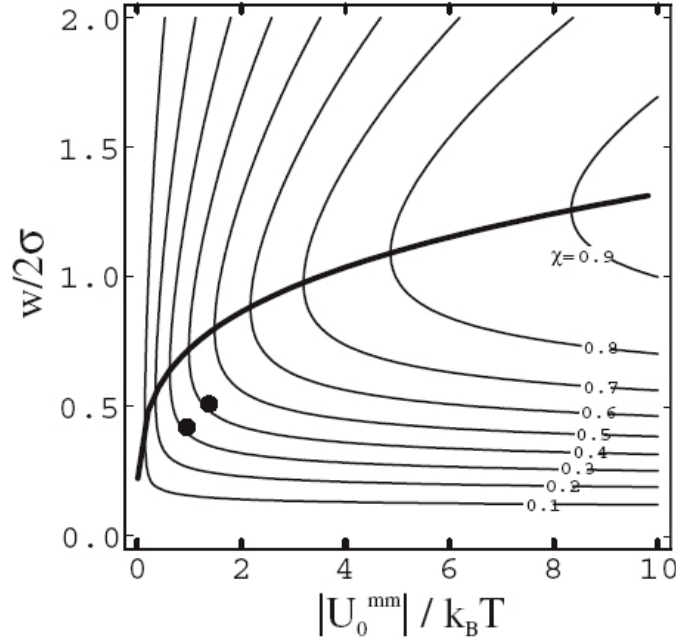


Figure 2.8 : Multiple plots of constant guiding fraction, χ , from a cold (molasses) source of Rb⁸⁷ atoms. The axes are ratios of, guide potential over cloud temperature (for x-axis) and guide waist over cloud diameter (for y-axis). The thick curve shows the optimum guide waist as a function of a ‘molasses-matched’ potential depth $|U_0^{mm}|$ in units of $k_B T$, which is proportional to the available power and does not depend on the guide waist. When the experimental parameters cloud radius, σ , cloud temperature, T and guide power, P are known, the optimal guide waist w can be read from this graph. The two dark points represent experimental data recorded with $P = 85\text{mW}$ and detuning, $\delta = 12 \times 10^3 \Gamma$ (where $\Gamma = 2\pi \times 6.1\text{MHz}$, the natural linewidth of the D_2 line). Reproduced from Wolschrijn *et al.*

The guided fraction is described as being dictated by only two dimensionless parameters: the relative size of the guide compared to the molasses size, w/σ , (guide waist, w , and cloud radius, σ) and the depth of the guide potential compared to the temperature of the cloud, $U_0/k_B T$. Intuitively the guided fraction tends to zero when

either the potential depth or the width of the guiding beam goes to zero. The fraction increases equivalently when either $|U_0|$ or w increases.

However, it is acknowledged that the above captured-fraction discussion does not account for guide beam focusing prior to fibre entry. A MOT cloud might not be located at beam waist if subsequent fibre-mode matching stipulates a beam waist located at fibre entrance. The numbers from Figure 2.8 would need to be scaled to account for guide divergence to give an impression of actual coupled fraction.

2.1.3 Optical Fibre-Guides, Conclusion

Factors pertinent to red-detuned fibre guiding have been discussed through review of selected published works. In summary, red-detuned fibre guides offer better flux localisation relatively far from the fibre walls and so easily surpass the short ranged Van der Waals attraction. However, grazing-incidence mode support within the hollow-core induces rapid intensity attenuation, with a cubed dependence on hollow-core radius. Furthermore, atom guidance within a high-intensity region causes flux heating through spontaneous emission scattering and viscous dipole interactions.

For comparison, review of publications concerning blue-detuned guiding^{23, 24, 25, 26, 27, 28} yields the following summary: Blue-detuned guides offer improved spontaneous emission rates by merit of their guidance within a low-field region. However they rely on an easily perturbed, and easily superseded, evanescent field for confinement. Hence, speckle and scatter-induced grazing-incidence modes are significant loss mechanisms in blue-detuned regimes. Multiple techniques exist to remove speckle. The weak evanescent fields require high laser power input.

Lower temperature source atoms improve the efficiency of both red- and blue-detuned potentials, however, associated lower longitudinal velocities increase sensitivity to speckle in blue-detuned guides.

All fibre-guides suffer significant coupling-loss whether coupling into their hollow-core or their annulus-surrounds.

Fibre bending can be used as a velocity selective filter in both red and blue regimes and optical mode displacement at bends only brings significant flux loss beyond a critical bend radius.

Future work on red-detuned fibre-guides will lie with PCF. In which spontaneous emission and viscous-dipole heating are significantly reduced thanks to the removal of severe light-attenuation within the core. Perhaps also in grazing-incidence launch of a dark hollow beam (DHB) into a hollow core for optical narrowing of the guided flux path²⁹.

2.2 Dark Hollow Beam Guidance in a Hollow Core

A recent publication by Wang *et al.* has illuminated a further configuration which combines low-scatter, blue-detuned DHB guiding, with the low-loss nature of a novel, capillary fibre which has a metallic coating on its inside core surface. The paper presents this experimentally realised fibre and a theoretical analysis of the loss mechanisms for MOT temperature atoms guided in a DHB supported as a true propagating mode within the metallic *hollow-core*. Succinct descriptions of the propagating optical modes within a 30 μ m hollow-core, the coupling loss, and the transmission efficiency is also given. Figure 2.9 illustrates their proposed atom loading and guiding technique, (reproduced from their publication).

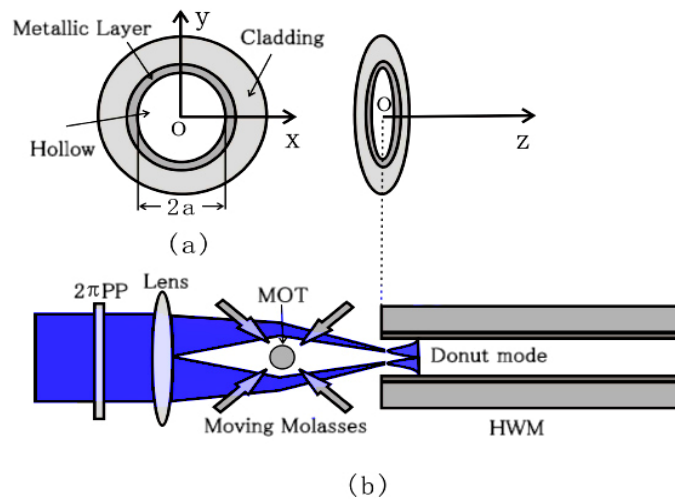


Figure 2.9 : (a) The structure of the hollow metallic waveguide (HMW) and (b) a schematic of the proposed atomic loading and guiding arrangement. A 2π phase plate (2π PP) is used to generate the hollow beam from the circularly polarized input Gaussian.

In the interests of brevity this work is not discussed further. Suffice to say the coupling of a DHB into a hollow-*core* is an exciting prospect for atom guidance, which raised the question of whether our PCF could support a DHB in its hollow core. However it is expected that this regime will require significant development before it is realised.

2.3 Chapter Conclusion

It is hoped an understanding of some key papers in the field of hollow-fibre atom guidance has been conveyed in this chapter. The merits of optical-fibre guides over magnetic fibre-guides have been summarised, as have the motivations for choosing red-detuned fibre-guides over blue-detuned equivalents. In particular the diminished length dependence of transmitted intensity in PCF is to be capitalised on for a more efficient red-detuned fibre-guide relative to capillary fibre. These works set the scene for my research which will experimentally demonstrate the benefits of optical atom guidance within PCF.

2.4 Bibliography

- ¹ C.S.Adams, E. Riis, “Laser Cooling and Trapping of Neutral Atoms”, Prog. Quant. Electr., Vol. 21, #1, p1-79, (1997).
- ² W. Ketterle, D.E.Pritchard, “Atom Cooling by Time-Dependent Potentials”, Phys. Rev. A., vol. 46, #7, p4051-4, (1992)
- ³ D. S. Durfee and W. Ketterle, “Experimental studies of Bose-Einstein condensation”, Optics Express, Vol.2, #8, p299, (1998)
- ⁴ Jae-Wan Kim, “A Study of Non-Dissipative Traps towards Bose-Einstein Condensation”, PhD thesis, submitted to Seoul National University, (2002).
- ⁵ Kai Bongs and Klaus Sengstock “Physics with coherent matter waves”, Institut of Physics Publishing, Reports on the Progress of Physics, #67, p907–963, (2004).
- ⁶ B.T. Wolschrijn, R.A. Cornelussen, R.J.C. Spreeuw and H.B. van Linden van den Heuvell, “Guiding of cold atoms by a red-detuned laser beam of moderate power”, New Journal of Physics vol. 4, #69 p1–10, (2002).
- ⁷ K. Dholakia, “Atom Hosepipes”, Contemporary Physics, vol. 39, #5, p351-69, (1998).
- ⁸ Heung-Ryoul Noh, Wonho Jhe, “Atom Optics with Hollow Optical Systems”, Elsevier Science, March, (2002).
- ⁹ Y. Song, “Hollow Beam Atom Tunnel”, PhD thesis, submitted to the University of Maryland, (1999).
- ¹⁰ E.A. Hinds, I.G. Hughes, “Magnetic atom optics: mirrors, guides, traps, and chips for atoms”, Journal App. Phys., #32, p119-146, (1999).
- ¹¹ R G Dall, M D Hoogerland, K G H Baldwin† and S J Buckman, “Guiding of metastable helium atoms through hollow optical fibres”, J. Opt. B: Quantum Semiclass. Opt. #1, p396-401, (1999).
- ¹² R.G. Dall, M.D. Hoogerland, D. Tierney, K.G.H. Baldwin, S.J. Buckman, “Single-mode hollow optical fibres for atom guiding”, Appl. Phys. B, #74, p11–18, (2002).
- ¹³ F. K. Fatemi, M. Bashkansky, and S. Moore, “Side-illuminated hollow-core optical fiber for atom guiding”, Optics Express, Vol. 13, # 13, p4890, (2005).
- ¹⁴ Markus Hautakorpi *, A. Shevchenko, M. Kaivola, “Spatially smooth evanescent-wave profiles in a multimode hollow optical fiber for atom guiding”, Opto. Comm. accepted for publication, (March, 2004).
- ¹⁵ F.Benabid, J.C.Knight, P.St.J.Russell, “Particle Levitation and Guidance in Hollow-Core Photonic Crystal fibre”, Optics Express, vol. 10, #21,(2002)
- ¹⁶ Heung-Ryoul Noh, Wonho Jhe, “Atom Optics with Hollow Optical Systems”, Elsevier Science, March, (2002).
- ¹⁷ Ol’Shanii M A, Ovchinnikov Yu B and Letokhov V S, Opt. Commun., #98, p77, (1993).
- ¹⁸ S.Marksteiner, C.M.Savage, P.Zoller, “Coherent Atomic Waveguidesfrom Hollow Optical Fibres: Quatized Atomic Motion”, Phys. Rev. A, Vol.50, #3, P2680, (1994).
- ¹⁹ M.J.Renn et al. JILA & University of Colorado Dept. of Physics, “Laser Guided Atoms in Hollow-Core Optical Fibres”, Physical Review A, Vol. 75, #18, p3253-56, (1995).
- ²⁰ E.A.J. Marcatile, R.A. Schmeltzer, Bell System Tech. J., p1783, July, (1964).
- ²¹ M.J. Renn, A.A. Zozulya, E.A. Donley, E.A. Cornell, D.Z. Anderson, “Optical-Dipole-Force Fiber Guiding and Heating of Atoms”, Phys. Rev. A, vol.55, #5, (1997).
- ²² X. Xu, Y. Wang, W. Jhe, “Theory of Atom Guidance in a Hollow Laser Beam: Dressed Atom Approach”, J. Opt. Soc. Am. B, vol. 17, #6, p1039, (2000).
- ²³ R.G. Dall, M.D. Hoogerland, D. Tierney, K.G.H. Baldwin, S.J. Buckman, “Single-mode hollow optical fibres for atom guiding”, Appl. Phys. B, #74, p11–18, (2002).
- ²⁴ S.Marksteiner, C.M.Savage, P.Zoller, “Coherent Atomic Waveguidesfrom Hollow Optical Fibres: Quatized Atomic Motion”, Phys. Rev. A, Vol.50, #3, P2680, (1994).
- ²⁵ E.Donley, Masters Thesis, University of Colorado, (1996).
- ²⁶ M.J. Renn, E.A. Donley, E.A. Cornell, C.E.Wieman, D.Z.Anderson, “Evanescent-Wave Guiding of Atoms in Hollow Optical Fibres”, Phys. Rev. A., Vol. 53, #2, p648, (1996).
- ²⁷ H.Ito, T. Nakata, K. Sakaki, M.Ohtsul, “Laser Spectroscopy of Atoms guided by Evanescent Waves in Micron-Sized Hollow Optical Fibres”, Phys. Rev. Lett., Vol. 76, #24, (1996).
- ²⁸ D. Muller, E.A. Cornell, D.Z. Anderson, E.R.I. Abraham, “Guiding Laser-Cooled Atoms in Hollow-Core Fibres”, Phys. Rev. A., Vol. 61, #33, p411, (2000).
- ²⁹ Z. Wang, M. Dai, J. Yin, “Atomic (or molecular) guiding using a blue-detuned doughnut mode in a hollow metallic waveguide”, Optics Express, Vol. 13, # 21, p8406, (2005).

Chapter 3

Laser Systems for Cooling, Guiding and detection of Atoms.

Introduction

In this chapter a number of optical and mechanical systems will be described. These are all essential for the guiding experiments reported herein and all relate to the application of laser light into the trapping volume. In particular cooling and guiding laser systems used throughout, their output characteristics, construction and the precise frequency stabilisation techniques required for generation and manipulation of a MOT will be discussed. Additional details are given on the shuttering of these laser beams and their use as optical probes for atom flux detection.

Cold atom experiments performed herein required laser outputs on frequencies matching the transitions of Rubidium (Rb), specifically isotopes Rb^{85} and Rb^{87} . The choice of isotope was dictated by laser wavelengths attainable from equipment at the time. The relative abundances of these isotopes, as emitted by the atom-ovens (described in chapter 4) was 72.15% : 27.85% in favour of Rb^{85} , hence experimental preference was given to Rb^{85} especially since detection sensitivity was an issue. The laser sources used can be broken into two categories; trapping and guiding. Both groups required a degree of control over their lasing frequencies, however, while guide beams needed a higher power output; typically employing a separate pump laser, trapping lasers required significantly more frequency stabilisation equipment.

All free-space light beam guidance work reported here (and a portion of the fibre guide work) was performed as a team effort between Dr. Daniel Rhodes and the author.

3.1 Trapping Lasers

A useful advantage of Rb is that its D2 lines lie at 780nm which is a wavelength easily reached with inexpensive diode lasers. Furthermore these diode lasers can be tuned by temperature or current control, thus making them ideal candidates for electronic locking; selectively feeding back some of the laser power via an extended cavity design reduces the linewidth of these diodes by approximately two orders of magnitude to $\sim 135\text{kHz}$, which in turn, allows us to obtain a suitable absorption spectrum for a feedback locking circuit. The absorption signal is used in a feedback circuit to control the cavity length and the drive current, via a piezo-electric transducer (PZT) and laser driver circuit, respectively. Thus stable locking to a specific atomic transition is achievable, where the PZT is used to counteract relatively low frequency, larger scale noise such as, some thermal drift, impacts on the optics bench, etc., while the current lock manages higher frequency noise such as loud voices and the higher resonances of impacts on the optics bench. A saturated absorption scan over the spectrum of Rb is shown in Figure 3.1 along with the associated energy transitions of Rb^{85} and Rb^{87} in Figure 3.2a) and b) respectively.

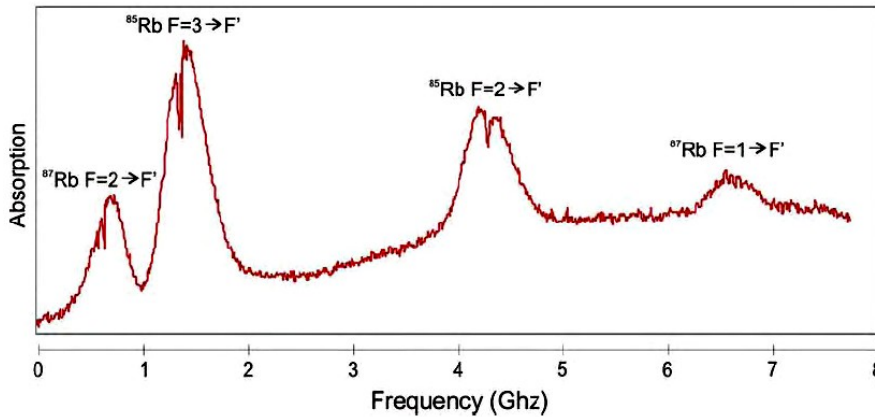


Figure 3.1 : An absorption scan across the rubidium transitions. The two left hand side peaks are the cooling transitions, the hyperfine transitions are on the right.

As described in chapter 1, formation of a MOT requires cooling and hyperfine repump beams, the energy transitions for these are indicated in Figure 3.2a) and b) as vertical red lines. The cooling laser was tuned and locked approximately 2Γ (where Γ is the natural line-width of the transition) below the frequency of the selected cooling transition, this was to provide the small red-detuning needed for the Doppler cooling process. For experiments involving Rb^{85} the cooling transition was $5S_{1/2}(F=3) \rightarrow 5P_{3/2}$

($F'=4$), while the hyperfine laser was locked to the $5S_{1/2}$ ($F=2$) \rightarrow $5P_{3/2}$ ($F'=3$) transition. Experiments involving the Rb^{87} isotope used the $5S_{1/2}$ ($F=2$) \rightarrow $5P_{3/2}$ ($F'=3$) transition for the cooling laser and $5S_{1/2}$ ($F=1$) \rightarrow $5P_{3/2}$ ($F'=2$) for the hyperfine. In theory, because the hyperfine laser is only pumping atoms that have fallen out of the cooling cycle (approximately only one in every thousand transitions), it does not need to be as finely stabilised as the cooling laser, however, in practice there was a visible difference in MOT brightness between well and badly positioned hyperfine lock points.

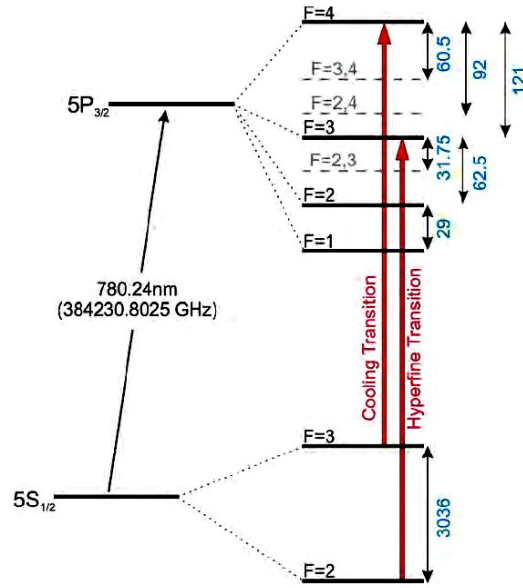


Figure 3.2a) : Energy level diagram of the Rb^{85} D2 lines. The values in blue are all MHz.

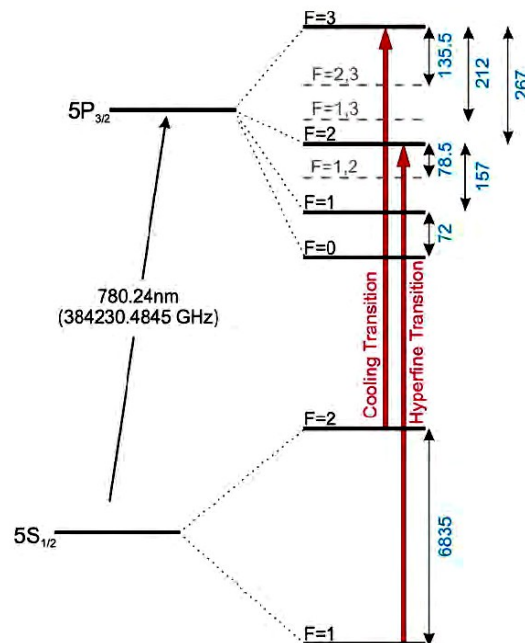


Figure 3.2b) : Energy level diagram of the Rb^{87} D2 lines. The values in blue are all MHz.

Locked at these wavelengths, the cooling and hyperfine beams are able to cool Rb atoms. But what keeps them stabilised on these precise frequencies in the presence of lab vibrations? To answer this, the construction of the lasers must be discussed. Three different arrangements of cooling beams were used alternately, these were **1)** a single extended cavity diode laser (ECDL), **2)** a master-slave diode chain, and **3)** a commercial TUI optics TA-100. The former two systems also catered for the *detection* of atoms; light was siphoned from cooling beams to provide on-resonance probe beams. However, numerous optics in the cooling beams such as, acousto-optic modulators (AOMs), isolators, mirrors, lenses, etc. limited the power remaining for effective cooling or detection. Thus the TUI cooling laser was introduced to compensate for the limited power. Using the resultant higher power output of 500mW (max) not only provided broader cooling beams (increasing the number of trappable atoms) but also freed up an entire ECDL solely for probing. It also provided enough power for a dual pass AOM system which allowed an additional molasses cycle in the MOT (described later in this chapter). The hyperfine beam came from a single ECDL, and remained so throughout.

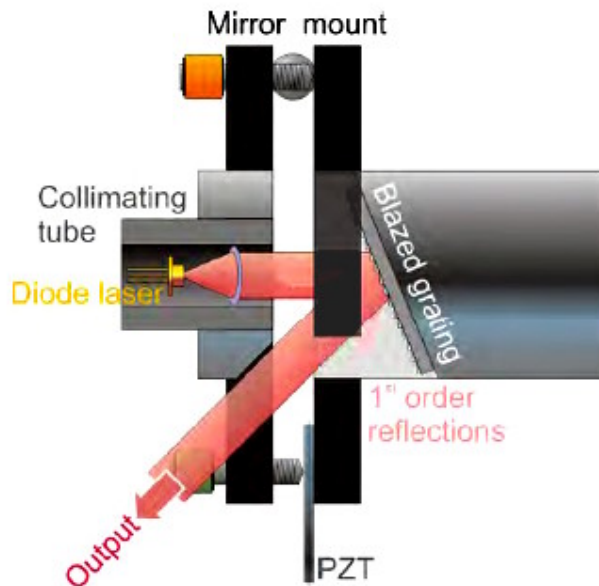


Figure 3.3 : A schematic of the in-house built extended cavity mounting. The circularised diode output is collimated then reflected off a blazed grating, the first diffracted order is fed back into the diode. The cavity length can be manually adjusted via the mirror actuators, and electronically controlled through the PZT sandwiched between the horizontal actuator (lower control in the image) and mirror mount face.

1) The Extended Cavity Diode Laser (ECDL)

This was the first arrangement used for generating cooling beams, it was built in-house in the Littrow geometry¹ using a diode laser mounted into a commercial clear quadrant mirror mount (Newport, P100-AC) which also holds a grating². The ECDL is shown schematically in Figure 3.3. One consideration when using diode lasers is the elliptical output, which could distort the shape of a trapped atom cloud. Correction before trap entry could be done through use of anamorphic prisms, a pair of cylindrical lenses or coupling through an optic fibre. However these complicate the experimental setup and can result in severe power loss. Such extra corrective optics were eliminated by use of Circulase diode lasers (Blue Sky Research), these were Hitachi HL7851G diode lasers (maximum output power 50mW at 785nm) which have had a small microlens placed a few μm from the semiconductor output facet. This releases a divergent, approximately circular beam (aspect ratio $\sim 1:1.1$). This is then collimated in a commercial collimating tube. A diagram of the diode and microlens array is shown in Figure 3.4.

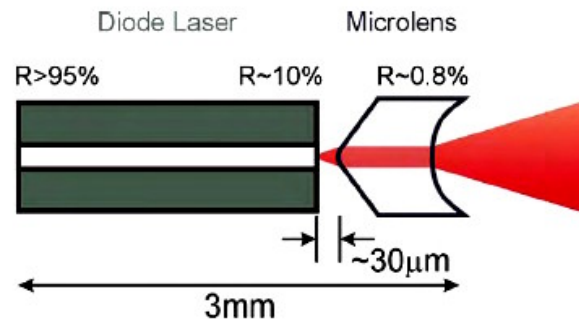


Figure 3.4 : Diode laser and microlens array. The microlens is only 250 μm thick.

The collimating tube was placed in a custom built holder for attaching to the mirror mount and a second custom machined (Optometrics, UK) holder for the grating, (1200lines/mm, blazed wavelength at 300nm), was positioned on the other side of the mirror mount so the mirror adjust screws could act to control the cavity alignment. The angle of the grating can be found from ;

$$m\lambda = d(\sin \theta \pm \sin \theta') \quad 3.1$$

where m is the diffracted order, θ is the angle of incidence, θ' is the angle of reflection and d is the line spacing of the grating. The grating (shown schematically in Figure 3.5) feeds back about 20% of the incident light into the diode cavity leaving ~30mW output power in the zeroth order beam which for trap entry. The laser should be rotated in its mount so that the polarisation of the laser matches the grating orientation, this optimisation is achieved by simply measuring the reflected beam power off the grating.

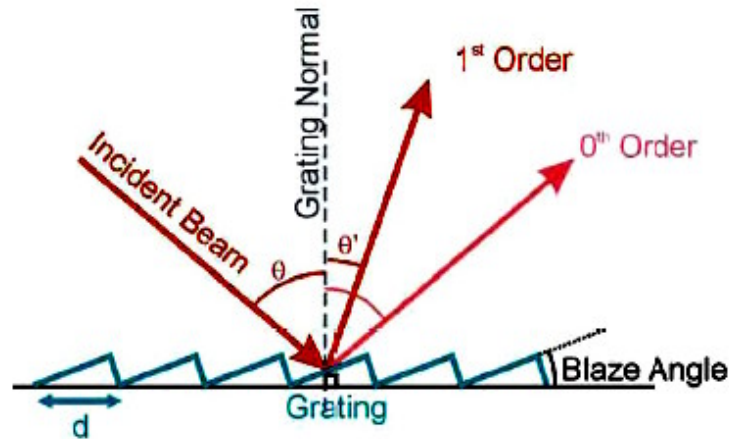


Figure 3.5 : A blazed diffraction grating where disparity between incident-beam angle and grating-normal produces preferential diffraction into a specific order for a characteristic wavelength known as the blaze wavelength. The blaze wavelength diffracts the most amount of light into this order and is selected away from the laser wavelength to ensure most incident light is reflected into the zeroth order since only a small fraction is required for extended cavity feedback.

Experimentally, the horizontal mirror actuator could be rotated one turn each way while maintaining extended cavity operation, whereas the vertical actuator could be rotated only half a turn each way before losing extended cavity condition. This is an intuitive disparity given the slab like dimensions of the diode lasing medium and the vertical alignment of the grating.

The entire assembly is mounted on a 90mm diameter, 40mm tall block of aluminium via a peltier element, driven by a commercial TEC controller (Wavelength Electronics, Inc.), to stabilise the temperature, (altogether shown in the photograph Figure 3.6).

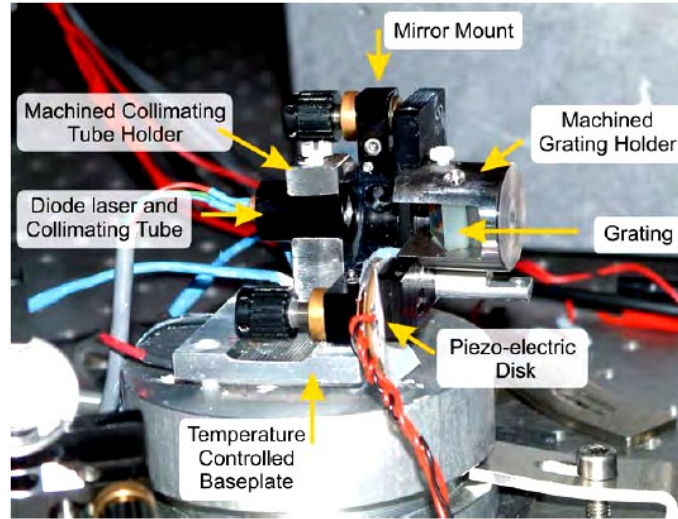


Figure 3.6 : A photograph of an ECDL used as a mainstay for hyperfine and cooling beams throughout experiments at St Andrews. For scale, the machined grating holder is 1" in diameter.

The diodes are initially cooled to $\sim 14^{\circ}\text{C}$ to pull the laser wavelength down to approximately 780nm, the frequency can then be controlled by altering the external cavity length; this can be done coarsely by rotating the horizontal adjustment screw of the mirror mount while fine tuning is achieved by applying a voltage to a piezoelectric transducer (PZT) placed beneath this screw, a continuous, mode-hop free tuning range of $\sim 5\text{GHz}$ is achieved using the PZT to scan the frequencies. A simple feedback circuit controlling just the PZT voltage on its own can be used to lock the laser, however, as mentioned earlier, extra stability can be found when additional control is exerted over the diode drive current (this counters high frequency fluctuations). The locking system is described later in this chapter.

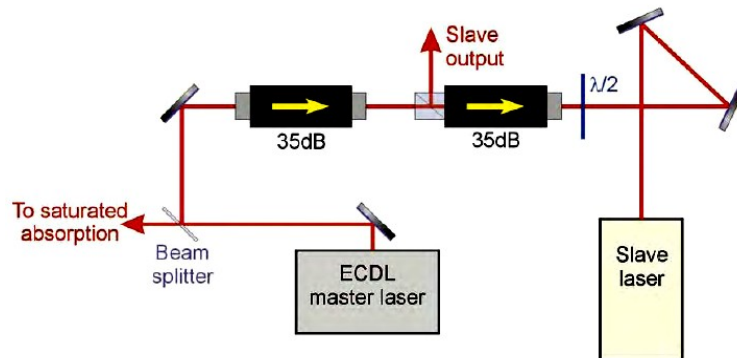


Figure 3.7 : An injection locked diode laser. Isolators were employed to prevent any interference from unwanted light reflected back into the master laser. The half-wave plate was included to match the polarisation of two lasers, (similarly the slave laser could be rotated in its mount).

2) The Master Slave ECDL Chain

The master-slave chain shown in Figure 3.7 was the second cooling beam arrangement employed at St Andrews, it was introduced to facilitate an increase in cooling beam power. The useful output from the single ECDL (described in the previous section) was $\sim 30\text{mW}$, this was enough power to create a MOT but the number of trapped atoms is proportional to the area of the beam (provided beam intensity, $I \geq I_{sat}$) so a method of increasing the available power was sought.

Sanyo make a higher power diode capable of 75mW output at 780nm , (DL-7140-201, which can also be bought circularised through Blue Sky Research). This Sanyo diode is more powerful than the Hitachi model used previously but the spectral quality is lower; it has a larger linewidth making it less practical for locking to the atomic transitions. The solution of injection locking gives access to the positive attributes of both diodes. The higher power Sanyo laser can be slaved to the output from the Hitachi ECDL; seeding a free running (slave) laser with a few μW of light from a second (master) laser will cause the slave laser to run on an identical mode to the master. If the slave laser is running at a frequency close to the master laser the presence of the injected beam reduces the threshold for cavity modes which match those of the incoming master and thus results in preferential lasing of the slave laser on the master's wavelength. In this way a beam with the higher power of the Sanyo diode and the spectral quality of the Hitachi can be sent to the trap. The seeding was set up as shown in Figure 3.7 with a beam-splitting optical isolator used to separate the input-master and output-slave beams.

3) The TUI Optics TA-100

The final laser system used was a commercially available, TUI Optics TA-100, which used a tapered amplifier to generate a maximum output of 500mW . The master oscillator (MO) is an ECDL in Littrow geometry. The beam from the diode is sampled through a $<90\%$ reflective mirror for the purpose of locking the laser. The diode used in the extended cavity is not circularised, however, the optics around the tapered amplifier include a cylindrical lens to beam-shape the beam upon exiting the amplifier. Because the tapered amplifier is a gain medium it also generates amplified

spontaneous emission (ASE) “wings” around the, now circularised output which needs to be apertured external to the laser system. Figure 3.8 illustrates the TUI setup.

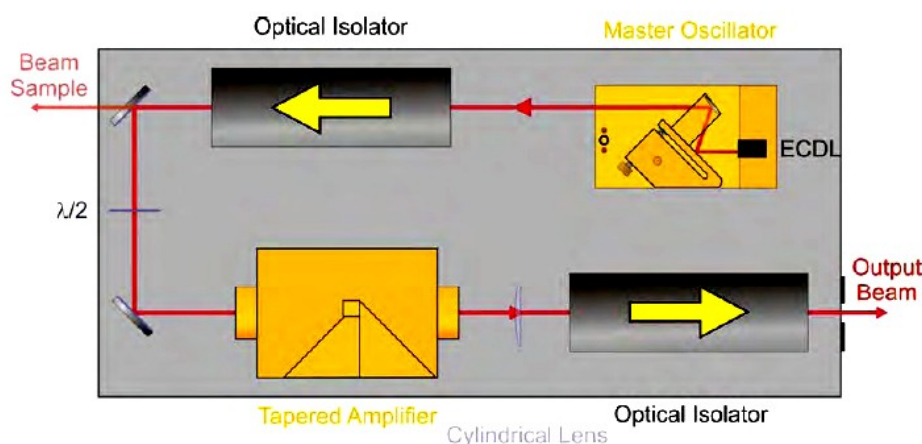


Figure 3.8 : A schematic of the TA-100 including isolators, Littrow geometry ECDL master oscillator (MO), tapered amplifier and cylindrical lens. Output from the MO is collimated but not circularised; lenses on the front and back facets of the tapered amplifier provide collimation for the amplified beam and the cylindrical lens provides circularisation.

3.2 Frequency Stabilisation

Now the required laser outputs for generating a MOT have been identified, the method of stabilising them for prolonged lab usage, (5 minutes at the very least), is described. The lasers have to be locked to within a few hundred kHz of the trapping frequencies (less than the natural linewidth of the atomic transition). They also have to maintain narrow-linewidths, single-mode outputs and be tunable over the transition spectrum. This is achieved through a negative feedback circuit which uses the absorption profile of the chosen atomic transition to provide an electronic signal which can be isolated in an in-house built “lock-box”. This box provides scaled feedback signals for both the grating PZT and laser driver to ensure stable laser output which dithers minutely around the lock frequency and has any drift from that frequency compensated for.

A basic servo locking system is shown in Figure 3.9, it requires electronic rendering of the signal (described in the next section) to which locking is desired and a reference signal with which to compare it. This comparison is used to create an error signal which is then fed through scaling electronics which provide a negative

feedback signal that is sent to the laser. The feedback is negative to cancel the effect of any noise and return the laser to the reference level. The error signal is inversely proportional to the gain of the feedback circuit, increasing the gain will pull the signal closer to the reference level (the dc response) but this is at the expense of the bandwidth of the system (increasing the “tightness” of the lock reduces the range of frequencies which can be compensated). This leads to a trade off between the transient response time and dc sensitivity of the servo locking system.

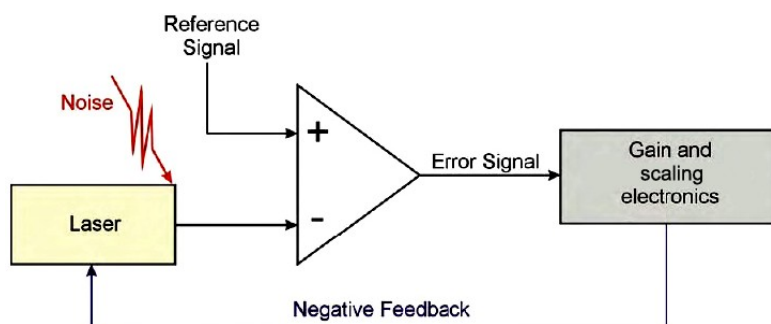


Figure 3.9 : Block diagram of a basic servo locking loop for laser stabilisation.

There is a risk of incurring a time lag in these systems; if the feedback signal sent to a corrective element (eg. PZT or laser driver) is at a frequency below the resonance of that element then the correction will follow the phase of the feedback signal and correct for the noise. If, however, the feedback frequency is above the natural resonance of the corrective element then the correction is delayed by π radians and the feedback becomes positive, acting as an amplifier to the noise and moving the laser even further from lock point. Thus, a simple negative feedback circuit, with constant gain across all frequencies, cannot correct for all frequencies of noise in a system.

In order to extend the locking bandwidth whilst keeping some dc sensitivity a dual-servo system was implemented. This removes problems associated with noise occurring at frequencies near a corrective element’s natural resonance. As mentioned earlier, the ECDLs were linked to two feedback controls, one for the PZT controlling the grating position, and one for the diode current from the laser driver. The PZT was used to correct for broadband deviations with a slow response time. High frequency noise was corrected by modulation, at up to 100MHz (two orders of magnitude faster

than the PZT), of the driver current. The cooling and the hyperfine lasers were individually locked in this way.

3.2.1 Doppler-Free Saturated Absorption

Now the method of obtaining an electronically rendered reference signal for locking can be described. This signal for the dual-servo locking system was generated through saturated absorption of a siphoned-off portion of a trapping laser passed through a Rb cell. This technique provided a method of distinguishing the hyperfine features of atomic transitions using a thermal cell of Rb. Ordinarily such features would be washed out through Doppler broadening of the laser signal from the motion of the atoms, however *saturated* absorption spectroscopy circumvents this symptom.

A single laser beam was split into two counter propagating beams of exactly the same frequency and overlapped inside a vapour cell, as shown in Figure 3.10. Only atoms with zero velocity along the directions of the beams will see identical frequencies from both directions and be able to interact with both beams. Atoms moving in a direction along the path of beams will observe opposite Doppler shifts in the two beams and will therefore only absorb light from one beam.

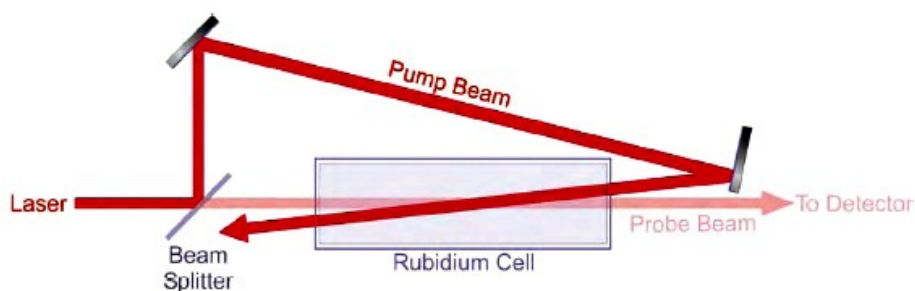


Figure 3.10 : Saturated absorption set up. Better overlap between pump and probe beams within the Rb cell generates more definition for atomic hyperfine transitions seen by the collecting photodiode detector.

One of the beams is made significantly more intense than the other and is thus designated the ‘pump’ beam, (typically a Fresnel reflection from a thin film pellicule provided sufficient power for the probe). The weaker, ‘probe’ beam is directed onto the photo-detector with as much overlap with the pump as possible; this improves visibility of the hyperfine transition. Due to Doppler shifting of the laser frequency,

the pump beam will excite atoms which have either no velocity in the pump direction or are moving in a direction which opposes the beam. The probe beam on the other hand will excite atoms which have either no velocity in the probe direction or those which are moving in a direction opposite to the probe beam, (same direction as the pump beam). Atoms with velocities which permit interaction with both beams are more likely to absorb from the more intense pump beam, these atoms are saturated by the pump and these atoms in this state do not interact with the probe as it passes. Therefore probe beam intensity transmitted to the photo-detector is greater at the frequencies at which the pump beam has already excited atoms; the resultant jumps observed in the intensity profile correspond to atomic hyperfine transitions and thus illuminate the hyperfine structure. A typical saturated absorption spectrum is shown in Figure 3.11

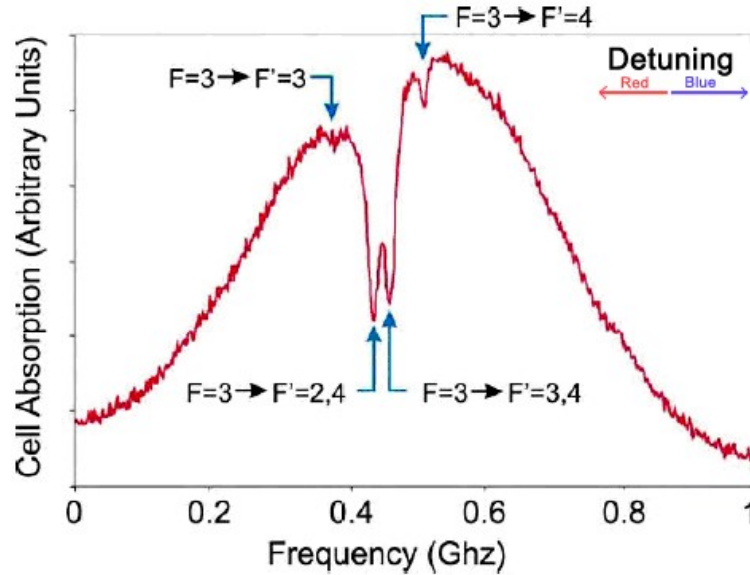


Figure 3.11 : Saturated absorption signal for the Rb^{85} $F=3 \rightarrow F'$ transitions illuminating the hyperfine transitions. Clearly the crossover transitions have the greatest definition. $F'=2$ is not visible, however its crossover with $F'=4$ is, this indicates an expected position for $F'=2$ just to the left of $F'=3$.

As well as the hyperfine spectra, larger dips are also observed, these correspond to cross-over transitions which manifest when the trapping laser frequency is exactly midway between two transitions. These are doubly transparent to the probe beam due to the increased number of atoms interacting; from both velocity subgroups (parallel and anti-parallel to the pump), and are therefore doubly distinct in the detected profile.

The photodiode detector collects the probe beam and thus receives a signal modulated by the Rb hyperfine structure and associated crossover resonances. In particular, the high definition of the crossover transitions makes them ideal for locking purposes.

3.2.2 Current and PZT Locking - ECDLs

The saturated absorption signal is fed into a locking circuit to stabilise the laser. The actions of this circuit are described below, (Figure 3.12 aids in the description).

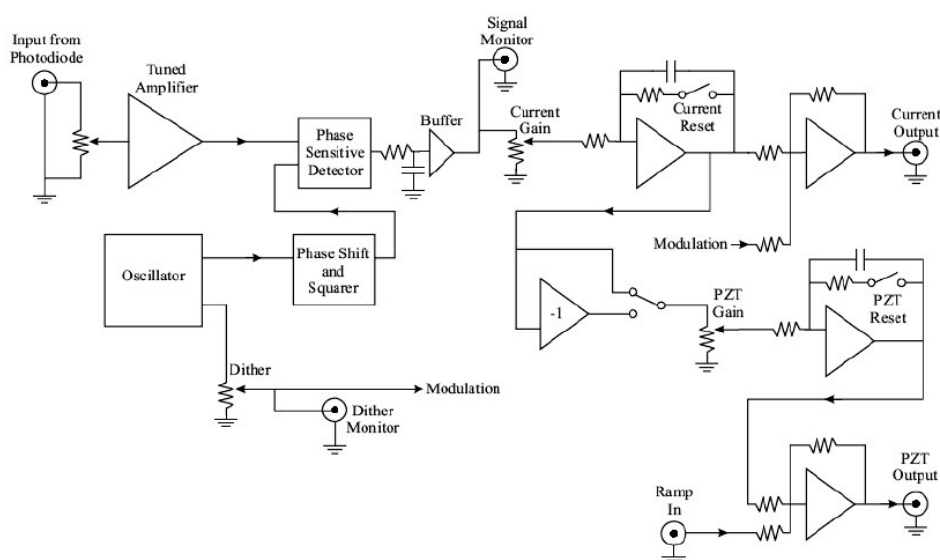


Figure 3.12 : Simplified circuit diagram of the Dual current PZT locking electronics. Inputs/outputs referred to in following text. Diagram reproduced from Dr G. Lancaster³.

The PZT is modulated by a triangular waveform which is scaled within the locking circuit, this allows us to scan across the atomic transition of interest. A sinusoidal dither is applied to the diode current (up to 100kHz) which ramps the frequency of the laser across the peak of the hyperfine feature chosen for locking. The saturated absorption signal from the photodiode is sent to an amplifier tuned to the dither frequency and then to a phase sensitive detector. This generates a dispersive signal which can be viewed on an oscilloscope. Integrating the dispersive signal over a short time base results in a high frequency error signal which is sent to the “current output”, integrating over a longer time base gives the dc error term which is sent to the “PZT output”. This processing should provide stable laser locking to one of the

atomic transitions for several hours. An example of the locking signal generated from the cooling transition is given in Figure 3.13. The error, or locking, signal is shown in red, it oscillates about a 0V level. The gain of the amplifier is reduced until only one crossover between the error and 0V level exists in view, at this point the feedback circuit is activated. A more thorough explanation of the locking electronics can be found elsewhere⁴.

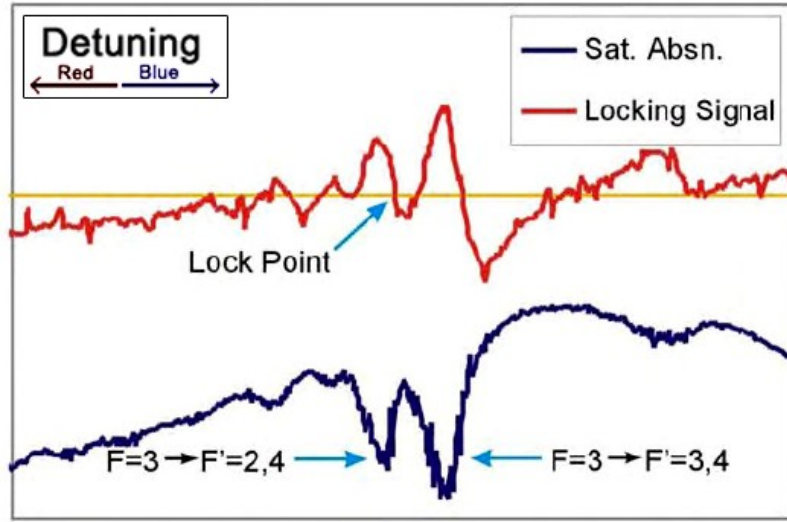


Figure 3.13 : Typical locking trace obtained from the dual PZT/current lock box. Possible lock points are selected by the points where the dispersive (red) signal and 0V ground line (orange) cross. The associated saturated absorption signal (blue) is also shown.

This method is a peak-locking method, as such, it still requires application of the 2Γ ($\sim 12\text{MHz}$) frequency offset to the red side of the cooling transition to allow Doppler cooling to function. This frequency shift can be achieved by passing the portion of laser output sampled for the saturated absorption setup through an AOM. The AOM was not placed directly in the cooling beam as this would have raised power and spatial-positioning issues when tuning the AOM. The AOM placement is shown in Figure 3.14.

The AOMs used (Isle Optics, LM080 and Gooch and Housego plc., M080) had an obligatory frequency shift of 80MHz with $\pm 23\text{MHz}$ tuning either side controlled by a voltage input to the AOM driver. This means it was not possible to lock the laser directly to the cooling transition and use the AOM to provide the $\sim 12\text{MHz}$ frequency shift required. The cross-over resonances provided much more

distinct signals and therefore provided more stable locking points. Thus it was beneficial to lock to a crossover transition and tune the laser from this lock frequency

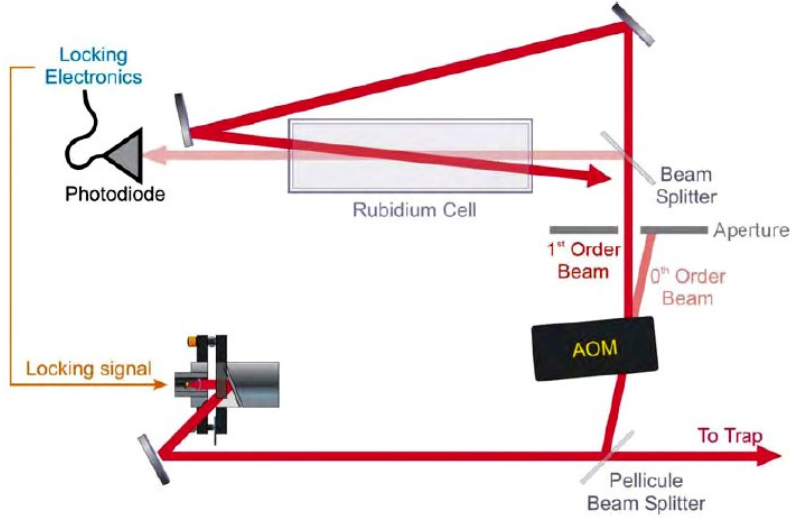


Figure 3.14 : AOM placement in the saturated absorption beam siphoned from the trapping laser. This allows the sat-abs setup (and hence the locking circuit) to ‘see’ a well defined crossover transition while the laser outputs a not-so-well defined $F=3 \rightarrow F'=4$ transition.

to the cooling frequency. This was performed by not actually tuning the laser but fooling the saturated absorption setup into perceiving a lasing frequency $X \pm 2f$ MHz distant from the actual output, (X was a frequency chosen to shift the lock point an AOM-manageable distance from the lasing frequency, $X \pm 2f \approx 80\text{MHz} \pm 15\text{MHz}$). Thus the laser would continue to lase on resonance while the saturated absorption setup would have the frequency-shifted AOM output to lock to. The D2 transitions used for cooling Rb^{85} are shown in Figure 3.2, from there it can be seen that the, well defined, $F' = (2,4)$ crossover transition is 92MHz from the cooling transition and so is within range of our AOM’s.

Adjustment of the AOM control voltage for trap size optimisation was achieved through a self-built electronic circuit. This circuit provided a calibrated read-out of the frequency deviation from the base 80MHz shift, up to $\pm 25\text{MHz}$, and passed the appropriate voltage to the Isle Optics AOM drive unit. The circuit is shown in Figure 3.15. The LCD display panel used was a Lascar DPM 700 meter, which provided a read-out accurate to a tenth of a MHz. The potentiometer marked with a red X was the control for altering the AOM shift. Adjusting the remaining two variable resistors while monitoring the AOM signal output (against a reference unshifted saturated absorption signal) allowed accurate calibration of read-out frequency

shift. Later re-calibration confirmed a good longevity of well-calibrated status, (all components commercially available from RS).

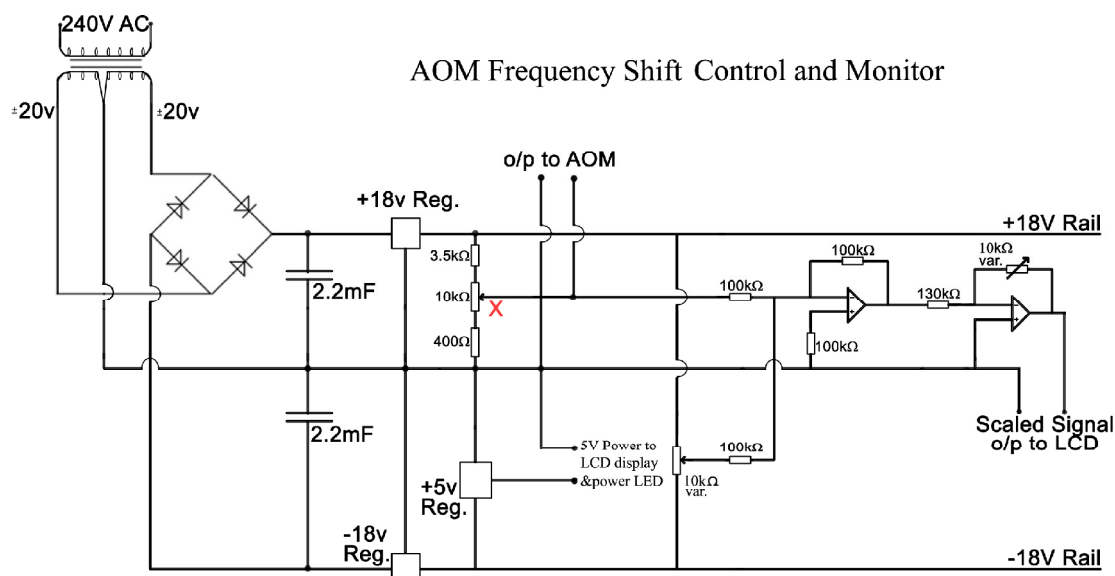


Figure 3.15 : Control and monitor circuit for AOM frequency shift of the cooling laser as part of the saturated absorption locking system. The signal output to the LCD display panel meter was scaled and calibrated to yield an accurate frequency read-out. 18V regulators require heat sinks.

Thus, by locking the cooling laser to the $5S_{1/2}(F=3) \rightarrow 5P_{3/2}(F'=2,4)$ line with a $\sim 80\text{MHz} + 15\text{MHz}$ shift from the AOM we can obtain a laser output direct from source with the -12MHz red-detuning necessary for trapping. The hyperfine beam did require AOM manipulation of the saturated absorption signal, it was locked to a transition which was distinct enough without resorting to crossover resonances.

3.2.3 Current and PZT Locking – TUI Laser

With the arrival of the TA-100 laser, referred to simply as ‘the TUI’, cooling beam locking was simplified by the removal of the AOM saturated-absorption system. The TA-100 had a modular control box with its own, optional, locking system built into the driver; this was a PID (proportional-integral-differential) stabilisation circuit that was automatically fed back to the master laser’s PZT and current values, via the scan control (SC110) and current control (DCC110) modules respectively. The previous ECDL dual current/PZT lock was locked to a point where an integrated signal crossed the 0 level, however the PID lock is fixed to a dc value. This means the

saturated absorption signal required careful isolation from other light sources to avoid a dc variation which would pull the signal away from the reference level and therefore change the lock point, (an interference notch filter with transmission at 780nm was used to cut out all other light sources from being detected on the photodiode).

The dc reference level was manually set to cross the saturated absorption signal at the desired point on the trace. Over this point the scan range of the PZT is reduced to zero and the PID regulator module is turned on. The regulator scans the PZT over a set range and stabilises to the point at which the locking signal crosses the reference level, if the reference level is not found the scan continues to a threshold value and starts again. The PID parameters were set initially by zooming in the PZT scan of the laser to the desired set point and turning the P, I and D values to zero. The PID board is turned on and the Integrator contribution (I) is increased until some feedback is observed in the output error signal (the laser can drift across the desired atomic feature whilst increasing the I value as it is not properly stabilised yet it, therefore it may be necessary to unlock it and reset the scan to centre on the reference level again), the proportional (P) and differential (D) levels are then increased until feedback is also seen on the error signal. Once these levels are found the P, I and D controls are turned down about one turn so the laser is less susceptible to jumping across the scan to other points where the reference level crosses. It was found that the factory settings in the PID control board were not adequate for locking to an atomic transition; the scan range and scan limit values (controlled by potentiometers inside the board) were set too high for the PID regulator to scan slow enough and over a small enough range to catch the lock point hidden within a narrow hyperfine feature. Simply adjusting the scan range and scan limit to their minimum values solved this problem.

3.3 Titanium Sapphire Guide laser

The laser used as the guide beam source in all experiments, save the later far-off resonance guiding, was a Spectra-Physics, Titanium-doped Sapphire (or $\text{Ti:Al}_2\text{O}_3$) laser, (model “3900S”), referred to as the “Titanium Sapphire”. This was pumped by a separate Spectra-Physics, frequency-doubled, Neodimium Yttrium Vanadate (Nd:YVO_4) laser (model “Millenia Vs”). This was a commercial, pre-packaged,

system, though it could not be treated as a ‘black-box’ since continually changing experimental requirements stipulated repeated calibration and adjustment. The Millennia laser provided 5W of 532nm light to optically pump the Titanium Sapphire crystal resulting in a final output of $\leq 1\text{W}$ with a tuning range of 650-1000nm (dependent on the intra-cavity optics used), this offered the versatility to operate in both red- and blue-detuned guiding regimes.

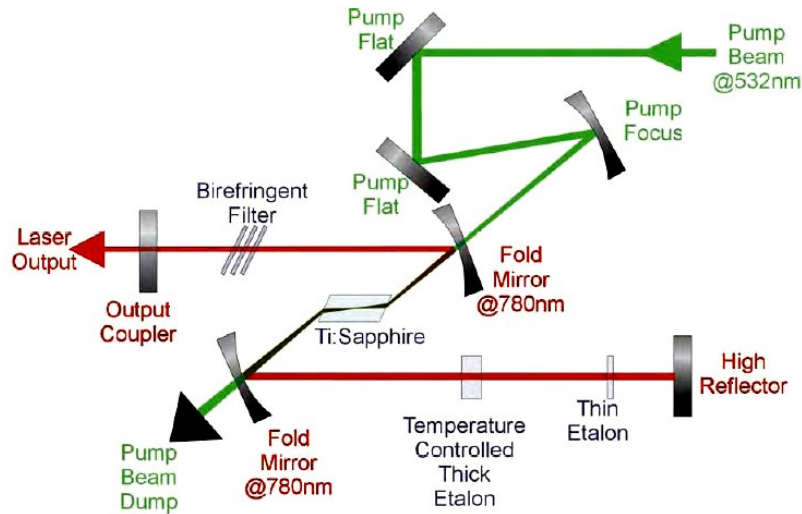


Figure 3.16 : Cavity components of the Titanium Sapphire laser. A birefringent filter and thick & thin etalons are used to reduce the number of lasing modes. An external refrigeration system was used to pump cooled water around the Titanium Sapphire crystal.

The guide beam is not required to have as narrow a linewidth as the cooling beams, this is because guiding is not dependent on resonance with any single hyperfine transition, rather the overall atomic transition which has a linewidth of 6.1MHz. Furthermore the guide is only required to have approximately $\pm 0.5\text{GHz}$ accuracy when detuning from resonance, (typical detuning was between 0 and 10GHz from resonance). The cavity arrangement is shown in Figure 3.16, this is a modified image from the operating manual⁴.

The number of lasing modes in the Titanium Sapphire crystal is reduced by several intra-cavity optics including a birefringent filter and two etalons. The first of these, the birefringent filter (or, “bi-fi”), is a composite of three retardation plates tilted to Brewsters angle. The slight ellipticity given to linearly polarised light on a single pass through these plates does not affect one specific frequency which will remain unchanged and see negligible loss when oscillating in the cavity. The

birefringent filter was the most coarse tuning element in the cavity with a bandwidth of 100GHz (around $\pm 0.2\text{nm}$ at 780nm o/p). The thin-etalon filter provides further mode reduction; it has a free spectral range (FSR) of 200GHz and reduces the laser bandwidth to 15GHz. It can be tilted to tune across the entire 100GHz bandwidth of the birefringent filter. Finally, the number of lasing cavity modes can be further reduced by use of the thick etalon; this is a 5mm thick etalon filter mounted in a temperature controlled socket. Controlling the temperature of the etalon (by way of the heating element's potentiometer), and hence its thickness, tunes across its 500MHz bandwidth with a FSR of 20GHz. A depiction of the lasing-mode selection process is shown in Figure 3.17. Ultimately two laser modes 200MHz apart receive sufficient gain to lase and are sent to the trap.

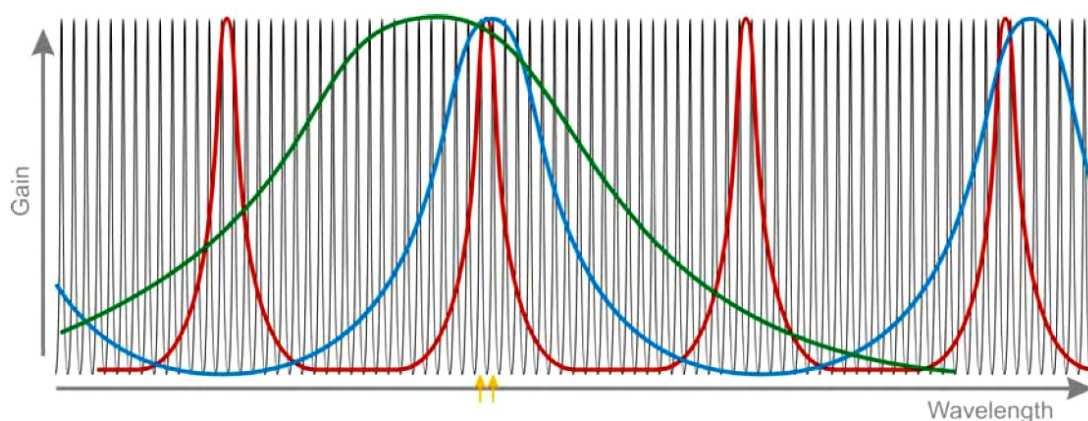


Figure 3.17 : Fictional depiction of possible operating modes of each filter/etalon within the T-Sapph module as dictated by the FSR and allowed modes of each. These are overlaid on a series of oscillations (black spikes) representing laser-cavity supported modes within the Ti-Sapph. optical path. The two operating modes receiving sufficient gain to lase (indicated by yellow arrows) exist only in a region where the passbands/allowed-modes of the Birefringent filter (green), thin etalon (blue) and thick etalon (red) overlap sufficiently well.

Frequency drift was a continual problem with the Titanium Sapphire laser, even gentle drafts (from the ventilation system) were sufficient to cause thermal or torsional shifts in the cavity alignment, thus causing a $\pm 1\text{GHz}$ tuning drift. These drifts were usually only a few seconds in occurrence, but were sufficient to obstruct experiments. A simple solution was found by suspending a thick curtain (laser-safety room-partition curtain) around the laser casing, fixed so as to permit cooling but eliminate flow across the laser and its pump.

Experimental tuning characteristics of the birefringent filter and thick etalon are illustrated in Figure 3.18a), b) and c). The output wavelength shift from these filters was calibrated in three ways: 1. an optical spectrum analyser providing accurate indication of mode movement, 2. analysis of laser output against a reference saturated absorption trace and 3. a wave-meter giving absolute wavelength readings.

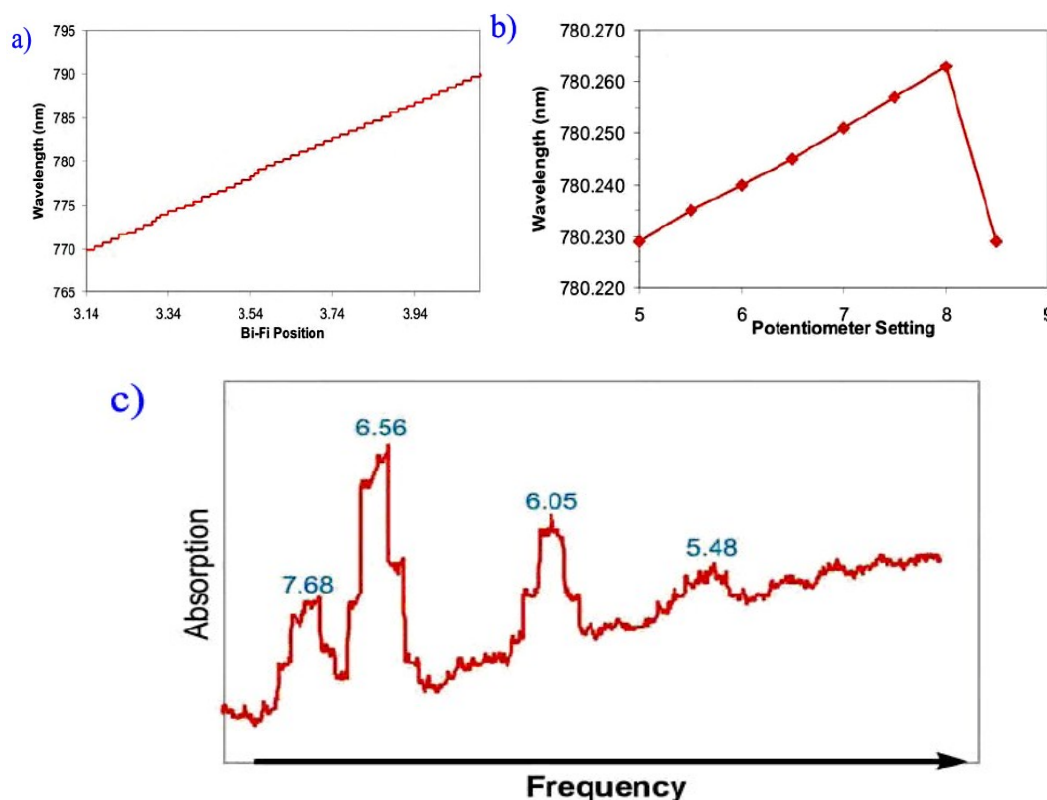


Figure 3.18 : **a)** With all other cavity elements in place tuning of the birefringent filter occurs in quantised steps as successive pairs of cavity modes dominate. The “Bi-Fi Position” axis refers to the micrometer actuator reading which controlled bi-fi tilt control. **b)** Tuning ramp of the thick etalon; temperature increasing as the potentiometer setting increases. The rapid drop at the end of the ramp is the mode-hop back to starting wavelength which occurs as the edge of the thick etalon bandwidth encroaches over the edge of another filters bandwidth. **c)** Using the thick etalon to scan across the absorption lines of Rb (compare to Figure 3.1). The blue numbers indicate heater potentiometer settings. Again the stepped nature of mode hopping is illustrated as the etalon forces jumps to adjacent modes.

3.4 Nd:YVO₄ Guide Laser

For a brief period a 1064nm Neodymium doped Yttrium Orthvanadate (Nd:YVO₄) laser was used for far-off resonance guiding experiments. These are

discussed in chapter 4. The laser source was a Spectra Physics model ZA 106C. It had a high quality, near diffraction limited, beam profile with an m^2 value <1.1 . However this was an OEM model, and as such was supplied with no documentation. This laser was loaned from another research group in St Andrews for the express purposes of guiding at a large detuning. At 1064nm the effects of spontaneous emission events can be ignored. It was not tuneable hence was treated as a black-box beam source capable of outputting 9W of continuous, linearly polarised, 1064nm light. The laser head was a totally sealed unit, so no information could be gleaned from internal components.

This laser was rapidly used and returned to its owner, it provided a good quality beam but the separation from Rb resonance and the short time window available reduced the impetus for full characterisation of its output mode(s). It was presumed to operate on a small number of longitudinal modes, (if not single mode).

3.5 Laser Shuttering

Most guiding experiments reported herein required precise timing of guide entry to the MOT region. Poorly timed guide exposure, particularly when near resonance could ruin results as effectively as poor alignment.

A series of mechanical shutters were used to block and release all relevant beams for each experiment. These were placed at beam focii or close to beam source to ensure a narrow cutting cross section; a broader beam would inflict a longer cutting time, and thus an intensity gradient across the trap as the beams were cut. Typically experimental procedure called for near-simultaneous trap-beam blocking and guide-beam release to facilitate cloud drop into a waiting guide; in this situation accurate timing was required to ensure guide exposure did not occur *before* cloud release.

The shutters used for all accurate work throughout were Newport, 846HP shutters, the timing of which was computer controlled using LabVIEW software and a National Instruments (NI) PCI-6602 data acquisition card with a CB68LP connector block (which provided up to eight triggering output signals). These provided pulses to trigger shutters in the trapping and guiding beams and to trigger a digital oscilloscope for data recording.

The shutters opened and closed on the leading edges of positive and negative pulses where the speed of closing and opening was dictated by the amplitude of an applied voltage. Beam cutting times of $\sim 1\text{ms}$ were achieved with a drive of $\pm 30\text{V}$. However the computer cards were unable to support such large voltages and associated current drains. Hence 5V pulses from the computer were passed through custom circuits, built by the author. These functioned as electronic “see-saws” where relatively large voltages could be triggered and rapidly switched in polarity repetitively. Though perhaps the term “see-saw” is misleading as this see-saw has a middle, rest-state, position, a key feature of the circuit. Consecutive, open and close, command pulses (on the two input lines) will cause the output to swing between full positive and full negative voltage, (see the circuit shown in Figure 3.19). As a necessary bonus, in the absence of command pulses, there will be no potential applied across the shutter, thus the shutter will remain in its latest state and can cool down. It must be noted that the shutters were not designed to run continuously, at such high voltages; where continuously can be defined as a prolonged repetition of pulses of more than a few seconds each. In particular a continuous output of an open/close command from the computer accidentally sent to a shutter, will result in physical melt-down of the shutter internals in under 60 seconds, (this occurred on more than one occasion). Experimenters must be particularly careful to avoid this situation as there is no obvious warning until the acrid smell of burning electrical insulation is detected.

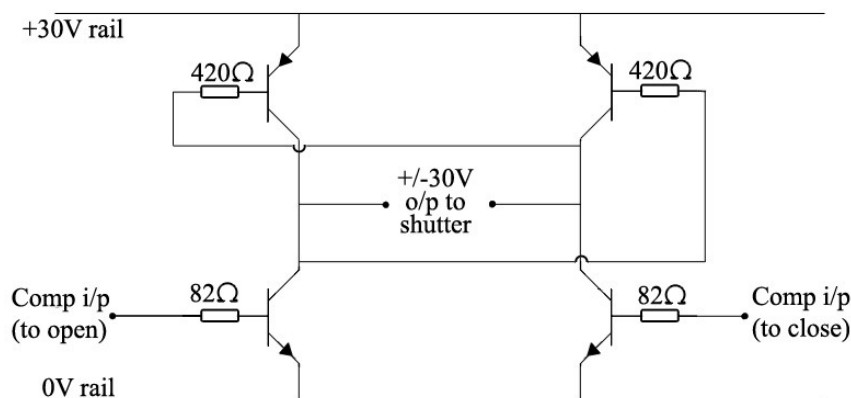


Figure 3.19 : Circuit design for Newport shutter control. The see-saw circuit allows transference of a $\pm 30\text{V}$ input to the shutter terminals following a timed 5V command pulse from the computer.

Calibration of shutter timing was performed by placing a photodiode behind each shutter and comparing the received signal timing with that of the oscilloscope trigger pulse (sent direct from computer to oscilloscope), this allowed compensation for the phase lag of all cable and components between computer and shutter (corrected by increasing/decreasing delay time on the LabVIEW program). A full experimental sequence for the timing of the shutters where the cooling beams were cut concurrently with the guide beam release is shown in Figure 3.20. After 5s the guide was cut and the cooling beams were re-activated to allow the MOT to reform.

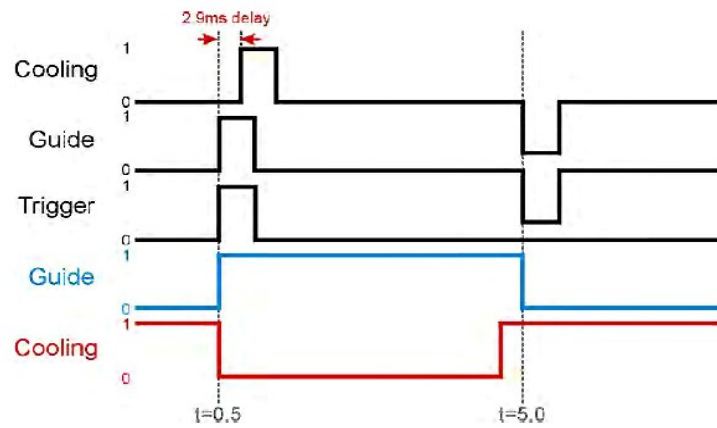


Figure 3.20 : Timing sequence for simultaneous release of MOT atoms and introduction of guide beam. The black lines are the 0.5s command pulses from the computer card to the guide and cooling control circuits and oscilloscope. The red and blue lines are indicate guide and cooling status : 1 \Rightarrow beam present in MOT, 0 \Rightarrow beam blocked. Note the necessary time delay applied to the cooling beams, this exists to synchronise the guide and cooling shutters; it compensates for the delay in the *guide* system.

3.6 Optical Atom Detection Systems

Perhaps the most important part of any experiment is proving that the desired effect has indeed occurred. Here the methods used for optical detection of guided atoms in all of my experiments are discussed. These are included in this chapter as they are heavily dependent on the laser involved and in particular its stabilisation.

In the case of atom manipulation, a positive detection result involves detection of a change in atomic flux in a specific location at a certain time. That is, a typical guiding experiment will have an expected location where atom flux is expected to

pass, and a certain time when a falling cloud (say) is expected to intersect a probe beam. Thus, both accurate spatial location of a probe beam and a CRO capable of high resolution over a broad temporal range was required. Fast photodiodes or photomultiplier tubes were also desirable for possible fluxes passing too rapidly to be detected by recorded CCD video footage.

The majority of experiments at St Andrews employed a laser probing system comprising of an in-house built ECDL (described earlier in this chapter) to resonantly interact with the atoms. When locked to a suitable Rb transition, the intensity of the output beam could be tailored to provide a probe operating in fluorescence ($I \geq I_{sat}$) or absorption ($I < I_{sat}$) capacity. Each provides a distinct way of collecting a signal from a passing atomic flux. These are described in the following sections.

The signal collection method for the fluorescence and absorption probes differed significantly. In a fluorescence probe system, the detectable signal lies at a very low intensity level and increases with increasing atom flux. Fluorescence photons scatter isotropically and are often swamped in a sea of background noise from extraneous reflections and external light sources. Thus a very low-light-level detector is required with a great deal of noise suppression. Conversely an absorption probe system detects a relatively high intensity signal which decreases with increasing atom flux. The higher signal level implies a more readily available detector and has the added advantage of removing the majority of noise concerns.

3.6.1 Fluorescence Probe

A typical fluorescence probe beam was held at an intensity a few times I_{sat} (up to a max of $\sim 50I_{sat}$) and had a flat, $5\text{mm} \times 1\text{mm}$, light sheet profile (see Figure 3.21). It was composed of $\sim 85\%$ cooling light tuned to the $5S_{1/2}(F=3) \rightarrow 5P_{3/2}(F'=4)$ transition and $\sim 15\%$ hyperfine light tuned to the $5S_{1/2}(F=2) \rightarrow 5P_{3/2}(F'=3)$ transition. A small portion of hyperfine light was sampled directly from the MOT hyperfine beam, while the cooling component was sampled from the MOT cooling source by a 70/30 beam splitter (70% continued to trap) and then passed through two AOMs, to achieve strong atomic resonance. Two AOMs were necessary due to the 12MHz offset of the cooling beam and the 80MHz baseline shift of the AOMs. The cooling

and hyperfine components were combined in a polarising beam splitter (PBS) cube and ultimately yielded $\sim 1.5\text{mW}$ of probe light.

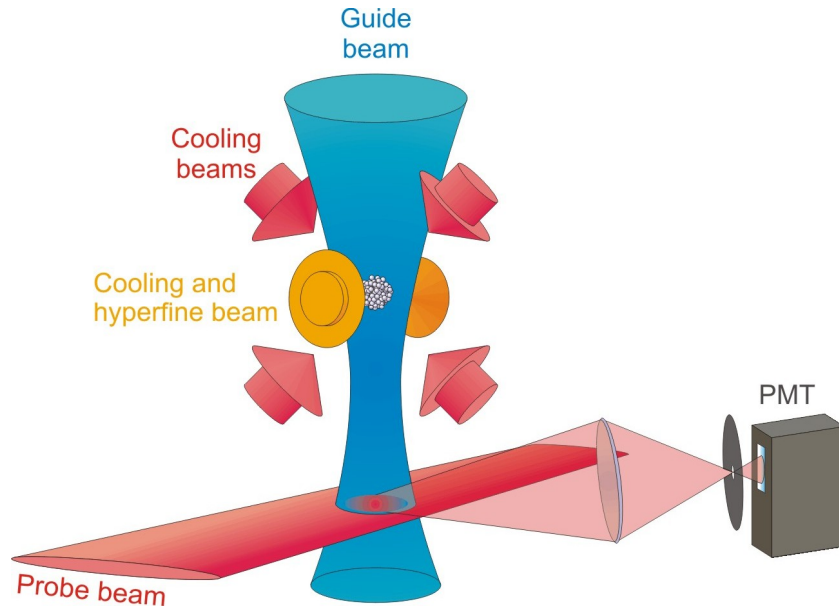


Figure 3.21 : Fluorescence probe setup for Gaussian guidance of a dropped cloud, (Guide shown in Blue here for contrast only; not to be confused with blue-detuning).

The probe beam could be directed to enter (via a flip mirror mount) along either of two perpendicular paths, both shown in Figure 3.22. Both on the horizontal plane, one ran normal to the large viewport windows entering just underneath the MOT beam opto-mechanics and the other ran through the small veiwports at 90° to the first. The latter was used when probing short distances beneath MOT centre (up to 2.5cm below) which were inaccessible in the other axis due to the MOT optics mounts. The probes could not be used simultaneously since atoms would be heated and disrupted by the first probe encountered.

When collecting fluorescence the probe beam was retro-reflected through a quarter wave plate (QWP) (replacing photo-detectors shown in Figure 3.22) to prevent a large radiation pressure imbalance kicking atoms from the probe beam. However a slight intensity imbalance remained due to the number of components in the probe path; effects of this are discussed in chapter 8.

The low-light-level detector used for fluorescence collection was an Hamamatsu, H7710-03 photomultiplier tube (PMT). This was mounted off-axis on a

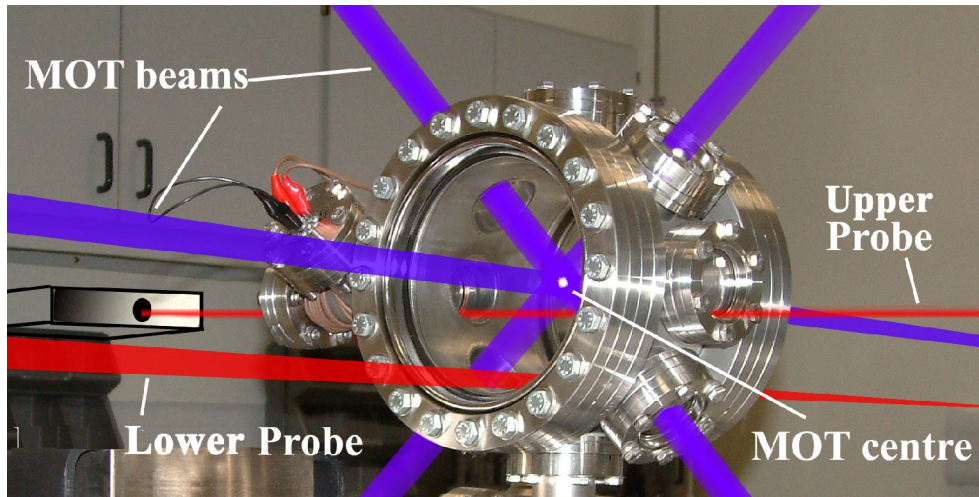


Figure 3.22 : A photograph of the Drum trap with cooling MOT beams and both probe paths indicated. The Drum trap has been stripped of all components in order to simplify the image. The distance a probe beam could reach from the MOT was limited by the size of the viewport accessed, and the awkward placement of external optics (not shown). The photodiode used for absorption probe measurements is shown in wire-frame at the end of the absorption probe beam, this was replaced with a retroreflector and QWP when using this axis for fluorescence probe measurements.

skew angle from the probe (as shown in Figure 3.21). The probe region, where atoms were expected to fall into the probe, was imaged through an $f=75\text{mm}$ ($f=38.1\text{mm}$ in the case of the fibre-guiding trap) lens positioned as close as possible ($\sim 100\text{mm}$ distant) and focused just prior to the PMT such that the signal light filled the entire detection surface (to improve detector efficiency). The PMT, its mount and collecting lens are shown in Figure 3.23. External lab light and, in particular, stray guide-light reflections inside the vacuum system forced numerous measures to prevent swamping of the expected low intensity signal. A $\leq 1\text{mm}\varnothing$ (adjustable) aperture was positioned at the focus to block unwanted light from inside the UHV system caught in the PMT's field of view. Extraneous lab light was suppressed by wrapping the optical path to the PMT with a tailored section of opaque laser-safety curtain and by mounting an interference notch filter (with 75% transmission at 780nm) immediately in front of the PMT sensor surface. Guide light reflected from the trap walls was at \sim same wavelength as the probe-scatter and of far greater intensity, thus it was especially difficult to filter without suppressing the desired signal. Hence a chopper was installed in the probe beam and a phase sensitive detection system used to further suppress noise from the guide. The output signal was finally displayed and recorded on a digital oscilloscope (Tektronix, TDS 360) with hard-copy output ability.

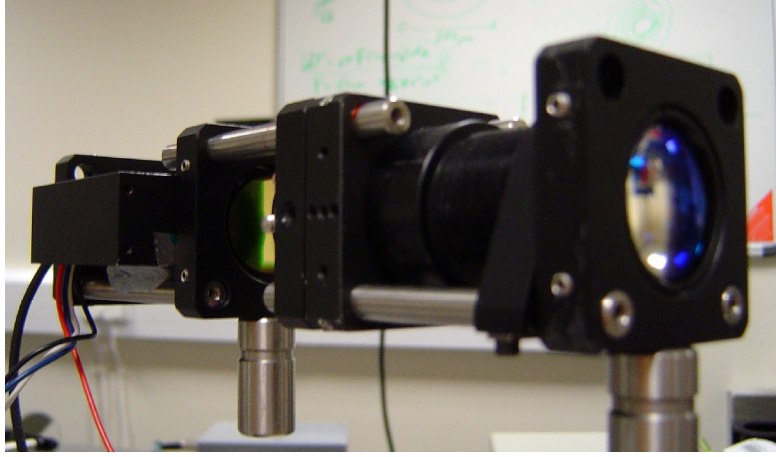


Figure 3.23 : A photograph showing the detection system for fluorescence probes used for the majority of dropped-MOT and fibre-guiding experiments performed herein. From left to right ; the PMT, an interference filter (passing a narrow notch around 780nm), a shadowing tube and an $f=38.1\text{mm}$ collecting lens. All these components and the fluorescence path were light-shielded when taking data.

3.6.2 Absorption Probes

The absorption detection system employed a custom built photodiode to monitor a beam of similar proportions to the fluorescence probe; $1\text{mm} \times 5\text{mm}$. The probe intensity was reduced (through an ND wheel) to $\sim 1/2 I_{\text{sat}}$ and directed under the MOT through the smaller viewport windows (see Figure 3.22). The retro-reflector was replaced with a photodiode. Since this system collected a relatively high intensity level many noise concerns were removed; no collection optics were necessary since the probe was sufficiently collimated to propagate $\sim 0.5\text{m}$ from trap centre to the photodiode. Thus opaque shielding around the probe beam path was the only significant noise suppressor since all other light sources did not propagate along the narrow path to the photodiode.

Unlike the fluorescence probe, the absorption probe diminishes in strength as atoms pass through it, thus the chief concern was to obtain optimum *contrast* between *atoms* and *no-atoms* signal levels. Optimisation required substantial patience as multiple tweaks to its intensity must be implemented over numerous cloud drops while also maintaining a dense MOT cloud and good guide-MOT-probe alignment, which is difficult to judge until the probe has good contrast; a cyclic path to achieve good signal strength *and* good contrast.

In order to align the absorption probe (when launched through the smaller viewports) it was tilted up to hit the MOT cloud and frequency locked on resonance such that atoms in the cloud would cast a shadow on a piece of card positioned just above the photodiode. Once the ‘shadowing’ was confirmed the beam would be pivoted back down onto the horizontal plane up to 5cm beneath the cloud. The photodiode and final probe-launch mirror were vertically translated in-sync so as to maintain horizontality. Occasionally this alignment was purposefully broken so as to prevent vertically skew reflections interacting with atoms before they fall into the main probe beam; in these cases the shift from horizontal was no more than $\pm 2^\circ$, and the distance of MOT to beam (at point of closest approach) was used as the defining probe height.

3.6.3 CCD Detection

A simplistic detection method was used in early experiments on the 10-way trap whereby video streams from the MOT-observing cameras (Pulnix NIR PE2015) were collected and separated into single digital stills images (at 25fps). The video stream was initially recorded on S-VHS magnetic-tape cassettes and converted to digital stills on a Studio DC10+ computer capture card. Subsequent analysis was performed by National Instruments Vision Builder software. This process is simplistic, with only basic imaging optics (described above) required to image MOT fluorescence onto the CCD chip. The only significant complexity came from the need to synchronise camera output with experiment initiation and with the first recorded frame of the cassette recorder. With the intention of arranging the first output frame to coincide with guide input, a re-sync command was sent to the cameras at the same time as a command was sent to the guide shutter to cause it to open. This primer signal had the undesirable effect of causing a loss of sync between the camera and S-VHS recorder, thus losing an indeterminate number of precious frames (each 40ms apart) during an effect which lasted $< 100\text{ms}$. However, a simple solution was presented by pre-initiating the recorders and cameras whereby the re-sync command was issued sufficiently in advance to have the recorder ‘catch up’ with the CCD frame rate. During the separation of the video stream into its constituent 25fps images, knowledge of the time window allowed accurate matching of captured images to known experiment timings.

3.7 Conclusion

The laser systems used for all atom guiding experiments in St Andrews have been described. Their construction, frequency stabilisation, tuning, and applicability towards guiding and probing have been discussed. The following table summarises the activities performed by the author with the equipment detailed in this chapter.

Equipment	Activity
Extended Cavity Diode Laser, (ECDL)	Atom cooling, hyperfine re-pumping, seeding (a slave laser) and fluorescence/absorption probing. These have been built from scratch many times, stabilised on a narrow-linewidth output and rendered frequency tuneable. Cavity tweaking and re-stabilising continued on a daily basis to compensate for thermal variation and gradual laser deterioration.
Titanium Sapphire Laser	Atom guidance in a Gaussian beam profile and generation of alternate spatial-profiles (eg. Bessel, Laguerre-Gaussian). This laser was re-aligned with its “Millenia” pump source, arranged to 780.24nm and calibrated to tune smoothly over a 12GHz range. Continual monitoring and correction of mode-jumping was necessary. Realignment, re-calibration and coolant maintenance, were regular duties.
Neodymium doped Yttrium Orthovanadate Laser, (Nd:VO₄)	Far-off resonance atom guiding in high-quality Gaussian beam profiles. No frequency tuning nor maintenance were required in the short time this was available. Beam profiling and frequency characterisation performed daily.
Electronic Control Circuits	Design, assembly and maintenance of circuits performed. These were necessary for AOM frequency-shift control, Newport-shutter control and speaker-shutter control.

Results of guiding experiments reported in the following chapters will refer to the laser systems detailed herein. Each vacuum trap will have further details regarding the arrangement of these lasers discussed in context with each experiment.

3.8 Bibliography

-
- ¹ M. W. Fleming and A. Mooradian, "Spectral characteristics of external-cavity controlled semiconductor lasers", IEEE Journal of Quantum Electronics, QE-17 44, (1981).
- ² M. A. Clifford, J. Arlt, J. Courtial and K. Dholakia, "High-order Laguerre-Gaussian laser modes for studies of cold atoms", Opt. Commun. #156, p300 (1998).
- ³ G. P. T Lancaster, "Experimental Studies of Diode Lasers and Cold Atom Guiding," PhD Thesis, University of St Andrews (2001).
- ⁴ Spectra-Physics, "Model 3900S, CW Ti:Sapphire Laser User's Manual," laser operating manual.

Chapter 4

Realisation of Magneto-Optic Traps for Atom Guiding

Introduction

In this chapter a description of the construction and maintenance of atom traps for use in free-space and fibre guiding experiments is given. This is intended as an introduction to vacuum traps, additional information specific to each batch of experiments is included in later chapters (in context with the experiments).

A diverse range of vacuum systems have been built in St Andrews for the purpose of guiding atoms along optical potentials. Each successive trap was designed to address specific problems of its predecessor, most often this was an issue of optical access, or facilitating greater guiding distance or offering physical mounts for internal components. Traps built for hollow-fibre guiding differed greatly from those built for free-space guiding, namely in size and component density within their vacuum. The larger-volume free-space traps used the same vacuum pumps and ultra-high vacuum (UHV) connections, but did not require internal optics mounting and thus were a great deal simpler to construct.

Throughout this thesis the term *free-space guiding* is in reference to atom guiding in light beams which propagate without external influence, similarly the term *fibre-guiding* pertains to atom guiding where the optical potential is maintained by an hollow optical fibre. All traps built throughout the course of this Ph.D. were designed and constructed by the author.

4.1 Atom Traps for Free-Space Guiding

Throughout this Ph.D. three UHV traps were built for free-space guiding experiments. Chronologically the first was the *Glass trap* which came pre-built following work by Dr. Gavin Lancaster (the authors predecessor). The second and third traps, called the *10-Way* and the *Drum Trap*, were built by the author. They all supported magneto-optic trap (MOT) clouds of Rubidium (Rb) atoms at $\sim 100\mu\text{K}$.

In general the laser and vacuum systems of each trap were separated between two adjacent tables. The delicate frequency stabilisation of the MOT lasers dictated an air cushioned, floating table to remove the majority of disruptive vibrations. Whereas the sheer weight of the vacuum system dictated a solid table mount, forcing it to suffer any building or lab vibrations. Daily drift of the floating table was compensated each morning by realigning MOT beams through apertures arranged on the trap table.

Before describing the particulars of each trap, it is necessary to detail the fundamentals of a vacuum system. To prevent repetition these will be given here and referred to in subsequent experiment-specific chapters.

4.1.1 Fundamental Trap Requirements

The superstructure of every Ultra High Vacuum (UHV) trap built by the author at St Andrews was an amalgam of stainless steel struts and crosspieces, each with knife-edge flanges which pressed into annealed copper gaskets when bolted to adjoining flanges. These parts are commercially available from Caburn, Kurt Lesker and Vacuum Products. Annealing of the gaskets helped reduce torsional stress across viewport flanges and provided good metal to metal vacuum seal between each flange piece. The design of each trap required accommodation of certain fundamental requirements of atom trap vacuum systems. These are:

1. maintenance of UHV pressure,
2. an internal source of atoms,
3. provision of optical access for observation and MOT laser entry, and,
4. anti-Helmholtz magnetic coils positioned to allow optical access.

1. Maintenance of UHV pressure

Many things contribute to the maintenance of UHV pressure, tight bolting of each flange to prevent leaks and continuous vacuum pump operation are the most prominent. Our low pressure was maintained by a 40ls^{-1} Varian, “Valcon Plus 40 Triode” ion pump, this gave a pressure of $\sim 10^{-9}\text{mbar}$ which was chosen to minimise the number of collisions with background thermal vapour; trapping can be performed at higher pressures (up to $\sim 10^{-7}\text{mbar}$) however the increased number of collisions significantly reduces trap lifetime. A turbo pump (Varian, Turbo-Dry 70) was used, in initial pump-down, to rapidly bring the whole system down to $\sim 10^{-6}\text{mbar}$ whereupon the ion pump could be activated. The two pumps operate at significantly different pressures and thus achieve pumping in dissimilar ways; where the turbo pump is a turbo backed diaphragm pump which physically draws particles out, the ion pump relies on a natural diffusion of particles into its internals wherein ionisation and subsequent attraction to a charged surface removes them from the vacuum system. It is important to realise this pumps dependence on diffusion; there is no ‘suction’ of particles. The turbo pump was attached via a ‘T’ piece with a built-in isolation valve, this allowed the pump to be cut-off from the system and so provided a simple, if crude, form of leak testing; an audible pitch change of the pump’s turbine highlighted any pressure difference when isolating/including the pump. Furthermore, the turbo pump connections provided a needle-valve for a more gentle, re-pressurising when returning to atmospheric pressure.

Cleanliness while assembling the trap was essential; a single greasy fingerprint inside the system could greatly increase pump-down times, or worse, coat nearby optics in an optically-disruptive film during evacuation.

Another important aspect of UHV maintenance was the *bake-out* procedure. This caused surface oxidation, water vapour and many other contaminants to outgas from the internal surfaces of the vacuum components (including the ion-pump diffusion surface). In doing so it facilitated evacuation down to trapping-feasible pressures of 10^{-7} - 10^{-9}mbar . Insufficient bake-out risked leaving a near-perpetual contamination source within the vacuum system. *Baking-out* involved connecting the

newly built vacuum system to the turbo pump and pumping it down while heating the whole system, ion pump included, to $\sim 150^{\circ}\text{C}$, for 2-3 days. It was found that slight preferential heating of key windows was advantageous for preventing oxide condensation within. This occurred once on a fibre-trap window and proved severely detrimental to any optical throughput.

After 2-3 days at $\sim 150^{\circ}\text{C}$ the temperature was lowered to $\sim 70^{\circ}\text{C}$, at this stage the ion-pump was turned on and the turbo pump was deactivated. Bake-out continued in this condition for a further day before the trap temperature was slowly lowered to room temperature.

2. An internal source of atoms

The atom sources used throughout all experiments at St Andrews were getter ovens from SAES Getters, UK. These were small $\sim 2\text{cm}$ long metal reservoirs containing several milligrams of Rubidium (Rb) which cracked open along an etched line when heated with sufficient electrical current, (3.5A-7A). Initial opening currents were several amps in excess of typical running currents since the first cracking and burn-off of contaminants required greater temperatures for short bursts, (limited by the in-flux tolerance of the ion pump). It was important when running at $\sim 9\text{A}$ (necessary for first opening) to quickly decrease the current when Rb is finally emitted; a few minutes at this current is sufficient to boil off the majority of Rb content. When cooled, the ampule re-seals sufficiently to trap the Rb once more. This seal is also what protects the Rb during the bake-out. Figure 4.1 shows the Rb oven design.

Following any continued use of the ovens, cutting their drive current produced a near immediate reduction in trap vapour pressure, however residual Rb which had emitted and adsorbed directly onto the trap surfaces was slower to evaporate back into the trap volume. In fact it should be noted that more Rb is removed from the trapping volume by the walls than the ion pump. Nevertheless, evaporation from the walls is generally low enough to avoid disturbing experiments and is not thought to have hindered optical detection.

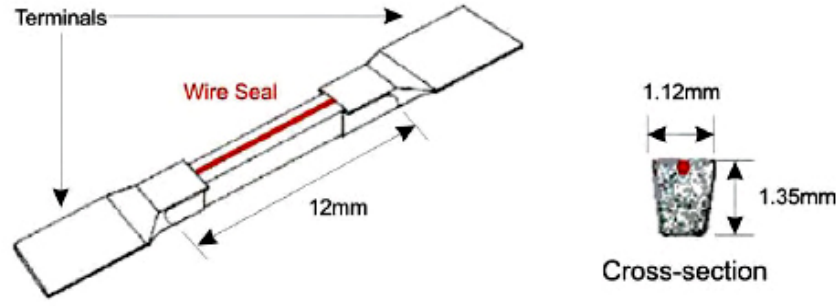


Figure 4.1 : The Rubidium ovens used for all atom experiments performed herein. These were screwed to Kapton cabling which ran inside the vacuum system towards an electrical feedthrough flange where the cabling was screwed to electrode contacts for external power input. Note the wire seal which thermally expanded to facilitate ‘cracking’ of the ampule and release of the Rb.

3. Provision of optical access for observation and MOT laser entry

In all free-space guiding traps (bar the Glass trap), the MOT and guiding regions were located within a single steel vacuum piece with viewport flanges bolted around this piece. Optical access was gained through these viewports but was hindered by essential mechanical mounts for optics and magnetic coils. Access was required for 6 crossed cooling beams, a single hyperfine, a guide and one or 2 probe beams. Occasionally the hyperfine beam did not enter as a single beam, it was split to enter with each cooling arm, however the optics required for this combination (beam splitters in particular) increased the level of interference within the cooling arms, (despite polarisation manipulation and anti-reflection coatings). Thus the hyperfine was more-often chosen to enter in a single diffuse beam ($\sim 1.5\text{cm}$ diameter at MOT location). This was of greater importance in the fibre-guide traps where hyperfine light was arranged to avoid contact with the fibre in order to prevent unwanted resonant modes within the fibre core.

On top of laser access a few direct lines-of-sight with no reflection-glare (which quickly saturates CCD’s and obscures MOT clouds) were required for optical monitoring via 2 or 3 CCD cameras. These clear lines of sight, were often blocked by

surrounding opto-mechanics. Figure 4.2 illustrates the typical level of congestion surrounding atom traps; the obscured trap location is highlighted by the crossing of 2 red trap beams, the observing CCD camera is highlighted with a blue surround.

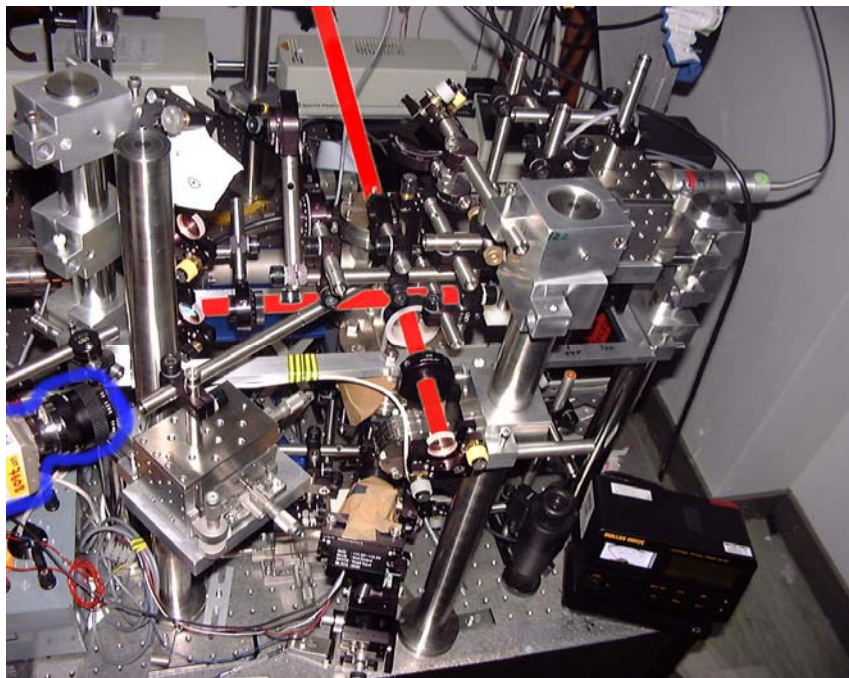


Figure 4.2 : A demonstration of the congestion surrounding a typical trap. Here the mounts necessary for guide entry, coil support and MOT beam entry obscure the trap location. The locus of two, highlighted cooling beams helps distinguish MOT location. The observing CCD camera is highlighted with a blue surround.

4. Anti-Helmholtz magnetic coils positioned to allow optical access

The position of the 2 symmetric magnetic coils was dictated primarily by a need to satisfy the anti-Helmholtz condition, this meant a location outside the trap had to be found where the coils could be positioned such that their separation was roughly equal to their diameter. Thus trap setup often dictated where the coils could realistically be positioned without obscuring laser entry or observation paths. Often the coils were simple bundles of wire, wound around the nearest section of trap. However larger traps dictated a greater removal from MOT centre and so a greater field strength was required. These coils had separate (often bulky) mounts to facilitate accurate positioning. Some coil mount designs are shown in Figure 4.3.

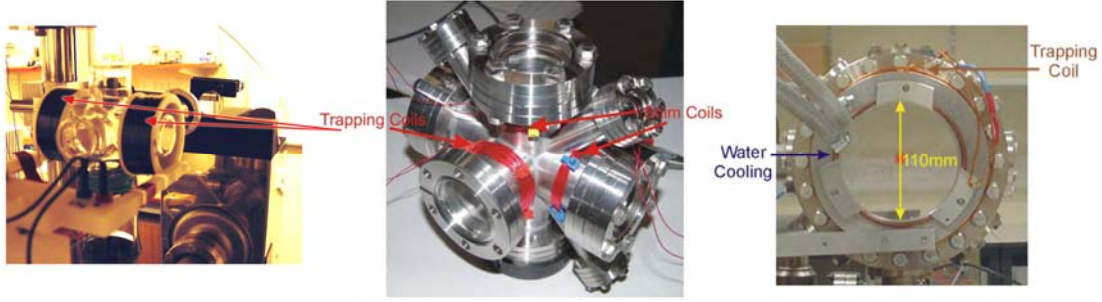


Figure 4.3: Various traps with magnetic coils indicated. From left to right these are a prototype Glass trap, the 10 way trap and the Drum trap. These show different coil mounts and sizes. SHIM coils are also shown (described below).

The anti-Helmholtz condition stipulates oppositely directed current flow in the two symmetric coils, this generates a field zero at the centre point (MOT location). The field gradient between the coils is the important feature for atom trapping; a linear gradient from a minimum of $\sim 6\text{G/cm}$ up to 15G/cm is adequate for trapping, with a target optimum at $\sim 10\text{G/cm}$. This was typically generated with between 50 to 80 windings (dependent on coil radius and wire thickness) with each coil driven by $\sim 2.5\text{A}$ current.

A typical coil installation began with the determination of an ideal mount position which would avoid optical intrusion, this in turn, specifies coil diameter ($2R$) and total separation (d). These were then used to calculate the approximate magnetic field gradient (in G/cm) between the two coils, per winding, per Amp of current. This was derived from the expression for magnetic field, B_z , of a single coil at a distance Z :

$$B_z = \frac{\mu_0}{4\pi} \frac{2\pi R^2 I}{(Z^2 + R^2)^{3/2}} \quad 4.1$$

where μ_0 is the magnetic permeability, I is the drive current and Z is the distance along the axis perpendicular to the plane of the coil passing through its centre. The corresponding approximation for the field gradient between the coils can be expressed as:

$$B_{grad} = 100 * \frac{d}{R} \left(\frac{d^2}{R^2} + 4 \right)^{-5/2} \left(\frac{48\mu_o}{R^2} \right) \quad 4.2$$

where the factor of 100 converts the units to Gauss per cm (cf. m) and the ratio d/R approximates to 2 for satisfaction of the Helmholtz-condition.

In addition to the essential MOT coils, two smaller ‘SHIM’ coils were often installed to provide three dimensional control of MOT position. They were centred on orthogonal MOT axes perpendicular to that passing through both MOT coils. They were useful when careful manoeuvring of the atom cloud into a fixed guide beam path, or over a narrow fibre entrance, was required. These adjustment coils did not require as much current or as many windings as the MOT coils; typically ~1A and ~30 windings. A SHIM coil mounted around a trap structure can be seen in Figure 4.3.

4.2 Realising a Magneto-Optic Trap for fibre-Guiding Experiments

In this section significant differences between free-space and fibre-guide ultra high vacuum (UHV) systems will be discussed. Pertinent design and construction features, along with important procedures for inserting and using a fibre in an ultra high vacuum environment will be described.

Three trap designs were implemented in fibre guiding experiments, these were labelled the “pyramid trap” the “QWP trap” and the “cross trap”. They were required to incorporate all the features of free-space guiding traps while housing numerous additional components necessary for supporting a MOT cloud above a hollow-core fibre. Importantly, these traps have to be more compact due to the need for optical fibre coupling into apertures of ~10µm diameter. Experiments performed on each are described separately in chapter 7. Coupling optics were typically no more than 38mm from MOT centre.

The extra number of components included inside a small fibre-guide trap volume inherently block one cooling arm. This means a mirror and quarter-wave plate (QWP) have to be included within the vacuum system to re-create that cooling beam around the fibre entrance. We chose glass cube structures fitted on the top and bottom of a steel UHV flange system as the generic fibre-guiding trap basis. This presented an exposed target for all beams and allowed the fibre to hang vertically into the lower glass cube for the probing region. The presence of a metal-glass interface doubly emphasised trap sensitivity to stress forces when bolting the trap together and when heating for bake-out.

4.2.1 Differences Between Free-Space and Fibre-Guiding Traps

The characteristics which make fibre-guiding traps distinct from free-space traps are;

1. The inclusion of a fibre; with associated mounts, heat shields and clearance for optical access at both ends of the fibre.
2. The inclusion of a MOT mirror and quarter wave-plate *inside* the UHV system.
3. Approximate vacuum isolation between MOT and detection chambers

These are elaborated below.

- 1. The inclusion of a fibre; with associated mounts, heat shields and clearance for optical access at both ends of the fibre.**

The majority of fibre trap design constrictions derive from a necessity for optical access. Both entrance and exit fibre facets must be correctly positioned for exposure to input guide light and for output monitoring, respectively. As will be detailed in chapter 7, the guide beam in our experiments is launched from an $f = 38.1\text{mm}$ lens and had to have a direct collinear path to the fibre hollow core. The volume in the MOT chamber also had to have sufficient exposure to all cooling beams (hence the long $\sim 35\text{mm}$ separation between fibre facet and trap cube roof). The exit

facet required similar exposure, though with a reduced surrounding volume. This volume needed only to allow a probe beam to pass under the fibre. A long working distance (LWD) microscope objective lens, focused on the fibre exit, provided confirmation of guide coupling into the fibre core.

Fibre and optics mounts inside each trap were designed & manufactured in-house. They were cut from 0.5mm thick steel sheeting and bolted to an internal flange surface. These served dual purposes; vertical fibre suspension at correct height and rigid support of the internal MOT mirror. These had an adverse effect of conducting heat from the nearby Rubidium oven to the mirror/QWP and fibre.

Radiative heating of fibre and optics was reduced through inclusion of heat shields. In early traps a thin sheet of polished steel was the sole heat shield, later designs sported the same shield plus a Berillium sheet which blocked line of site to every area of the fibre, the mirror and the QWP, yet still left a large area for Rb vapour to disperse into the trapping volume.

To hold the fibre in position something was required to grip it while not crushing it. The first 2 traps employed a magnetic clamp; a small magnetic bar, similar to that found on a fridge-magnet was built onto the mount structure and combined with a 15mm×5mm iron plate. The plate had a narrow groove etched vertically (along the 5mm axis) which encouraged fibres to settle therein, sandwiched between the plate and the magnetic bar. The associated magnetic field was deemed to have no significant effect on either fibre-guided atoms transiting nearby or the MOT above.

However manipulation of the metal-plate fibre-grip was awkward and often led to non-vertical fibre positioning. Its magnetic nature subjected the fibre to a slight crushing force. This was not quantified, however attention was drawn when the 1st incarnation of the QWP trap was deconstructed to reveal a fibre stuck to the magnet; it is believed heat conductance through the mount induced melting of the fibre cladding during trap operation. Subsequent transmission checks indicated the fibre inner structure was unaffected by this heating, however fear of distorting the supported optical mode prompted creation of a more gentle mount.

This led to the mount structure employed in the latter QWP trap and Cross trap. Here the fibre is held by a relatively weak, strained steel foil strip, tack welded to one side of the mount only. The strip was 15mm×3mm, its elasticity allowed sufficient fibre grip and its reduced width aided fibre adjustment. Heat transfer was unavoidable with metal mounts, but this design did not crush the fibre to the same extent, thus reduced fears of mode distortion.

Neither fibre-grip method permitted multi-fibre mounting. The groove width in the steel plate and the curvature of the strained foil prohibited grip of extra fibres. Re-shaping of the grips was forsaken in favour of quick trap assembly. Fortunately a dust-blocked fibre was never encountered throughout fibre-guiding experiments.

2. The inclusion of a MOT mirror and quarter wave-plate inside the UHV system.

A significant divergence from free-space trap design is made with the inclusion of a MOT mirror *within* the vacuum chamber. As will be described in chapter 7, the internal mirror was never a standard mirror, its design and construction underwent many revisions. It had to be mounted internally as the input cooling light could not pass the fibre mount and flange assembly to reach an external retro-reflecting mirror. This imposed a loss of beam steerage, however it brought the locus of all essential cooling beams into one compact volume above the fibre facet.

A half-wave rotation of input cooling beam polarisation is also required. Thus a quarter-wave plate was fitted between the MOT region and mirror. This brought the mirror and QWP into problematic close proximity with the atom oven; heat transfer to, and subsequent expansion of, the QWP is blamed for a shortening of trap lifetime. Cloud lifetime was limited to <3 minutes prior to QWP warp deteriorating cooling ability. This was a strong motivator for the inclusion of radiative-heat shields, however these could not prevent conductive heating through the flange and mount surfaces; ultimately limiting trap lifetime to <10mins before a ~5 minute cool down period was needed.

The fibre protruded through a 1mm diameter aperture in the mirror/QWP ensemble. Such apertures, and in fact, all mirror cutting and drilling was performed by Mr. Fritz Akerboom. Metallic coating of mirror/QWP surfaces was performed by the author using an Edwards 306, electron beam evaporator, provided courtesy of Professor T. Krauss. 200nm of Gold deposited on top of 20nm of Nickel. Provided reflectivities not below 85% for any mirror created, (Nickel was necessary for Gold adhesion to glass). Deposition of Silver for higher reflectivity was not permitted due to its prolific contamination of all metal sources within the evaporator.

3. Approximate vacuum isolation between MOT and detection chambers

The volumes surrounding each end of the fibre were used for fibre loading and flux detection. The detection volume required suppression of any unguided atom flux in order to reduce background fluorescence noise levels. Hence, either two separate vacuum systems (each with associated pumps) were required, or, as herein, the fibre could be passed through multiple narrow apertures; through flanges and thick mirrors in order to reduce unguided atom diffusion. The length of these narrow passages provided sizable surface areas for atoms to adsorb onto and eliminated any direct line of sight path. In this way background levels in the detection chamber were held a few orders of magnitude below those of the loading chamber, (calculated by fluorescence of passing probe beams)

Better isolation was always desirable for “cleaner” detection signals. This could be obtained through greater separation of the two chambers, however separation is limited by the choice of fibre length, in turn dictated by the level of optical guidance exhibited by the fibre. Traps utilising quasi-PBG fibre require loading and detection chambers in close proximity because of the rapid depletion of light intensity within the fibre, (recall Equation 1.38). The advent of PBG fibres diminished this length dependence however the series of fibre-trap systems described herein began with non-PBG fibre. Hence traps were constructed around short fibre lengths; ranging from 15cm down to 6.6cm chronologically. These short lengths still permitted competition with published work since their cores were narrow enough to demonstrate superior transmission properties relative to capillary fibres. Equation 1.38 denotes a cubed dependence on core diameter for transmitted intensity in a

capillary fibre, PBG fibre is not bound by this constriction thus selection of narrow core PBG fibre was encouraged and limited only by the minimum laser spot size achievable for guide coupling into the core

Additionally, the fibre exit volume was often designed to accommodate a 2nd MOT region beneath the fibre in order to provide an auxiliary detection method.

Thus the optical access for atom cooling, probing and monitoring ultimately dictated the volume left available for an Rb oven, fibre mount, mirror, QWP, electrical feed-through cables and the fibre.

4.2.2 Superstructure Assembly

One custom and two standard steel flanges were purchased from Vacuum Generators and used as the superstructure for all fibre-traps herein. The design for each flange can be seen in Figure 4.4. Relevant features of the custom flange are, 1. the side ports for vacuum and electrical feedthrough, 2. the volume within the central cavity, which dictated the number of components mountable, and 3. the flat external surfaces necessary for successful vacuum seal between glass cubes and flanges.

An exploded schematic of the QWP trap is shown in Figure 4.4. As well as the components shown, an atom oven, two heat shields, cable connectors and fixing bolts were also squeezed in while leaving an unhindered path for the fibre. This tight packing brought the electrically conducting Rb oven worryingly close to adjacent metal mounts; insulation was prohibited in the vacuum environment for fears of excessive out-gassing (except for the Kapston cabling which was supplied with a vacuum compatible insulative coating). The custom and middle flanges had narrow central apertures of 5mm and 3mm respectively. The pathway between MOT and detection volumes was effectively capped by a mirror, with a narrower 1mm aperture, attached to the underside of the lowest flange.

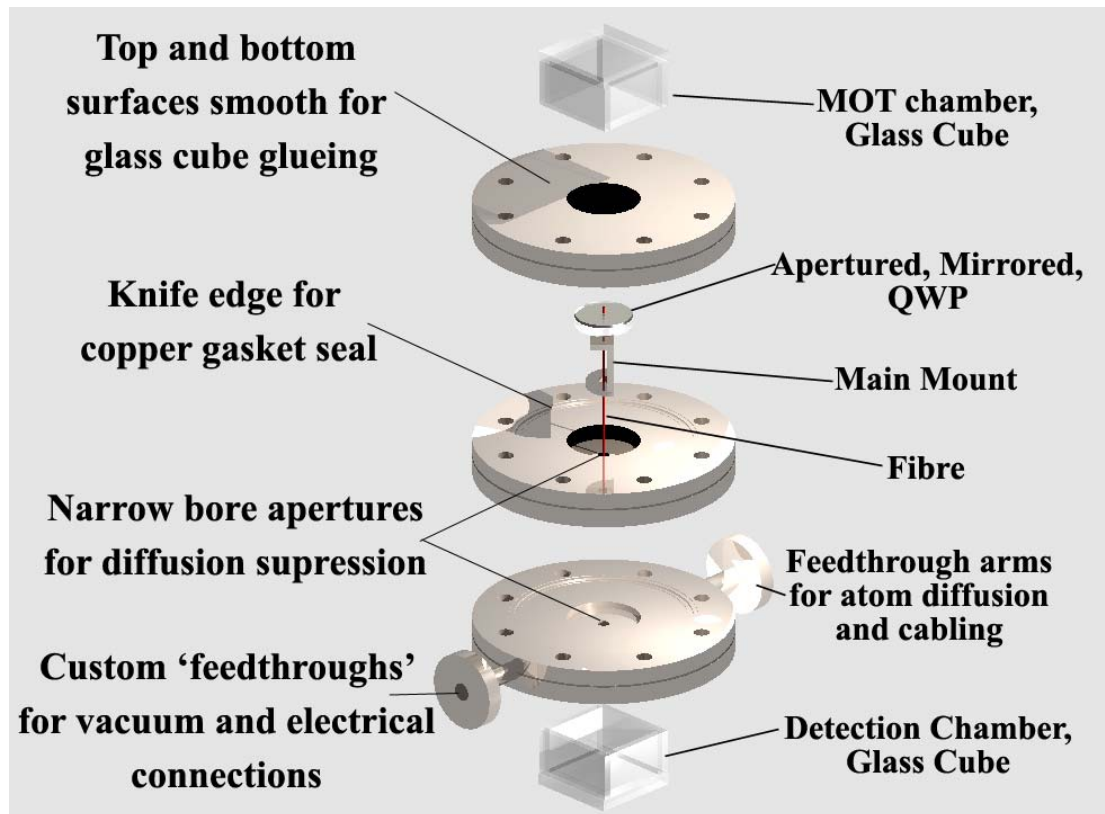


Figure 4.4 : Exploded schematic of the QWP trap. This shows the general shape of all main mirror mounts used in all fibre traps; everything fitted onto the mount had to be narrow enough to fit through the aperture in the upper flange. all fibre-guiding traps reported herein were formed by these three flanges. Note the narrow apertures in the lower two to limit diffusion. All were switched to hardened steel after the Pyramid trap. Figure courtesy of Dr. D. Gherardie.

Glass Cubes

Optical quality glass cubes were purchased from Helma Optics, these housed the MOT and detection chambers. Their walls were a uniform 4mm thick and each was cut to height from factory dimensions of 40mm×40mm×70mm o/d. They were bonded to the flanges using Epotek H77 vacuum compatible 2 part epoxy (available from Promatech).

All glass cubes mounted on fibre traps had a “one use” nature due to de-warping of the metal flanges on return to atmospheric pressure, (despite use of hardened steel flanges). Destructive disassembly stipulated thorough grinding and cleaning of flange surfaces to present a smooth surface for the next cube.

4.3 Fibres in an Atom Trap

This section describes all aspects pertinent to inclusion of a hollow fibre in an ultra high vacuum system in St Andrews. Assembly procedures, the problematic insertion process and later optics issues are discussed.

4.3.1 Assembly

Similar to free space traps, all internal components had to be thoroughly degreased prior to chamber evacuation. Prolonged bake-out periods and fogging of key access areas were fears exacerbated by the obligatory cube fracturing should a return to atmospheric pressure be needed. Solvent cleaning of all internal surfaces required full attention particularly in tapped bore holes or on the fibre itself. In the 2nd incarnation of the QWP trap described later in this chapter, ineffective cleaning and insufficient out-diffusion during bake-out, was blamed for obscuring an important observation surface.

Fibre segments were selected by merit of their hollow core diameter and transmission efficiency at 780.2nm. A narrow core was desirable to illustrate PBG fibre superiority over capillary equivalent, conversely a core broad enough to encompass the incident guide beam was required for efficient coupling and atom loading. A selection of fibres were provided by co-workers at Bath University¹, as knowledge of the desired fibre characteristics and manufacturing ability improved, the suitability of each successive fibre improved. The exact specifications for each fibre used are tabulated in chapter 6.

Prior to mounting in a trap, each fibre was cleaned of all grease and cut to the desired length. The presence of fibre cladding was found to be acceptable within a vacuum; fears of excess out-gassing were allayed after trap evacuation. Fibre cleaving was performed using a Fujikara CT-07 fibre cleaver; regardless of diameter settings PBG fibre required repeated scoring from the cleaver's knife-edge.

¹ Dr. F. Benabid, Professor J. Knight, Professor P. Russel, Optoelectronics Group, Bath University, UK.

Core Blockage and Fibre Insertion

Core blockage was a primary concern during trap assembly. Blockage was most likely to occur during initial insertion into trap superstructure; the fibre/mirror mount, its associated mechanics and in particular, the flange walls, provided numerous surfaces along which the fibre could scrape, possibly collecting contaminants as it did so. Fibre insertion was a two person task requiring much dexterity. Both people were required to monitor fibre position in separate axes while simultaneously repositioning additional components. Despite thorough cleaning, exposure to laboratory environment implied a possible accumulation of dust within the trap. The *order* of construction for constituent trap components imposed a time delay between fibre mounting and final trap sealing, a period in which rogue dust particles could block the fibre; particularly during the 150°C epoxy curing process. Ultimately, confirmation of core clarity could only be attained after trap assembly and evacuation.

4.3.2 In Operation

In practice hollow-core fibres were found to be almost completely passive objects within the UHV system. They contributed no noticeable outgassing and their cladding withstood high-temperature bake-outs. A definite warping was seen when high intensity ($\sim 300 \text{ MW m}^{-2}$) guide light was poorly coupled into the crystal-structure, however this warping was completely elastic. Similarly, elastic warping was also noticed during oven heating. This was a more prominent problem as it incurred continual re-alignment of the input guide beam. It was surmountable through pre-heating of the ovens prior to fibre alignment, or short oven-operation for single-shot experiments.

Guide and Cooling Launch Optics

The primary concern for fibre performance during experiments was the guide coupling. This required particular attention in all traps in which vertical cooling beams propagated \sim collinear to the fibre, (those which suffered LVIS outflux from MOT centre). Here both the guide beam and vertical cooling light was launched from the same optics. An example of this is shown schematically in Figure 4.5.

Intuitively, there are more factors restricting the effectiveness of a guide beam in a fibre-guide trap than there are in a free-space trap. Notably, the necessity of locating guide focus at fibre entrance rather than MOT centre, the dependence on guide/fibre collinearity and the overall transmission efficiency of the fibre. These issues impose a high dependence on accurate guide launch, particularly when attempting to guide LVIS atoms. Collinearity is desirable in order to encourage LVIS atoms to couple more efficiently into the hollow core. Furthermore, collinearity is also important between the flux and the guide beam.

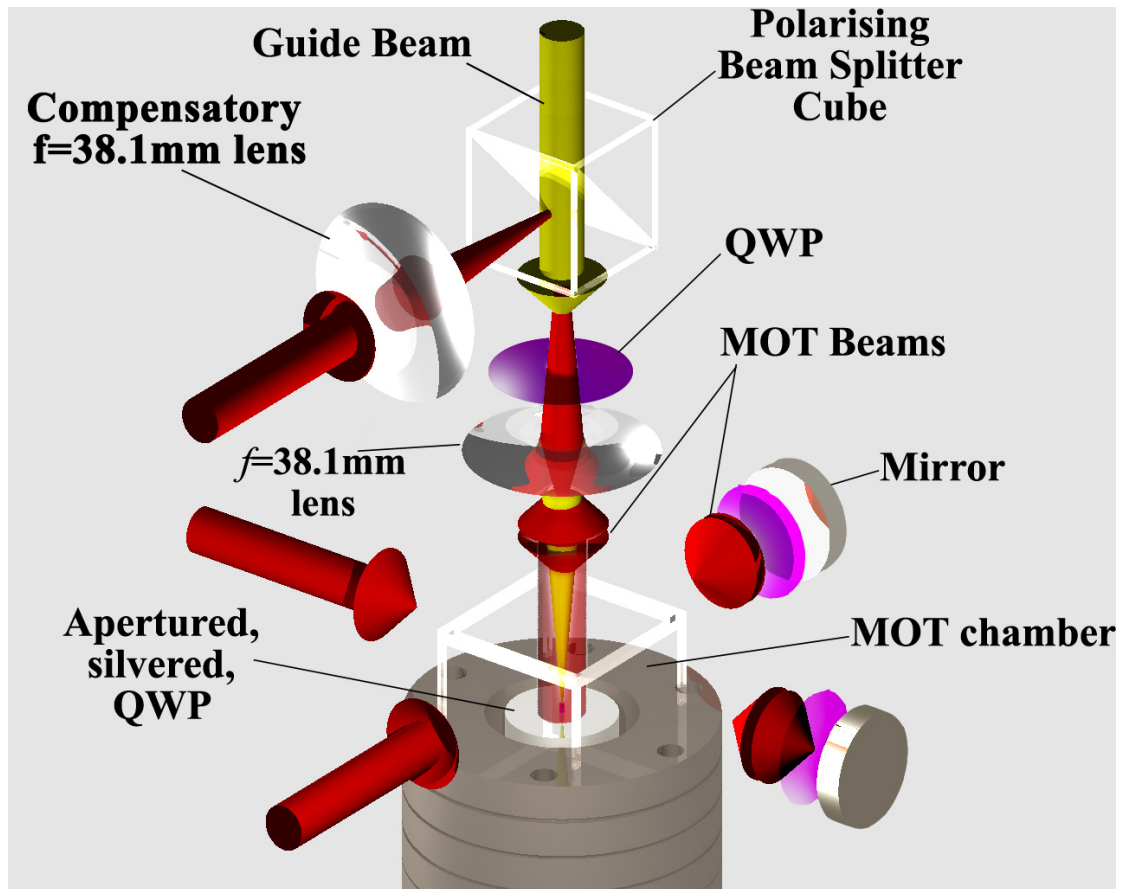


Figure 4.5 : A schematic of beams and required optics for trap and guide laser entry to the QWP trap. Note, the half-wave plates required for efficient transmission/reflection in the polarising beam splitter (PBS) cube have not been shown; (one is placed in the topmost trapping beam and one in the guide, before each enters the PBS). This resulted in an elliptically polarised guide, the effects of which have not been fully characterised. Figure courtesy of Dr. D. Gherardie.

Guide light coupling was achieved through use of a HeNe laser retro-coupled into the fibre through the exit facet. The resultant fibre output was used to perfect the

position of the guide optics to ensure it's collinearity with the fibre. Guide light emitted from the fibre was then collected and collimated by the LWD objective. Beneath the LWD microscope a glass slide deflected ~6% of the fibre output to a CCD camera and allowed the remaining light to pass to a Melles-Griot power meter. Combined, these facilitated final tweaking of the guide coupling optics.

It was imperative, while aligning a vertical cooling beam with the fibre that optics shared with the guide were not disturbed. This was strictly enforced so as to maintain optimum fibre coupling. Hence the guide-launch $f=38.1\text{mm}$ lens and PBS cube (shown in Figure 4.5) remained stationary while the 'compensator' $f=38.1\text{mm}$ lens and the further-removed cooling-beam mirrors, were adjusted to maximise MOT-light output from the fibre hollow-core.

4.4 Conclusion

In this chapter the design and construction of various UHV chambers have been discussed. These were designed to facilitate atom-guidance in free-space propagating optical-potentials and hollow-fibre propagating potentials.

The following list summarises activities performed by the author which have been discussed in this chapter.

10-Port Trap This was built and subsequently maintained while performing experiments on 1. Gaussian, far-off resonance enhancement of LVIS-atoms in the transient and steady state cases, ...
2. Collinear Laguerre-Gaussian (LG) guiding of LVIS atoms,
3. Oblique LG guiding of LVIS atoms, 4. Pierced oblique LG guiding of LVIS atoms.

Drum Trap – 2 builds This trap was built, used, deconstructed, re-built and is still in use today. It hosted the majority of free-space guiding experiments. These included, 1. near-resonance red-detuned Gaussian guiding of dropped MOT clouds, 2. investigation of

a second molasses cycle, 3. guiding efficiency comparison of high-order Bessel and LG beams

Mirror Deposition	Performed in a metal-deposition evaporator for mirrors used within fibre-guiding traps; specifically, all reflective surfaces used within the Pyramid trap, and both builds of the QWP trap.
Pyramid Trap	This trap was designed, built and subsequently maintained while attempts were made to guide thermal vapour atoms and later ‘2D slowed’ atoms into and through a 15cm length of quasi-photonic crystal fibre.
QWP Trap – 2 builds	This trap was designed, built, deconstructed, re-designed, re-built, and subsequently maintained while attempts were made to guide atoms from a LVIS into and through a 15cm, (and later 6.6cm) length of true photonic crystal fibre. Additional work was done on the dropping of the LVIS emitting MOT into the guide and fibre.
Cross Trap	This trap was designed, built and subsequently maintained to facilitate guidance of a ‘clean’ MOT (without LVIS outflux) into a 6.7cm length of true photonic crystal fibre. Much work was done on many custom components fitted inside (see figure 8.13).

The descriptions in this chapter provide an insight into the fundamental requirements of an ultra-high vacuum atom-trap, and the required additions for inclusion of a hollow-core fibre. Further refinements to these traps are given in context, within descriptions of the respective experiments, these are given in chapter 5 for red-detuned free-space guiding experiments and chapter 7 for all fibre-guiding experiments.

Chapter 5

Free-Space Red-Detuned Atom Guiding Experiments

Introduction

In preparation for fibre-guiding experiments our ability to guide atoms in free-space light beams was investigated. These experiments were, for the most part, split equally between Dr. Daniel Rhodes and myself. Where Dr. Rhodes favoured blue-detuned dark hollow beam guiding, I favoured red-detuned Gaussian guiding as this was more appropriate to upcoming hollow fibre guide experiments. Only work pertinent to future fibre-guide experiments will be described here. A full description of our free-space guiding experiments can be found in Dr Rhodes thesis¹. The main focus of my research did not lie in free-space guiding at all, it was in hollow fibre guiding. All free-space experiments reported herein were necessary steps towards guiding atoms in hollow-core fibres. Importantly the extra work performed on free-space guiding gave a better understanding of atom guiding in general prior to work detailed in chapter 7.

In this chapter I will discuss guiding of atoms in red-detuned laser light. Experiments were performed in three vacuum traps, two of which are discussed here and the third is included in Appendix i. The design features of these traps along with experimental procedures and the data captured are presented herein.

Laser light with a Gaussian intensity profile was used to guide the atoms at near resonance and far-off resonance detunings. Initially thermal vapour was used as a source of Rubidium atoms however a desire for more controllable atoms motivated a

switch to a low velocity intense source (LVIS) and ultimately to a cold MOT-cloud. Atom reaction to guide detuning, power and intensity profile is included in the following sections as is the response to guide introduction in the transient² and steady state regimes.

5.1 Collinear Far-Off Resonance Gaussian Guiding in the 10-Port Trap

In this experiment an atom flux path was extended through use of a collinear far-off resonance guide beam. A Gaussian profiled guide was chosen due to simultaneous research being carried out into optical fibre coupling (discussed in chapter 7). This indicated Gaussian profiles had the best throughput efficiency and provided the least amount of scatter from the fibre entrance facet thanks to their lack of surrounding rings.

A far-off resonance detuning was chosen to allow guiding to occur with a negligible radiation pressure influence. Hence the 1064nm Neodymium Yttrium Vanadate (Nd:YVO₄) laser described in chapter 2 was used as the beam source. At this wavelength the guide is sufficiently distant from Rb⁸⁵ resonance that atom heating and any longitudinal acceleration from radiation pressure can essentially be discounted.

The 10-Port trap was used for these experiments. This was designed with no internal obstructions and with optically flat glass in its viewports. Hence a clear guiding path could be presented to the atoms and they could be viewed with no distortion from the trap windows.

This set of experiments differed from other recent Gaussian guiding work^{3,4,5,6} because we did not use a molasses cooled cloud for the primary atom source. A transient effect which had previously been noted by Houde *et al.* was investigated. In their work the transient effect was described as a ‘momentum kick due to the energy variation’ but was not investigated in any depth.

In the following sections pertinent aspects of collinear guiding of LVIS atoms are described. Flux enhancements in both the steady state and transient regime are investigated. An improvement over regular LVIS flux level is seen in both regimes; more so in the transient case. This was important for the potential benefit of improved transfer efficiency into atom beam splitters; key components of future atom optics.

5.1.1 Particulars of the 10-Port trap

The 10-Port trap was in operation for ~10 months of the author's PhD. Described in chapter 4.1, with the following specifications:

The main trapping volume was contained within a single, steel, 10-way cross piece, purchased from Vacuum Generators. Eight of the steel arms leading from this piece were on a single plane and consisted of 2 sets of 4 arms. One set terminated in the regular 70mm \varnothing flanges for bolting to viewports or the ultra-high vacuum (UHV) superstructure. The other set terminated in 35mm \varnothing flanges with small optical-quality viewports for cloud monitoring and fluorescence imaging/probing on 2 NIR CCD cameras. (This was an immediate improvement over the rippled surfaces of the forerunning "glass-trap"). The 10-port piece can be seen in isolation in Figure 5.1a), and while trapping in Figure 5.1b). The surrounding, UHV pipes and cross pieces facilitated turbo and ion pump connections, Rb-oven electrical feedthrough and cooling beam entry.

An extended guiding/probing volume was supported in an additional UHV viewing cube bolted to the 10-Port piece on the opposite side to the rest of the UHV system. This was a basic cube with five 70mm \varnothing viewports bolted to each available flange, it provided laser throughput and possible cloud observation at 115mm from MOT centre, via a 26mm \varnothing hole drilled through an intermediary flange connecting it to the 10-Port piece. This cube can be seen on the right hand side of the 10-port piece in Figure 5.1b) (beneath the red highlight).

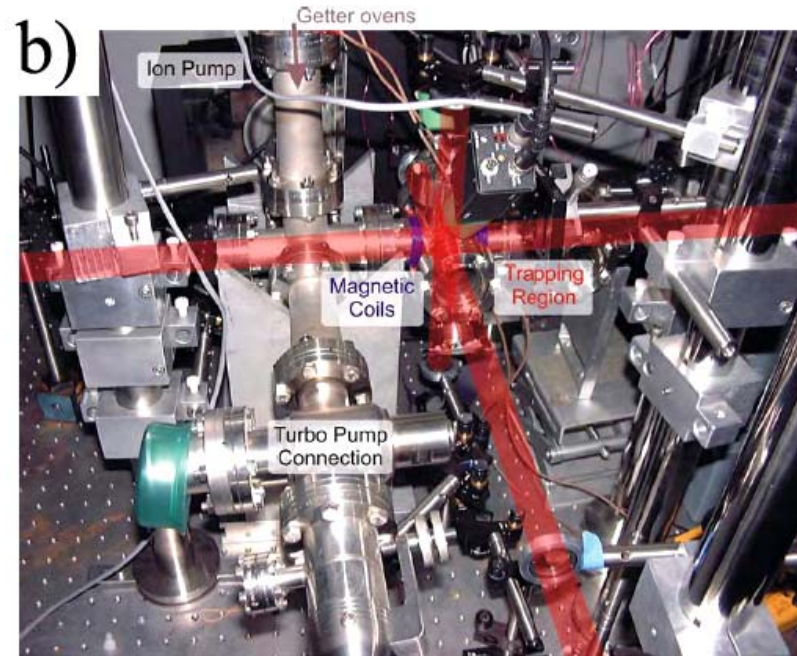


Figure 5.1 : a) the 10-Port piece on its own with only viewports and magnetic coils attached. b) the 10-Port trap fully installed with the paths of the cooling beams overlaid in red. The extended-viewing cube can just be seen to the right of the 10-Port piece.

The magnetic quadrupole field was generated by two coils with 70 windings of 0.6mm \varnothing wire wound directly onto two of the opposing, larger diameter, arms on the 10-Port piece (shown in Figure 5.1a above). These were typically run on currents of $\sim 1.4\text{A}$, sufficient for the target $\sim 10\text{G/cm}$ field gradient between the coils. Currents down to 1A could produce a small cold cloud, however, such clouds were not dense enough to be of use in guiding experiments. Supplemental shim coils of ~ 23 wraps

each were wound around the upper-vertical and horizontal-orthogonal (to MOT coils) arms of the 10-Port piece. These were driven at $\sim 0.5\text{A}$ to provide direct tweaking of the cloud position along the vertical and horizontal axes.

The same lasers employed on the glass trap (see Appendix i) were used for the 10-Port trap. These are described in chapter 3. The master-slave combination of an extended cavity diode laser (ECDL) and Circulase diode provided a total of 70mW of cooling beam light, (these are described in chapter 3). The cooling beams were expanded to $\sim 1.5\text{cm}$ \varnothing before entering the trap. A single ECDL produced 20mW of hyperfine light which was allowed to gently diverge across the trap centre in one direction. Multiple propagation directions were tried for hyperfine entry with no noticeable difference in MOT quality, though it was recognised that guiding outwith the MOT region would require continued hyperfine presence to ensure all atoms were kept in the $F=3$ ground state and thus in continuous interaction with the cooling light. Similarly, hyperfine light in the probe region maximised detectable fluorescence, however the risk of increasing spontaneous emission heating also persisted.

5.1.2 LVIS Generation

Thermal vapour guiding as not attempted as our guide was not deemed powerful enough to influence such energetic atoms. Thus the trap volume was evacuated to 10^{-10} mbar and a MOT cloud became the atom source for experiments.

Atoms were extracted from this cloud through use of an intensity imbalance in one MOT beam axis⁷, this was introduced by placing a glass slide with an opaque spot in the retro-reflected cooling beam. This allowed atoms to sluice out from MOT centre within the shadow region of the retro-reflected arm. An example of resulting LVIS outflux can be seen in Figure 5.2. On route to the MOT, the shadow from the opaque spot underwent slight diffractive filling, hence a $\sim 1\text{mm}$ spot generated a $\sim 800\mu\text{m}$ diameter LVIS flux. Care was taken to ensure spot sizes did not envelope the entire MOT volume. When the MOT diameter was smaller than achievable spot sizes the slide was positioned such that the LVIS shadow overlapped only a small portion

of the cloud, thus ensuring sufficient balanced MOT volume to replenish LVIS outflux. Typical atom flux rates in the LVIS beam were $\sim 10^6 \text{s}^{-1}$. The incoming guide beam was arranged collinear to the LVIS plume. The optics arrangement is illustrated in Figure 5.3.

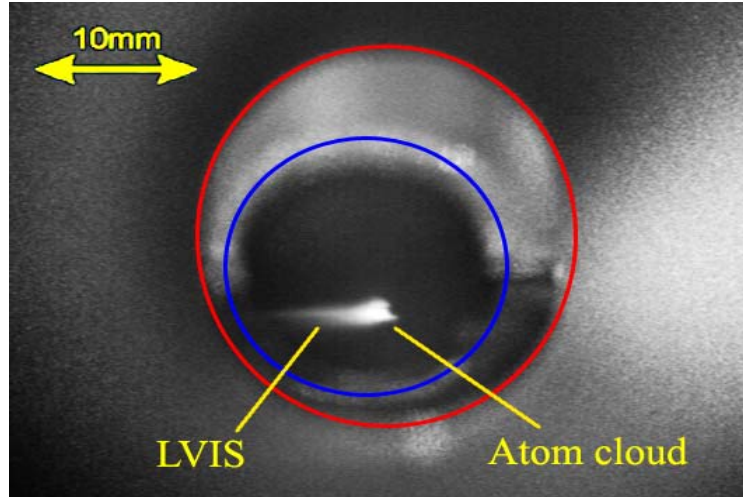


Figure 5.2: A captured CCD still showing the length of LVIS generated. The atom outflux of this one was calculated to be 10^7s^{-1} . Field of view through the 10-Port trap's $\sim 5\text{cm}$ long, narrow diameter arms. The red and blue circles indicate the end of the access arm and the opening of the opposite arm, respectively. The LVIS flux can be seen extending almost out of view. To distinguish atom fluorescence an observation angle must be chosen such that no bright areas are seen behind the cloud.

A second, competing method of LVIS production involved replacing one of the retro-reflected MOT arms with an LG beam. This was attempted for a short time on the 10-Port trap, however, difficulties arose with available MOT beam power following passage through the LG generating hologram; the LG output existed in the first diffracted order, which only held $\sim 35\%$ of the input Gaussian power. Thus sufficient power to match the intensity of the counter propagating MOT arm was difficult to maintain without diminishing the other MOT beams and so reducing trapping volume. Furthermore, a LG profile focused to provide a narrow LVIS diameter provided a narrow overall MOT beam and so reduced the number of atoms drawn into the MOT from this axis. This method of LVIS generation was abandoned shortly after a few experiments showed a lesser LVIS quality than the glass-slide method.

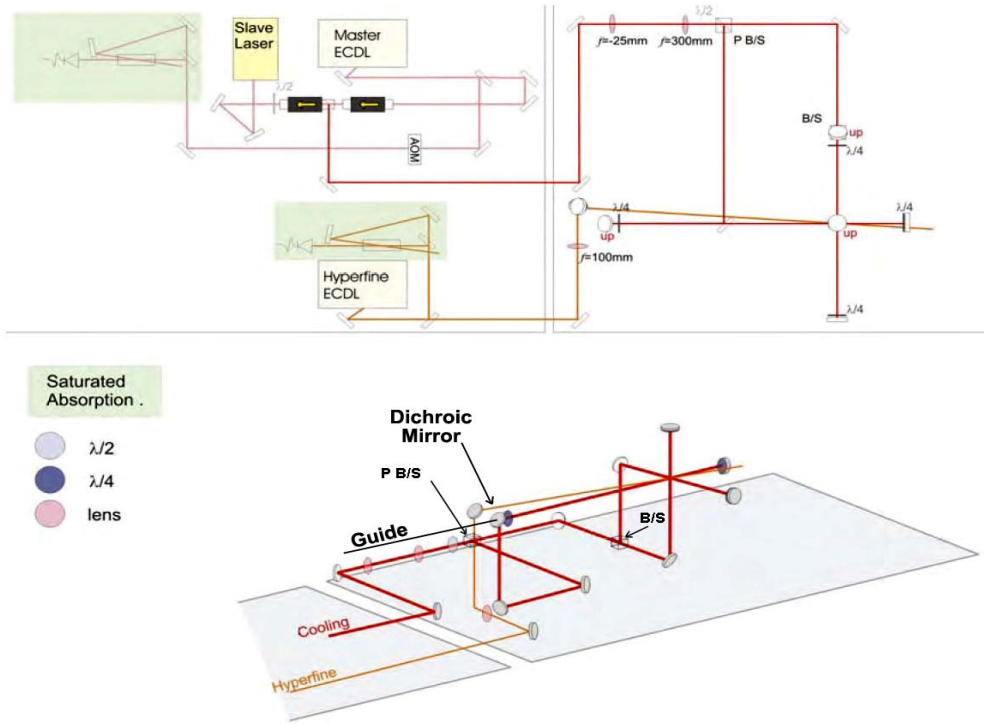


Figure 5.3: Optical arrangement for collinear experiments in the 10-Port trap. The lasers were mounted on a floating optics table, supported on Newport pneumatic float legs, to minimise disruption of the frequency locking systems. The trap table was mounted on solid fixed height legs. P B/S and B/S are polarising and 50/50 beam splitting cubes, respectively. Schematic courtesy of Daniel Rhodes.

5.1.3 Atom Detection

Atom fluorescence was imaged onto two near infra-red (NIR) CCD cameras, observing through the narrow diameter trap arms at 90° to each other. Inch diameter, $f=38.1\text{mm}$ lenses, positioned as close as possible to the viewports, collected and focused the fluorescence onto the CCD chips. Images were captured with a $\sim 10\text{mm}$ field of view clearance around MOT centre, as is shown in Figure 5.2. Focusing was achieved by mounting the cameras on single-axis translating stages.

Care was taken to prevent contrast-reducing reflections or glare entering the camera's line of sight directly behind the atoms. Although this could, for the most part, be removed later when stills of the background light were subtracted from the data

images, it was feared excess light would saturate the CCD pixels and possibly diminish the perceived flux path.

The 25 frames per second (fps) video streams captured from the CCDs were stored digitally and separated into single images (separated by 40ms) by computer. The luminance of these images was then measured for cloud/effect analysis.

5.1.4 Guiding Procedure

The wavelength separation of the 780nm cooling light and 1064nm guide light allowed use of a dichroic mirror to couple the guide into the trap collinear to a horizontal MOT beam. The horizontal cooling beam defined the LVIS flux direction, hence launching the guide through the same mirror allowed collinearity between guide and LVIS.

The 10W cw Nd:YVO₄ laser yielded up to 9W of usable 1064nm guide light in a TEM₀₀ mode profile, such high powers were required to maintain dipole potential so far-detuned from resonance. No attempt was made to tune the guide frequency. Beam waists of 100 μ m to 500 μ m were used, but the majority of data was taken at the larger end of this range to ensure better overlap with, and so better coupling from, the LVIS.

At maximum power of 9W, the guide beam could generate a dipole potential of only 13 μ K at its 500 μ m beam waist. This meant the guide was only capable of confining transverse velocities up to 6cm/s, well below typical LVIS velocities (of \sim 30cm/s). Thus, only atoms with small transverse velocity components could be strongly guided, however, unguided atoms would tend to re-cycle back into the MOT region due to the surrounding MOT beams and thus, atoms lost from LVIS would eventually re-cool sufficiently for guiding.

Atoms leaving MOT centre in the \sim 800 μ m diameter LVIS plume were constantly exposed to cooling beams in both transverse axes. This meant that while

the atoms were subjected to a high intensity ($\sim 9\text{W}$) beam which could potentially cause heating, this was minimised by cooling from the transverse beams. Thus there was little or no heating and no extra fluorescence from spontaneous emission of the guided atoms in this experiment. Importantly this implied that all detected atomic fluorescence originated from excitations stimulated by the trapping light alone. It is acknowledged that the AC stark shift would warp the atomic energy levels in the guide path, however, this was estimated to be of the order of only 1%. This negligible level, combined with the single source of atom fluorescence, implied atomic flux density could be assumed to be approximately proportional to the atomic fluorescence detected.

5.1.5 Guiding Results

Two CCD cameras were used to capture a video stream of the evolution of LVIS during guide exposure. Decomposition of this video stream revealed a small improvement of 8% in the steady state fluorescence level along LVIS length (errors were minimal due to analysis of multiple runs, $<1\%$). This result however was overshadowed by the novel transient response observed immediately following guide entry. In the transient regime a surge in atomic fluorescence of up to 35% over that of regular LVIS fluorescence was seen $\sim 160\text{ms}$ after guide introduction. Various guide powers were used, but a minimum threshold of 7W was necessary to observe transient effects, below this only the $<10\%$ steady state increase was visible. This threshold is due to the thermal energy of the LVIS flux, whereby the dipole potential influence of a guide under 7W is too weak to effect the energetic atoms. Figure 5.4 shows the fluorescence enhancement observed in both the steady state and transient regimes. It is this surge that constitutes Houde's "momentum kick" and derives from the non-adiabatic potential variation experienced when the guide is introduced; our "non-adiabatic kick".

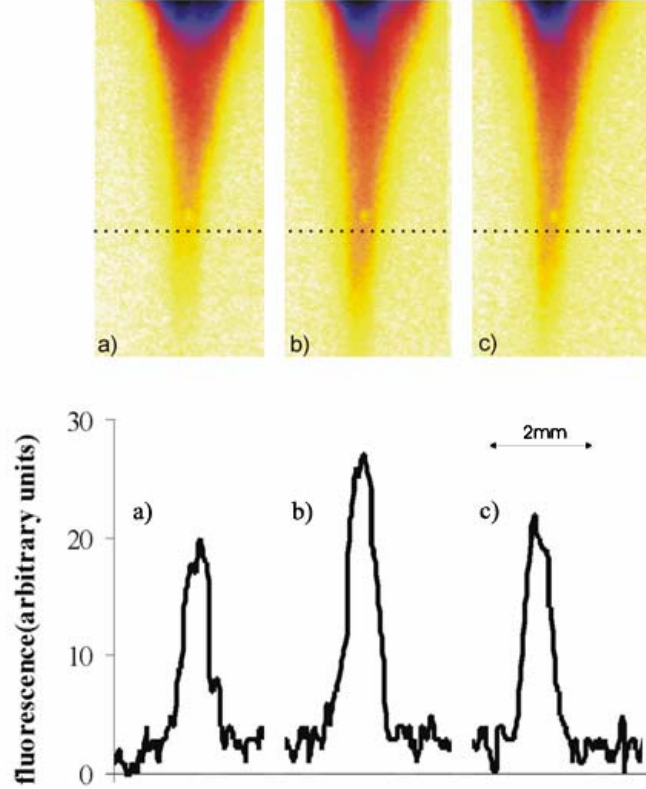


Figure 5.4 : Comparison of LVIS profiles a) without and b), c) with a collinear 9W, 1064nm, TEM₀₀ guide present. In the upper (false colour) images the LVIS profile is shown with a dotted line drawn at 5mm from MOT center. The lower graphs show intensity plots of the LVIS fluorescence (atom flux) measured along this dotted line. Figures b) and c) show the LVIS response to the guide 160ms (transient), and 1s (steady state), after guide incidence, respectively. The pale spot seen in the extremities of the LVIS flux is caused by contaminants in the lens system of the camera; its origin proved elusive until after experiments were completed.

Following each surge, a characteristic exponential decay down to steady state fluorescence was seen. Analysis of the recorded images for 9W and 7W guides provided the data shown in Figure 5.5. These had best-fits (with only one free parameter), which revealed a characteristic decay time of 0.45s. This surge decay time forwards use of a beam chopping system to realize a pulsed atom transfer scheme. Provided sufficient MOT refill rates can be maintained, such an arrangement could be used to improve transfer of atoms to a spatially separated conservative trap (magnetic trap). Trap build-up times at St Andrews were in excess of 5s, however this could be made comparable to the decay time by increasing the current through the atom ovens, so increasing vapor pressure within the trap.

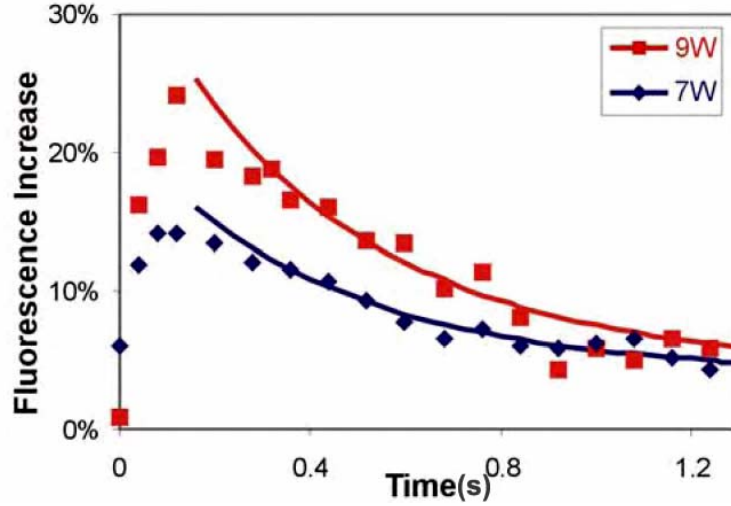


Figure 5.5 : Increase in atom fluorescence over regular LVIS level for collinear 7W and 9W 1064nm, TEM₀₀ guide beams. These data are averages of several runs, the solid lines are exponential best-fits which yield a characteristic decay time of 0.45s for a return to ~10% steady state flux rate. The peak fluorescence shown here is less than that shown in Figure 5.4 due to the averaging process.

In summary a steady state flux increase of 8% was observed in an LVIS flux when a 9W, 1064nm Gaussian guide was introduced. This increase was due to a slight increase in transverse confinement. Importantly, a transient 25% increase in guided flux was seen ~160ms after the guide was introduced. This decayed exponentially back to the steady state after a characteristic decay time of ~0.45s. This non-adiabatic ‘momentum kick’ which is expected to play a central role in far-off resonance guiding and in developing atom beam splitters.

It was noted that the transient surge in atoms may prove useful if fibre-guide experiments require a method of increasing the guided flux via a ‘pulsed’ operation.

5.1.6 Concluding Comments on the 10-Port Trap

A major drawback of this design was the restricted field of view permitted by the narrow diameter arms of the 10-Port piece; atoms could only be probed up to ~10mm from MOT centre. Nevertheless this drawback was not prohibitively detrimental for the 10-Port trap and many experiments were performed in this. These

included; collinear LG enhancement of a LVIS flux, an investigation of oblique LG guidance⁸ from a LVIS and the transient response of cold atoms to a far off resonance guide beam.

The inability to guide atoms far enough prevented clear observation/probing in the attached viewing cube. Thus it was decided the efficiency of the guide beam should be improved. It was switched back to the near-resonance Titanium Sapphire source to obtain a stronger dipole potential. Furthermore guide effectiveness would be improved by ensuring the next trap incarnation supported dropping of a cold cloud. In this way lower temperature atoms can be presented to the guide hence increasing its efficiency.

A larger central volume in which both guiding and probing could be performed with uninterrupted probe access over the entire flux flight path was also called for. This would allow more accurate laser probing in place of video capture and would remove the need to have an extra UHV chamber bolted onto the side of the trapping volume.

The recurring observation/access limitations forced a drive towards a UHV structure where observation issues were eliminated and where sufficient future-proofing for expansive experiments were catered for. These goals motivated the design of the Drum trap. Experiments performed therein are described in the following section.

5.2 Dropped Cloud Near-Resonance Guiding in the Drum Trap

The Drum trap provided unprecedented optical access for both CCD observation and laser probing. The number and size of connected viewports offered an ideal geometry for dropped-MOT experiments where released atoms could be accelerated towards a waiting probe beam under the influence of gravity alone. The Drum trap has remained in service for longer than any other trap; it is still used for free-space guiding experiments in St Andrews today.

The increased visibility of the atom cloud in the Drum trap presented a useful opportunity to characterise the cloud more fully than in previous experiments. Thus early experiments involved analysis of; the trap filling time, the cloud's response to magnetic field variance and the attempted addition of a molasses cycle to the cooling process. Later experiments used dropped MOT clouds with laser probes up to 5cm from MOT centre to investigate a range of optical guiding potentials. These included, hollow LG and Bessel beam guiding, dynamically reconfigurable guide profiles and red-detuned Gaussian guiding. The Gaussian guides were of particular interest to me as this ground work would provide an understanding of what was to be the primary method of coupling atoms from a MOT into the narrow aperture of hollow fibres (discussed in chapter 7).

This final section on red-detuned guiding will discuss design features of the Drum trap, briefly re-cap atom probing methods then describe a series of near-resonance Gaussian guiding experiment. Here the roles of guide detuning and guide power are investigated in order to optimise guided flux volumes for later fibre coupling experiments.

5.2.1 The Drum Trap Particulars

Figure 5.6a) and b) are pictures of the Drum trap vacuum assembly. They show the broad, drum-like tube that was the main trapping volume; this had two 150mm diameter viewports mounted on either end and a further 8 flanges around its circumference. Six of these were fitted with 35mm \varnothing viewports, one with a 't' piece for optical throughput and oven connection, and the remaining one connected to the rest of the UHV system and ion pump.

Despite its sheer weight, the Drum trap was perhaps the easiest of traps to assemble; the large flat components were easier to clean and provided fewer tight spaces to fit bolts into. Fear of breaking the large windows enforced slow bolt-tightening up to vacuum seal level.

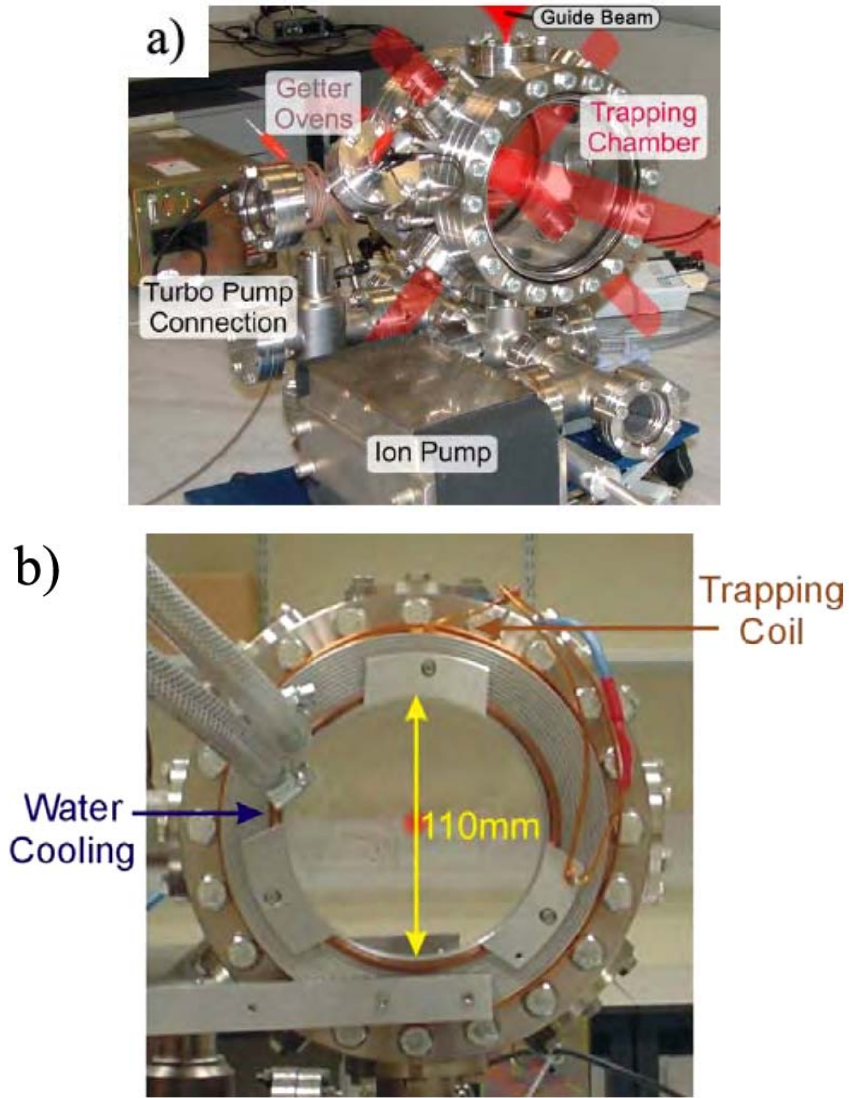


Figure 5.6a) & b) : Photographs of the Drum trap before all MOT optics were mounted around it. In a) the paths of the 6 cooling arms shown, the topmost viewport is thus left clear for guide entry. Similarly a viewport on the underside of the connecting 6-way piece allows the vertical guide to exit with a minimum of glare and reflection. Image b) shows the location of the MOT coils and their water-cooled mounts. The coils were typically run at $\sim 15\text{A}$ each.

The use of LVIS atoms in previous experiments was helpful for coupling into guides propagating largely collinear to the LVIS path, however, this inherently involves kinetic energies greater than those of MOT atoms. Dropping the cloud into a waiting guide yields atoms with smaller velocity components, and so better guiding efficiencies (see chapter 3.6 for MOT release method). To facilitate a guide beam propagating collinear to falling atoms the vertical axis had to remain clear of MOT optics. Thus cooling beams were arranged on 45° diagonals in the vertical plane with

a vertical guide arranged between them. Figure 5.6a) and Figure 5.7 illustrate the optical setup used here. The lower 6-way piece connecting the drum to the UHV system had a viewport on the underside, thus guides could enter vertically and exit with a minimum of scatter and reflectance.

The magnetic quadrupole field for this large trap was of great concern when considering coil winding. A large field was required to produce the 10G/cm gradient across the 160mm drum length. This was hampered by the need for large diameter coils so as not to diminish optical access. This field would require ~ 1000 wraps at 1A, which was not practical. It was decided the drive current (cf. number of wraps) should be increased to achieve the desired field strength, this stipulated broader wire diameter to reduce resistive heating. Aluminium coil mounts, surface-machined to have heat-sink style grooves, were built to hold coil diameters of 135mm (shown in Figure 5.6b). An indent for good thermal contact with a copper water pipe was also machined in. These features helped with heat dissipation from the 83 wraps of 1.5mm diameter Kapston cable tightly wound onto them. Both coils were typically driven at ~ 15 A from two Kingshill Electronics 20A supply boxes. The water cooling from a high pressure (120psi) cold water system, allowed regular running temperatures of $\sim 35^\circ\text{C}$. They were positioned against the side of the drum just within the radius of the flange bolts (to reduce MOT-coil separation).

The familiar NIR CCD cameras were used for cloud observation. In particular these were used to arrange guide alignment and confirm MOT quality before each experiment. The single-lens $2f$ systems used to focus light onto the CCDs in previous experiments were replaced with commercial zoom lenses. These provided greater control over the focal distance, depth of field, size and contrast of the captured images.

5.2.2 Atom Detection

The numerous viewports on the Drum trap allowed both fluorescence and absorption probes (described in chapter 2) positioned up to 50mm below MOT centre. These provided more sensitive detection relative to CCD recording. The on-resonance probe light was sampled from a separate locked ECDL passed through a beam splitter to supply fluorescence and absorption probe beams alternately.

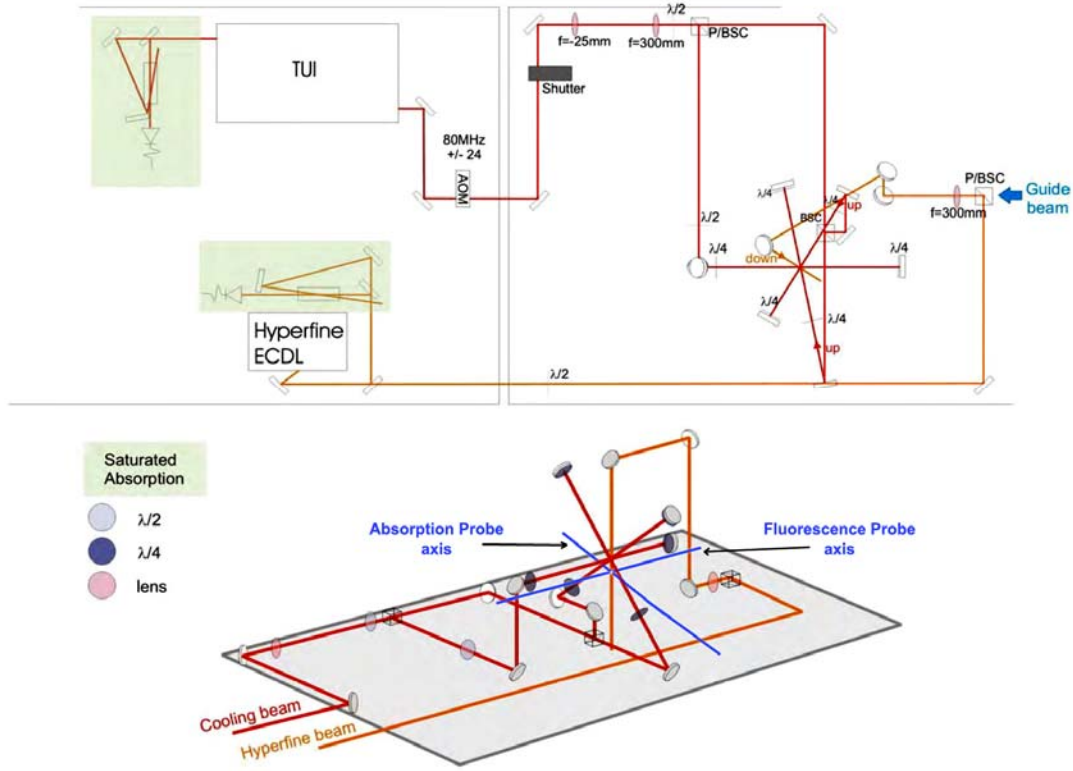


Figure 5.7 : Optical setup for cooling, hyperfine and guide light entry to the Drum trap. Probe beam axes are indicated in blue. The trap was mounted on a separate table from the laser sources as it required a hard-mounted table due to its weight. The laser sources however required a table with vibration damping legs (Newport, Nitrogen filled, floating legs were used). Schematic courtesy of Dr Rhodes.

A probe beam entering through the main window was arranged to skim cooling-beam optic mounts in the horizontal axis and have 50mm vertical translation from MOT centre (shown in blue in Figure 5.7). A second orthogonal major probing axis was arranged to pass through the middle 35mm diameter horizontal viewports, however this could only permit probe translation up to 10mm beneath MOT centre due to the viewport's diameter. In general, the beam directed through the larger viewports operated as a fluorescence probe, and had an associated higher intensity level $I > I_{sat}$. This passed through the trap and was retro-reflected through a quarter wave plate (to prevent interference effects). Any fluorescence produced by passing atoms was then imaged onto an off-axis photo-multiplier tube (PMT, Hamamatsu, H7710-03). The probe launch mirror and PMT were carefully positioned and mounted on xyz-translation stages to allow matching vertical translation when altering the

probing height. The other probe was setup in an absorption mode with $I \leq I_{sat}$. It was passed through the trap and directed onto the surface of a sensitive, fast photodiode which detected the *drop* in light level associated with absorption imaging. Both probe systems had significant levels of optical shielding, namely interference filters and plenty of opaque card fitted to block any extraneous lab light. Further information on fluorescence capture technique, and its application in characterising atom cloud filling time and magnetic field dependence is given in Appendices ii and iii.

5.2.3 Guiding Procedure

Near-resonance red-detuned guiding was performed, to investigate the dependence on power and detuning of Gaussian profile guide beams. This intensity profile was chosen as it would match that used when coupling into a hollow-core fibre (see chapter 7). Optimisation of such a guide was a goal of this thesis.

The Titanium Sapphire (Ti:Saph) laser was chosen as the guide beam source due to its frequency proximity to Rb^{85} resonance, and its simple tuning abilities. The near resonance output would ensure a strong dipole potential for guiding and a few GHz detuning would allow removal of the majority of stimulated emission heating. The Titanium Sapphire beam was passed through a telescope system of an $f=300\text{mm}$ lens and an $f=100\text{mm}$ lens to produce a beam waist of $125\mu\text{m}$. This was not the most ideal beam size for coupling from a 1 - 1.5mm diameter MOT. However, the available power from the Titanium Sapphire source was limited to 430mW, hence a narrower beam waist was desirable for increasing dipole potential of the guide. In particular this was important when the effects of radiation pressure were to be removed by detuning further from resonance. For comparison, a 400mW, 10GHz, 0.25mm diameter guide can yield a dipole potential equivalent to 1.4mK, whereas a MOT-matched beam of 1.5mm diameter will generate only 0.41mK. Guides of these powers are capable of confining transverse velocities of 63cms^{-1} and 35cms^{-1} , respectively.

Dropped MOT profiles were captured with and without the guide present so as to calculate the flux enhancement over that of a free-falling cloud. The guide was detuned 2GHz, 6GHz, 10GHz and 200GHz from resonance, and was yielded from

430mW down to ~ 25 mW at each detuning. The large jump to 200GHz was achieved by allowing the laser a single mode-hop across its thin etalon mode structure; the free spectral range (FSR) of the thin etalon was 200GHz. Smaller detunings were achieved by varying the temperature of the thick etalon (as detailed in chapter 3). At a probe height of 3.5cm extra detunings of 12Ghz, 14Ghz, and 18GHz were used to investigate any reduction in radiation pressure.

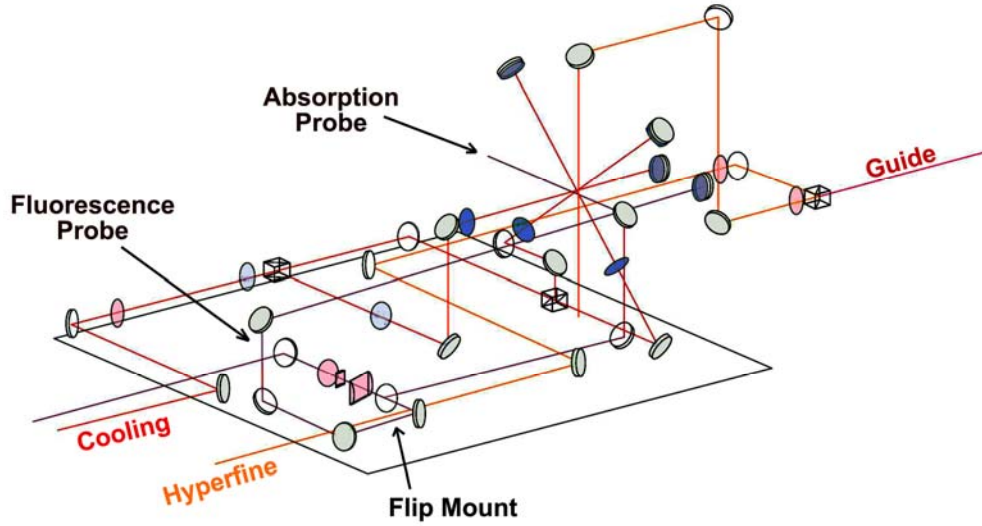


Figure 5.8 : A more detailed schematic of the optics arrangement used for Gaussian guiding in the Drum trap. Note the inclusion of Hyperfine beam in the guide path, the flip mount used to switch between probe beams and the cylindrical lenses used to provide a \sim flat probe ‘light sheet’.

A more detailed schematic of the beam arrangement is shown in Figure 5.8. Here $f=25$ mm and $f=50$ mm cylindrical lenses are shown in the probe beam, these were used to create a 5mm \times 1mm probe ‘light-sheet’. The broad probe profile was used primarily to ensure good guide–probe overlap; after ~ 5 cm travel it was surprisingly easy for the guide beam to miss the probe region. It was also hoped a broad probe would better capture the faint signal of an unguided (free-falling) cloud and thus allow comparison, at all probe heights, between guided and free-falling flux levels. The narrow vertical profile also increased the spatial measurement resolution as the flux fell through it.

A small portion (~ 2 mW) of hyperfine light was combined with the guide in order to keep guided atoms in the cooling cycle and so increase their interaction with

the probe beam. In hindsight this may not have been as advantageous as first thought since only ~ 1 atom in every 1000 oscillations will de-excite to the hyperfine level, so over the longest guiding distance used this amounts to ~ 50 atoms de-exciting. Conversely the hyperfine light may increase spontaneous emission and so reduce the guided flux. However, later calculations indicated such a small light level was unlikely to effect the flux at all.

The TUI Optics, T-100 tapered amplifier laser (TUI) replaced the ECDL-Circulase master-slave setup previously used for the trapping beams. It was locked directly onto the $5S_{1/2}F=3 \rightarrow 5P_{1/2}F'=4$ transition of Rb^{85} via its own internal locking circuit. Each cooling arm entered the trap with 12mW of power in a circularly polarised, $\sim 1.5\text{cm}$ diameter beam. The hyperfine beam was generated from the regular ECDL and locked to the $5S_{1/2}(F=2) \rightarrow 5P_{3/2}(F'=3)$ transition. The two probe beams were provided by a single ECDL (previously used for the trapping beam).

The addition of computer controlled shutters (described in chapter 3.5) to both cooling and trapping laser systems, allowed accurate dropping of the MOT cloud. Newport 846HP shutters provided a beam cutting time of $\sim 1\text{ms}$. A LabVIEW controlled National Instruments (NI) PCI-6602 timing/data-acquisition card (with a CB68LP connector block) generated accurate timing signals enabling synchronisation of guide entry with MOT drop.

The MOT was established with ovens running at $\sim 4\text{A}$ and the coils running on $\sim 15\text{A}$ each, this provided a cloud of $\sim 10^7$ atoms. The Gaussian guide was carefully aligned vertically through MOT centre; this required monitoring of the CCD images while the guide was on-resonance so as to spot the correct amount of cloud disruption (from guide-induced spontaneous emission heating). Correct alignment could be judged roughly from the angle of the shadow swept out by the guide. Subsequent trial MOT drops, using the closer-proximity absorption probe for detection, allowed optimisation of this alignment.

Absorption and fluorescence probes were selected by use of a flip mount (shown in Figure 5.8). Note that it was not possible to run both absorption and

fluorescence probes simultaneously since one would disrupt the atom flight path prior to contact with the other. Fluorescence probing was used as the main data collection method, (the absorption probe was used primarily for alignment and setup purposes).

5.2.4 Guiding Results

Fluorescence profiles were taken at distances of 1, 2.3, 3.5 and 5cm beneath MOT centre. These profiles were entered into a Mathematica program which served to isolate the cloud fluorescence and perform a 10,000 step, iterative best-fit operation to fit a Gaussian profile to the signal. The Gaussian shape was deemed the best match for a falling cloud, ballistically expanding in the vertical axis while accelerating under gravity towards the probe. The ‘best fit’ curves were accurate matches to the guided signal, as such, they are shown in this chapter in place of raw data streams to allow combination of multiple signals on one graph.

Figure 5.9 is a plot of the fluorescence signal resulting from a 430mW, guide detuned 6Ghz from resonance. It is shown here to demonstrate the nature in which data are collected. On its own this tells us when the centre of the cloud passed the probe beam (signal peak at 0.0152s), the number of atoms conveyed in the guide (area under curved section) and an indication of the strength of radiation pressure between guide detunings (position of peak relative to free-fall signal peak). The accuracy to which the solid angle of fluorescence captured towards the detector is known dictates the error level in these atom-number measurements. Here a 14% error level is assumed on all flux calculations.

Combining multiple traces into one graph provides a better comparison of guided flux volumes, radiation pressure push and flux enhancement over that of a free falling cloud. Figure 5.10 shows the fluorescence profiles resulting from a series of guided fluxes detected 1cm beneath MOT centre. These atoms were subjected to the 250 μ m diameter guide, detuned 2Ghz from resonance, over a range of beam powers from 25mW up to 430mW. Of particular interest is the low free-fall cloud signal. This gives contrast to the surrounding guided flux levels and indicates a substantial flux improvement can be gained even with guide beams of modest power.

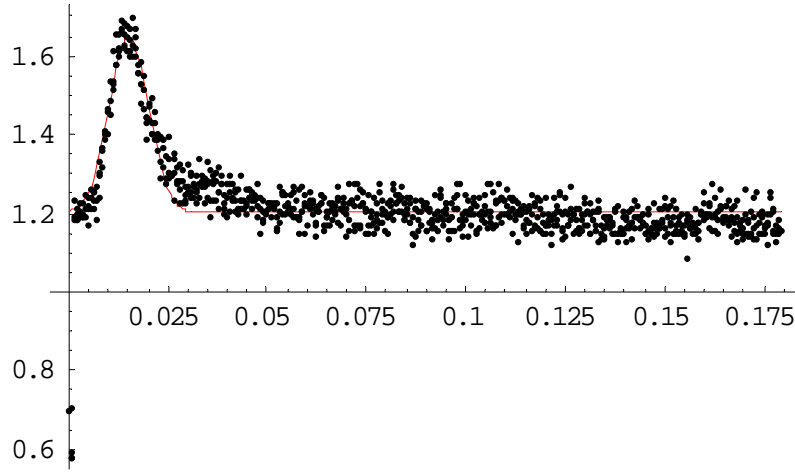


Figure 5.9 : A fluorescence trace capturing passage of atoms within a 430mW, 6GHz detuned, 250 μ m diameter Gaussian guide. 1000 data points are collected in every trace. The red line is a Gaussian best-fit curve, specifically fitted to the flux fluorescence. There is slight disparity between the tail end of the flux fluorescence and the fitted curve. This is caused by atoms lagging behind the guided flux. They are believed to fall into 2 groups; atoms originally counter-propagating against the guide within the MOT volume before release, and atoms which have escaped the guide and entered an oblique route towards the probe.

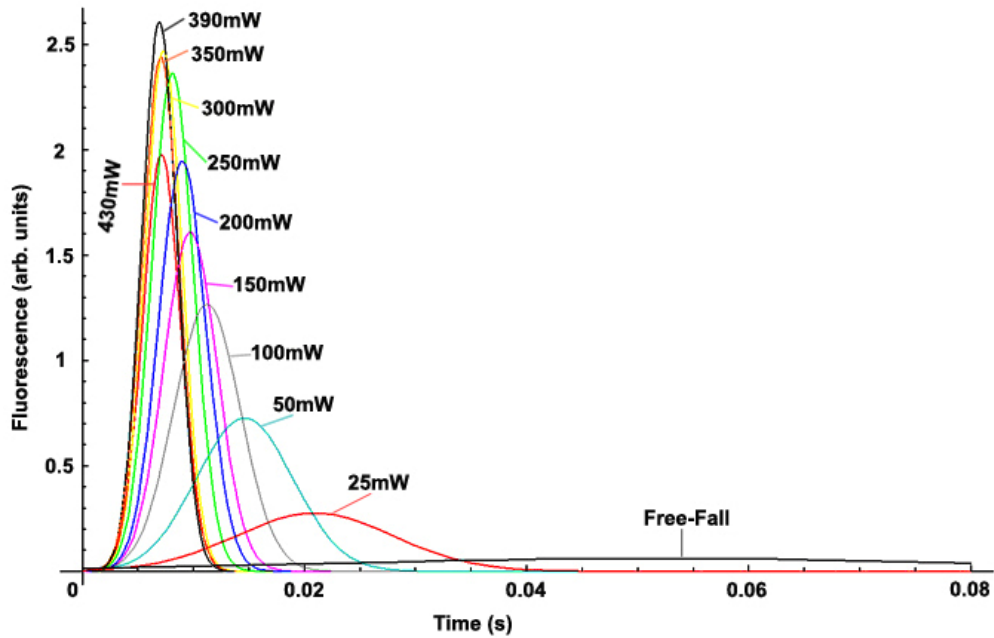


Figure 5.10 : Fluorescence traces produced by atomic clouds falling 1cm into the probe beam. A 2GHz guide is applied at numerous powers as indicated. Note the low area under the free-fall trace (relative to the guided traces) and the decreasing radiation pressure with decreasing guide power. The roll-off at higher power is also seen as spontaneous emission heating increases with power.

Investigating Radiation Pressure Pushing

It was hoped the majority of radiation pressure could be circumvented with $\sim 10\text{GHz}$ detuning of the Titanium Sapphire source. If so, the efficiency of the Gaussian guide could be evaluated solely on the merit of its transverse confinement as denoted by its dipole potential. However, the detuning required for radiation-pressure free guiding was not practical with the Titanium Sapphire laser (due to a need to maintain calibration). The following section discusses this.

The peak of a free-fall fluorescence trace gives the time taken for the cloud to fall into the probe beam under the influence of gravity alone. Thus, it gives an example of a flux completely free of radiation pressure pushing. Weak, or far detuned guide beams impose less radiation pressure and so have fall times approaching the free-fall case. The height/position of each probe under the MOT dictated a characteristic free-fall time. These times are shown in Figure 5.11 next to values predicted for probes at the stated height. The discrepancy between experimental and predicted values comes primarily from inaccurate probe-MOT separation and, for the larger separations, from the low, noisy signal levels presented to the computer for Gaussian fitting. The average disparity is $\sim 16\%$ this implies an error between $\sim 0.3\text{mm}$ and $\sim 8\text{mm}$ in the distance the atoms have travelled. The disparity at 3.5 and 5cm is believed to be more from the fitting of low signal levels. At these distances the unguided signal is difficult to distinguish from background noise. Nevertheless it must be stated, the *absolute* time of flight is not the significant feature here. The *difference* between this and the time of a guided flux is the important element for indicating levels of radiation pressure.

The laser sources were mounted on nitrogen-floated optical tables, these inflict a daily drift on laser positions as the table resettles in the changing lab temperature. Efforts were made to minimise this, however it is believed a small amount of drift is also responsible for a small portion of the predicted and detected free-fall times.

Probe (cm)	Height	Free-Fall Time (s)	Predicted Fall-Time (s)
1		0.052	0.045
2.3		0.074	0.068
3.5		0.121	0.084
5		0.126	0.101

Figure 5.11 : Experimental and predicted times of flight for free-falling MOT clouds. These are the times taken to travel from MOT centre to probe beam centre. The disparity between predicted and experimental figures is a result of inaccurate probe beam placement

Figure 5.12 and Figure 5.13 show fluorescence profiles taken at 1cm and 5cm beneath the cloud. Here the guide is held at constant power (430mW) while the detuning is switched between 2GHz, 6GHz, 10GHz and 200GHz.

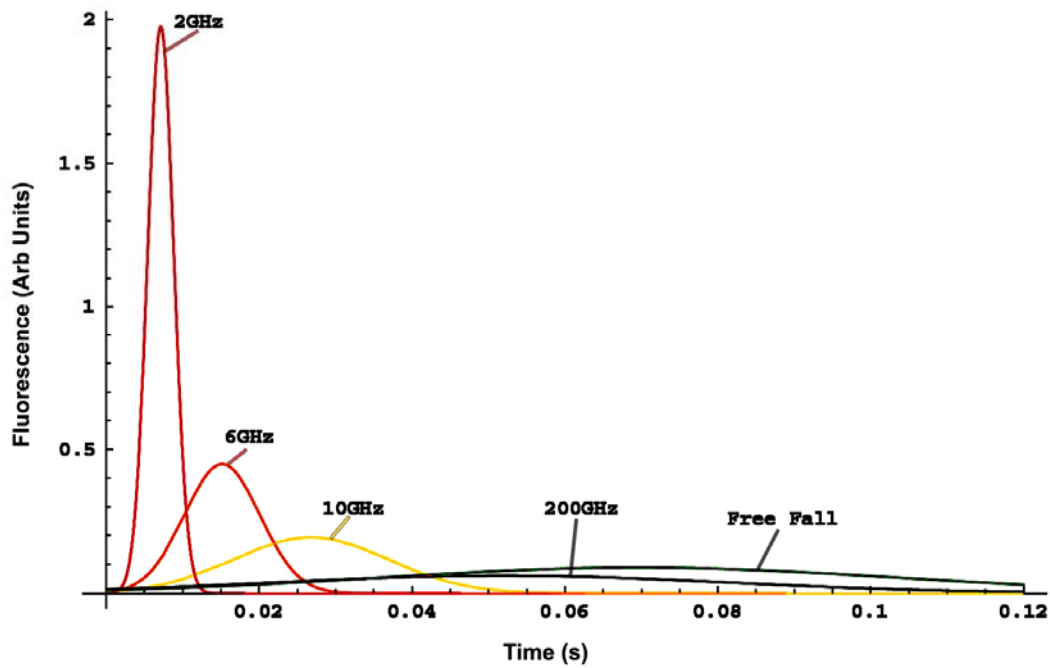


Figure 5.12 : Fluorescence profiles captured at 1cm beneath MOT centre, with a constant power guide of 430mW and increasing detunings. Note the 200GHz trace indicates a flight time longer than that of the free-falling case, this is due to inaccurate fitting of the low signal level.

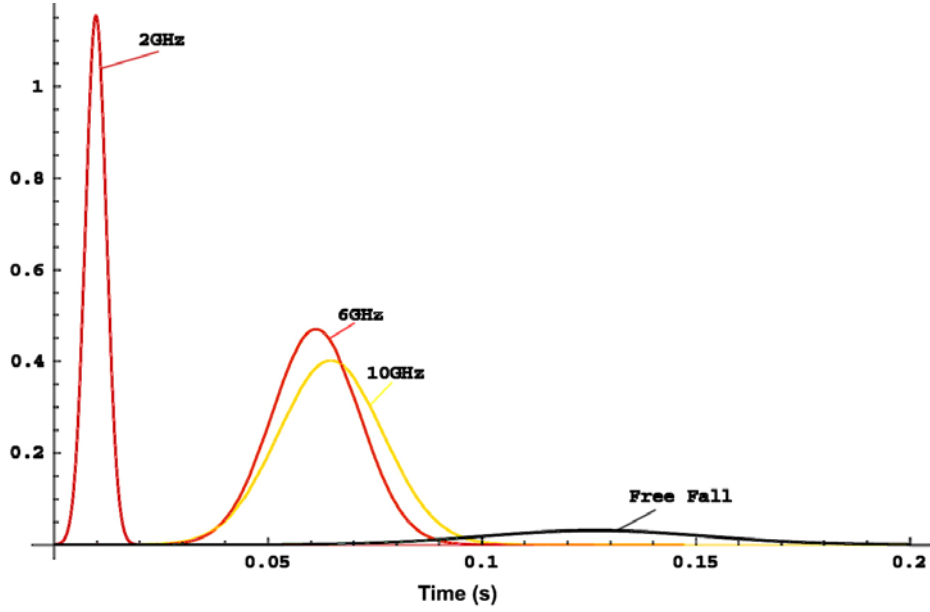


Figure 5.13 : Fluorescence detected at 5cm probe height, with guides of constant 430mW power and increasing detunings. The flight times are all slightly stretched due to the longer flight, however the 2GHz guide inflicts sufficient radiation pressure pushing to force the cloud into the probe at a ~similar time to that of the 1cm case.

The time of cloud passage, given for each probe height, highlights the influence of substantial radiation pressure at 2GHz detuning, however, this is significantly lower at the mid detunings of 6 and 10GHz. A clear reduction in atomic flux is also seen. This indicates a lessening of transverse atom confinement which is explained by the reduction in dipole potential associated with detuning from resonance.

Increased guide detuning, applied at the same power level, brought the time for MOT passage closer still to that of the free-falling cloud. These guides of 12, 14, 16, and 18GHz were applied when the probe was positioned 3.5cm beneath the cloud. They are summarised in Figure 5.14, where the flux flight time is plotted against guide detuning. Achieving these detunings required adjustment of the Titanium Sapphire's thin etalon; the thick etalon mode-hops to positive detunings (blue-detuning) if pushed beyond 10GHz. Hence, the thin etalon was adjusted to shift the gain bandwidth slightly, allowing the thick etalon to tune over its normal bandwidth but centred on a different frequency (see Figure 3.17 for an illustration of the FSR lasing modes of the Titanium Sapphire etalons).

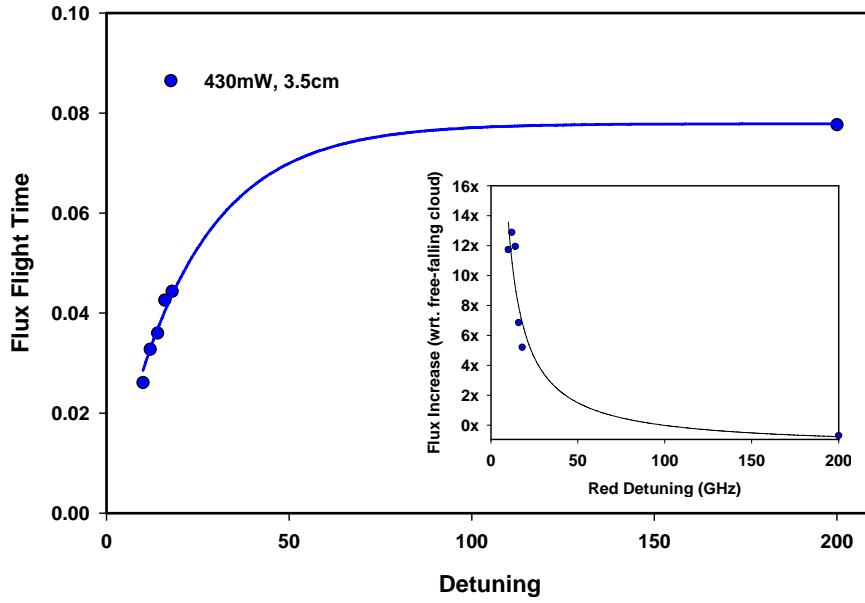


Figure 5.14 : The time of flight for guided dropped clouds increases towards that of a free falling cloud, as the radiation pressure component is removed from the guide beam. A detuning of $\sim 50\text{GHz}$ can be seen to provide a near ‘pushless’ guide. The inset graph shows the deteriorating flux enhancement (for the same guide beams) as the detuning increases; a small flux enhancement is still visible for a detuning of $\sim 50\text{GHz}$. These data were taken at maximum power of 430mW with a probe positioned 3.5cm beneath MOT centre. The fitted blue curves are a simple exponential with 2 free parameters.

Despite hopes of bypassing the majority of radiation pressure force within the regular tuning range of the Titanium Sapphire’s etalons, Figure 5.14 indicates that a minimum detuning of $\sim 50\text{GHz}$ is necessary for this. Such radiation pressure turn-off threshold compares well with the figure published by D. Muller⁹ where a blue-detuned guiding regime is seen to have a pressure threshold of 40GHz ; the discrepancy being attributable to the levels of dipole force available in blue and red detuned guides.

Beyond $\sim 80\text{GHz}$, the flux, in the inset of Figure 5.14, is seen to diminish below unguided levels. This creates a detuning window between 50GHz and 80GHz which could be important for future guiding experiments, particularly in red-detuned hollow-core fibre guides where atoms are held in the light for distances greater than those here.

Radiation pressure will scale linearly with beam intensity, however, it is predicted to vary with an inverse square dependence on detuning (for small detunings $\delta < \gamma$, see equation 1.4). Further detuning with increased intensity should provide a suitable guide with little radiation pressure. Nevertheless, difficulties in reaching the detunings shown in Figure 5.14 (particularly in holding them while maintaining frequency calibration) halted investigations into the elimination of radiation pressure. A study of threshold detunings over multiple power levels, to minimise radiation pressure, was marked as a worthwhile set of experiments for future work; fibre related experiments forced time constraints on Gaussian guiding work.

Investigating Flux Enhancement

The remainder of the red-detuned guiding experiments examined the flux enhancement over 2, 10 and 200GHz detuning. The furthest detuning practical for noticeably enhanced guiding; 10GHz, was selected for inspection of flux enhancement over a range of beam powers.

The increase in detected flux over that of an unguided falling cloud was calculated from the integral of Gaussian curves fitted to the fluorescence-probe signal (as before). Since the plots are records of the amount of light collected into the PMT, the area underneath them, (scaled to account for PMT gain), provides the number of photons collected from the fluorescence. As discussed in Appendix ii, this number is only a small fraction of the light emitted isotropically. Thus, calculation of the solid angle allows an estimation of the total number of photons emitted while in the probe beam. The speed with which the atoms fall through the probe is then estimated (using the time of flight indicated in the traces). This in turn, gives the time spent in the probe. The characteristic scatter rate for the probe intensity is then used to give a figure for the number of photons emitted per second per atom while in the probe. Ultimately this emission rate is combined with the number of photons emitted isotropically to give an absolute indication of the number of atoms conveyed in the guide.

The number of atoms guided to the probe is expressed here as a multiplication factor over the number detected in a free-falling cloud (in the same probe). In this way guiding efficiency can be better displayed. Figure 5.15 shows this flux improvement in guides detuned 2, 10 and 200GHz from resonance.

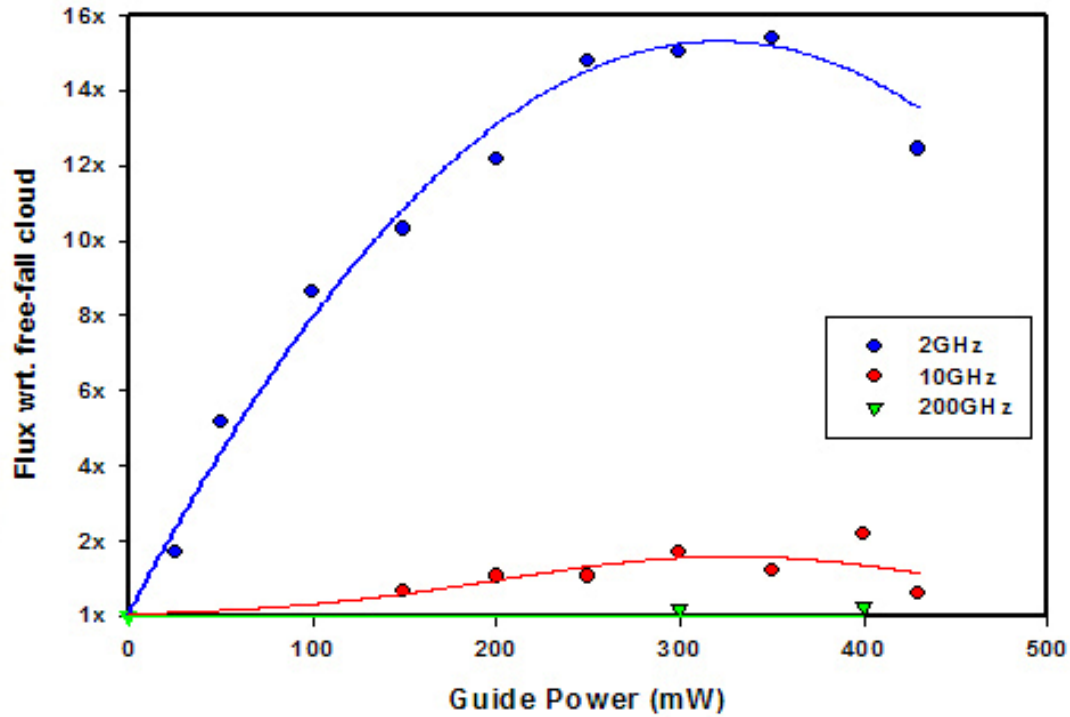


Figure 5.15 : Flux enhancement of a dropped cloud displayed as an improvement factor over the unguided, free-falling case. Atoms were guided 1cm into the probe beam. The 200GHz guided atoms only fractionally surpass the free-fall figures. Gaussian profiles with 3 free parameters were fitted to the data.

The pushing radiation pressure of the 2Ghz guide vaults its guiding efficiency above other detunings. Whereas the 200GHz guide only peaks above the zero line at powers above 300mW; its dipole potential is too weak below this. The fall-off after the peak is due to increasing spontaneous-emission atom loss as the guide power increases.

Similar graphs, showing the flux enhancement with 10GHz guides at 2.3cm and 3.5 cm probe heights, are shown in Figure 5.19. Collating these into one graph was not productive as the traces were confusing when placed on the same scale. More

importantly ‘flux enhancement factor’ is not a good way to compare guides probed at different heights since the detected flux for the free-falling cloud decreases as the probes get further from MOT centre. A better comparison can be gained from analysis of Figure 5.18. Here the absolute atom numbers collected from the probe beams at each height are shown. **Typical flux levels of ~10% of the MOT volume, that is $\sim 10^6$ atoms, were conveyed in the Gaussian guides.**

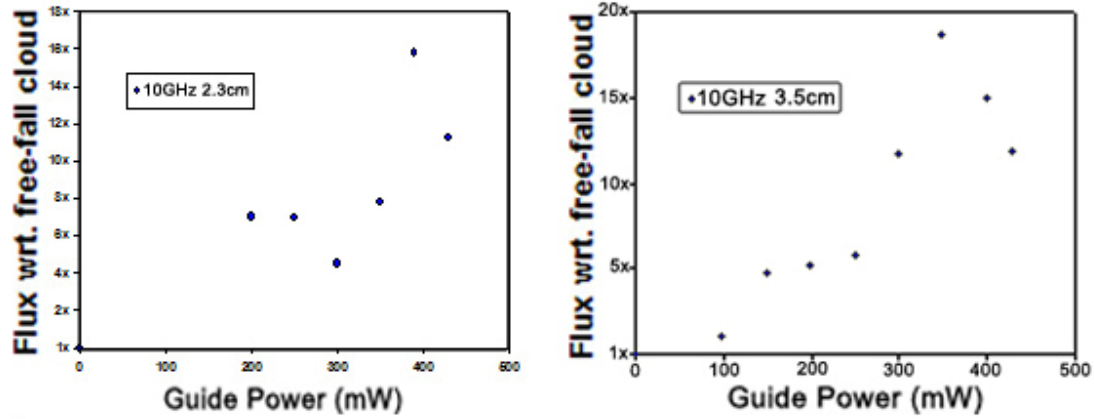


Figure 5.16: Flux enhancement with 10GHz guide beams. From left to right, probe heights are 2.3cm and 3.5cm. Gaussian fitting for these curves did not work well. This was because of a recurring dip seen on the left hand side of all flux enhancement traces. Here the dips were severe enough to prevent fitting.

From Figure 5.16, enhanced guiding can clearly be seen in 10GHz guides up to ~ 20 times that of a free falling cloud. It must be noted, direct comparison of the flux enhancement between 1cm, 2.3cm and 3.5cm probe heights is misleading. However, a few important points are shown, and repeated in each profile. These are; a limiting guide power of 350mW – 400mW ($I = 7.13\text{MW/m}^2 - 8.15\text{MW/m}^2$) which serves to cap guiding efficiency, and a dip in the enhancement profile at $\sim 250\text{mW} - 300\text{mW}$ ($I = 5.1\text{MW/m}^2 - 6.1\text{MW/m}^2$). The efficiency cap is explained by the predicted increase in spontaneous emission associated with increasing beam power (as noted for Figure 5.15). This again is a useful limit to remember for future guiding experiments; the dipole potential of a 10GHz guide conveying Rb^{85} atoms is inefficient when its intensity breaches $I \approx 7.1\text{MW} - 8.1\text{MW}$. For reference, this intensity and detuning yields a dipole potential depth equivalent to 1.3mK – 1.4mK and a scattering rate of $1.4 \times 10^6\text{s}^{-1} - 1.5 \times 10^6\text{s}^{-1}$. This should be able to confine atoms with transverse velocities up to $62\text{cm/s} - 64\text{cm/s}$. Such large transverse capture velocities imply the

majority of atom loss is attributable to guide-cloud diameter mismatch. Approximately 10^5 scattering events occur during the time of flight (over 3.5cm), which is expected to have a minimal contribution to the atom loss.

The dip in the enhancement profile works to bolster the validity of our experiments as it reinforces results obtained by Renn *et al.* at JILA¹⁰, in their 1996 paper¹¹ detailing the heating of atoms in a red detuned guide. In their work, atoms are coupled into a red-detuned guide for passage through a hollow core fibre, and they report “a viscous component of the dipole force” which “heats the atoms, and causes an exponential attenuation of atom flux with distance”. Figure 5.17a) to d) show the flux dependence on guide detuning and intensity observed at JILA. These graphs display (more eloquently) the hole-burning effect also experienced here in St Andrews.

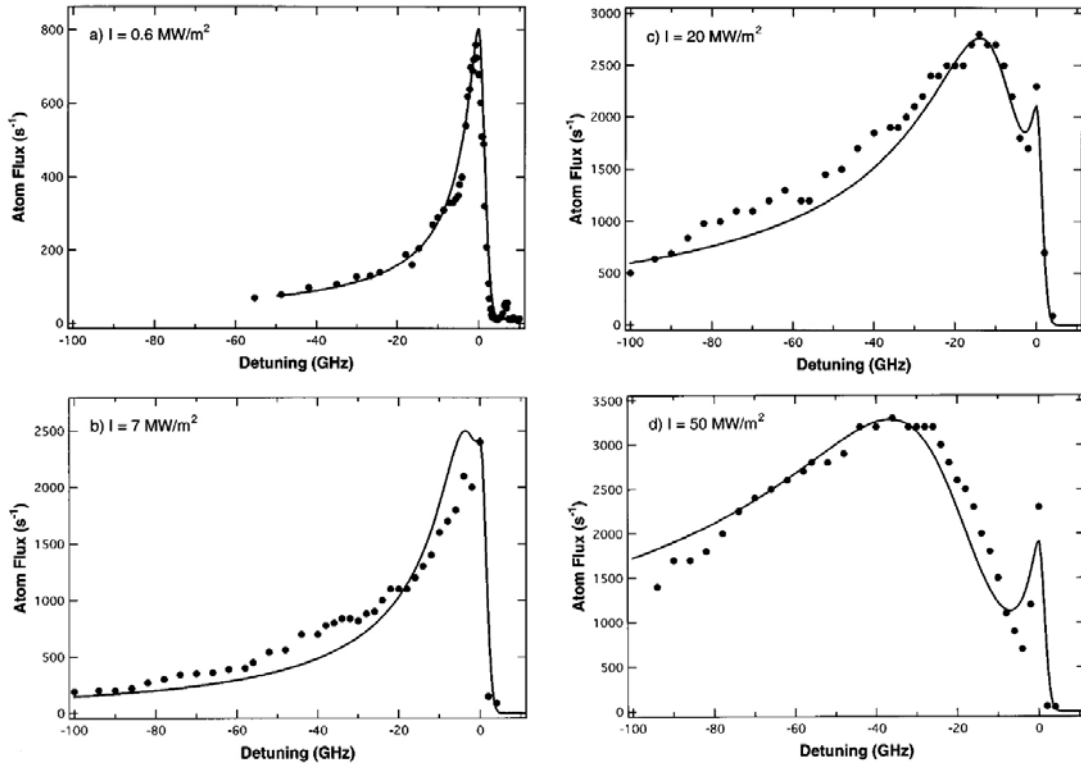


Figure 5.17 : Atom counts observed by Renn *et al.* working at JILA and the University of Boulder, Colorado. These are displayed as functions of the guide detuning (c.f. power) and were detected on exit from hollow capillary fibres of 3.2cm and 6.1cm, for a) and b)-d) respectively. The “viscous heating term” reduces guiding efficiency for a range of detunings immediately following the initial radiation pressure surge. Figure reproduced from Renn *et al.*

Where Renn *et al.* observed a rapid decrease in guiding ability for a 7MW/m^2 guide detuned to $\sim 2\text{GHz}$ red (a negative detuning in Figure 5.17 means red-detuning), we observe this decrease between 5.1 and 6.1MW/m^2 at a detuning of 10GHz red. This is in reasonable agreement with their results, where the small disparity comes from the temperature difference of source atoms in each experiment. Renn *et al.* used thermal vapour atoms, therefore making their atoms less susceptible to guide conditions. Our atoms retain much of their cold properties ($\sim 100\mu\text{K}$ temperature, accelerating in only one axis), thus feel the effects of the guide sooner; at lower detunings and intensities.

The ‘viscous heating’ term is understood by means of the dressed-atom picture, briefly discussed in chapter 1.3.4. Here, the intensity of the guide causes spatial warping of the energy levels of atoms travelling in the guide path. This warping stems from the AC-Stark effect and results in a progressive heating of the atom dependent on the number of spontaneous emission events it undergoes. This number is increased by the presence of the intense guide. Thus, a cycle of heating is initiated which serves to spontaneously excite atoms out of the guide.

A 10GHz beam provides a weaker transverse confinement than a matching 2GHz beam, however, its reduced radiation pressure component (relative to the 2GHz guide), implies atoms successfully coupled into it should remain so for a longer distance. Atoms coupled into the 2GHz guide will suffer a greater likelihood of spontaneous emission heating and so be ejected sooner. Thus, a simple argument for more efficient guiding would be to increase the detuning to a point between the drop-off of spontaneous emission ($\propto 1/|\delta|^2$) and the drop-off of dipole force ($\propto 1/\delta$). This is in fact an ideal way to guide an atomic flux, however, the high radiation-pressure regime should not be disregarded so easily.

For short travel times a significantly higher flux rate can be achieved in the detuning range immediately following guide turn on. This is explained by the fact that despite a high probability of atom heating, the atoms are pushed so quickly they have a reduced *time* in which to be excited from the guide. Thus high volumes of atoms can be rapidly transferred despite an impending heating effect.

There is no happy medium between these two regimes. Either large volumes of atoms (with a broad range of energies) can be guided over short distances in the high radiation-pressure and high dipole-force regime, or lower temperature atoms can be guided longer distances in the detuning window in-between radiation pressure turn-off and dipole potential turn-off. Guide parameters between, or outwith these operating windows, offer little opportunity for flux conveyance.

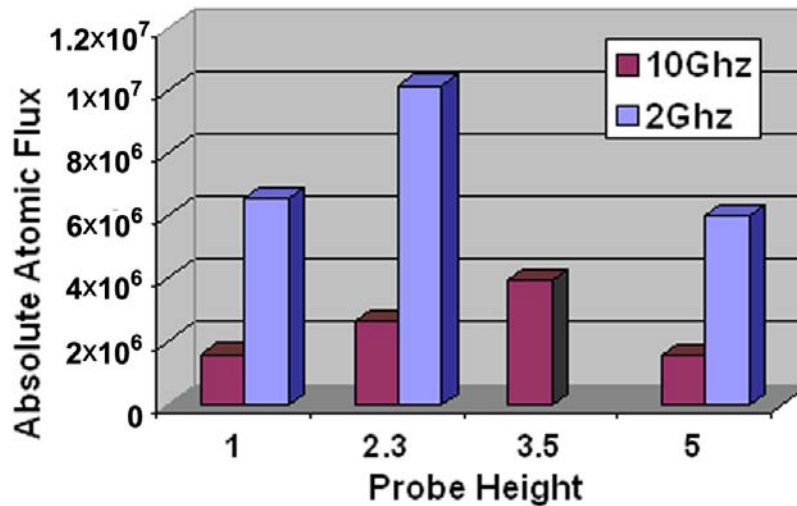


Figure 5.18 : Comparison of absolute atom numbers detected over all probe heights at 2 and 10Ghz red detuning. Data for the 2Ghz guide at 3.5cm was not collected; this probe height, a glaring omission here, was an additional level whose role was not clear at the time of data capture.

A test of this hypothesis would be to measure the *rate* of decrease of atom flux between the 2.3, 3.5 and 5cm probe heights in the 2 and 10Ghz guided flux signals shown in Figure 5.18. Comparison of the gradients between the 2.3 and 5cm flux levels indicates this theory is correct; the 10Ghz guide flux has decreased 5 times quicker than the 2Ghz guide. However, this data is suspect without the intermediate 3.5cm, 2Ghz measurement; the 10Ghz measurement shows a rise in flux which would need to be overshadowed by the 2Ghz guide for the theory to remain sound. This will perhaps be completed in subsequent Guassian guiding experiments.

5.3 Conclusion

Atom traps have been constructed, laser systems built, and electronic control circuits built in order to manipulate cooled Rb atoms in red-detuned optical potentials. These experiments are summarised below:

In the 10-Port trap:

- Gaussian far-off resonance enhancement of LVIS, in the steady state and transient regimes.

In the Drum trap:

- Gaussian guiding of dropped MOT clouds.
- MOT characterisation (Appendices ii and iii).
- Investigation of a second molasses cycle (Dr. Rhode's thesis).

These experiments represent sequential steps towards a better understanding of red-detuned atom guiding. Two methods of coupling atoms from a MOT into a guide have been practiced; LVIS overlap and MOT free-fall. By merit of its cooler atoms, the latter has been established as the preferred technique for higher output coupling and for more efficient distance guiding. Importantly, Gaussian guides for atom guiding have been investigated in both far-off and near-resonance detunings. Atom flux response in the steady-state and transient regime has been reported. The possibility of using a Gaussian guide in a pulsed mode to enhance guided atom flux levels has been suggested.

Experiments in the Drum trap have provided an effective demonstration of red-detuned guiding. The effects of guide detuning and power on guided flux levels are now well understood. Specific characteristics of red-detuned guide beams such as an initial radiation pressure surge following guide turn-on and the subsequent viscous heating are also well understood.

Baseline figures have been determined for the ideal intensity and detuning of a red detuned Gaussian guide operating in the high radiation-pressure regime; $\sim 7\text{-}8\text{MW/m}^2$. Similarly figures have been noted for the region of increased spontaneous heating (to be avoided); $\sim 5\text{-}5\text{MW/m}^2$ at 10Ghz (and progressively higher detunings as

the intensity increases). Finally, a detuning of $\sim 50\text{GHz}$ is indicated as the threshold for elimination of radiation-pressure effects in a guide beam of 8.8MW/m^2 intensity (430mW in the 0.25mm diameter beam). This is expected to scale with the root of the intensity.

A study of threshold detunings at which radiation pressure diminishes below levels suitable for guiding has been suggested as a worthwhile future experiment, along with experiments to confirm the fall-off rate of radiation pressure at fixed guide intensity over low detunings.

The factors affecting scattering rate and dipole potential are now better understood. Thus the red-detuned-guide experiments have provided important preparatory foundations for atom to fibre coupling experiments.

5.4 Bibliography

-
- ¹ D. P. Rhodes, Doctoral thesis, “*Experimental Studies of Cold Atom Guiding Using Hollow Light Beams*”, Feb, 2005.
- ² J. G. Livesey, D. P. Rhodes, D. McGloin, K. Dholakia, “*Transient response of a cold atomic beam in the presence of a far-off resonance light guide*”, J. Mod. Opt., Vol. 50, #11, p1751, (2002).
- ³ L. Pruvost, D. Marescaux, O. Houde, H. T. Duong, “*Guiding and cooling of cold atoms in a dipole guide*,” Opt. Commun. #166, p199, (1999).
- ⁴ K. Szymaniec, H. J. Davies, C. S. Adams, “*An atomic fountain guided by a far-off resonance laser beam*”, Europhys. Lett., #45, p450, (1999).
- ⁵ H. J. Davies, C. S. Adams, “*Transferring laser-cooled atoms to a spatially separated magnetic trap using a far-off resonance optical guide*“, J. Phys. B, #33, p4079, (2000).
- ⁶ O. Houde, D. Kadio, L. Pruvost, “*Cold Atom Beam Splitter Realized with Two Crossing Dipole Guides*”, Phys. Rev. Lett., #85, p5543, (2000).
- ⁷ Z. T. Lu, K. L. Corwin, M. J. Renn, M. H. Anderson, E. A. Cornell, C. E. Wieman, “*Low-Velocity Intense Source of Atoms from a Magneto-optical Trap*,” Phys. Rev. Lett. #77, p3331, (1994).
- ⁸ D. P. Rhodes, J. G. Livesey, G. P. T. Lancaster, J. Arlt, K. Dholakia, “*All optical guiding and splitting of a cold atomic beam*”, Conference paper, QELS '02. Technical Digest, p90, (2002).
- ⁹ D. Muller, E. Cornell, D. Z. Anderson, E. R. I. Abraham, “*Guiding Laser Cooled Atoms in Hollow-Core Fibres*”, Phys. Rev. A. #61, 033411-1, (2000)
- ¹⁰ JILA is a joint institute of the National Institute of Standards and Technology and the University of Colorado.
- ¹¹ M. J. Renn, A. A. Zozulya, E. A. Donley, E. A. Cornell, and D. Z. Anderson, “*Optical-dipole-Force Fiber Guiding and Heating of Atoms*”, Phys. Rev. A, Vol. 55, #5, p3684, (1996).

Chapter 6

Experimental Fibre Characterisation

Introduction

The ultimate goal of this thesis was to successfully couple atoms into and through, a hollow core photonic crystal fibre in a red-detuned guiding regime. This meant a hollow core (HC) fibre with high optical transmission through its core had to be found. To the author's knowledge no atom guiding experiments have yet been performed in photonic crystal fibre (PCF), however a few have been successfully carried out in capillary fibres^{1,2,3,4,5,6}. These all used relatively large hollow-core diameters on the order of a few tens of micrometers, and guided over lengths ranging from ~2cm to 23cm (with the majority closer to 3cm). Thus the HC diameter of a competitive PCF should be narrow enough to demonstrate superior optical transmission (sufficient to support atomic guidance) while remaining broad enough to allow laser coupling with far-field optics. Similarly this transmission should be maintained over a length comparable, if not greater than, that demonstrated by capillary fibres. This chapter discusses the work performed in search of a suitable fibre.

A multitude of hollow-core fibres from Bath University, UK were analysed. These were often revealed to be capillary and not PCFs. My intention was to find PCF providing the lowest attenuation of 780nm laser light within its HC. True photonic bandgap properties were searched for in order to circumvent the extremely high attenuation of narrow core capillary fibres.

Within the first 3 years of my PhD an ideal fibre was unavailable. However a quasi-PCF was found which offered the possibility of atom guiding, thus a fibre trap vacuum system was built and guiding attempts were made. Fibre analysis continued in parallel with free-space and fibre-guide experiments. Ultimately, a suitable PCF was identified and entered into a new fibre trap. The results of all guiding experiments are discussed in chapter 7. A lack of data raised questions regarding the resolution of

our optical detection methods and prompted a continued search for more efficient fibres.

In this chapter relevant fibre parameters will be described along with a brief description of the procedure for analysing fibres received from Bath University. Transmission efficiency of fibres will be compared while various parameters are altered, namely length, structure and input numerical aperture (NA).

6.1 Important Fibre Parameters

The ideal situation for a fibre guide is 100% throughput of any light coupled into its core. In regular high-index-core fibre light is naturally maintained in the core encouraging high throughput efficiencies approaching ~96% transmission over 1km. However, hollow-core fibre suffers extraordinary loss of light from the core out through its walls. This worsens as the core narrows, thus, maintaining high intensities within a hollow core requires specific tailoring of the surrounding structure.

For reference, the conventional method of particle guidance within a capillary hollow core involves evanescent leakage of blue-detuned light inwards to deflect atoms from the fibre walls (described in chapter 1). This type of guiding was not attempted here since light frequencies supported within the hollow core would, by nature of the PCF, be rapidly expelled from the surrounding crystalline structure. Thus any blue-detuned evanescent field would be rapidly suppressed and propagating atoms would be exposed to Van der Waals forces.

Fibres analysed herein can be classed as either, quasi-photonic crystal fibres (Q-PCF) or proper photonic crystal fibres (PCF). The key feature of all of these is an ability to reduce the prohibitive optical attenuation of narrow core fibres. They do this through use of a crystalline structure of silica and air surrounding their hollow-core. They attempt to maintain high intensities in their core in one of two ways; for Q-PCF the crystal structure in the core-surrounding layer brings a reduction in refractive index which provides relatively weak optical confinement based upon regular index guiding. In PCF a full 2D photonic bandgap acts to trap light transversely, confining it

with a near 100% efficiency, eliminating all loss mechanisms except those associated with initial coupling into the fibre.

Optical Transmission

A benefit of the crystalline structure of both Q-PCF and PCF is the increase in optical throughput relative to hollow capillary fibre. Even the weakly confining Q-PCF offers an order of magnitude more throughput than that of capillary fibre especially in narrow cores. This can be evidenced in a simplified form of equation 2.9 where the attenuation length of capillary fibre is seen to be dependent on core diameter $2a$, and wavelength λ ;

$$l_{1/e} \approx \frac{2.4a^3}{\lambda^2} \quad 6.1$$

where $l_{1/e}$ is the propagation length at which light in the hollow core of a capillary fibre falls to $1/e$ of its input value. Thus a $12.5\mu\text{m}$ diameter capillary would inflict a $1/e$ drop in guiding potential in under 0.5mm propagation (at 780nm light), which translates as under 0.25% transmission after 2.4cm fibre length. Conversely a 2.4cm segment of Q-PCF at St Andrews, entitled “POS-6”, had a more narrow $11\mu\text{m}$ core diameter which provided $\sim 50\%$ transmission. Furthermore, a $12.5\mu\text{m}$ core diameter PCF entitled “BG19-800” was observed to transmit 70% irrespective of length; coupling loss was the only source of attenuation. These figures show that PCF has the potential to perform well as an atom guide purely through vastly improved optical throughput.

A key area of research in fibre fabrication is the specific design necessary for efficient confinement, however in this research I was limited to the fibre structures provided by Bath. Though this was in fact a large number of different structures, only the latest fibre, “PG19-800” offered full bandgap operation at 780nm . The majority of fibres analysed demonstrated a Kagome lattice structure⁷. This is a mechanically strong triangular lattice which forms from the drawing of close packed capillaries in

the pre-form. The photonic crystal fibres demonstrated the most ordered Kagome form, whereas the Q-PCF segments all demonstrated slightly skew, distorted versions.

It is not clear whether better ordering or changes in air-filling factor (ratio of air to silica in the crystal structure) were responsible for the improved transmission of photonic bandgap (PBG) fibres. The air filling factor is key for quasi-PCF guiding, however creation of a PBG is dependent on a multitude of parameters: lattice spacing, number of unit cells between core and surrounds, air-filling, structure design, defect state diameter, to name only a few.

Core power transmission was the most important parameter when judging a fibre's eligibility for trap entry. Thus guide light was launched into the core of each fibre structure and the power output recorded. This was measured against two factors; the fibre length and the NA of the input light. The former was important only for fibres not exhibiting full bandgap properties (since a functional bandgap implied a negligible power loss over practical laboratory measurable distances). The latter, dictated the diameter of the TEM_{00} beam input to the fibre-coupling lens, (discussed in section 6.2).

Core mode-matching while testing fibres was hindered by the need to mimic the trap environment; a glass partition and numerous optics lay between the guide launch lens and fibre facet when the full vacuum trap was built. Thus ~38mm was stipulated as the minimum lens-apex to fibre-facet separation to ensure practical, usable, fibre analysis results. This prevented use of microscope objectives for simple fibre coupling, instead far-field anti-reflection convex lenses were used.

In total 36 different fibres were tested, of these 10 were revealed to be basic capillary fibres, 32 were Q-PCF and 4 were PCF. All were tested a minimum of 3 times each (up to 25 times for promising fibres). When long reels of fibre were received tests were performed on segments from multiple positions along its length so as to ensure localised manufacturing defects did not give false transmission figures. Two fibres demonstrated acceptable support of 780nm light.

Transmission measurements were intended to be taken over similar fibre lengths for all fibres. However as upcoming vacuum trap designs changed, fibres were cut to match requirements of these traps. An initial design predicted experiments involving 2.4cm fibre segments, this trap did not come to fruition. Later traps set a 15cm fibre length standard, which was finally shortened to 6.7cm for the latest fibre-trap incarnation. This was not ideal for later fibre comparison, nevertheless a good impression of transmission was gleaned for each.

Summary

Red-detuned guiding was selected due to expected difficulties in coupling blue-detuned light through the crystal structure, and importantly, to take advantage of PCF's main benefit; its low loss. PCF guidance could eliminate the severe attenuation drawback of previous red-detuned capillary guides. The important parameters under experimental control were the fibre's length, the guide light input NA and the spot size of the input beam. Transmission figures were captured for varying fibre structures, varying input NA and in some cases varying fibre length.

6.2 Transmission Measurement

This section details the optical arrangement and results of transmission tests of selected hollow core fibres at 780nm wavelengths.

In order to mimic later in-trap conditions fibres were mounted on a fixed platform while a launch lens (typ. $f=35\text{mm}$) and microscope objective ($\times 50$ long working distance (LWD) objective) were positioned at either end on Newport XYZ translation stages. A rudimentary beam splitter was used to split the output transmitted light and allow simultaneous viewing and power measurement, on a Pulnix PE2015 CCD camera and Newport 840c power meter, respectively.

The spacing between the fibre end facet and launching optics was also matched to that necessary within the trap (for all trap components to fit between). In this way problems associated with guide laser coupling and output analysis could be

identified before isolation within a vacuum system. Figure 6.1 schematically illustrates the optics arrangement for fibre transmission experiments.

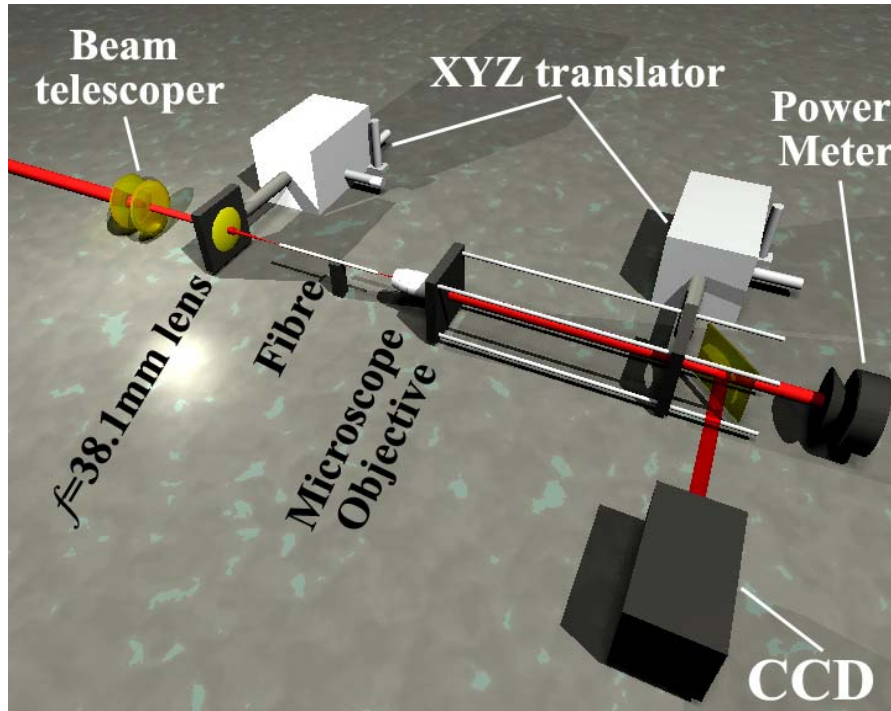


Figure 6.1 : Stripped down schematic of the optics and fibre mount used for coupling guide light into the fibre. The yellow optics are, from left to right, 2 collimating convex lenses (varied throughout to provide a typically $\sim 3.5\text{mm}$ diameter guide beam), the $f=38.1\text{mm}$ launch lens mounted on an XYZ translator, and a glass slide used to sample $\sim 6\%$ of the fibre output. The microscope objective was typically $\times 50$ strength. (Note, an extra fibre support-aperture is not shown here, this was used to minimise fibre vibration and reduce extraneous light hitting the detector).

Laser light was provided by the Titanium Sapphire guide beam tuned $\sim 2\text{GHz}$ from Rb^{85} resonance. This was expanded to 1mm diameter for input to a fibre launch lens.

Many fibres arrived in our laboratory with no identifying labels or literature, thus for ease of identification at the time, a few fibres were labelled using arbitrary symbols, (eg. Δ , \mathbb{C} , Ψ , \star). On arrival fibres were cleaved to provide a clean facet for input/output coupling. An image of one of these is shown in Figure 6.2.

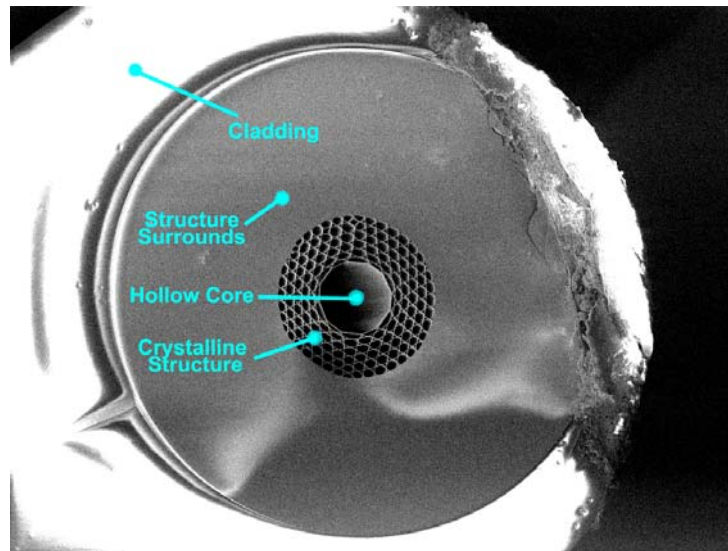


Figure 6.2 : A scanning electron microscope (SEM) image of an end facet of a Q-PCF entitled “Blue4”. The hollow core is $28\mu\text{m}$ in diameter. The structure is based on a Kagome pattern. The surface can be seen to fragment on the upper right hand side, this is attributed to stress fractures occurring while bending to cleave the fibre. The broad cladding can be identified by the saturated white, out-of-focus border; it is further receded from view due to it being stripped back $\sim 1\text{cm}$ from the end of the fibre.

Guide-Beam and Fibre-Core Modes

Mode mismatch between guide and core-supported modes was capable of severely reducing coupling efficiency. This could easily override other loss mechanisms such as improper NA or non-collinearity of guide and fibre if unnoticed. To prevent this, guide waists presented to the fibre core were arranged to be 92% that of the core diameter. This was the typical width of the fundamental mode supported within the core; a figure provided by Bath university which proved accurate in experiments. Too large an input spot led to light impacting on the surface of the fibre and being lost to the silica, too small a mode often implied an excessive input NA and hence loss of light through the silica again (despite successfully entering the core).

Fibre Numerical Aperture

It was important to identify the characteristic input numerical aperture (NA) of a fibre for two reasons, firstly to establish efficient optical coupling and secondly to help predict the output path of atomic flux. This was achieved by launching a Helium

Neon (HeNe) laser into the fibre exit facet (retro-launching). Its visible 633nm wavelength allowed its path to be traced and thus its rate of expansion to be measured on exit from the fibre. Despite the disparity between HeNe and guide light wavelengths, an approximate input NA for the guide light could be calculated, and thus, a desirable input beam diameter to the launch lens set accordingly. During atom guiding experiments the NA would give an indication of guide dipole potential persisting between fibre and probe region. This would have a confining effect on flux divergence, albeit a rapidly diminishing one.

The retro-fired HeNe laser proved to be the superior method for guide alignment; two apertures positioned sufficiently far upstream (in the guide beam path) permitted accurate matching of input guide to output HeNe.

After many fibres had been tested it was found that most NA and spot size requirements could be met with a standard AR coated, convex, $f=38.1\text{mm}$ launch lens with a few standby lenses for the beam telescope, (rare exceptions benefited from a longer $f=50.2\text{mm}$ or $f=62.9\text{mm}$ launch lens). The launch lens was mounted on a Newport XYZ translation stage to aid coupling adjustment. Typically, beams input to this were collimated at $\sim 3.5\text{mm}$ diameter, with a $\pm 1\text{mm}$ variation for better mode matching.

6.3 Fibre Transmission Results

6.3.1 Transmission Efficiency

The purpose of all fibre analysis reported herein was to identify fibres suitable for atom guiding experiments. Capillaries, when identified, were dropped in favour of structured fibres hence they are not included here. Many fibres with poor transmission efficiencies were also dropped after their optimum throughput was attained, these too, are not included here. An arbitrary naming regime was applied to many of the fibres received; this was forced by a lack of data available on each. The table below contains

information on the best-transmitting fibres analysed throughout this thesis, all figures are quoted at optimum coupling condition specific to each fibre;

Fibre ID	Core Diameter (μm)	Length (cm)	Best Transmission
“BG19-800” (PCF)	12 μm	15cm	66.9% / -1.7dB
“Blaze 800” (PCF)	9.2 μm (short axis), 9.5 μm (long axis)	15cm	39% / -4dB
“SMF28-FC-5” (Q-PCF)	15 μm	6cm	21%
“ Δ ” (Q-PCF)	9 μm	2.4cm, 4cm, 15cm	59.8%, 30.1%, 8.7%
“Blue 4” (Q-PCF)	28 μm	4.8cm – 15cm	34% - 4.8%
“Pos6” (Q-PCF)	11 μm	2.4cm - 15cm	54% - 8%
“8 μm ” (Q-PCF)	8 μm	15cm	5.6%
“22 μm ” (Q-PCF)	22 μm	15cm	5.2%
“ \star ” (Q-PCF)	11 μm	2.3cm – 14.5cm	65.5% -3.6%
“ \diamond ” (Q-PCF)	10 μm	3.9cm	46.6%
“ \hookleftarrow ” (Q-PCF)	10 μm	4.2cm	32.9%
“Pos5” (Q-PCF)	12 μm	2.3cm	46.9%

Figure 6.3 : Transmission figures, coupling optics and fibre statistics for fibres deemed most suitable for guiding atoms within. Ranked from top to bottom, best to worst. Transmission percentages are given under optimum coupling conditions. Note, throughput is also given in dB for the length independent PCF. Insufficient data was captured with the Q-PCF to allow separation of coupling loss from other length dependant mechanisms, hence there are no figures in dBm.

NA and Core Diameter Relationship

In general a counter intuitive relationship between NA and core diameter existed, that is, as the core expanded, a greater dependence on input light collinearity was observed. A slightly oblique launch angle or large solid-angle (of input light to the core), reduced transmission through broad cores more so than in narrower cores. However the less stringent NA requirements of narrow core fibre was easily overridden by moderate mode mismatch between the achievable input beam waist and the supported core mode. An input spot with $\pm 3\mu\text{m}$ mismatch between it and the core-mode diameter resulted in a $\sim 30\%$ transmission drop, dropping exponentially after the $\pm 3\mu\text{m}$ mark. For input spots smaller than the core-mode this loss came from an NA restriction, for spots larger than the core mode the loss was due to sharp break-up of the input wave-front between the core and crystalline structure.

PCF Loss Mechanism

As expected the primary source of optical loss in fibres demonstrating a PBG was the coupling process. It is believed the imposition of a minimum 38mm separation between fibre entrance facet and launch lens prevented near 100% transmission through the “BG19-800” and “Blaze-800” fibres. Successive shortening of these fibres showed \sim constant transmission efficiencies, thus indicating photonic bandgap properties. Figure 6.4 illustrates transmission efficiency through various lengths of BG19-800 PCF.

Q-PCF also confirmed its predicted decrease in throughput with increasing length; this is shown, in the table-summary above, through comparison between the $\sim 2.4\text{cm}$, $\sim 4\text{cm}$ and 15cm fibre lengths, (cut at these lengths for expected upcoming trap dimensions). A graph of this data is not included due to the sporadic fibre lengths used; as upcoming traps were designed newly arrived fibres were tested with lengths dictated by these designs and thus little consistency existed between successive fibre tests. This is regrettable, nevertheless the fibres of choice, the PCF, were fully tested.

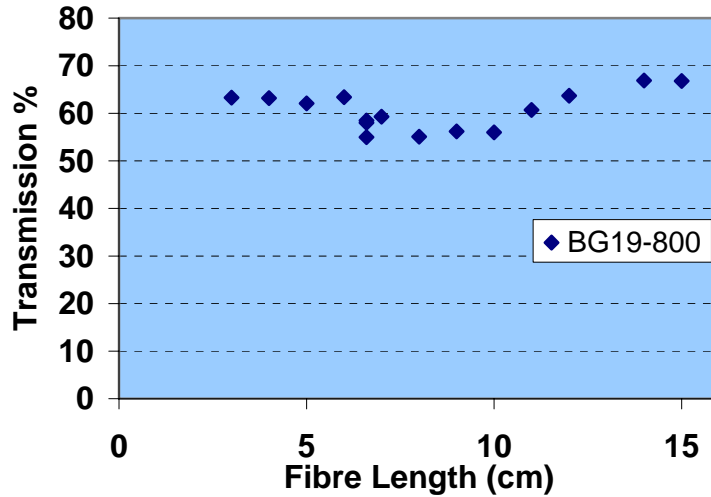


Figure 6.4 : Transmission efficiency plotted against fibre length for PCF entitled “BG19-800”. Note the near constant transmission irrespective of fibre length. The dip in the centre is attributed to varying coupling quality, (ie. launch collinearity and cleave quality) ; it is not believed to be due to any PBG effects.

Polarisation Maintenance

A fibre’s ability to maintain a linear polarisation state was measured. A linearly polarised laser source was coupled into the hollow core. A Polaroid, linear polariser sheet, was inserted between the microscope and power meter in the detection arrangement shown in Figure 6.1 (polariser not shown). This was rotated while the power output from the fibre core (only) was measured.

It was found that a linearly polarised Gaussian coupled into a PCF segment was partially rotated such that, after 15cm transit, $6\% \pm 2\%$ was retarded 90° into the orthogonal axis, producing a slightly elliptical beam. However a 15cm Q-PCF segment maintained polarisation state to a lesser degree; $26\% \pm 2\%$ retarded into the orthogonal axis producing quite an elliptical polarisation.

Mode Profiles

As a possible alternative to Gaussian guiding, a Laguerre Gaussian (LG) beam was launched into the hollow cores of the “BG19-800” and “Blaze-800” fibres in the

hope that the LG intensity profile would be maintained during transit. If so, it would offer the possibility of even tighter atom confinement in a blue-detuned light-pipe, itself confined by the allowable modal area of the hollow-core. This mode compression could help bring fibre atom transport a step closer to single-atomic-mode operation^{2,8}. In this state the atom flux path is compressed such that adjacent cold atoms are held closer to each other, thus it is easier for their de Broglie wavelengths to overlap and so begin coherent interaction.

However, the LG mode was not supported within their cores. A large drop in optical transmission was seen and the input LG profile was converted into a messy approximation of a Gaussian profile. As discussed in chapter 1, input profiles are transported in LP fibre modes and generally reform into Gaussians on exit; it is believed LG modes do not convert well into LP modes and LG profiles are not natural progressions on output.

6.4 Fibres Selected for Atom Guiding

Fibres “Blue 4”, “Blaze 800” and “BG19-800” were chosen for trap use. They were used in this order in successive fibre traps; the “Pyramid trap”, the “QWP trap” and the “Cross trap”, respectively. In terms of transmission and fibre core diameter (initially chosen broad to increase atom flux capture), each fibre was the best available at time of use; the PCF fibres were not available till the last year of my tenure.

6.5 Conclusion

A simple system for simultaneously monitoring the spatial output profile and the power output from the hollow-core of crystal fibres has been constructed and used to record data from 36 different fibres. Over 200 separate segments of fibre have been cleaved, mounted and measured.

A series of quasi-photonic and photonic crystal fibres have been compared for their ability to transmit 780nm light in a trap environment, where they are held at least

38mm from the coupling lens. Ideal parameters for a Gaussian beam incident on a 38.1mm lens have been established for the efficient coupling into the hollow cores of these fibres.

The most suitable fibre for atom guiding experiments is labelled “BG19-800”. Consistent transmission efficiencies up to 66.9% through its 12 μ m diameter hollow core have been recorded for all lengths measured (up to 15cm). Greater throughput, up to ~75%, has been observed when coupling with a super-long working distance microscope objective, however the 30mm working distance and broad barrel of this lens make it impractical for fibre-guide trap environments. At time of publishing BG19-800 remains the best candidate for guiding experiments.

6.6 Bibliography

-
- ¹ M.J. Renn, D. Montgomery, O. Vdovin, D.Z. Anderson, C.E. Wieman and E.A. Cornell, “Laser-Guided Atoms in Hollow-Core Optical Fibers”, *Phys. Rev. Lett.*, Vol. 75, #18, p3253.
 - ² M.J. Renn, E.A. Donley, E.A. Cornell, C.E. Wieman, D.Z. Anderson, “Evanescent-wave guiding of atoms in hollow optical fibers”, *Phys. Rev. A*, Vol. 53, #2, p53, (1996).
 - ³ D. Muller, E. Cornell, D.Z. Anderson, E.R.I. Abraham, “Guiding Laser Cooled Atoms in Hollow-Core Fibres”, *Phys. Rev. A*. #61, 033411-1, (2000).
 - ⁴ H. Ito, K. Sakaki, M. Ohtsu, W. Jhe, “Evanescent-light guiding of atoms through hollow optical fiber for optically controlled atomic deposition”, *Applied Physics Letters*, Vol. 70, # 19, pp. 2496-2498, (1997).
 - ⁵ B.T. Wolschrijn, R.A. Cornelussen, R.J.C. Spreeuw and H.B. van Linden van den Heuvell, “Guiding of cold atoms by a red-detuned laser beam of moderate power”, *New Journal of Physics* vol. 4, #69 p1–10, (2002).
 - ⁶ R G Dall, M D Hoogerland, K G H Baldwin and S J Buckman, “Guiding of metastable helium atoms through hollow optical fibres”, *J. Opt. B: Quantum Semiclass. Opt.* #1, p396-401, (1999).
 - ⁷ F. Couny, F. Benabid, and P. S. Light, “Large-pitch kagome-structured hollow-core photonic crystal fiber”, *Opt. Lett.* 31, 3574-3576, (2006).
 - ⁸ Z. Wang, M.Dai, J. Yin, “Atomic (or molecular) guiding using a blue-detuned doughnut mode in a hollow metallic waveguide”, *Optics Express*, Vol. 13, #21, p8406, (2005).

Chapter 7

Experimental Fibre Guiding of Atoms

Introduction

The aim of this chapter is to detail the experiments performed to observe atom guiding in “holey” photonic crystal fibre (PCF). This air-core *photonic band gap* fibre makes feasible for the first time practical and enhanced atom guiding using red detuned light over long distances (potentially metres) within flexible light pipes. Atom guiding has already been discussed in chapter 2 and the experiments performed in the red detuned regime shown in chapter 5. In published work researchers have predominantly worked in the blue detuned regime due to atoms propagating in low light regions but primarily due to the fact that red detuned guide light decays away rapidly (see equation 2.9) within hollow core fibres.

The use of holey PCF fibre permits atom guiding in the red detuned regime, far-off resonance over very long lengths without the attenuation associated with standard glass capillaries. These techniques are of considerable interest, in a world-wide context, for atom lithography and atom-optics component development: atom guiding in fibres offers an important route for building atom interferometers.

This chapter details the first steps towards hollow core red-detuned guidance and explains all the experimental steps with the aim of guiding cold atom ensembles, cold atomic beams and standard atomic vapour. At the outset we state that the attempts to guide have to date been unsuccessful but this is attributed to the detection scheme we have employed. Details will be given of a new hot wire detection scheme that analogously with previous studies of atom guiding will permit us very low atomic number detection. We have already developed this system and trials are currently ongoing.

In essence we deal with the development of three sources of atoms positioned above a holey fibre: a MOT, an LVIS beam and atomic vapour and discuss experiments on each in turn and the effectiveness of the guide. In particular we concentrate on the optical detection scheme and considerations for its deployment.

7.1 Guide Details

We use a Ti-Sapphire laser at 780nm with a linewidth of 500MHz which could be tuned 0-200GHz but not fully continuously over this range as discussed in chapter 3. Smooth tuning over a 12GHz band was easily achievable. For the majority of guiding attempts this band was chosen to start on-resonance. Occasionally this was shifted to tune from 10GHz to 22GHz and further, from 20GHz to 32GHz, red of resonance. However guide calibration was difficult to maintain at such detunings, so the bulk of work was performed over a regular 1 to 12GHz detuning. Tuning jumps of 200GHz were achieved with an intra-cavity birefringent filter and were occasionally applied to remove atom heating in transit.

Guide powers and detunings were chosen to sufficiently confine transverse momentum and reduce spontaneous emission of propagating atoms. As a general starting point an intensity of 54.57MW/m^2 propagating in the a 6.6cm long hollow-core, with a 6GHz red-detuning, was estimated as the threshold where confining dipole potential overcame heating from spontaneous emission. This level was generally achieved with around 10mW beam input to the coupling lens.

Figure 7.1 illustrates a simplified experimental setup for a fibre-trap. The vacuum system and input beams are shown (the hyperfine beam would be split to enter with the cooling beams, or would enter in a slightly diverging beam in on any one of the arms. The guide beam was telescoped and coupled into the fibre from an $f=38.1\text{mm}$ lens mounted external to the vacuum system (on a Newport XYZ translator), this is not shown in Figure 7.1 as its mount would completely obscure the MOT chamber.

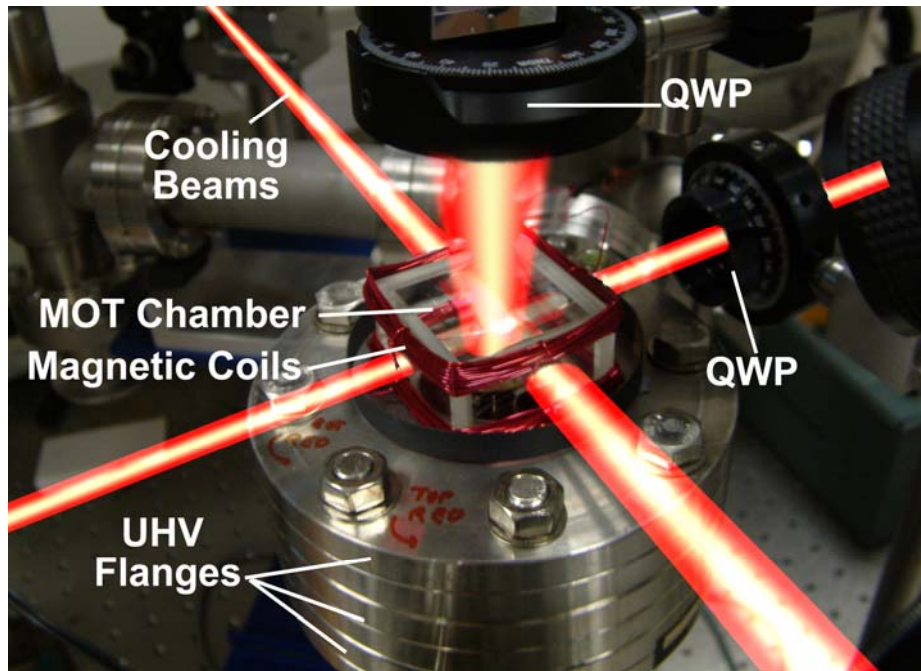


Figure 7.1 : The 2nd QWP trap with cooling beams superimposed. The MOT magnetic coils are shown wrapped around the MOT chamber. Note, a key omission here is the guide coupling lens, this would be positioned between the MOT chamber and the upper QWP mount, it was removed for this picture.

Throughout all fibre-guiding experiments guide light coupling into the fibre's hollow-core was paramount, so guide-beam waist was located at fibre entrance, and any MOT beams and magnetic fields were arranged around this to ensure the atomic source was located in the guide path. Efficient coupling into 12 μ m-28 μ m diameter hollow cores with minimal power loss from scatter and coupling was difficult to arrange. It was extremely sensitive to fibre collinearity and numerical aperture matching. Even weak thermal lensing of optical components was sufficient to completely inhibit coupling.

Individual atom guiding attempts were performed in one of three ways, 1. with a continuous guide of fixed power and detuning, (incrementally increased for successive attempts), 2. with a 'flashed' guide of fixed power and detuning, 3. with a continuous fixed-power and slowly increasing detuning (typically from 1GHz to 12GHz red). Each power and detuning setting was applied \sim 15 times in order to average-out background noise.

Dipole Potential Along the Flux Path

Unlike free-space guide beams, the intensity, and hence dipole potential, of fibre-guide light, does not vary smoothly along the entire atom flux path. In a fibre guide an atom will experience a dipole-potential, with a steep gradient on approach to the fibre, a discontinuous drop ($\sim 30\text{-}50\%$) upon fibre coupling, and power attenuation within the fibre (see figure Figure 7.2). Such variation of confining potential forces consideration of which stage to optimise for efficient atom throughput. Experiments herein employed multiple guide intensities in attempts to optimise each stage, ultimately intensities capable of exceeding the required potential depth at all stages simultaneously were applied.

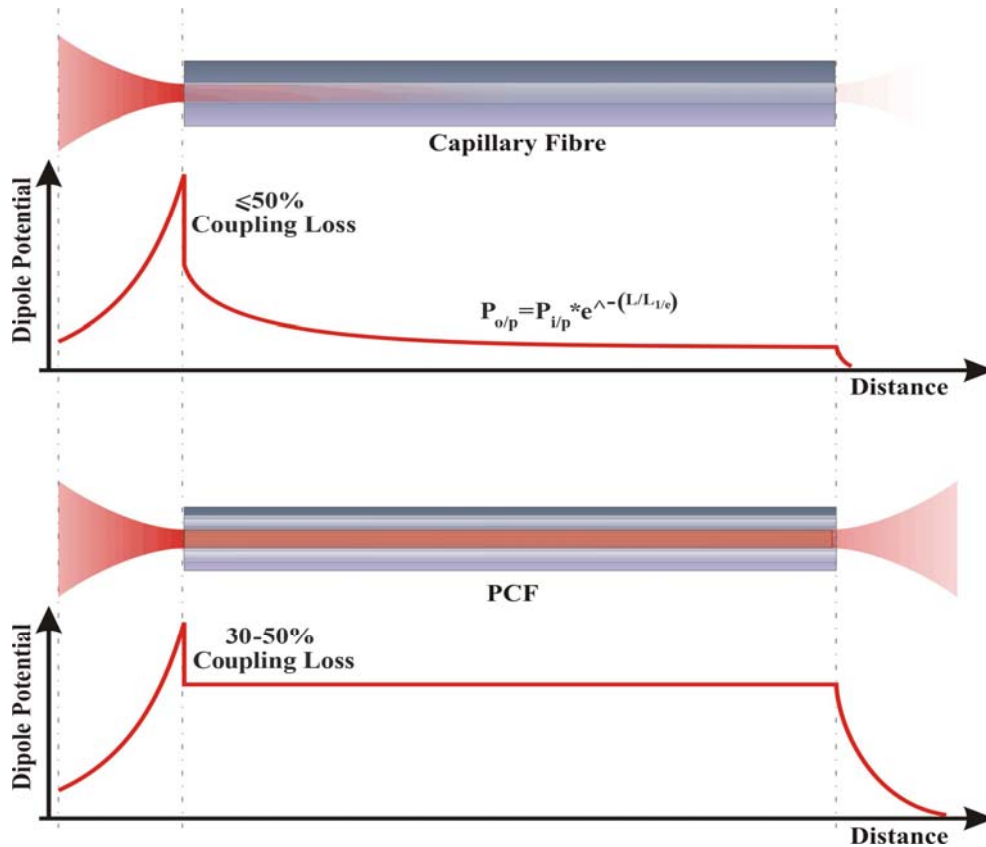


Figure 7.2 : Schematics depicting a capillary fibre (or Q-PCF) and a PCF. Beneath each an approximate depiction of the dipole-potential experienced at the coupling, core-propagating and emission stages. The curves here are not calculated nor experimental, they are intended to give a *relative* understanding of the power-loss profiles of each of the 3 separate regions worthy consideration when selecting input guide power, (However the coupling loss values are experimental values). Image courtesy of Dr.D. Rhodes.

It was expected a $\sim 3\text{mm}$ diameter guide of 10mW power, 6GHz red-detuning would yield a potential depth of 0.127mK at a position 6mm above beam waist/fibre entrance. This would be able to capture atoms released from a MOT cloud with transverse velocities up to 19.3cms^{-1} (average atom velocity in a $\sim 100\mu\text{K}$ MOT is $\sim 13\text{cms}^{-1}$). On entry to a $12\mu\text{m}$ fibre hollow core, the guide suffers coupling loss (50%) but is now tightly focused, so its potential depth improves to 175mK in a beam of $\sim 10.8\mu\text{m}$ full width (this is the mode diameter supported in a $12\mu\text{m}$ hollow-core). Once within the fibre, the guide was expected to be able to confine atoms with transverse velocities up to 7ms^{-1} .

The earliest fibre guiding trap built in St Andrews used a quasi-PCF segment and hence suffered $\sim 70\%$ guide attenuation over its length. However later builds incorporated photonic crystal fibres in which minimal power loss occurred along their length, hence guiding potential remained approximately constant.

7.2 Atom Flux Detection System

This section will discuss aspects pertinent to the fluorescence detection system used in the fibre traps. Points raised here are in addition to those previously considered in chapter 3 and 4. Further description of each specific probe arrangement is included in the later, trap specific sections.

A fluorescence-probe detection system was used in all fibre-guiding experiments. Fluorescence detection was used instead of absorption probing to ensure the highest detection sensitivity; a photomultiplier tube (PMT) and phase sensitive detector (PSD) were combined to provide as much sensitivity as possible.

Fluorescence-Probe Beam Arrangement

An extended cavity diode laser (ECDL), described in chapter 3, provided a probe beam of intensity $I \approx 5I_{\text{sat}}$ ($I_{\text{sat}} = 1.6\text{mW}/\text{cm}^2$). This was tuned to the $5S_{1/2}F=3 \rightarrow 5P_{3/2}F'=4$ cooling transition of Rb^{85} for use in the majority of fibre-guiding experiments. It was collimated, directed under the fibre (through the flux

path) and retro-reflected through a quarter-wave plate (QWP). Care was taken to keep the probe normal to the surfaces of the detection cube so as to prevent stray reflections interacting with falling atoms before the main probe beam.

Probe centre was positioned 2.2mm beneath the fibre exit aperture. This allowed it to fit under the fibre without clipping the fibre end; probe light striking the fibre may enter and drive atoms into the fibre walls prior to fibre exit. Following a lack of data the probe was raised closer to the fibre in attempts to improve atom interception.

The spatial profile of the probe beam was varied between experiments. The desire to bring the centre of the beam closer to the fibre exit-aperture motivated an elliptical probe ‘sheet’ profile, oriented flat on the horizontal plane with dimensions 4mm×1mm. Fears of unbalanced angular momentum components between the input and retro-reflected arms of this probe returned the probe to a circular collimated Gaussian profile of ~4.3mm diameter.

Photomultiplier Tube Arrangement

The same detection system as described in chapter 3.6.1 (and shown in figure 3.21) was used for fluorescence detection in the fibre-guiding experiments. In brief, fluorescence was detected through use of a, Hamamatsu, H7710-03, Photomultiplier tube (PMT) and phase sensitive detector (PSD). As shown in figure 3.21, an iris and $2f$ optic system provided a 1:1 imaging ratio of the probe region onto the PMT. The optics system consisted of a cage plate assembly with an $f=38.1\text{mm}$ lens mounted at one end, $2f$ away from the atom flux. An iris was mounted on the other side of the lens and positioned $2f$ from it. The PMT was mounted just far enough from the iris to allow signal light to efficiently fill the PMT’s sensor surface. Thus the iris diameter defined the volume of probe region visible in the PMT’s field of view (FoV) (shown in Figure 7.3). The PMT and its optics assembly were shrouded in an opaque cover and mounted on a Newport XYZ micro-translator. Probe laser light was tuned to the $5S_{1/2}F=3 \rightarrow 5P_{3/2}F'=4$ cooling transition of Rb⁸⁵.

The detector position was fine tuned through use of a CCD camera temporarily mounted in place of the PMT on its optics assembly. When the CCD chip was positioned exactly where the PMT's sensor would sit, we were able to see what the PMT 'sees' beneath the fibre. Once aligned perfectly with the fibre it was lowered vertically to view the centre of the probe beam immediately below the fibre. The aperture in the $2f$ system was essential for removing a large amount of background noise light. Figure 7.3 a), b) and c) give an impression of the amount of light that required filtering out. In particular guide-light leaked from the fibre walls and scattered from the end facet causing spurious noise.

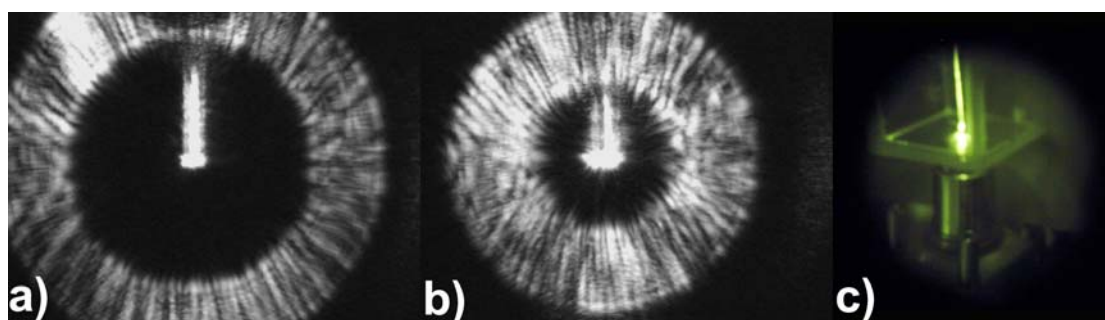


Figure 7.3 : **a)** The view available to the PMT with the noise-reducing aperture closed to its smallest diameter of 1mm, **b)** with the aperture opened to ~ 1.5 mm. The PMT is lowered to remove the fibre from view before experiments commence. **c)** a photograph taken through an IR viewer, showing detection-chamber glass cube with a fibre hanging within, (this was an early trap design; later traps had supports to prevent the fibre swaying). The fibre is glowing as there is guide light coupled into it. The analysing microscope objective can be seen beneath the glass cube.

An aperture, and thus FoV, of 1mm diameter (minimum aperture diameter) was used throughout the majority of detection attempts. This was increased only in later experiments within the Cross Trap where an increase in noise was tolerated in order to increase the visible probe region area; a maximum of 3mm diameter was reached before complete saturation of detection equipment occurred.

An extra $f=38.1$ mm curved mirror was installed coaxially with the collecting lens on the opposite side of the detection cube. It faced towards the PMT and was precisely $2f$ away from the probe region. Hence it functioned as a signal capture lens, doubling the detected signal level by refocusing its collected fluorescence back through the detection cube, beneath the fibre and into the PMT optics stack.

Noise

The primary noise source in the detection chamber was scattered guide light. All other light could be suppressed by shielding the trap, by tuning the PSD system or by tweaking the probe alignment. Despite the chopped probe, the detected signal increased to saturation when the guide was incident on the fibre. This was attributed to, 1. the large amplitude of the guide light and 2. vibration of the suspended fibre end. The guide amplitude forced adjustment of both PMT and PSD gain settings away from those appropriate to fluorescing atoms in a probe field, thus perceived background noise level was increased. Despite mounting the entire trap on Sorbithane pads, the hanging fibre suffered pendulum like oscillations induced by vibrations transmitted through the superstructure of the UHV system. The oscillations were weakly damped by the fibre's tensility and, in later trap designs, by surrounding surfaces. They caused guide-scatter to fluctuate at matching frequencies and created signal amplitudes up to 10 times the regular signal level. Figure 7.4 demonstrates typical noise levels seen in raw captured signals.

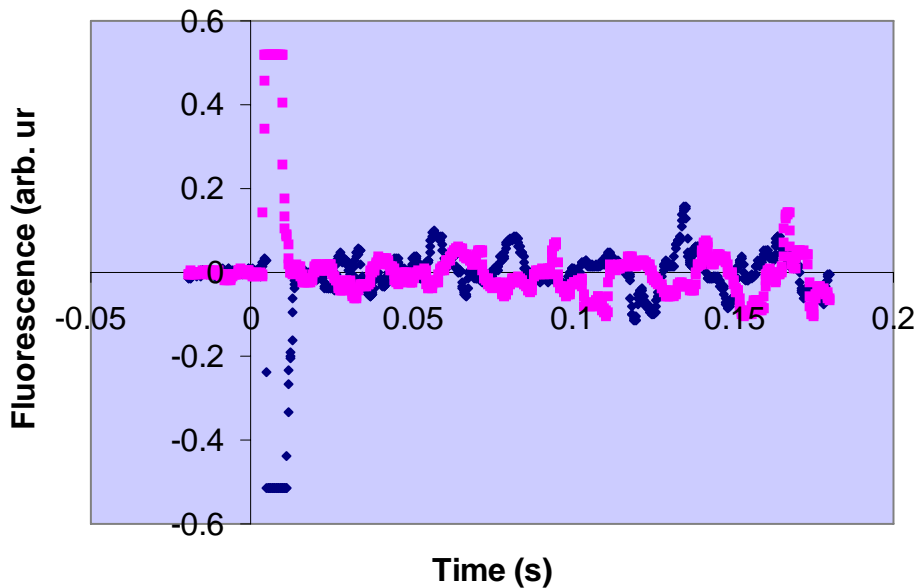


Figure 7.4 : Two sets of raw fluorescence-probe data captured using a 10mW guide beam detuned 10GHz red from resonance. Oscillations building in magnitude from left to right are seen in both, these are fairly calm examples indicating no serious vibrations at this time (readings obscured by vibration were typically not recorded). The large spike just after the origin, marks the appearance of guide light. Note how flat the signal is prior to guide appearance. The spike saturated the PSD in arbitrary polarity. However setting a fast time constant on the PSD (10 μ s) allowed rapid suppression of the initial noise spike. Noise from fibre vibration was in addition to this.

The narrow, convoluted path between MOT chamber and detection chamber is expected to have prevented almost all Rb diffusion into the detection chamber. Hence noise fluorescence from background Rb vapour was mostly discounted in the detection cube. Furthermore, the narrow-linewidth of the extended cavity diode laser used for the probe, implied a significant fluorescence contrast between thermal vapour and guided cold atoms (due to the order of magnitude greater Doppler broadening of vapour atoms).

Flux Divergence

It is acknowledged that an atom flux will diverge on exit from a fibre, intuitively the divergence rate will increase with narrowing core diameter. The guide beam will also diverge on exit, following the fibre's characteristic NA. Similarly, it was feared that slight intensity disparity between the input and retro-reflected probe beams (due to Fresnel reflections and mirror inefficiency) may push falling atoms out of the PMT field of view thus reducing available fluorescence.

Throughout the course of experiments, probe positions beneath the fibre were positioned progressively closer until there was no possibility of atom divergence outwith the probe region, similarly the PMT field of view was widened sufficiently to encompass all possible flux paths.

Estimates of flux divergence based on transverse velocities of atoms on the limit of guidance, and estimates of the atom push from probe disparity were made. However these were both deemed to contribute very little to our experimental work, and so will not be discussed here.

7.3 Atom Fibre-Guiding Experiments

In the following sections multiple trap designs are discussed for their ability to support an atomic source in close proximity to a hollow-fibre. Techniques used to develop cold atomic sources and position them in close proximity to the fibre are outlined. The methods used in attempts to optically guide atoms into and through the

fibres are made. These methods build on those previously used to guide in free-space beams, differences arising from the need to focus into the fibre core are illuminated.

Fibre guidance was attempted with Rb atoms of 3 different velocity groups, these were; room temperature vapour, LVIS atoms and dropped-MOT atoms. Hence guide beams were required with sufficient dipole potential to confine transverse atom velocities of $\sim 300\text{ms}^{-1}$, $\sim 2\text{ms}^{-1}$ and $\sim 17\text{cms}^{-1}$, respectively.

Each fibre-guiding trap was designed and assembled by the author and was labelled by its main mirror design; 1. the Pyramid trap, 2. the mirrored, apertured, quarter-wave plate (QWP) trap and 3. the Cross trap, (see Figure 7.5) All additional electronics required for control of acousto-optic modulators and rapid shutter switching were also designed and built by the author, (with the help and advice of Mark Ross, and Jim Park of St Andrews Physics Dept.).

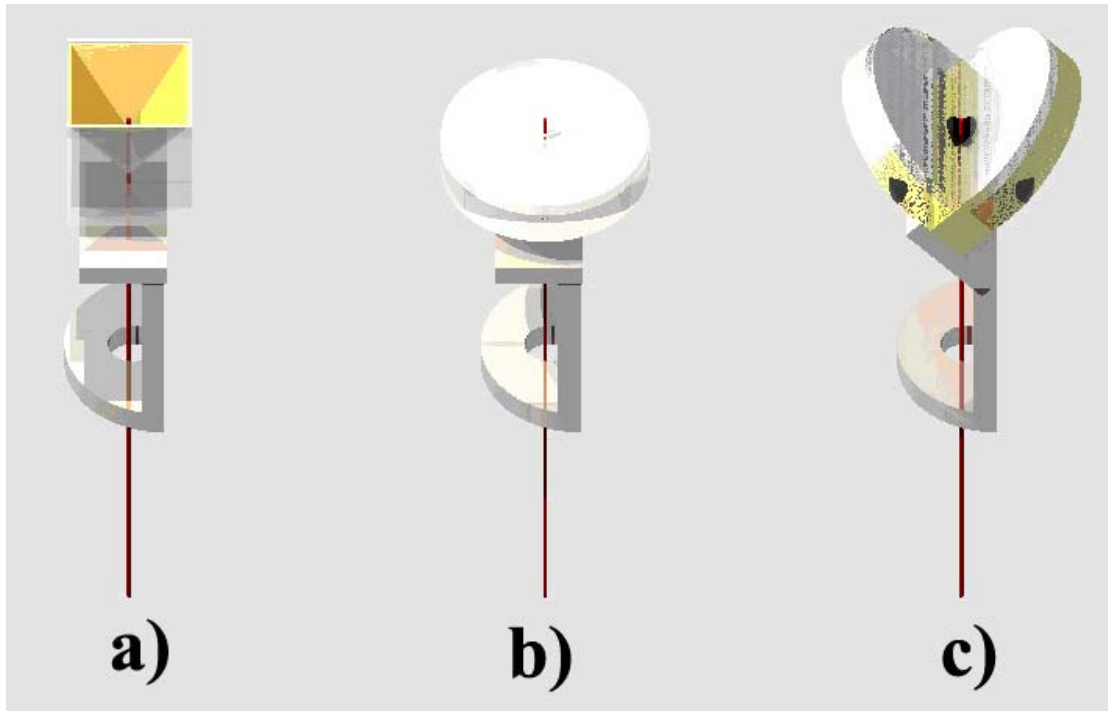


Figure 7.5 : The fundamental differences between each fibre-guiding trap lay in the main MOT mirror sections at the heart of each. **a)** the pyramid trap, **b)** the QWP trap and **c)** the Cross trap. Figure courtesy of Dr.D.Gherardie.

7.3.1 Thermal-Vapour Guiding

Vapour guiding required a lower number of beams input to the vacuum chamber (no cooling or re-pump) and so was simpler to realise. Similar to early experiments by Renn *et al.*¹ the guide beam was the only optical input required in the atom-loading chamber. The atoms in vapour-guiding experiments had higher velocities relative to cold-atoms and so had a greater chance of escaping an optical potential. However, the simplicity of construction encouraged performance of this experiment as part of the build-up towards cold-atom guidance experiments. The lack of magnetic coils and cooling/hyperfine optics freed up space around the trap, affording more flexibility for positioning of analysis cameras and probe optics.

An intermediary step between vapour guiding and cold-atom guiding was attempted in some circumstances where formation of a cold cloud was prohibited by trap physicalities. In this situation, coils and horizontal beams were aligned and tuned to provide an “atom slower” region where it was hoped atoms would cool in two dimensions leaving residual velocity components only in the guide axis. It was hoped this would increase the likelihood of successful guidance relative to the more energetic vapour guiding.

The Pyramid Trap

As the first fibre-guiding trap built, the Pyramid trap served as an elimination process for the more simplistic guiding and detection methods.

The intended MOT region of this trap can be thought of as a cube from which a pyramid shaped volume has been excavated, (see Figure 7.6). The inner facing surfaces were silvered to provide mirrors at 45° to the horizontal. A 1mm wide square aperture passed through the centre of the cube from the apex to its underside. The aperture served to allow fibre entry but created a shadow in the retro-reflected cooling beam which completely enveloped the MOT region. Thus no cold cloud was visible, however it was hoped the atoms were slowed in the horizontal axes and so rendered more easily guidable.

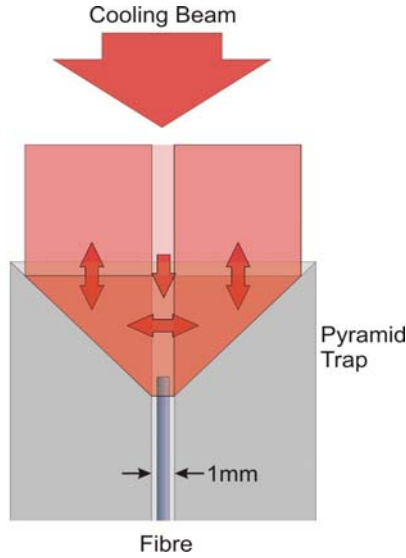


Figure 7.6 : A schematic of the intended trapping volume of the ‘Pyramid’ trap, shown side on. Thermal vapour, with a possible x-y axis cooling, was presented to the fibre. The guide beam was focused into the fibre collinear with the cooling beam. MOT cloud formation was also attempted by directing input cooling light at an oblique angle to the fibre axis; however the LVIS shadow was too broad to permit any MOT formation. Figure courtesy of Dr. D.Rhodes.

The selected fibre was 15cm long and labelled “Blue4”. It had a hollow-core of $28\mu\text{m}$ diameter and did not employ proper PBG interference. It was a quasi-photonic crystal fibre (Q-PCF) with typical transmission efficiencies of $\leq 10\%$ at 15cm. This was the best transmission available at the time.

Equipment available at the time dictated use of Rb^{87} isotope. Trap geometry forced the guide beam to pass through a QWP prior to the coupling lens. The transmission efficiency of the fibre was independent of polarization, however atom guiding efficiency may have been reduced due to use of a circularly polarised guide. This represented an unknown variable which may have contributed to the lack of data.

In a first wave of experiments, guiding was attempted with Rb^{87} thermal-vapour using guide intensities of $162\text{MW}/\text{m}^2$ and $487\text{MW}/\text{m}^2$, input to the $28\mu\text{m}$ diameter hollow core (100mW and 300mW respectively). The guide was detuned 4GHz below the $5S_{1/2}F=2 \rightarrow 5P_{3/2}F'=3$ cooling transition. It was first applied in ‘flashes’ of a few seconds duration while the probe region was observed, then at a constant intensity of $162\text{MW}/\text{m}^2$ while the detuning was ramped from resonance to

~10GHz red. Prolonged higher intensity runs were not performed for fear of damaging the fibre.

Simple CCD observation was used as the detection method for these tentative, guiding attempts; a Pulnix, PE2015 NIR camera and commercial zoom lens provided a focused view of the fibre and fluorescence-probe region below. To eliminate the possibility of atoms being driven into the hollow-core walls by scattered on-resonance light leaking into the fibre, the probe beam was directed to completely avoid the fibre. It was centred 2mm beneath the exit facet and was shaped into a 4mm×1mm light ‘sheet’ by two cylindrical lenses of $f=160\text{mm}$ and $f=60\text{mm}$ focal lengths.

In a second wave of experiments, a phase sensitive detector (PSD) was used in conjunction with both fluorescence and absorption probing systems. Trapping fields were introduced and tuned to the $5S_{1/2}F=3 \rightarrow 5P_{3/2}F'=4$ cooling transition of the Rb^{85} isotope in the hope of slowing atoms and improving guided flux. The greater abundance of this isotope was also expected to increase flux volumes.

Pyramid Trap Summary

Guiding was attempted with thermal vapour and a possibly ‘transversely slowed’ source of atoms. Figure 7.7 lists the guide parameters attempted along with the corresponding fibre-guide transmission efficiencies.

It is acknowledged that CCD detection of fluorescing atoms was optimistic at best. Principle design flaws deemed to have been negative influences on atom guidance when using this trap were, its inability to support a cold cloud and poor transmission efficiency of the fibre. The following QWP trap was built with a better fibre to improve the transmission and a more simple internal MOT-mirror to facilitate MOT formation.

Guide Power	Detuning	Transmission
5mW (8.1MW/m ²)	4GHz	8.5%
10mW (16.2MW/m ²)	4GHz	6.5%
50mW (81MW/m ²)	4GHz	6%
100mW (162MW/m ²)	0-10GHz (ramp)	6.1%
100mW (162MW/m ²)	4,6,8,10, 12GHz	6.1%
200mW (324.7MW/m ²)	4GHz	6.4%

Figure 7.7 : Guide powers and detunings coupled into the “Blue 4” fibre within the pyramid trap. Transmission efficiency of light coupled into the 28 μ m diameter core is also shown. There is no figure for the 300mW transmission measurements as the fibre could only withstand brief flashes at this power before warping out of alignment.

7.3.2 Guiding From a LVIS

Creating a LVIS of atoms required a full atom-cooling opto-mechanical arrangement; 6-way cooling beams, hyperfine re-pump beam, guide and probe beams plus magnetic coils surrounded the trap. Theoretically a full MOT arrangement would produce a cold cloud which could be positioned above the fibre ready for guidance into the hollow core. However, the aperture in the cooling beam mirror, necessary for fibre protrusion, prevented formation of a perfect cold cloud; LVIS streams were formed instead. Resultant higher atom velocities raised many questions regarding the efficiency of atom coupling into both the guide beam and the fibre, particularly when perfect collinearity between guide and LVIS was not achieved.

Drawbacks included a general depletion of cloud volume due to continual LVIS outflux and importantly, a guide potential at MOT location less than at fibre entrance. The MOT region was forced millimetres away from the fibre in order to prevent it being engulfed in the LVIS shadow. Because the guide was tightly focused into the fibre core this distance held the MOT in a much lower dipole potential than at fibre entrance. At a typical distance of 6mm from the fibre facet the MOT would experience a dipole potential only 0.038% of that experienced at guide waist. Cloud heights closer to the fibre facet, where guide potential was greater, were desirable for fibre coupling efficiency. However, MOT proximity to the fibre facet was limited by the diameter of the LVIS shadow in the retro-reflected vertical cooling beam. With a LVIS aperture present, the cloud could not approach the fibre facet closer than 3mm without being engulfed within the LVIS shadow. Two techniques were applied to reduce the fibre-cloud separation (Figure 7.8).

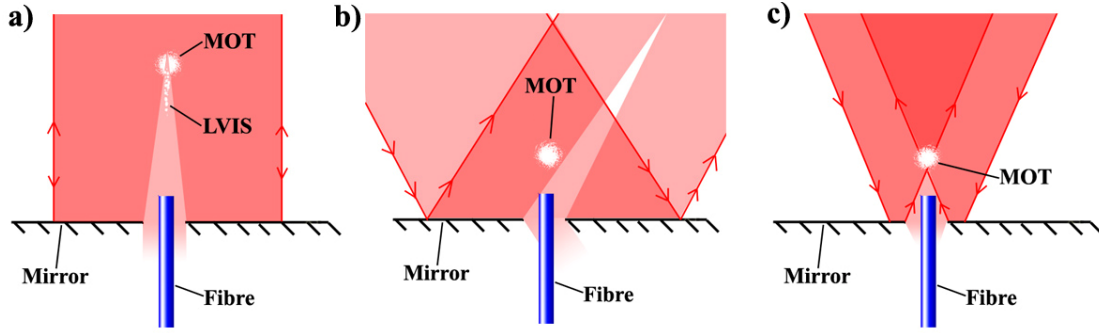


Figure 7.8 : Schematic images of cooling light (red) incident on an apertured mirror with a fibre protruding through it. In **a)** regular collimated cooling light is seen naturally diffractively filling the LVIS shadow. The diffraction rate dictates how close the MOT can be to the fibre. This image is not to scale, typically the 1mm diameter MOT in this configuration had a $\sim 0.8\text{mm}$ LVIS-hole through its centre. In **b)** angled cooling light is used to lower MOT height by deflecting the LVIS shadow (angles shown here are greatly exaggerated). In **c)** input cooling light is focused such that the LVIS shadow fills much sooner, again lowering the MOT height (angles are greatly exaggerated). Figures **b)** and **c)** are ideal cases, in practice the LVIS shadow never cleared the MOT region before cooling beam alterations distorted the cloud beyond use. Thus a ‘clean’ MOT was not achievable with near-vertical cooling light and the MOT height had a closest approach of 3mm to the fibre facet.

The above schemes were limited in effectiveness by 1. degradation of MOT quality and 2. tilting of the LVIS flux away from fibre collinearity. The latter ultimately dictated trap re-design without a LVIS flux. Filling the LVIS shadow region with cooling light retro-launched up through the fibre, was precluded by fears of excess spontaneous emission of atoms while in fibre transit.

An important drawback of LVIS-emitting MOT regions is the increased velocities involved. Atoms are emitted with approximately $V_{\text{longit}} = 14\text{ms}^{-1}$ and $V_{\text{trans}} = \sim 1.97\text{ms}^{-1}$ it was feared any disparity between LVIS path, fibre axis and guide beam axis would result in a loss of flux. Hence cooling beams were arranged collinear to the fibre; to align the LVIS path with the fibre (and so, the guide)

A good size match between guide diameter and MOT cloud was also desirable² for efficient atom capture into the guide. At 6mm from waist, the guide was typically $\sim 550\mu\text{m}$ in diameter; thus covering a significant portion of the $\sim 800\mu\text{m}$ diameter LVIS volume.

The QWP Trap

The quarter-wave plate (QWP) trap received its name from a modified QWP mounted as the MOT mirror within the MOT-chamber glass cube. A 1mm diameter aperture (in the centre) and a reflecting metallic coating (on one side) were affected in-house. The phase retarding upper face was exposed to the incident vertical cooling beam. Thus providing an 85% reflective mirror which returned a 90° phase shifted beam containing a shadow region ~1.3mm in diameter; an increased width due to tiny fractures surrounding the 1mm bore. The aperture was intended to facilitate fibre protrusion and generate a LVIS of atoms directed towards the fibre entrance. When illuminated with collimated light the shadow diffractively filled after a few centimetres.

The QWP trap had 2 incarnations prior to succession, both employing the same mirrored, apertured QWP, but with differences in fibre length and associated mount mechanics. The first build supported a 15cm segment of PCF entitled “Blaze800” fibre. This had a 9.2-9.5µm diameter hollow-core, and demonstrated ~40% transmission of input guide light. The second build supported a 6.7cm segment of the same “Blaze800” fibre. The move to a shorter fibre (and trap) length was intended to boost guided flux levels so as to yield a detectable level.

The general design can be seen in Figure 7.9 (showing the 1st QWP trap build) and Figure 7.10. It reused the home-made fibre/mirror mount from the Pyramid trap to hold the QWP. The cooling, hyperfine and guide laser sources remained unchanged, as did the choice of target Rb⁸⁵ isotope. The same magnetic field gradient of ~12Gcm⁻¹ was maintained (for both QWP traps).

Both trap builds were mounted on sorbithane sheets at all load bearing points to minimize fibre vibration (for cleaner probe signals). However complete removal of fibre vibration was not achieved.

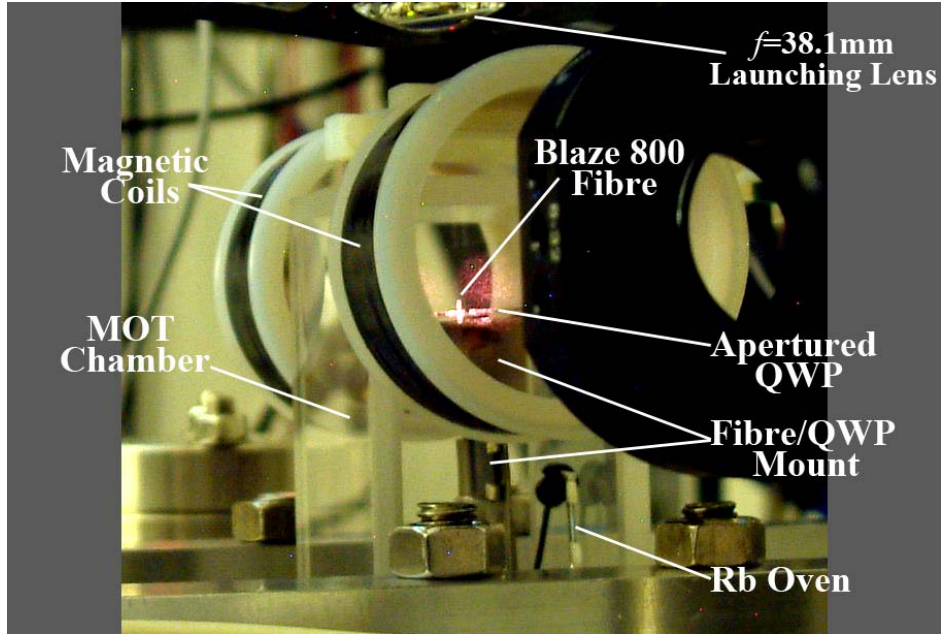


Figure 7.9 : A photograph of the 1st QWP trap. Later versions of this trap were identical save for shorter glass cube and fibre mount heights. The QWP itself is seen side on as a thin line in this picture. The tip of the fibre is seen protruding from the centre of the QWP, it is glowing in a deliberately misaligned hyperfine re-pump beam.

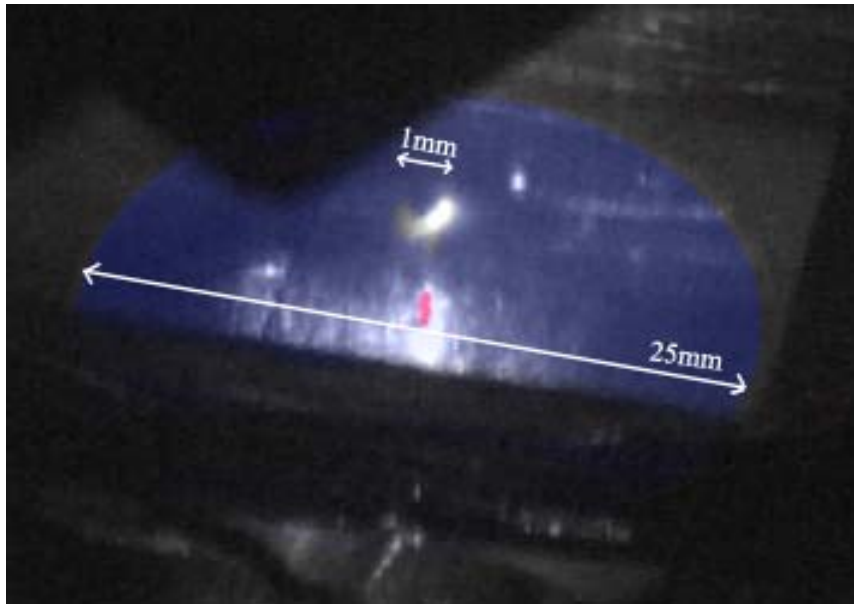


Figure 7.10 : Colour enhanced image looking down on the apertured QWP of the “QWP trap”. The near-tauroidal MOT region (white) can be seen above the protruding fibre (red) and the aperture. Feint LVIS emission can be seen directed towards the fibre. No guide was present for this image. The dark triangle encroaching on the top of the image is the mount for the coupling $f=38.1\text{mm}$ lens. The dark diagonal bar obscuring the lower third of the image is the opaque corner of the glass cube.

QWP Trap – 1st Build, Procedures

In the first incarnation of the QWP trap the lower trap cube suffered a build-up of grease on its inner surface during bake-out. It is believed this was a result of poor cleaning of a threaded bolt hole inside the vacuum system. The grease formed a fine layer of globules on the lower, inner glass-cube surface directly beneath the fibre. It obscured observation of the fibre and importantly, disrupted, visual confirmation of guide-fibre coupling. This may have played a significant role in preventing efficient guide coupling, since a large transmission difference exists between approximately similar looking output profiles.

Experiments in the first build were truncated due to the grease build-up. However guiding attempts were made in a similar fashion to those of the Pyramid trap. Care was taken to align the LVIS flux with the fibre and the guide beam. Powers up to 50mW were incident on the $f=38.1\text{mm}$ fibre launch lens. This power was the approximate maximum before fibre warping was observed. Multiple ‘flashed’ and ‘continuous’ guide exposures were performed, at fixed and ramped detunings (0-10GHz red).

QWP Trap - 2nd Build, Procedures

In the second QWP trap, guiding was attempted over the same range of guide-beam parameters as in the 1st QWP trap. Additionally detunings of 200Ghz were applied at powers of 0.1mW-50mW.

An unwanted curve was pressed into the fibre by a $\sim 1\text{mm}$ resettling of the QWP during the bake-out process. This curve occurred in the top few millimetres of fibre length and is estimated to have angled the entrance aperture by $\sim 3^\circ$ from its original axis (accurate measurement hampered by lack of access). Despite having no discernable effect on optical transmission levels it may have displaced the fundamental mode within its core closer towards the fibre walls. Higher velocity LVIS atoms may have been lost to the fibre walls here.

LVIS flux collinear to the fibre was still sought, so cooling beams were tilted to match the fibre tip. Similarly the guide launch lens was pivoted slightly to match the coupling angle. With these slight alterations, the MOT region was not noticeably diminished, however it is conceded that the MOT may have suffered a reduction in atom density.

Given the LVIS nature of the QWP-trap a perfect MOT-drop was impossible; dropped atoms would, at best, be detected in addition to the higher velocity atoms arriving at the probe a few tens of ms earlier. Nevertheless, in addition to guide ‘flashing’ and detuning-‘ramping’, (over 0.1mW-100mW, and 1GHz-10GHz red-detuning), ‘Cloud dropping’ was also attempted with remnants of the LVIS MOT. Doubts existed regarding the population remaining for MOT-dropping, however the aforementioned bend in the fibre raised concerns regarding loss of LVIS atoms in transit. Dropped cloud remnants provided colder atoms hence they were dropped in an identical manner to that of the free-space guiding experiments (see chapter 5), with the added condition of ensuring cloud-fibre-guide collinearity prior to each drop.

Design Limitations of the QWP Traps

Multiple scattered diffractions were seen from micro fractures surrounding the QWP aperture. These may have disrupted atom flux en route to the fibre core by generating obstructive modes around/within the fibre entrance. These were minimised by reducing the input cooling beam intensity from a peak of 45.8mWcm^{-2} per input beam, to just above I_{sat} intensity of 1.6mWcm^{-2} . MOT structure appeared unaffected, but its fluorescence, monitored through CCD cameras indicated an optimum cooling intensity of 16mWcm^{-2} (where it was set). Measurements were not performed to quantify cloud density

Hyperfine re-pump light was removed from the vertical cooling beam, to prevent it coupling into the fibre core. In the core it would increase the spontaneous emission rate (along with the cooling light propagating in the core; inherent in LVIS geometries). The hyperfine light was redirected to enter the trap in one arm only, its 1mW of hyperfine light was incident on the QWP MOT region redirected to enter solely through the horizontal arm. Furthermore, care was taken to prevent *any* cooling or hyperfine light in the horizontal plane interacting with the fibre.

The tall metal mount had no heat shield to block heat from the Rb oven. Proximity of the oven to the support ($<1\text{cm}$) and to the fibre ($\sim 1.5\text{cm}$) allowed radiative heating to warp the main mount causing slight displacement and tilt of the QWP mounted above. This completely uncoupled the $\sim 9\mu\text{m}$ diameter guide beam from the $9.2\text{-}9.5\mu\text{m}$ diameter core of the “Blaze 800” fibre. This warping was exacerbated by fibre heating from the input guide following warp-induced decoupling.

In the 2nd QWP trap the mount was shortened and the whole MOT-chamber was more congested, this incurred the worst warping (of mount and fibre) despite an interceding double layer heat shield. On top of this warping, thermal expansion of the QWP limited MOT lifetime for each trapping/guiding session to ~ 5 minutes. This heating is attributed to a combination of radiative and conductive heating from the Rb oven.

QWP Trap Summary

Guiding was attempted with LVIS atoms and, in part, with cold MOT atoms falling from the remnants of an LVIS MOT. Figure 7.11 lists the guide parameters applied. Fibre transmission remained constant throughout experiments thanks to the PBG nature of the “Blaze 800” fibre. However no atom flux was detected from the fibre.

Principle factors deemed to have been negative influences on optical guidance in the QWP trap were, an inability to support a ‘clean’ MOT, a long $\sim 6\text{mm} \pm 3\text{mm}$ MOT-to-fibre separation implying a weak guide at MOT centre, an accidental fibre bend, perpetual fibre warping (from guide and oven heating), warping of the main mount and thermal expansion of the QWP limiting trap lifetime.

The fluorescence probe system used here was the best available with equipment present at the time. A discussion on the most likely reason for a lack of detected atom flux is given in section 7.4

Guide Power	Guide Intensity	Detuning	Transmission
0.1mW-50mW	$132.5\text{W/cm}^2 - 66.3\text{kW/cm}^2$	8GHz	39%
8.5mW	11.3kW/cm^2	0-8GHz	39%
5-85mW	6.63kW/cm^2	8GHz	39%
85mW	11.3kW/cm^2	0-8GHz	39%
8.5mW	11.3kW/cm^2	8-10GHz	39%
3.7mW, 3.8mW, 6mW, 10mW, 12mW, 15mW, 20mW, 30mW, 37mW, 50mW	$4.9\text{kW/cm}^2 - 66.3\text{kW/cm}^2$	200GHz + 400GHz	38%

Figure 7.11 : Guide powers and detunings coupled into the “Blaze 800” fibre within the QWP trap. All powers are measured just before fibre entry prior to the 60% coupling-loss. All detunings are red of resonance, (negative). Transmission efficiency through the 9.2-9.5 μm diameter core is also shown, this remained constant due to its PBG nature.

7.3.3 Guiding from a MOT

A trap without an aperture in its cooling beams, would have no LVIS outflow and consequently suffer none of the related difficulties. Cloud proximity could be lowered almost arbitrarily close to the fibre entrance. Dropped MOT guiding could be used; this would make use of the coldest temperatures available and so maximise guide efficiency.

The Cross Trap

The cross trap benefited from the experience gained from all previous trap designs. The primary design goals were to provide a ‘clean’ MOT region with no LVIS outflow draining the MOT, easily arranged collinearity between cloud, guide and fibre, and the ability to bring the MOT region within 1mm of the fibre aperture. This was achieved with the mirror and QWP assembly shown schematically in Figure 7.12. A magnetic field gradient of $\sim 12\text{Gcm}^{-1}$ was set, similar to previous traps.

The Cross trap, was the latest trap to have hosted fibre-guiding experiments at St Andrews (pending the upcoming ‘Hotwire’ trap). It did not suffer from obligatory LVIS outflux and so cold clouds of Rb^{85} atoms could be repeatedly dropped into guide beams for channelling into waiting hollow core fibres. Diagonal cooling beams allowed a MOT-fibre closest approach of 0.5mm which allowed a dipole potential of $\sim 5.3\%$ of that at fibre entrance, though still small, this is 2 orders of magnitude greater than that 6mm from the fibre (as in QWP trap).

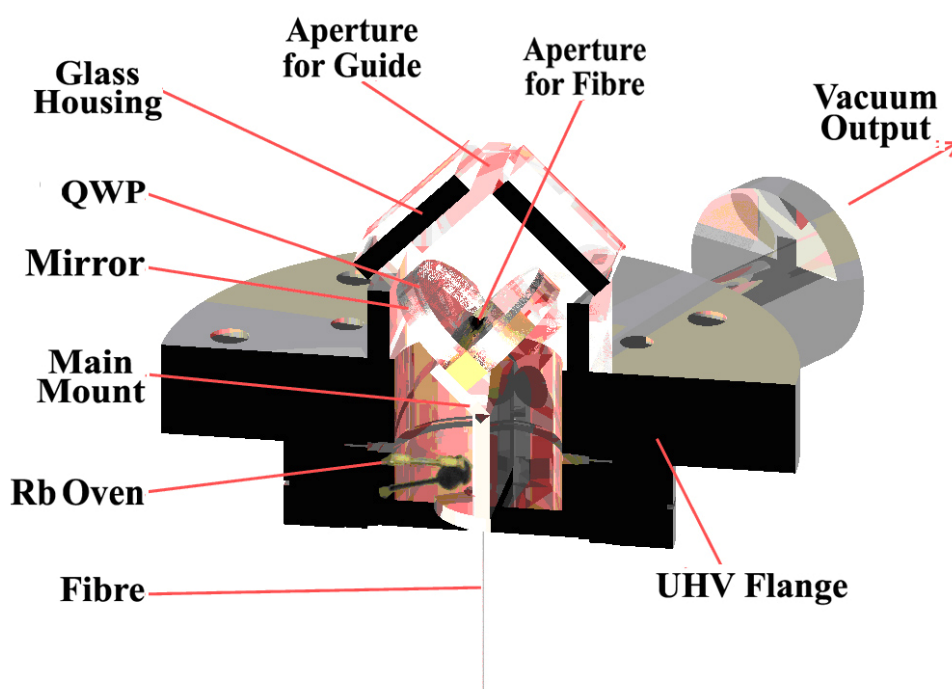


Figure 7.12 : A schematic of the Cross Trap. Missing from the image is the electrical wiring for the Rb oven, the 2 heat shields sandwiched between the oven and main mount and the 2 copper fibre-grips screwed to the brass bar (shown in yellow). The brass bar held the mirror and QWP segments, this had a 1mm hole drilled diagonally through it to accommodate the fibre. It also had 2 tapped holes for attaching the fibre-grips. The mirrors and QWPs were mounted at 90° to each other. The MOT chamber looks spacious here, this was not the case. Image courtesy of Dr. D.Gherardie.

The advantages of *near*-fibre launching are deemed of greater importance than cloud-guide size ratio, hence attempts to re-locate the MOT into a broader guide (further from fibre entrance) were not made.

A Beryllium alloy heat shield protected the fibre and mirror assembly from radiative heating from the Rb oven, which was in close proximity ($\sim 5\text{mm}$ from the

central mount, ~1cm from the mirror assembly). The central mount supported the mirror assembly and a 6.6cm length of Blaze-Photonics “FB_BG19_800nm”. This fibre had a hollow core diameter of 12 μ m and a 780nm transmission efficiency routinely passing 60%; the best achieved in this thesis (with the stipulated $f=38.1$ mm coupling lens). The 30% core diameter increase relative to the previous “Blaze_800” fibre was expected to improve the likelihood of atom guiding.

This trap configuration had further positive aspects; no fibre bend, no fogging of the lower trap cube, no trapping beams directly incident on the fibre, thus no resonant light within the fibre to heat or push atoms from the guide. The guide and cooling beams no longer shared launch optics so arranging efficient coupling and good MOT quality was a relatively trivial process.

Some negative aspects were unavoidable with the current equipment, these included, a lack of solid brace for the 1cm of fibre protruding into the lower trap cube, conductive heating of the QWPs (which suffered thermal expansion after only ~4 minutes of oven operation), and the resolution limit of the now customary optical detection system.

Nevertheless all negative aspects were not preclusive of possible guided flux detection; the QWPs allowed 3 or 4 data runs before thermal expansion depleted the MOT, the fibre vibration was minimised by using a short fibre, sorbithane padding and by working when less people were present in the building. The detection resolution (at the time) was still deemed sufficient for flux detection, and was improved further by tweaks described below.

The collimated 4.3mm diameter probe beam set at $10 \times I_{\text{sat}}$ and tuned to the $5S_{1/2}F = 3 \rightarrow 5P_{3/2}F' = 4$, cooling transition, had, for the first time, a further 5.3mWcm⁻² of hyperfine ($5S_{1/2}F = 2 \rightarrow 5P_{3/2}F' = 3$) light included; this was expected to provide a fractional increase in detectable flux as it recycled atoms which had fallen out of the cooling cycle back into resonance with the fluorescence probe.

A lack of data encouraged a progressive dilation of the PMT aperture, thus the PMT field of view expanded from 1mm to 3mm. However, the benefit of increased

probe coverage was mostly counteracted by the necessary PMT gain reduction following increased noise bleed through the aperture. The PSD time constant, τ_{psd} , and associated chopper frequency, f_{chop} were augmented to increase temporal resolution of the probe system; settling on 10 μ s and 200Hz, respectively. A wider bandwidth was covered and the duration of each noise spike was noticeably shorter than in previous experiments, but it is debatable as to whether amplitude resolution was improved or not.

Procedure

Dropped MOT guiding was performed exclusively on this trap. Drop heights from 4mm down to 0.5mm above the fibre entrance were tried. The guide was incident 20 μ s prior to cooling-beam cut. Fluorescence was recorded over a 200ms time window, starting 20ms prior to cloud drop and extending 180ms after. Atoms stationary prior to cloud drop were expected to travel from MOT to probe region in ~120ms.

Guide Power	Guide Intensity	Detuning	Transmission
1.2mW, 5mW	9.5MWm ⁻² , 50MWm ⁻²	0-8GHz	57%
6mW	53MWm ⁻²	0-8GHz	57%
10mW	80MWm ⁻²	3, 4, 5.5, 6, 10, 12, 200GHz	57%
25mW	200MWm ⁻²	4, 10, 40, 200GHz	57%

Figure 7.13 : The parameters for dropped-MOT guiding performed in the Cross trap. Each condition was repeated ~10-20 times to obtain a clear average. Additional control runs (with all other noise sources present but guaranteed no-atoms) were performed every 4 runs.

Occasional fluorescence recordings extended the data window up to 450ms to allay fears of delayed atom passage. Dropped-cloud data runs were repeated on average ~17 times for each guide frequency and intensity level. Additional control runs using a vacant MOT region were performed approximately every 4 runs to provide a contrasting negative result and aid with noise subtraction when processing.

Dropped-MOT fluorescence was recorded for the guide beam parameters shown in Figure 7.13. These intensity figures are loosely consistent with those applied

by Renn *et al.* in their 40 μ m diameter fibre. The fibre length is also similar. However, the detection system is grossly dissimilar.

Cross Trap Summary

In terms of mechanical design and feature positioning the Cross trap was almost an ideal trap; optical access was optimal, the MOT-fibre separation was very small and the fibre-probe separation was similarly short. Nevertheless an atom flux from the fibre was not detected.

If the same configuration were to be maintained, better insulation between the Rb oven and trap flanges would be recommended. A damped brace for the fibre end and, of course, superior fibre transmission would be beneficial.

The only improvement to the optical probe system which the author can suggest, is to use an elliptical probe beam aligned with its major axis on the *vertical* plane. A ~6mm tall, 2mm wide beam, positioned directly under the exit facet (and retro-reflected), could be collected by a cylindrical lens (~38mm focal length in one axis only). Imaging a cylindrical fluorescence profile onto the PMT would allow more efficient filling of the rectangular PMT sensor, and more importantly, the increase in probe region would keep a greater number of atoms fluorescing simultaneously. Thus providing more fluorescence for detection at the loss of temporal resolution.

7.4 Fluorescence Probe Detection Efficiency

Each vacuum trap designed throughout atom guidance research at St Andrews has so far been prompted by a mechanical impediment discovered while experimenting. However the Cross trap revealed no obvious problems; all major impediments had been successively designed-out. Nevertheless there were no atoms detected. Hence our attention turned to the probing system and in particular the minimum fluorescence level it could detect. We began to doubt the sensitivity and noise suppression capabilities of an *optical* detection system. This prompted investigation into the minimal detectable flux rate of our probe and the flux we could optimistically expect through the fibre.

It is acknowledged that loss mechanisms such as spontaneous emission heating, viscous heating and collisions with background vapour will all serve to reduce guided flux numbers, but these have not been included in calculations here as their contribution cannot be properly calculated without first achieving a detectable flux.

Minimum Detectable Flux Level

In order to ascertain a minimum detectable flux level for the fluorescence probe and PMT, data from earlier red-detuned Gaussian guiding experiments in the Drum trap were used (experiments reported in chapter 5). Dropped cloud profiles captured at the furthest distance from the MOT (5cm) with no guide beam present, are taken as approximations to the lowest detectable flux level as these signals were barely discernable from the minimal noise levels present at the time. An ideal situation is assumed for these calculations; that is, all atoms exiting the fibre are caught within the PMT field of view and travel through it approximately vertically.

Figure 7.14 shows an average of the profiles used. Here the signal amplitude can be seen to be almost swamped within the background noise. Given the lack of guide beam and the signal averaging used, this noise level can be defined as the lowest possible level achievable in our trapping systems. The noise level in any trap was seen to increase by an order of magnitude when a guide was introduced. A fibre-guiding trap will have more noise in general due to the closer proximity of all surfaces, however calculations are made here for an ideal situation where the majority of noise is suppressed.

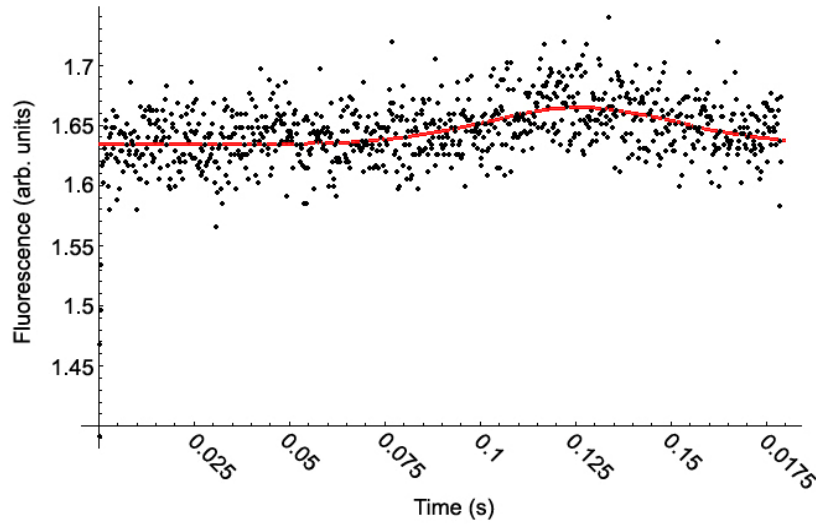


Figure 7.14 : Raw fluorescence data illuminating a dropped cloud incident on a probe beam 5cm distant. The cloud passes through the probe at $t=0.126\text{s}$. A Gaussian best fit is shown in red, this is almost engulfed in the background noise. Lower amplitude signals failed interpretation in our best-fit programs. The lack of guide beam implies this noise level represents the best achievable with a fluorescence probe arrangement in our UHV system. It was therefore deemed appropriate to use this averaged data to find a value for the lowest detectable flux level in the fluorescence detection system.

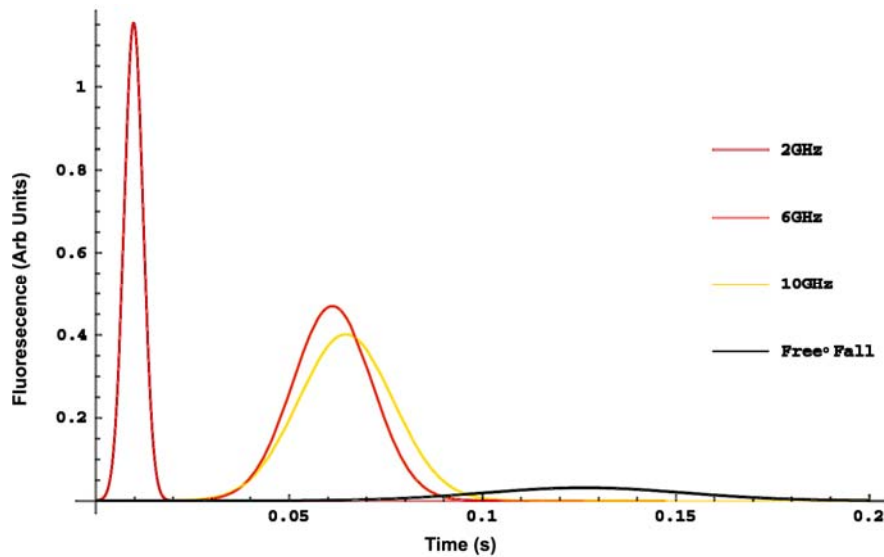


Figure 7.15 : A comparison between fluorescence signals captured 5cm beneath the cloud. The black “free-fall” line shown is the same dropped cloud data seen in Figure 7.14. Profiles are also shown for clouds exposed to 2, 6 and 10GHz red-detuned guide beams. These are best-fit profiles and have had their ground levels normalised to lie on the x-axis hence a depiction of the noise level cannot be gained; these are shown here only to convey the relative size of guided and free-falling signals.

Figure 7.15 demonstrates the relative amplitudes of detected signals in the red-detuned Gaussian guiding experiments. The “free-fall” signal shown is the same best-fit profile shown in Figure 7.14. This is shown to emphasize the near-undetectable level of the “free-fall” data used for the minimum detectable signal approximation. Signals beneath this average level were not recognisable in our Gaussian fitting software.

In the above dropped-cloud data, a short time increment (0.01s) at peak flux is taken as the time over which to average the collected fluorescence. Knowing the peak recorded number-of-photons collected by the PMT at this point, and the characteristic scatter rate in the known probe intensity, and finally the scaling factors to account for visible solid-angle and PMT gain, yields a near-direct calculation of $3.8 \times 10^5 \text{s}^{-1}$ for the minimal detected flux rate in the Drum trap probe system.

However the probe systems in the *fibre-guiding* traps are based on an $f=38.1\text{mm}$ collection lens in a $2f$ system, (c.f. an $f=75\text{mm}$ lens). Also, the Drum trap fluorescence-capture lens was positioned 100mm from the probe region, (not the standard $2f$ arrangement). This implies a reduction of the minimum detectable level by a factor of 17.2. Further still, the curved mirror positioned on the opposite side of the fibre-trap detection cube served to double the amount of fluorescence collected in the fibre-guide detection system (assuming perfect efficiency). Thus an approximate **minimum detectable flux rate on the order of 10^7 atom/sec** is established for the fibre-guide fluorescence probe system. This assumes vertical atom motion through an intensity balanced retro-reflected probe beam, and holds only for dropped-MOT velocities (LVIS atoms will fluoresce a factor of 13 times less in a similar probe) .

This figure does not give a favourable outlook for our detection system when compared to that of Renn *et al.*³ (who recorded a peak flux rate of ~ 3250 atoms/sec in their red-detuned fibre-guide experiment with a guide of 50MW/m^2 intensity and a 6.2cm long fibre with a $40\mu\text{m}$ diameter hollow-core). This flux level implies successful detection in an optical system is unlikely. However, it is also likely a significant error margin exists in this minimum-flux figure, possibly a few orders of magnitude. Nevertheless it is conceded that successful optical detection is unlikely,

and more time should have been spent on this. The ongoing fibre-trap work, using a hotwire and channeltron detector, promises to eliminate this oversight.

Expected Flux Level

Given the similar intensities of optical and magnetic fields employed in both free-space-guiding and fibre-guiding traps, experimental values of MOT-volumes observed in the Drum trap will be used to provide a rough “ball-park” figure for expected atom density in the MOT-cloud of the fibre-guiding trap.

Thus assuming $\sim 2 \times 10^7$ atoms in the MOT cloud and an optimistic transfer of $\sim 10\%$ of the MOT volume into the incident guide, we can expect a maximum flux level of **$\sim 2 \times 10^6$ atoms per cloud-drop coupled into the guide beam**, (in the interest of finding a best-case number we will ignore LVIS sourced atoms). Approximating optical coupling loss into the fibre core, we shall assume a 50% loss of flux on fibre entrance. Finally if we assume 50% transmission loss along the fibre to account for spontaneous emission heating and any extraneous optical modes from fibre anisotropies or very-slightly skew coupling, **output flux total would be in the range of $\sim 5 \times 10^5$ atoms from a dropped MOT.**

Now to equate this output flux number to a detectable flux rate, we can look again at data collected in the free-space Gaussian guiding experiments (similar to those in Figure 7.15) and make another assumption. A dropped cloud, having already fallen through 5cm of a 2GHz detuned free-space guide beam, is seen to have a Gaussian velocity distribution with a FWHM width of ~ 10 ms. This is the result of acceleration from both gravity and radiation pressure. If we are staying with the best case situation where we are most likely to detect a guided flux we will also set our guide to a detuning of 2GHz. Our fibre guided cloud will travel 70.5mm from MOT to probe region (through the 6.6cm fibre). If we assume the acceleration will be approximately similar to that in the free-space regime then we can expect a figure of $\sim 500 \text{ms}^{-2}$, and a velocity distribution resulting in the entire cloud passing the 1cm diameter probe region within ~ 10 ms. However any given velocity set within the distribution will only spend ~ 1.2 ms in the probe region (due to acceleration from

guide and gravity). Thus the peak flux rate measured by the PMT within the 1.2ms of probe exposure is an evaluation of the peak of the ~ 10 ms Gaussian velocity distribution (given the known total number of atoms). **Ultimately this yields a fibre-output flux rate of $\sim 9 \times 10^5 \text{s}^{-1}$.** Unfortunately, even with all the best-case assumptions, **this is an order of magnitude less than that detectable by our optical probe system.**

It is acknowledged this is a very coarse series of approximations and errors are likely to vary the above flux rate by an order of magnitude; theoretically bringing the flux rate to within detectable range. Nevertheless the lack of data, combined with the disparity between minimum-detectable and expected flux rates prompted our move to an ion detection system, which is described in chapter 8.

7.5 Conclusion

Magneto-optic traps for the purpose of guiding atoms through hollow-fibres have been designed and constructed. Experimental design has been refined sufficiently to allow cold atom sources to be brought within 0.5mm of the entrance aperture of fibres protruding into the trapping volume. Attempts have been made to guide atoms into the narrow hollow-cores of these fibres, (9.3 μm , 12 μm and 28 μm diameter each). Thus far no positive data has been taken. However, this is primarily attributed to a lack of sensitivity in the detection system. It is the authors opinion that atom fibre-guiding has been performed, but not observed.

To summarise, activities performed and reported in this chapter include:

- **Design and construction of three fibre traps (plus one re-design/build).**
- **Manifest of cold atom sources in close proximity to fibre apertures.**
- **Progressive refinement of a fluorescence probe system.**
- **Identification and suppression of numerous mechanical hindrances to atom trapping and optical guidance within each trap.**

It is acknowledged that many flux-loss mechanisms have not been accounted for in calculations reported herein. In fact it is possible the spontaneous emission heating from our guide may even have been the largest source of atom heating.

However complete characterisation of fibre-guide loss mechanisms cannot be achieved until the first basic flux rate has been observed. This is expected to occur in the latest fibre trap currently in use St Andrews (described in Chapter 9).

The optical detection system used throughout this thesis is attributed as the primary reason why positive data has not been recorded. Thus, the best recommendation for the fibre-guide system described above would be one which is already being implemented in St Andrews; an ionising hotwire and channeltron detector combination. This is briefly outlined in chapter 8.

7.6 Bibliography

-
- ¹ M.J.Renn et al. JILA & University of Colorado Dept. of Physics, “Laser Guided Atoms in Hollow-Core Optical Fibres”, Physical Review A, Vol. 75, #18, p3253, (1995).
- ² B.T. Wolschrijn, R.A. Cornelussen, R.J.C. Spreeuw and H.B. van Linden van den Heuvell, “Guiding of cold atoms by a red-detuned laser beam of moderate power”, New Journal of Physics, Vol. 4, #69 p1, (2002).
- ³ M. J. Renn, A.A. Zozulya, E.A. Donley, E.A. Cornell, D.Z. Anderson, “Optical-dipole-force fibre guiding and heating of atoms”, Phys. Rev. A., vol.55, #5, p55, (1997).

Chapter 8

Thesis Conclusion

8.1 Summary of Activities

In the course of this thesis I have designed and built three free-space and three fibre-guiding atom traps from scratch. I have built and maintained laser sources for cooling and guiding of Rubidium atoms, and have developed electronic circuits for computer control of trap beam entry.

I have performed atom guiding experiments using free-space propagating beams in both red- and blue-detuned regimes. These are detailed in the following list;

- o Near-resonance red-detuned Gaussian guiding of dropped-MOT clouds (see chapter 5)
- o Far-off resonance Gaussian guiding of LVIS atoms in transient and steady state regimes (see chapter 5).
- o Collinear and oblique guiding of LVIS atoms in high-order Bessel and Laguerre-Gaussian beams (see appendices i and iv).
- o Oblique guiding of LVIS atoms in a punctured Laguerre-Gaussian guide (see appendix iv).
- o Comparison of high-order Bessel and Laguerre-Gaussian beams for dropped-MOT atom-guiding efficiency (see Dr Rhodes' thesis – available through St Andrews Physics dept. Optical Manipulation web site).
- o Comparison of different azimuthal index of spatial light modulator generated Laguerre-Gaussian beams for dropped-MOT guiding efficiency, (see Dr. Rhodes' thesis).
- o Initial investigation of a second molasses cycle on a MOT cooling cycle, (see Dr Rhodes' thesis).

In Gaussian free-space guiding experiments, typical guided ensembles of $\sim 10^6$ atoms ($\sim 10\%$ of total MOT volume) were recorded for guided dropped-MOTs. This number reduced to $\sim 10^5$ atoms for detunings greater than -2GHz , and for distances greater than 23mm .

I have characterised a series of hollow-core fibres for their transmission of 780nm guide light while under fibre-guide trap conditions. Cold atomic-beams and cold-atom clouds have been successfully positioned above the entrance apertures of hollow crystal fibres. LVIS generating apertures drilled in MOT mirrors have been established as detrimental influences on the quality of MOT clouds in close approach to fibre facets.

I have performed atom guiding experiments over one quasi-photonic crystal fibre and two photonic crystal fibres. The sensitivity of our optically based flux detection system has been identified as a strong candidate for the lack of data.

Fibre-guide traps have been progressively refined such that the most beneficial advancement would be an upgrade of the flux detection system. To this end a new fibre trap has been designed and constructed, this is described in section 8.3.

8.2 Critique

The following is a list of procedures and physical changes which the author thinks may be of use in future atom guiding experiments or was not wholly satisfied with after conclusion of previous experiments.

Procedural :

- A greater detuning range could be used in dropped MOT guide work to investigate the $\sim 50\text{GHz}$ predicted turn-off point of radiation pressure forces discussed in section 5.2.4.
- Improvement in the effectiveness of every guide applied could be achieved if further work could be done on the addition of a second molasses cycle. This

work, (not reported herein) was truncated due to time limitations. Better characterisation of both, computer pulse timings and spatial beam shifts from the acousto-optic modulator may help identify the source of signal anisotropy.

- For atom guiding in general, a far-off resonance guide beam of superior power to that reported in chapter 4, would offer the possibility of guiding with significant suppression of spontaneous emission heating. This would allow better characterisation of the transient effects reported in section 5.1.5

Design :

- If in-house drilling techniques permit, smooth edged mirror apertures down to a few hundred μm diameter would allow formation of a very narrow LVIS flux and possibly sustenance of a more complete MOT cloud while positioned above a fibre. This may help guided atoms overcome any disruptive scattering on route to the fibre entrance and help them pass through weak, parasitic, high-order modes within the hollow core.
- If our optical detection system is to be re-used for any further flux measurements, an improvement to the minimum detectable level could be gained by using an elliptically shaped probe region, vertically aligned to have atomic flux drop through its major axis. This would ensure a higher number of atoms were fluorescing at any one time, and they would do so for a time longer than that of a narrow probe. Furthermore the elliptical shape would better fill the PMT sensor surface; further improving fluorescence probe efficiency.

8.3 Hotwire Fibre-Guiding Trap

The most practical change recommended for our fibre-guide traps is an upgrade to a superior flux detection system. Features which should be retained include, the support of a ‘clean MOT’ (no LVIS outflux), a lack of cooling and hyperfine light in contact with the fibre, a clear path between guide launch-lens and fibre entrance (no cooling optics in between) and sufficiently fine control of MOT

location to enable fibre-MOT separations down to $\sim 0.5\text{mm}$. Features which should be suppressed, if possible, would be fibre vibration and both conductive and radiative heat transfer from the Rubidium oven.

Hence the latest fibre-guiding trap incarnation, dubbed the “Hotwire trap”, has retained the Cross trap’s exterior glass housing and mirror/QWP assembly and has a few important additions to address the concerns above. A schematic of it is shown in Figure 8.1.

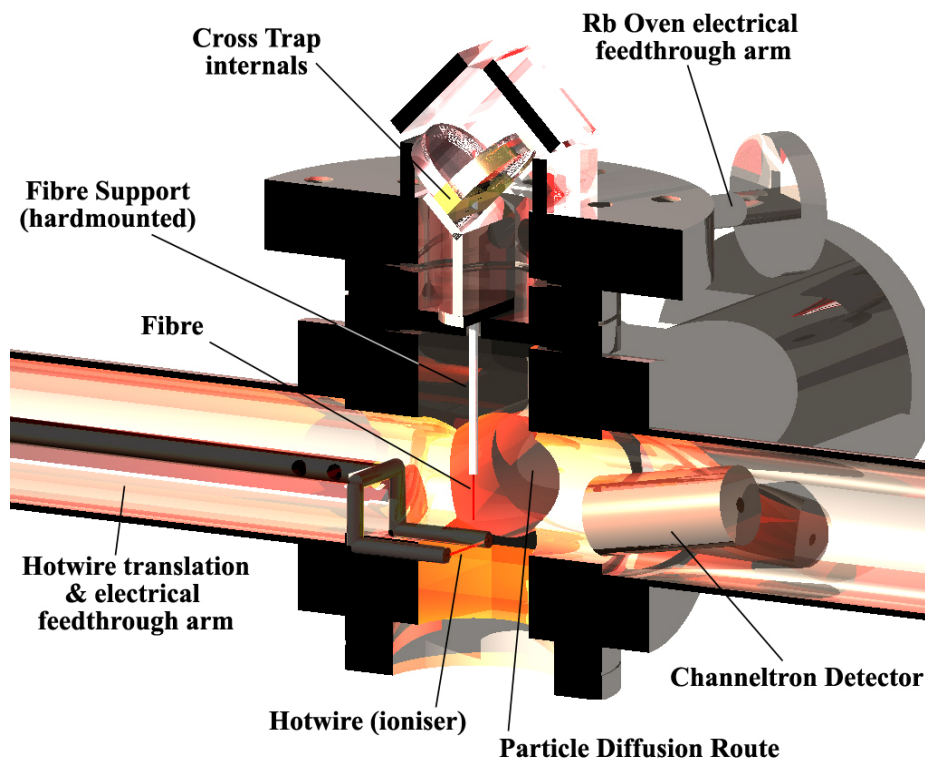


Figure 8.1 : A schematic of the latest fibre trap constructed at St Andrews designed by David Gherardie. Notably the detection system is now changed to a hotwire and channeltron detector. There is also a 4mm diameter pipe (not shown) running from the MOT chamber down through the flanges into the diffusion-output arm; this serves to aid evacuation of the MOT chamber, and ensures the diffusing particles do not drift towards the hotwire detection area.

A commercial 6-port UHV connection cube serves as the main detection chamber and connection hub for UHV components, this is shown better in Figure 8.2. Notably a 1cm length of $\sim 75\mu\text{m}$ diameter Rhenium wire is exposed beneath the fibre to ionise any emitted flux. The wire is electrically heated to $\sim 2000^\circ\text{C}$, at which temperature incident atoms will be ionised and subsequently re-emitted in an

approximate hemispherical pattern (centred on a path normal to the wire surface). A channel electron multiplier (CEM) detector is positioned in a slightly elevated position relative to the hotwire (as high as the UHV pipe would allow) and faces down towards it. In this configuration the $\sim 4\text{mm}$ wide detection aperture of the CEM sits within the natural emission region of the ionised atoms. On top of this, the ion flux collected into the CEM is significantly increased by an applied potential of $\sim 1000\text{V}$. Hence it will collect a considerable percentage of wire emitted ions. In fact we predict a detection efficiency of $\sim 35\%$ of all atoms discharged from the fibre. This will make even small flux rates easily detectable.

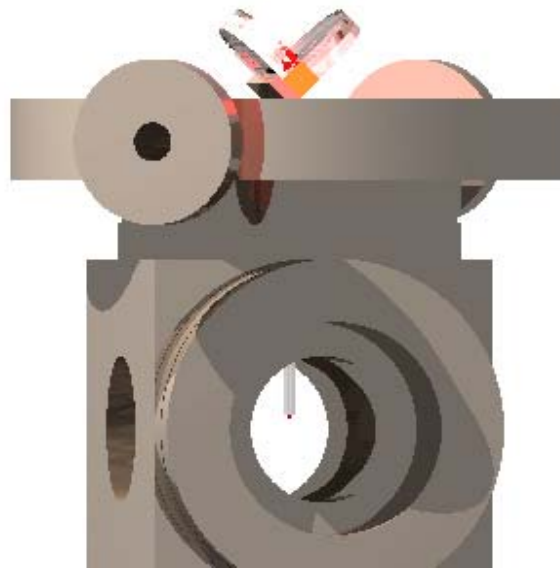


Figure 8.2 : Side view of the hotwire trap model. Shown here without glass housing around the mirror and QWP assembly. Fibre length is 6.9cm. Image courtesy of Dr.D.Gherardie.

Furthermore the hotwire (and hence detection point) can be translated in one axis across the output flux path (see dark grey arm running in the left UHV pipe in Figure 8.1). In this way a profile of the atom output NA can be obtained thus providing important information on the loss rate due to viscous/spontaneous heating and attenuation of the dipole-potential along the fibre. Positive results from this trap will provide figures for flux dependence on guide power and guide detuning, and of course on the fibre's atom transmission efficiency.

In terms of fibre access, a near identical system to that of the cross trap exists. That is, input guide coupling will be performed by the same 38.1mm lens, and output mode analysis will be performed by a new super-long working distance (S-LWD) $\times 20$ microscope objective. Alternatively, dependent on viewport condition after bake-out, a S-LWD $\times 10$ objective may be used for fibre analysis and the new $\times 20$ may be used for fibre input coupling; its working distance of 30.1mm has been accounted for in the design of the MOT-chamber housing, hence optical coupling efficiencies through the “BG19_800” fibre are expected to approach $\sim 75\%$ irrespective of fibre length (this is the figure achieved when not constrained to use the 38.1mm coupling lens). The fibre length currently mounted within the trap is 69mm.

The above reasons, combined with previous experience of fibre-guiding traps, encourages sincere confidence in the guiding, and importantly, detecting ability of this trap. We remain cautious yet very optimistic that this trap will satisfy the original goal of this thesis by successfully observing a guided atom flux.

8.4 Relevance and Outlook

Overall, it is believed this research has contributed to the furtherance of the field of optical atom guiding. Within the remit of free-space guiding both optical potentials and transient effects of guide beams have yielded novel results. More importantly multiple possible routes to a successful result in fibre guidance have been eliminated in sequence and the next step identified and created (hotwire detection).

It is believed this is an important field to work in since positive results are expected to produce such devices as atom interferometers, atomic gyroscopes, and 3D atom lithographers. The author believes these will have sizeable positive effects in multiple demographics.

As stated, the furtherance of this research depends on a successful fibre guiding result. If this is not forthcoming, thorough analysis of the optical mode structure within hollow-core photonic bandgap (PBG) fibre will likely be the next research topic. However, if/when hollow-core PCF guided atoms are detected (in our

team, or any of the three known competing teams^{1,2,3}), optimisation of all the guiding factors discussed herein will be the first goal, likely followed by extension of the guide path. Bose Einstein Condensates will most probably be the desired atom source and long distance guiding in novel PBG fibre structures^{4,5,6,7,8} will be a major research topic (e.g. in-fibre flux manipulation and/or filtering).

Work is currently ongoing in St Andrews to detect fibre-guided atom flux.

8.5 Bibliography

-
- ¹ Klaus Sengstock, Universität Hamburg, <http://www.physnet.uni-hamburg.de/ilp/sengstock/en/AtomGuiding.php>
- ² Tetsu Takekoshi, Brian Patterson, Brooke George, Randy Knize, “Atom guiding in hollow core photonic bandgap fibers”, (U.S. Air Force Academy), (2006).
- ³ Wolfgang Ketterle and Carl Wieman, MIT, http://cua.mit.edu/ketterle_group/home.htm
- ⁴ Myers, S.; Dawes, J.; Fussell, D.; Magi, E.; Eggleton, B.; Eggleton, B.; McPhedran, R.; de Sterke, M., “Reduction of spontaneous emission in tapered photonic crystal fibres”, Lasers and Electro-Optics Society, 18th Annual Meeting of the IEEE, Pages 451 – 452, 22nd-28th Oct. (2005).
- ⁵ F. Couny, F. Benabid, and P. S. Light, " Large-pitch kagome-structured hollow-core photonic crystal fiber," Opt. Lett. 31, 3574-3576 (2006).
- ⁶ Jeong I. Kim, “Analysis and Applications of Microstructure and Holey Optical Fibers”, Ph.D. Thesis, Virginia Polytechnic Institute and State University.
- ⁷ “Atom Optics with hollow optical systems”, Heung-Ryoul Noh, Wonho Jhe, Elsevier Science, preprint submitted 2nd March, (2002).
- ⁸ See leading manufacturer “Crystal-Fibre” website : <http://www.crystal-fibre.com/products/airguide.shtm>

Appendix i

Bessel Beam Guiding in the Glass Trap

Bessel beams are known for their narrow central features and extended ‘diffractionless’ propagation. Early work at St Andrews involved use of the lowest order, J_0 , Bessel function to provide a beam with a central maximum for guiding atoms. This was chosen in particular for its ability to achieve particularly narrow central features suitable perhaps for coupling atoms into narrow core hollow fibres.

A J_0 Bessel beam was initially passed through thermal Rubidium (Rb) vapour and aligned to pass through an aperture in a plate dividing the trapping volume. This provided 2 distinct trapping volumes; one populated by Rb vapour and the other a ‘clean’ vacuum in which to detect guided atoms. A second batch of experiments repeated this procedure with the addition of a cold atom MOT in place of the thermal vapour. Guiding was not achieved in any detectable manner due to trap design.

These experiments were performed in a vacuum trap labelled the ‘Glass’ trap. A description of this trap and of Bessel beam generation is given below. This is followed by procedural details of the Bessel guiding experiment and the intended experimental direction indicated by the Bessel guiding result.

Particulars of the Glass Trap

The first trap used in the course of this PhD, the Glass trap, differed greatly from other free-space traps as it’s main chamber for atom manipulation was located in a custom blown-glass section. This piece, shown in Figure 1, was manufactured by our resident glass blower, Fritz Akerboom, (a skilled craftsman responsible for all our blown-glass and precise fibre mount structures).

The partition was made of 1mm thick glass and had a 1.5mm \varnothing aperture at it’s centre. It effectively divided the vacuum chambers as atom vapour had a negligible diffusion rate through the aperture. Thus only guided atoms could feasibly enter the detection chamber. An extra outflux tube blown into the wall of the detection chamber

provided a pump-out path for atoms in this chamber (the tube was deemed narrow & contorted enough to prevent atom influx).

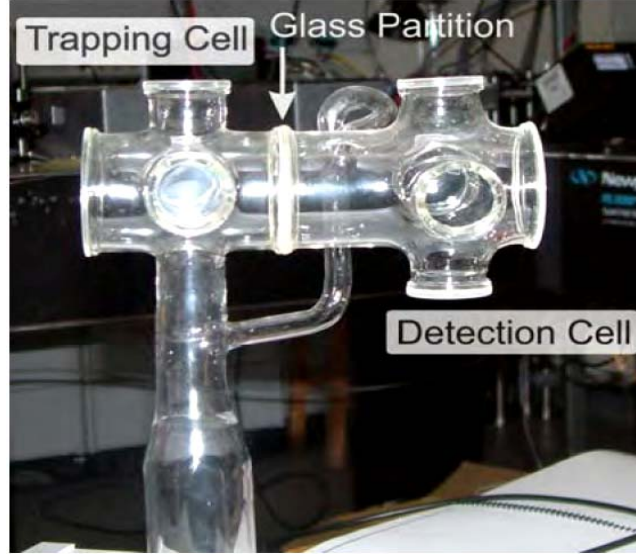


Figure 1 : The Glass trap, shown without trapping and SHIM coils. The glass partition served to isolate the Rb vapour in the volume of the trapping cell. This ensured lower noise levels in the detection cell.

Laser light entered through optical-quality glass windows bonded to the blown structure. A sixth MOT arm entered vertically through the adjoining steel vacuum system on the underside of the trapping volume. Typical MOT clouds of $\sim 10^7$ atoms were generated in $\sim 1\text{mm}\varnothing$ clouds.

LVIS Generation

LVIS generation in the glass was made problematic by the aperture in the glass partition. The necessity of aligning the cloud with the aperture forced the LVIS-generating beam shadow to be similarly aligned through the 1.5mm aperture. This caused the diffractively filling LVIS shadow to mix with a high level of distortion from the edges of the glass aperture. This resulted in a highly distorted LVIS plume which was wispy and insubstantial at best. Nevertheless typical LVIS atom flux rates of $\sim 10^6\text{s}^{-1}$ were achieved; guiding was attempted with these LVIS remnants.

Bessel Guiding Procedure

It was hoped atoms would be optically guided from the Rb populated chamber through the aperture into the detection chamber where a waiting probe beam would confirm their passage. Thus the guiding ability of the guide beam could be confirmed and its efficiency investigated.

Thermal Rb atoms were found to have too high a transverse kinetic energy, hence a MOT with a LVIS tail directed towards the aperture was created to provide atoms already moving in the desired guide direction and with lower transverse momentum. A CCD still of trapped atoms in the glass trap is shown in Figure 2.

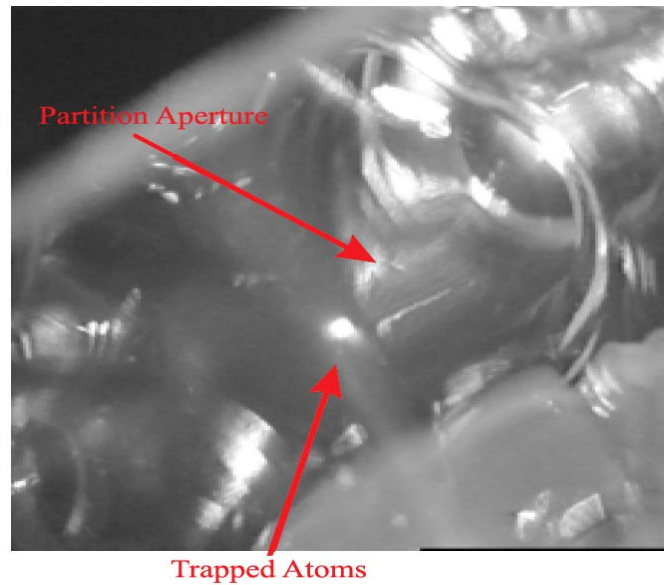


Figure 2 : Atoms trapped in the Glass trap. The cloud is seen before the magnetic coils were used to translate the cloud into alignment with the aperture and before the LVIS inducing shadow was introduced. The surrounding glass structure looks very distorted due to the shape of the glass wall through which the camera is looking; this was a drawback of the glass trap.

The J_0 Bessel function projected into the trap along the main axis through the partition aperture. The central feature of the projected Bessel profile had a diameter of $\sim 200\mu\text{m}$. It propagated at this diameter with a Rayleigh range of $\sim 28\text{cm}$, which was centred on the MOT. Its red detuning was varied from 0 to 10GHz from resonance and its power was varied from 100mW to 500mW. The narrow central feature of the Bessel was thought ideal for passing through the 1.5mm diameter aperture, however it

was approximately a tenth of the MOT cloud diameter, this miss match raised fears of low coupling efficiency from LVIS into the guide.

Bessel Guiding Results

The aperture separating the two chambers was the downfall of this design as it was found to disrupt the passing cooling beam. Micro-fractures surrounding the drilled hole caused phase and amplitude distortions in the passing beam such that a large interference effect skewed the atom cloud and generated a greatly distorted LVIS when aligned with the aperture. Attempts to shadow the aperture with a black-spot mask in the incident cooling beam proved fruitless as the $1.5\text{mm}\varnothing$ was greater than the width of the cloud, thus no stable MOT could then be supported. The guide passing the MOT then the aperture, collinear to the cooling beam, was not effected by the aperture until entering it. Thus the quality of the guide within the aperture (and immediately after it) may not have been optimum for guiding atoms through. Regardless, the lack of stable atom cloud to guide from, forced experiments to stop.

There were also important concerns regarding the amount of power available to the central guiding feature in the Bessel beam; the interference pattern spread a significant portion of its intensity throughout the surrounding rings. This may have contributed to the lack of thermal atom guiding.

Hence, it was decided another trap design offering clear optical access should be considered. In this trap a more simple guide with an easily defined power distribution should be used. The 10-way trap was built immediately after and experiments on red-detuned Gaussian guiding were continued on this.

Appendix ii

Method of MOT Characterisation

It was often necessary to have figures for, the number of atoms in the MOT cloud and the cloud dependence on magnetic coil current. Knowing the cloud volume early in the atom-oven's lifespan allowed later comparison when oven output was thought to be waning. Here we briefly discuss the method used to obtain this figure.

A small portion of the fluorescence emitted from atoms in the cooling cycle was captured and scaled to give an approximate number of atoms. This was achieved by positioning a 2", $f=90\text{mm}$ lens as close as possible to trap center ($\sim 180\text{mm}$) against one of the small viewports (see Figure 1). A photodiode was then placed at a distance where the captured fluorescence would fill the photodiode surface. A tapered opaque tube shielded the space between the lens and photodiode to reduce noise.

Voltage levels were recorded with and without a cloud present to allow background signal removal; with no cloud present the cooling beams still stimulate emission from the background vapor pressure. The fluorescence with all beams on and the magnetic coils deactivated was subtracted from the cloud-present level. It is conceded that the magnetic field will alter the background fluorescence level because of the Zeeman effect, however the total change is negligible compared to the fluorescence of the cloud.

Next a calibrating, weak laser beam was sent to the photodiode and set to generate the same voltage level as produced by the cloud. This provided a power level equivalent to the light captured from the atoms, however this is only a small fraction of the total light emitted isotropically. The solid angle subtended between the MOT and the lens was found by measuring the diameter of the lens accessible to the passing fluorescence. The solid angle was used to scale up the power received to a total level corresponding to the entire cloud fluorescence and so the number of photons emitted per second was obtained. Finally this power was divided by the scatter rate (number of photons emitted per second) of single atoms, given in equation 1.7, where the

incident intensity was taken as the sum of the trapping light hitting the cloud. The resultant figure is an approximation of the total number of atoms held in the MOT cloud. Numbers for this trap were typically around 2×10^7 atoms in a 1.5mm diameter cloud.

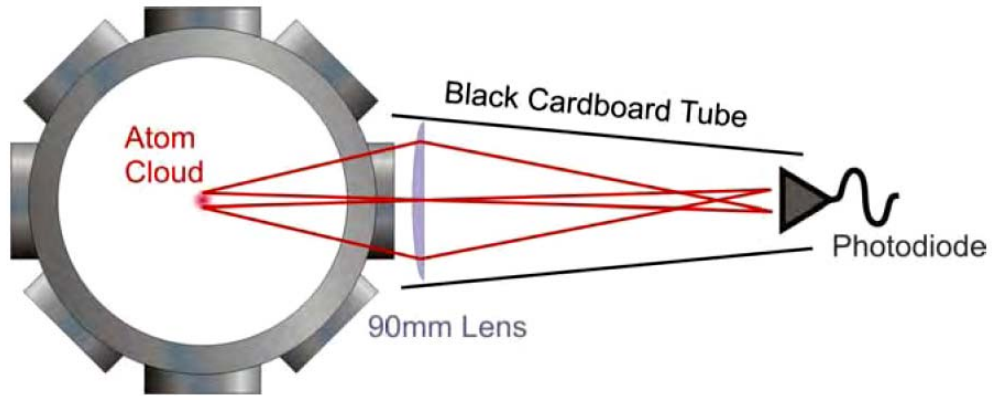


Figure 3 : A schematic showing the arrangement for collecting fluorescence from the MOT cloud. The lens was positioned $\sim 180\text{mm}$ from MOT center. This allowed an approximate calculation for the number of atoms in the cloud.

With this process as a blue-print, the contribution of some of the major MOT components could be investigated. That is, the effect of oven current on trap filling time and the magnetic coil current on the number of atoms.

Appendix iii

Measurement of Trap Filling Time

Trap filling time was of importance when attempting to minimize the time between successive cloud drops; particularly when a time limit was set by unwanted thermal expansion surrounding optics. The cloud size was monitored over time while the Rb ovens were held at constant drive. A digital Tektronix TDS360, oscilloscope recorded the fluorescence signal over tens of seconds. As expected, quickening of trap filling time was seen with increasing background vapor pressure. Atom build up followed an exponential form similar to that of a capacitor charging, described by;

$$N(t) = N_0(1 - e^{-t/\tau}) \quad \text{a)}$$

where τ is the time constant for the trap filling time (also the average time an atom will remain trapped). Figure 1 shows the number of atoms and the filling times of the trap. Trap volumes were varied between those shown below, with occasional spikes up to $\sim 3.5 \times 10^7$ to aid detection of long-distance cloud drops.

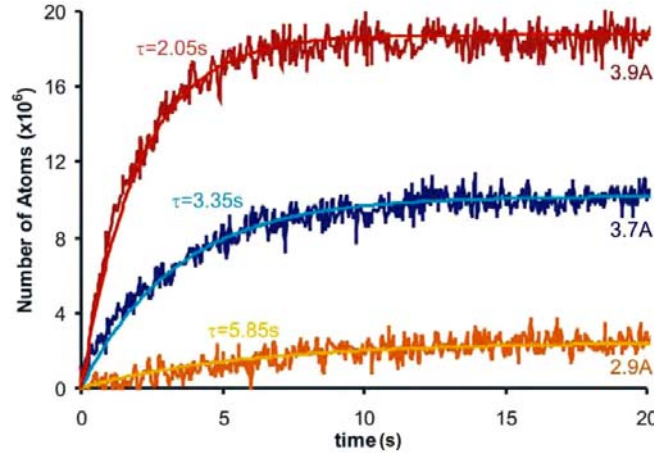


Figure 4 : Cloud filling as a function of time at 3 different oven currents (indicated). The smooth curves are best-fit lines from equation a). The trap filling time, τ , decreases with increasing vapor pressure (increasing oven current).

In a similar manner, cloud size was monitored as the coil currents were varied; increasing coil current provided tighter confinement due to greater positional dependence associated with steeper field gradients. However this prevented the cloud expanding continuously and created an upper limit for the cloud size.

Appendix iv

Oblique LG Guidance from a LVIS

Following successful collinear LVIS extension experiments, (see Dr. Rhodes thesis), we investigated guidance of LVIS atoms at an oblique to the LVIS flux. This was an important step towards an atomic beam splitter. LG profiles were used as guiding potentials due to their low intensity centre; offering low spontaneous emission atom transit.

Red-detuned guideⁱ and Raman pulsesⁱⁱ have been used to split atomic ensembles. Our experiment proved significant as the results contrasted significantly with those of Yan *et al.* who performed a similar experimentⁱⁱⁱ where LVIS atoms were directed vertically with gravity and were intersected by a counter-propagating, 8° oblique hollow light guide. They report a splitting of ~50% of atoms from LVIS into the hollow guide. However we believe they may have mistaken atoms *deflected* from the outside of guide for atoms *guided* within.

Procedure

An LG $l=3$ guide beam was directed on the horizontal plane, $\sim 8^\circ$ oblique to the LVIS. This setup was as close as possible to that of Yan *et al.* The experimental geometry is shown in Figure 1 with the angles exaggerated to better illustrate the arrangement (and effect on the atoms).

An LVIS of $\leq 900\text{mm}$ diameter was created and a guide beam diameter of $\sim 600\mu\text{m}$ was chosen for optimal atom capture. A maximum power of 180mW in an LG $l=3$ profile was used. Two CCD cameras were positioned orthogonally to each other and used for beam alignment and data capture.

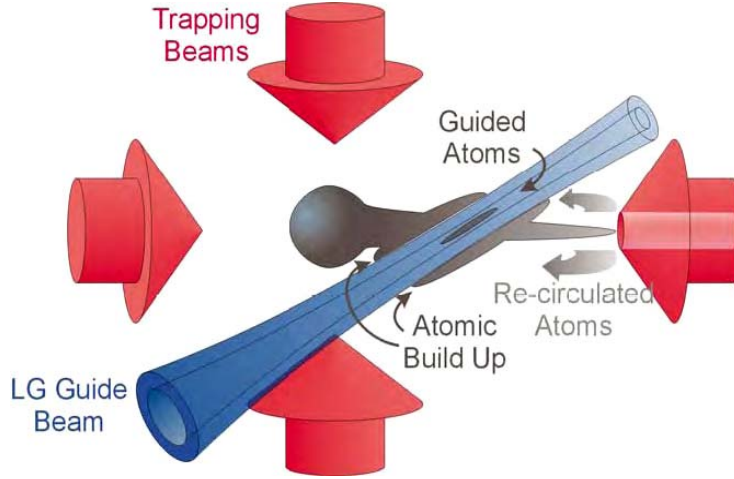


Figure 5 : Experimental geometry for LG guide entry oblique to LVIS flux. The angle separation between guide and LVIS has been exaggerated from its experimental 8° . Note atom build-up on either side of the guide beam and the small number of atoms present within the hollow guide.

Results

Two dark lines, corresponding to the walls of the guide parallel to the CCD viewing axis, were expected to appear across the LVIS flux. These were visible due to atom heating from the guide. A build up of atoms on either side of the guide and a little in the hollow region was seen, however no flux was observed propagating along the guide centre. Captured CCD results are shown in Figure 2.

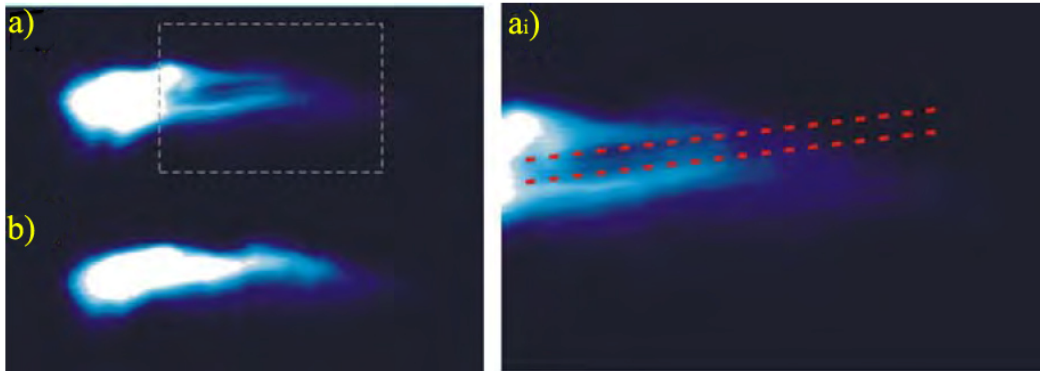


Figure 6 : CCD images of, a) a LVIS with a $600\mu\text{m}$ diameter oblique guide incident and b) the same LVIS with no guide beam. In ai) a closer inspection of a) highlights the guide path in red. Two dark lines reveal the guide walls and a build up of atoms on either side of the guide. A narrow trail of atoms can also be seen in the guide centre, however this trail does not extend beyond the LVIS shadow region, nor is it a substantial number of atoms.

It was necessary to ensure the guide was on the same plane as the MOT beam so that the 8° was the only angular displacement from the LVIS flux. Obliquity in multiple axes could result in a false negative result which would look similar to that above. However many, purposefully misaligned, beams were viewed from multiple angles to confirm correct alignment (final arrangement viewed in 2 axes to confirm). Much work was done to confirm the lack of atoms *within* the guide beyond regular LVIS length and to determine the source of the atom build up around the guide.

Consideration of Results

The LG $l=3$ guide, at an angle of 8° , can confine atoms with a maximum transverse velocity of 1.3m/s. Thus it should be able to capture a sizable number of relatively slow moving LVIS atoms. The lack of guiding can be explained by the fact that the guide resembles a closed pipe. Atoms flowing along LVIS will first encounter a potential-wall, if they have sufficient longitudinal velocity to carry on through this wall they will experience an identical wall a few hundred microns later. These atoms have already shown they have sufficient energy to traverse one wall thus the second identical wall will similarly fail to capture them. Thus atoms which pass through one side of the ‘pipe’ will pass the guide completely and will likely be recycled back towards the MOT cloud by the surrounding cooling beams.

This explains the build up of atoms on the underside of the guide beam; these atoms are recycling back towards MOT centre and being interrupted by the guide beam during their cooling process. Thus the guide will only *disrupt* the atoms path; either they will ricochet off the guide into the cooling beams or will build up against the side of the guide. Even a guide passing through MOT centre will have very few atoms entering the guide core as these would be unable to cool and fall into MOT/guide centre. In retrospect these are fairly intuitive results and are indicated in Figure 1

These theories were confirmed by translating a TEM₀₀ beam of matching size and detuning to that of the LG guide through the MOT and LVIS; the same pattern of LVIS and MOT distortion was seen including the *deflected* atom build-up on the guide walls. The effects of guide detuning and position were also investigated. They

were found to confirm the above results and demonstrated the expected turn-off of guide influence with greater detuning from atomic resonance.

Comparison with Published Work

In comparison, the LVIS splitting reported by Yan *et al.* presented no difficulties with coupling into a closed light-pipe, and notably no effect on LVIS itself. An image from their results is shown in Figure 3, here the plume emitted from the LVIS is said to be a flux guided within the dark hollow beam. The author believes this is actually a *deflected* atom flow mistaken for a *guided* atomic flux.

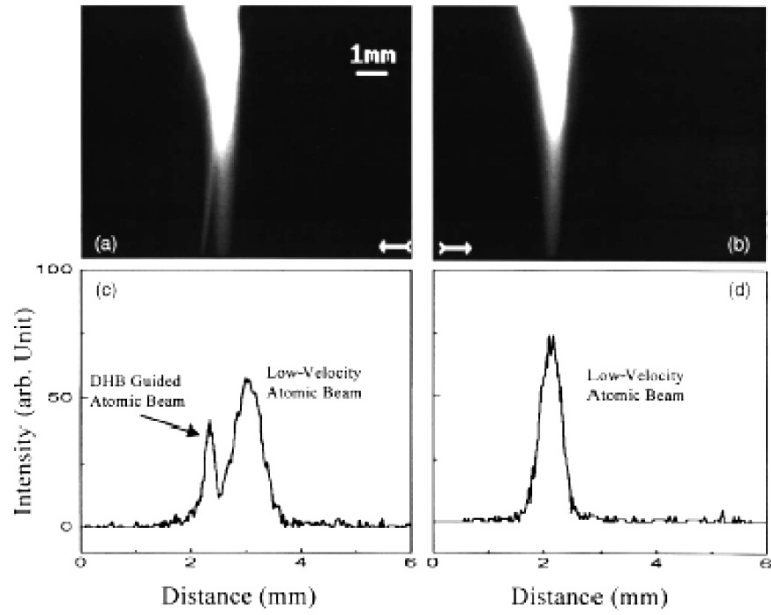


Figure 7 : Results of LVIS splitting published by Yan et al. in their 2000 paper³. Note, the lack of LVIS perturbation from the guide beam, and a ~50% flux coupling into the guided atomic beam. The upper images a) and b) are CCD stills with and without the hollow guide and the lower graphs c) and d) are intensity profiles taken along a line at the marked position.

Pierced-Pipe Oblique LG Guidance

In St Andrews we implemented a solution whereby a gap in the dark hollow beam (or ‘light-pipe’) was introduced in the region where atoms were due to impact. That is, an opaque obstruction was carefully translated such that it pierced the circular profile of the LG beam at its waist. The pierced profile was imaged into the trap and

the obstruction rotated azimuthally around the beam till the imaged aperture faced the oncoming LVIS atoms. A schematic of this setup is shown in Figure 4.

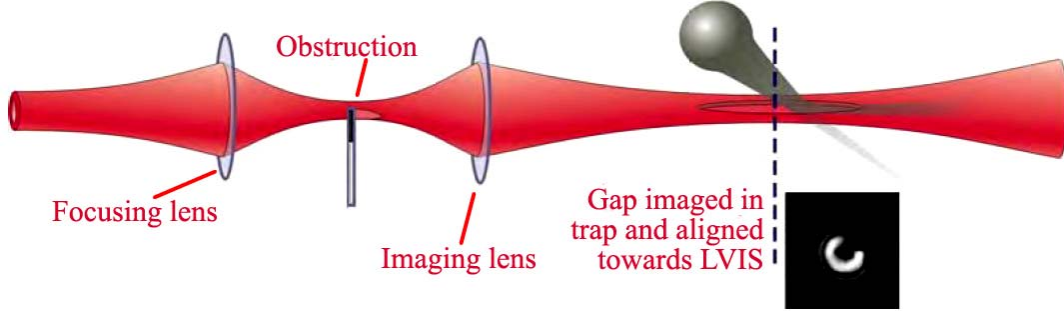


Figure 8 : Schematic showing the arrangement of focusing $f=500\text{mm}$, and imaging $f=300\text{mm}$, lenses used to image the pierced LG profile into the LVIS flux path.

An advantage of the pierced-LG technique is the beam's ability to diffractively repair itself after the obstruction. Theoretically the LG could provide a beam of uniform, symmetric, intensity around its profile before, and a short distance after, the obstruction. Thus the atoms would experience more efficient capture *and* prolonged confinement.

Pierced Pipe Oblique LG Guidance, Results

Analysis along the Rayleigh range of the pierced guide showed the aperture persisted for a distance greater than 20cm; far beyond the range of guiding, and beyond that measurable on our optical table.

Thus the LVIS atoms in our experiment never truly experienced full 2D confinement, however the far side of the LG profile provided a barrier sufficient to deflect them in the guide direction while inside the semi-closed 'light pipe'. Figure 5 and Figure 6 illustrate the resultant flux enhancement.

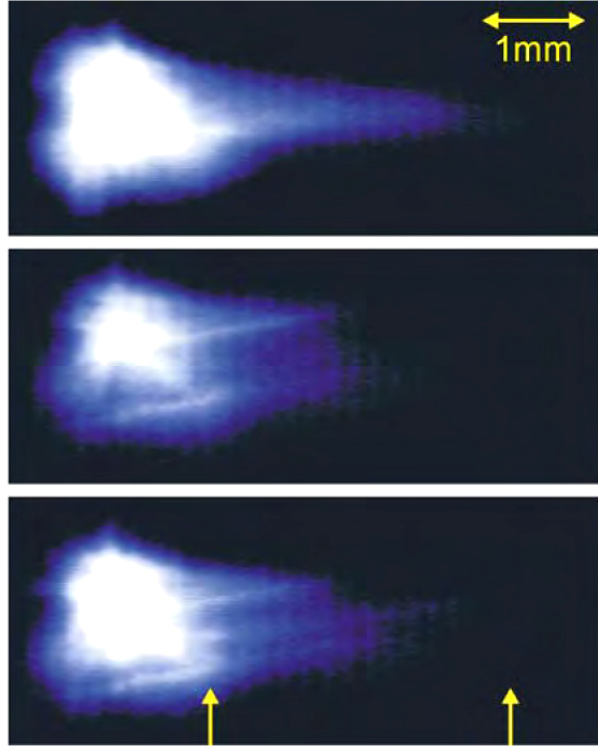


Figure 9 : CCD images of the LVIS atoms with and without incident guide beams. At top, an unperturbed LVIS flux. Middle, the same LVIS with a conventional 180mW LG $l=3$ guide beam incident at 8° to flux direction. Bottom, the same LVIS with a 'pierced' 180mW LG $l=3$ incident at 8° obliquity. Note the increase in fluorescence in the centre of the $600\mu\text{m}$ wide guide profile. The yellow indicators mark the length profiled in Figure 6. (The vertical striations are an unavoidable interference pattern generated in the camera lens optics).

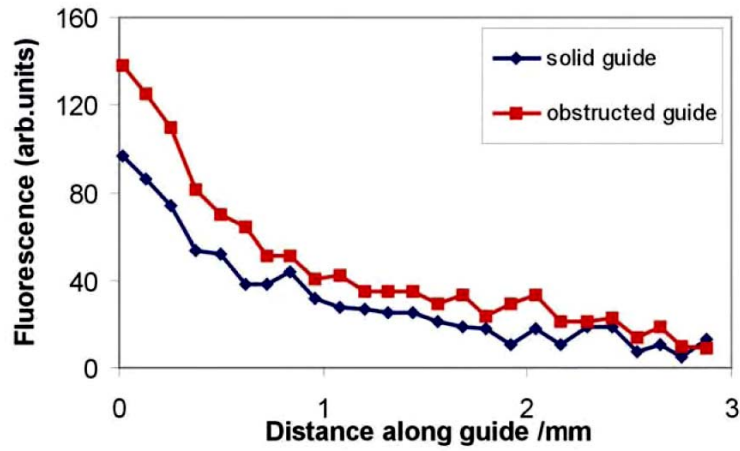


Figure 10 : Intensity profiles taken along the flux shown in Figure 5, sampled between the yellow markers. The pierced guide is shown to have a $\sim 50\%$ increase in flux along its length.

The insertion of the obstruction into the guide clearly provided an increase in atom coupling into the centre of the LG profile. The atomic flux in the centre is ~50% higher than that of the standard LG (measured at a point 2mm from MOT centre). It is believed this measurement would be higher if the aperture closed sooner; some atoms are expected to have ejected back through the open aperture following collision and repulsion from the internal guide wall.

Computer simulations indicated alternate beam profiles which would serve as better guides. However these were not investigated further. This work is presented here in order to highlight possible inaccuracies in published work and to give an account of the authors research.

Bibliography

-
- ⁱ O. Houde, D. Kadio, L. Pruvost, “*Cold Atom Beam Splitter Realized with Two Crossing Dipole Guides*”, Phys. Rev. Lett., Vol. 85, #26, p5543, (2000).
- ⁱⁱ M. Kasevich and S. Chu, “*Atomic Interferometry Using Stimulated Raman Transitions,*” Phys. Rev. Lett., #67, p181, (1991).
- ⁱⁱⁱ M. Yan, J. Yin and Y. Zhu, “*Dark-hollow-beam guiding and splitting of a low-velocity atomic beam*” J. Opt. Soc. Am. B, #17, p1817, (2000).

Cut,
print that,
check the gate,
that's a wrap.